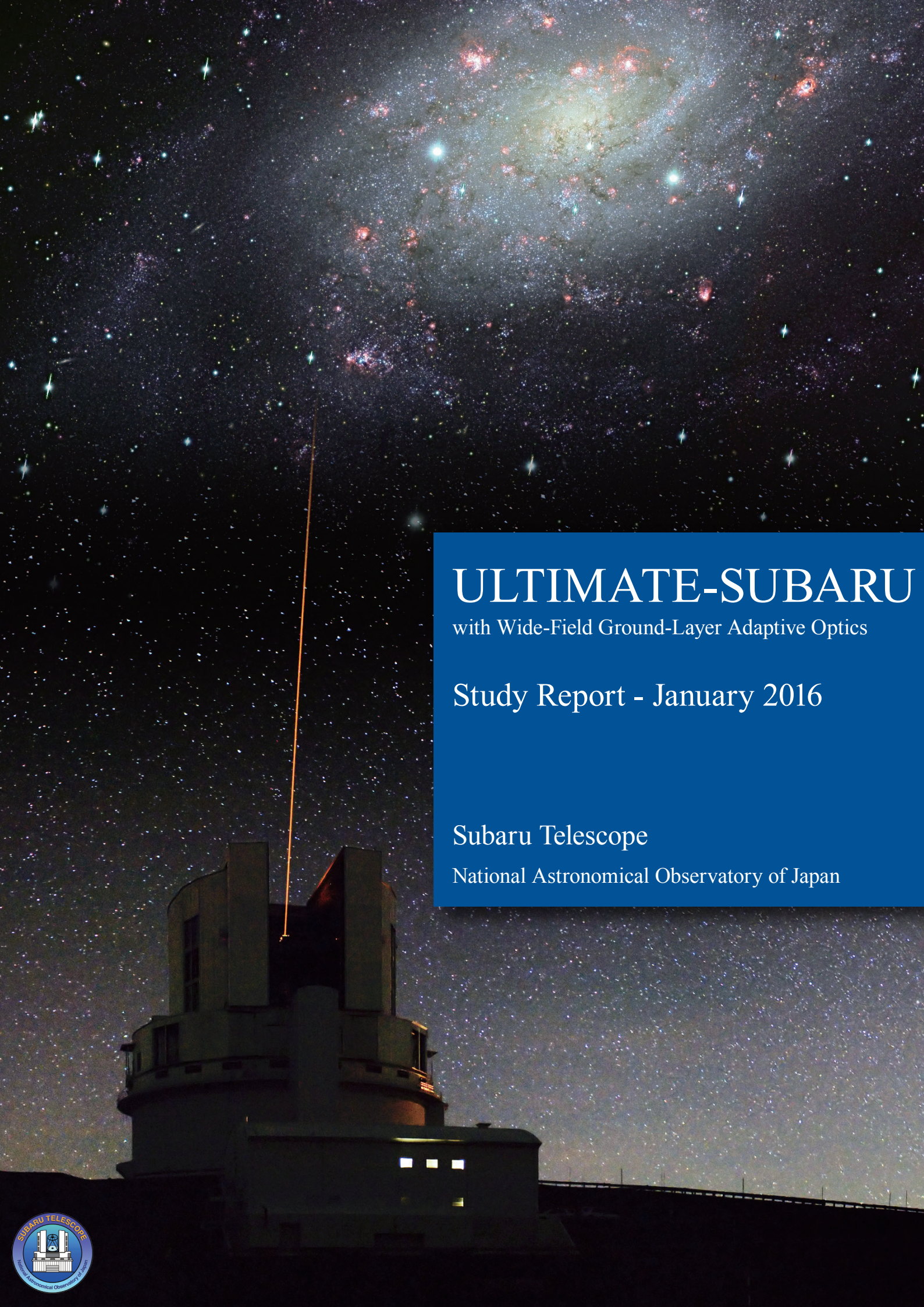

ULTIMATE-SUBARU

with Wide-Field Ground-Layer Adaptive Optics

Study Report - January 2016

Subaru Telescope

National Astronomical Observatory of Japan

ULTIMATE-Subaru Study Report 2016

ULTIMATE-Subaru working group & science team

ver. 2016/1/13

Contents

Team Members

ULTIMATE-Subaru Working Group

Masayuki Akiyama	Tohoku University
Nobuo Arimoto	Subaru Telescope
Christophe Clergeon	Subaru Telescope
Maximillian Fabricius	Subaru Telescope
Takashi Hattori	Subaru Telescope
Yutaka Hayano	National Astronomical Observatory of Japan
Ikuru Iwata	Subaru Telescope
Tadayuki Kodama	National Astronomical Observatory of Japan
Yusei Koyama	Subaru Telescope
Olivier Lai	Subaru Telescope
Yosuke Minowa	Subaru Telescope
Kentaro Motohara	University of Tokyo
Yoshito Ohno	Tohoku University
Shin Oya	National Astronomical Observatory of Japan
Hideki Takami	National Astronomical Observatory of Japan
Naruhisa Takato	Subaru Telescope
Ichi Tanaka	Subaru Telescope

Science Team and External Collaborators

Jessica Bloom	University of Sydney
Julia Bryant	University of Sydney / Australian Astronomical Observatory
Fuyan Bian	Australian National University
David Brown	Australian Astronomical Observatory
Julia Bryant	Australian Astronomical Observatory
Andy Casey	Australian National University
Masashi Chiba	Tohoku University
Scott Croom	University of Sydney
Richard Dekany	Caltech Optical Observatories, California Institute of Technology
Simon Ellis	Australian Astronomical Observatory
Peter Gillingham	Australian Astronomical Observatory
Masao Hayashi	National Astronomical Observatory of Japan
I-Ting Ho	Australian National University
Yuji Ikeda	Photocoding
Masatoshi Imanishi	Subaru Telescope
Daisuke Iono	National Astronomical Observatory of Japan
Lisa Kewley	Australian National University
Jin Koda	Department of Physics and Astronomy, Stony Brook University
Kotaro Kohno	IoA, University of Tokyo
Jon Lawrence	Australian Astronomical Observatory
Sarah Leslie	Australian National University
Chris Lidman	Australian Astronomical Observatory
Yuichi Matsuda	National Astronomical Observatory of Japan
Noriyuki Matsunaga	University of Tokyo
Alan McConnachie	Herzberg Institute of Astrophysics
Kimihiko Nakajima	Observatoire de Genève, Université de Genève
David Nataf	Australian National University
Shogo Nishiyama	Miyagi University of Education
Yumiko Oasa	Saitama University
John Pazder	Herzberg Institute of Astrophysics, National Research Council of Canada
Tae-soo Pyo	Subaru Telescope
Adam Schaefer	University of Sydney
Andy Sheinis	Australian Astronomical Observatory
Takatoshi Shibuya	ICRR, University of Tokyo
Luc Simard	Herzberg Institute of Astrophysics (HIA)
Nick Staszak	Australian Astronomical Observatory
Ken-ichi Tadaki	Max-Planck-Institut für Extraterrestrische Physik
Yoko Tanaka	Subaru Telescope
Julia Tims	Australian Astronomical Observatory
Pascal Xavier	Australian Astronomical Observatory
Tomoyasu Yamamuro	OptCraft
Tiantian Yuan	Australian National University
Ross Zhelem	Australian Astronomical Observatory

Acronyms

AGN	Active Galactic Nucleus
AO	Adaptive Optics
ASM	Adaptive Secondary Mirror
DM	Deformable Mirror
ExAO	Extreme Adaptive Optics
FoV	Field-of-View
FWHM	Full Width at Half Maximum
GC	Galactic Center
GLAO	Ground-Layer Adaptive Optics
HST	Hubble Space Telescope
IMF	(Stellar) Initial Mass Function
JWST	James Webb Space Telescope
LAE	Lyman α Emitter
LBG	Lyman Break Galaxy
LGS	Laser Guide Star
LGSAO188	Subaru 188-element laser-guide-star adaptive optics system
LTAO	Laser Tomography Adaptive Optics
MAOS	Multi-Thread Adaptive Optics Simulator
MCAO	Multi-Conjugate Adaptive Optics
MOAO	Multi-Object Adaptive Optics
MOS	Multi-Object Spectroscopy
MW	Milky Way
NBF	Narrow-Band Filter
NGS	Natural Guide Star
NFIRAOS	Narrow-Field Infrared Adaptive Optics System
PSF	Point Spread Function
SDSS	Sloan Digital Sky Survey
SED	Spectral Energy Distribution
SFR	Star Formation Rate
SMBH	Super-Massive Black Hole
TMT	Thirty-Meter Telescope
TTGS	Tip/tilt Guide Star
WFE	Wavefront Error
WFS	Wavefront Sensor
WISH	Wide-field Imaging Surveyor for High-redshift

Chapter 1

Executive Summary

1.1 Background

ULTIMATE-Subaru is a project to develop the next-generation adaptive optics (AO) system and new instruments utilizing the capabilities of the new AO system, and to carry out unique and strong scientific programs with them. The future infrared instrumentation for Subaru Telescope has been an important issue for Subaru users community from 2000s. Following the Subaru Advisory Committee's recommendation published in 2009, in 2011 Subaru Telescope organized the working group for the next-generation AO involving some researchers in universities in Japan. With conceptual studies and simulations with working group members and discussions among community through science workshops, we have developed the fundamental requirements based on the science cases and specifications for the AO system and the instruments. With the advent of Hyper Suprime-Cam and Prime Focus Spectrograph, it is now clear that the central strength of Subaru Telescope is a combination of wide-field instruments and light collecting power with large aperture mirror. The working group selected Ground-Layer AO (GLAO) as the first priority candidate of the next-generation AO system because it matches quite well with the overall Subaru Telescope's strategy toward wide-field surveys.

1.2 ULTIMATE-Subaru Science Overview

The GLAO system of the ULTIMATE-Subaru project is expected to provide a significant seeing improvement (typically from $0.4''$ to $0.2''$ at K-band) across a wide field of view ($15'$). For point sources (size$\lesssim 0.2''$), we can narrow the photometric aperture and the spectroscopic slit width by a factor of $\sim$2 which corresponds to the sensitivity gain of 0.75 magnitude for the same integration time. For extended sources (size$\gtrsim 0.2''$), we will not sufficiently gain the sensitivity, but instead we can now spatially resolve the internal structures of individual galaxies on a physical scale of 1.5 kpc at $1 < z < 5$ or 0.37 kpc at $z \sim 0.1$ for imaging, slit spectroscopy and IFU observations.

These unique features are greatly enhanced by the dedicated wide-field NIR instruments to be built. We have three such options; wide-field imaging camera with a bunch of narrow-band and medium-band filters, multi-slit spectrograph, and multi-IFU spectropgrah. The combination of GLAO and the companion wide-field instruments will bring some break-throughs in various research areas. Our science cases proposed in this document are summarized in Table 1.1.

1.2.1 High-redshift galaxy science

For high-z galaxies, we aim to conduct the following 5 unique core researches. (1) Ultra-deep, wide-field narrow-band imaging survey (in J-band) in between the OH sky lines will find proto-galaxy candidates at $z > 8$ for future follow-up spectroscopy with TMT (Section 3.1). (2) High resolution narrow-band

Category	Science case	Required instruments & observations	Sec.
High-z (imaging)	Detection of LAEs at $z > 7$	ultra-deep NB imaging (Y and J)	§ 3.1
	Spatially resolve Hα at z=1–3	deep+wide NB imaging (mainly K)	§ 3.2
	Balmer break out to $z \sim 5$	medium-band imaging (mainly K)	§ 3.3
High-z (spec)	Large spec. survey for $z \sim 2$ galaxies	MOS spectroscopy (JHK)	§ 4.1
	IFU survey for z=0.5–1 galaxies	multi-IFU spectroscopy (JH)	§ 4.2
Low-z & Galactic	Paα survey for $z < 0.3$	wide NB imaging (K)/wide-field IFU	§ 5.1
	NIR emission mapping of local galaxies	wide BB+NB imaging	§ 5.2
	Globular clusters in Galactic center	wide BB imaging/MOS spec.	§ 5.3
	S-stars & nuclear star clusters in GC	wide BB+NB imaging	§ 5.4
	Dark matter profile in the Milky Way	R>2000 MOS or multi-IFU spec.	§ 5.5
	Chemical measure of Galactic disk stars	R>3000 MOS spec. (mainly J)	§ 5.6
	Parsec-scale jets in SF regions	wide NB imaging (e.g. FeII, H_2)	§ 5.7
	Low-M end of IMF with YBDs/PMOs	wide JHK imaging + MOS spec.	§ 5.8

Table 1.1: Summary for the science cases propsed in this document and their requirements for instruments on ULTIMATE-Subaru.

imaging of high-z star-forming galaxies will tell us where in galaxies new stars are being formed, how the star-forming activity propagates with cosmic times and how it depends on stellar mass and surrounding environment (Section 3.2). (3) Deep medium-band imaging of compact high-z galaxies will tell us how the stellar mass grows with cosmic times and trace its history back to $z \sim 5$ by capturing the Balmer break features with medium-band filters that split the K-band (Section 3.3). (4) Deep spectroscopy of a truly statistical sample of high-z galaxies ($1 < z < 3.5$) in particular at K-band and kinematics along the slits based on the line profiles and velocity offsets will tell us how the turbulent disks and central bulges are formed and how the gas is removed from the system and star formation is quenched due to feedback (Section 4.1). (5) Multi-IFU observations assisted by GLAO of an unprecedentedly large sample of galaxies at the cosmic noon ($1 < z < 3.5$) will tell us the internal physical properties such as spatial distributions of dust extinction, ionizing states and gaseous metallicities (Section 4.2).

These studies are all strongly benefited by its wide field search and thus high multiplicity together with the high spatial resolution that ULTIMATE-Subaru project can uniquely offer. These will provide excellent targets to TMT for detailed spectroscopic and IFU analyses in 2020s and beyond.

1.2.2 Low-redshit galaxy and the Milky Way science

In addition to the high-redshift galaxy sciences, the expected performance of ULTIMATE-Subaru is ideally suited for a wide variety of astronomy fields. For nearby galaxies (at $z < 0.3$), we can spatially resolve Paα emission line on sub-kpc scale within individual galaxies, allowing us to pinpoint heavily obscured star-forming regions within dusty galaxies (Section 5.1). For our local neighborhood, the wide-field of view of ULTIMATE-Subaru will enable us to cover the entire structure of the galaxies with just one pointing, allowing an extremely efficient, detailed studies on e.g. the physical origins of shocks prevailing in the galaxies with a detailed NIR emission line diagnostics (Section 5.2).

The ULTIMATE-Subaru can also provide a powerful tool for the Milky Way science, particularly for studies on very crowded and/or heavily extincted regions. One of the most important targets would be the Galactic center, where the stellar density and the obscuration are extremely high, hence requiring observations with high spatial resolution at NIR. For example, we will be able to resolve member stars associated with globular clusters (and streams emanated from them) in the Galactic center, and to study their chemo-dynamical properties (Section 5.3). A wide-field astrometric approach will also shed new light on the formation of the Milky way. The combination of high spatial resolution and the wide-field coverage of ULTIMATE-Subaru will allow us to study the origins of S-stars (young B-type stars in the GCs), and potentially discover the hidden cluster remnants (Section 5.4).

The ULTIMATE-Subaru can provide a powerful tool fo a follow-up spectroscopy of some on-going (as well as the future) deep NIR photometric surveys. For example, by performing a systematic follow-up spectroscopy of stars in the Galactic center (which will be detected by WFIRST), we will be able to get spectra of stars at the other side of the Galactic center, and thus to perform a complete mapping of the dark matter profile within ∼2-kpc from the Galactic center (Section 5.5). The unique capability of the deep and wide-field spectroscopy also allows chemical measurements of cepheids or star clusters in the Galactic disk, as a follow-up spectroscopy of other photometric survey (e.g. VVV survey; Section 5.6). Another important target would be Galactic star-forming regions. We can apply the NIR emission line diagnostics to study the physical origins of shocks prevailing star-forming regions (Section 5.7). Also, by searching (substellar) YSOs by making full use of the deep K-band photometry with ULTIMATE-Subaru, we will also be able to study the variety/universality of the low-mass end of IMF (Section 5.8).

1.2.3 Synergy with TMT, and space missions in 2020s

We stress that all the science cases proposed here require wide-field NB imaging, moderate-/high-resolution NIR spectroscopy, or K-band imaging, all of which are not available with WFIRST. It is of course true that space telescopes are clearly stronger in terms of NIR "broad-band" photometry, but ULTIMATE-Subaru can provide an excellent, highly complementary science which can enhance the science outputs from deep broad-band photometric survey performed by WFIRST in early–mid 2020s.

1.3 Subaru Wide-field AO

There are two major wide-field AO, Ground-Layer AO (GLAO) and Multi-Object AO (MOAO). We, the working group of next generation AO system for Subaru Telescope, investigated both AO systems and made a trade-off study, including science case, synergy of other instruments at Subaru Telescope, competitiveness at the ELT era.

GLAO will achieve seeing improvement over the entire $\phi \gtrsim 15'$ field of view (FoV) by correcting only the distorted wavefront caused by the ground layer of the Earth's atmosphere. Although the Strehl ratio achievable with GLAO should be much less than those by other AO systems which provide diffraction limited images, GLAO can correct images over much wider FoV compared to the existing AO systems. On the other hand, MOAO only correct the wavefront errors toward multiple specific objects within a patrol area. Thus discovered science objects are only the targets to observe.

We made numerical simulations to evaluate performance of these systems with Subaru Telescope.

1.3.1 Ground Layer AO (GLAO)

Our major results from simulations for GLAO are as follows.

- Under a typical natural seeing condition (FWHM$\sim 0.4''$ in K-band), GLAO can provide the stellar size of FWHM $\sim 0.2''$ in K-band.
- Factor of 1.5–2 gains are expected on ensquared energy for point sources, compared to observations under natural seeing.
- Approximately uniform wavefront correction over FoV diameter $\sim 20'$ will be achieved. The maximum FoV is limited by mechanical and optical structures of the telescope and instruments.

Since the fraction of the turbulence at the ground layer atmosphere is measured to be relatively dominant in Maunakea, Subaru GLAO could provide good performances.

1.3.2 Multi-Object AO (MOAO)

Our major findings with simulations for MOAO are as follows:

Item	Specification
Guide stars	4 LGS, NGS(2∼4)
Location of guide stars	The edge of FoV $> 15'$ (LGS), Within the FoV (NGS)
Wavefront sensors	Each guide stars (Guide star oriented)
Wavefront sensor type	Shack-Hartmann
Tip-tilt wavefront sensor type	2×2 Shack-Hartmann wavefront sensor or pyramid. (visible or NIR)
Sub apertures	> 100
Frame rate of wavefront sensor	> 500Hz
Deformable mirror	Adaptive secondary mirror
Actuators	∼1000
AO control type	GLAO (LTAO, ExAO modes)

Table 1.2: Basic specification of next generation AO at Subaru Telescope.

- Wavefront correction of MOAO is better than that of GLAO system by using 6 LGSs within a field of regards (FoR) of a radius smaller than $\sim 3'$.
- Tip-tilt guide stars should be close to the target within a FoR to achieve good AO performance. Consequently, the sky coverage of MOAO might be fairly similar to the FoV of the current AO188, a single conjugate AO system with LGS.

Through these studies we have understood expected performances of GLAO and MOAO with the Subaru Telescope in reasonably realistic observing conditions. MOAO will achieve high Strehl ratios for multiple targets, but for the case with 8m-class telescopes, their sky area where MOAO can perform well will be limited; MOAO should be a strong system for 30m-class telescopes. On the other hand, GLAO can provide seeing-improved wide-field images which would not be easily achieved with 30m-class telescopes. Such capability is greatly complimentary to 30m-class telescopes. We concluded that GLAO is the primary candidate for the Subaru next-generation AO.

Therefore, GLAO is our primary candidate as Subaru Telescope Next-generation AO system. It will achieve FWHM $\sim 0.2''$ @K-band over the entire $> 15'$ field of view, under a typical seeing condition.

The strawman basic specifications of GLAO are shown in Table 1.2

1.4 Instrument Overview

In the next decade, the Subaru telescope will offer unique wide-field imaging and spectroscopic capabilities at the prime focus using Hyper Suprime Cam (HSC) and Prime Focus Spectrograph (PFS). To further strengthen the Subaru's wide-field capabilities, we have studied the feasibility and conceptual design of wide-field instruments at near-infrared (NIR) with an aid of ground layer adaptive optics (GLAO) system. Our studies of the GLAO performance and optical design of the telescope suggest that we can expect to obtain uniform seeing improvement (FWHM$\sim 0''.2$ in K band) over the field of view (FoV) of $\phi \leq 16'$ at the Cassegrain focus.

We have conducted the conceptual studies of the ULTIMATE instruments: the wide-field imager, the multi-object slit (MOS) spectrograph, and the multi-object integral field unit (IFU) spectrograph, which fully utilize the capabilities of the GLAO corrected spatial resolution and the widest FoV. Table 1.3 summarizes the baseline specifications of the instruments.

In this study, we found that there are several possible optical designs that almost covers $\phi < 16'.0$ FoV for wide-field imager and multi-object slit spectrograph. However, the cryogenic and mechanical studies of the MOS spectrograph suggest that the total weight of the instruments exceeds the tentative weight limit of the Cassegrain focus, meaning that the MOS spectrograph at the Cassegrain focus is not technically feasible. Alternatively, we have studied a feasibility of installing TMT/IRMS, which is a MOS spectrograph for TMT, at the Subaru Nasmyth focus until IRMS starts its commissioning at TMT.

The conceptual study of the multi-object IFU spectrograph has been conducted by Australian Astronomical Observatory (AAO). The conceptual design uses a number of fiber bundle IFUs, which are attached underneath of the wide-field corrector optics installed at the Cassegrain focus and are deployable anywhere on the focal plane using robotic positioners, called "Starbug", developed by AAO. The fibers from the IFUs will be connected to any near-infrared spectrograph (we consider MOIRCS in this study). We performed the performance modeling of the ULTIMATE instruments, suggesting that the ULTIMATE will provide 1.5−3.0 times higher sensitivity compared to the observations under natural seeing condition. The combination of the sensitivity improvement by GLAO and the wide-field coverage by the ULTIMATE instruments will provide very unique and strong survey capability at the Subaru telescope.

Table 1.3: Instrument fact sheet

	Imager	MOS	Multi-Object IFU[a]
Wavelength Coverage	0.8-2.5μm		
Plate Scale	0.10 arcsec/pix		0.15 arcsec/spaxel
FOV	$\phi \leq 16'$		IFU: $1''.18 \times 1''.18$, Patrol area: $\phi \sim 15'$
Filters	YJHK + NB filters	0.9−2.4 μm	0.9−1.8 μm
Spectral Resolution	−	∼3000 ($0''.4$ slit)	500−3000
Multiplicity	−	∼100 slits (TBD)	8−13 IFUs (TBD)
Detector	4×H4RG(Teledyne)		2×H2RG(Teledyne)
Efficciency[b]	∼ 48%(J,H), ∼40%(K)	∼33%(J),∼35%(H,K)	∼7%(J),∼10%(H)

[a] In case of using MOIRCS as a spectrograph.
[b] Total Efficiency includes atmosphere, telescope, and instrument (optics + detector).

1.5 Development Plan

We consider that the GLAO is a major upgrade of Subaru telescope. The GLAO development team should be based on Subaru Telescope, NAOJ, because the system development is heavily connected to the overall telescope system, and we need significant telescope modifications to achieve wide field-of-view at the Cassegrain focus. The instrument development can be fairly independent from the GLAO development, but the information should be shared very closely and the interface between the telescope, the AO system, and instruments needs to be clearly defined to ensure the development of the components go smoothly and those systems work together effectively.

While we have been trying to obtain external funds from the grant-in-aid programs, the size of the budget (we estimate around 25M USD) required for the GLAO development and telescope modifications makes the investment from Subaru Telescope's operation budget essentially important, and we consider such investment is appropriate as the GLAO is the major upgrade of the telescope. For ULTIMATE-Subaru instrument development, we expect major involvement of non-Japanese institutes as well as collaborations with universities in Japan. The budget of the entire project (GLAO, telescope modifications, wide-field imager, and multi-object IFU spectrograph) will be 50–70M USD.

One important note is that the Adaptive Secondary Mirror / GLAO system can be attractive to instrument development groups, and it will enhance the possibilities of future instrumentations for Subaru Telescope to keep the telescope productive and competitive.

The earliest possible commissioning of the GLAO system will be around 2023.

Chapter 2

Introduction

2.1 History of Subaru Next-generation AO Project

Subaru Telescope Science Advisory Committee (SAC) is an association of scientists in universities and institutions in Japan. As a representative of Japanese optical-infrared astronomical community, they have made advisory comments and recommendations to Subaru Telescope, NAOJ. In the recommendation report published in March 2009, SAC listed desirable future instruments of Subaru Telescope. There are four candidates, namely,

1. Very Wide-field optical imager (which refers Hyper Suprime-Cam),
2. Wide-field multi-object spectrograph (which refers WFMOS that now turns into Prime Focus Spectrograph),
3. Wide-field near-infrared (NIR) camera, and
4. NIR integral-field spectrograph.

The third and fourth candidates are NIR instruments. Unlike Hyper Suprime-Cam (HSC) and Prime Focus Spectrograph (PFS), there has been little activity on the study of such future NIR instruments for Subaru Telescope. In response to such recommendation from Japanese community, in 2010 Subaru Telescope initiated internal discussions on future instrumentations. During the course of such discussions, we recognized the significance of wide-field adaptive optics system and wide-field NIR instrument corresponding to such wide-field AO as a strong candidate of the Subaru future instrument in NIR wavelengths.

In September 2010 'Subaru Future Instrumentation Workshop' [1] was held at IPMU, Univ. of Tokyo. Although the main topic of the workshop was PFS, there was a session for Subaru future AO, and Ground-Layer AO (GLAO) has been mentioned as a good candidate.

2011:

In January 2011 Subaru Telescope have formed the working group for the Subaru next-generation AO system (ngAOwg) which consists of not only scientists in Subaru Telescope but also some members in Japanese universities, and started conceptual study of the next-generation AO system. On January 18th 2011, in connection with Subaru users meeting, the second Subaru Future Instrumentation Workshop [2] has been held in NAOJ HQ in Mitaka, Tokyo. In the workshop the instrument development in Japan (in universities and in NAOJ) and plans of new PI-type instruments for Subaru have been discussed.[3]

We had the first science workshop for Subaru next-generation AO [4] in September 2011 in Osaka. In

[1] http://www.naoj.org/Projects/newdev/ws10/

[2] http://www.naoj.org/Projects/newdev/ws11a/

[3] Following this workshop, more general workshop for optical and infrared instrument development and technology workshop was organized. From 2012 the workshop has been held annually.

[4] http://www.naoj.org/Projects/newdev/ws11b/

the workshop initial simulation results comparing capabilities of GLAO and Multi-Object AO (MOAO) as well as expected instrument sensitivities have been presented, and the limitation of MOAO Field-of-Regard / AO correction with 8m telescope has been quantitatively reported. However, the science cases did not always prefer GLAO, but some science cases request higher Strehl ratio with other flavors of AO such as LTAO or MCAO.

2012:

In Subaru users meeting in January 2012 a special session for next-generation AO was been held and, discussions following the workshop in 2011 and subsequent studies have been made.

In August 2012 the first study report Subaru Next-Generation AO has been published to Japanese community [5]. It was written in Japanese, and it includes science cases with new AO system, results of simulation studies (GLAO, MOAO, and expected sensitivities), AO system study, and concepts of new infrared instruments. In the report, based on the results of AO simulations and scientific demands, the working group has decided that GLAO is the first priority candidate of the Subaru Next-Generation AO system.

Following the conclusion of the first study report, in October 2012 GLAO science workshop was held in Hilo, Hawaii, inviting Japanese researchers mainly working on extra-galactic astronomy. Because the choice of the AO type has been made, the feasibility of science cases and requirements to GLAO/instrument specifications have been discussed more clearly compared to previous workshops.

In parallel to these working group activities and community discussions, Subaru Next-Generation AO system has been listed as one of key middle-class future projects in optical and infrared astronomy for the future plan in astronomy / astrophysics section of Science Council of Japan. Also, ngAOwg submitted a proposal of JSPS grant-in-aid (Kiban-S) as a kick-off of the development (fiber laser system as an upgrade of the existing LGS system). The proposal was not successful.

We initiated discussion about possible collaboration with Canadian community. Some researchers are interested in scientifically, and also discussions on technical side, especially on instrumentation, have started.

2013:

In June 2013 the second GLAO science workshop [6] was held in Sapporo. The first workshop in 2012 was relatively small and invited small number of researchers to identify key science cases. This second workshop involved larger number of scientists, and broader science cases including Galaxy Archaeology and exoplanets have been discussed. Also, there were several Canadian researchers joined the workshop and contributed to science cases and discussions. John Pazder (HIA/NRC, Canada) made a technical note on the concept of four barrel design of wide-field imager, which is attached to this report as an appendix. Before the workshop the project name 'ULTIMATE-Subaru' has been determined.

Subaru Telescope explained the outline and goals of the ULTIMATE-Subaru project to NAOJ project meeting, which involves NAOJ director general and management. They requested to refine the plan with clearer development organization. Also, it was requested to make the Subaru instrument plan with clear decommission timelines.

In December 2013 Andrew Sheinis (AAO, Australia) visited Subaru Telescope and suggested an idea of using Starbugs fibre positioner for an ULTIMATE-Subaru instrument. This suggestion initiated a collaboration between AAO and Subaru Telescope on ULTIMATE-Subaru.

[5] http://www.naoj.org/Projects/newdev/ngao/
[6] http://www.naoj.org/Projects/newdev/glaows13/

2014:

In July 2014, we had ULTIMATE-Subaru mini Science Workshop [7] with Chris Lidman and Andrew Sheinis (AAO) at NAOJ HQ in Mitaka, Tokyo. This workshop focused on the scientific potentials of Multi-Object Integral Field Spectrograph (M-IFS) with Starbug fibre positioner which AAO proposes.

2015:

We continued the collaboration with AAO on technical and scientific feasibility of M-IFS. Also, in Japanese community, efforts to update science cases presented in the first study report published in 2012 have started. These efforts have turned into this study report 2016.

For organization, the discussion of partnership with Canada and Australia is on-going. The scope of these partnerships includes broader cooperations with these community / institutes on operations of Subaru Telescope in general, but both communities also have strong interests in ULTIMATE-Subaru. We also submitted two JSPS grant-in-aid proposals for development of new AO system for Subaru Telescope aiming at starting from 2016.

2.2 Synergy with ELTs and Space Missions in 2020s

We aim at starting operation of GLAO in early 2020s (see Section 8 for details). The middle of 2020s is the epoch when Extremely Large Telescopes (ELTs) such as the Thirty Meter Telescope are expected to start their first-light observations. ELTs will have light collecting power and spatial resolution substantially superior to the current 8–10m class telescopes. Observations with ELTs will enable us to explore much fainter targets, and investigate very details of internal structure of various objects. On the other hand, wide-field (i.e., FoV larger than $\gtrsim 10'$) observation with ELTs are extremely challenging. Wide-field capability of Subaru Telescope has been extended by the telescope modification and installation of the new prime-focus camera Hyper Suprime-Cam (HSC; 1.5 deg. diameter), and the massive fiber-fed spectrograph Prime Focus Spectrograph (PFS)[8] is expected to start science observation at the end of 2010s. The scientific roles of Subaru Telescope in 2020s have been discussed extensively within Japanese community. With the advent of HSC and PFS, it is clear that Subaru Telescope occupies unique position among existing 8–10m telescopes in terms of survey capabilities, and wide-field capability ensures strong synergy between Subaru and ELTs; Subaru Telescope will be a strong target provider for TMT and other ELTs for detailed characterizations. ULTIMATE-Subaru well aligns with such overall strategy of Subaru Telescope. Although the wide-field capability in near-infrared instruments is limited compared to optical instruments such as HSC and PFS, $\sim 15'$ field-of-view currently proposed for ULTIMATE-Subaru instruments will be the widest among 8–10m telescope infrared instruments.

There are also two important space-based survey-oriented missions in near-infrared in progress to be launched in 2020s. One is Euclid and another is WFIRST. Both have near-infrared wide-field imager and spectrograph. In Table 2.1 imager instruments of Euclid, WFIRST and ULTIMATE-Subaru are compared. Euclid has a smaller telescope aperture and spatial sampling is coarser than WFIRST and ULTIMATE-Subaru. It plans to make an all-sky survey, and in that sense it has slightly different nature from WFIRST and ULTIMATE-Subaru. Thanks to the low background noise and plenty of observing time of the space-based missions, WFIRST's survey area and depths are quite compelling. However, the warm temperature of telescope and instrument limit WFIRST's wavelength coverage up to 2 μm. ULTIMATE-Subaru's imaging (and possibly spectroscopic) capability at $> 2\mu$m supplements the data to be produced by WFIRST. Moreover, as we discuss in the science sections, ULTIMATE-Subaru should be able to install multiple narrow and medium-band filters and enhance variety of scientific programs at later stage, which cannot be realized with space missions. Therefore, ULTIMATE-Subaru has good

[7] http://www.naoj.org/Projects/newdev/ngao/20140728/
[8] The spectral coverage of PFS is 0.38μm – 1.3μm.

synergy with space missions and can provide capabilities which cannot be accomplished by Euclid and WFIRST.

	Euclid	WFIRST-AFTA	ULTIMATE-Subaru
Telescope aperture (m)	1.2	2.4	8.2
Imager FoV ($\deg^2$)	0.55	0.28	0.12
Wavelengths (μm)	0.55–2.0	0.9–2.0	**0.0–2.3**
NIR detectors	16 2k×2k	18 4k×4k	4 4k×4k
Pixel scale ($''$/pix)	0.3	0.12–0.14	0.15
Survey depth (5σ, AB mag)	24	26.2–26.9	24.9^{*1}
Survey area	all-sky	2,200 $\deg^{2*2}$	TBD
Expected launch date / first light	2020	2024?	2023
Lifetime (years)	6	6	—
Primary institute	ESA	NASA	NAOJ

Table 2.1: Comparison of Euclid, WFIRST-AFTA and ULTIMATE-Subaru wide-field imager. $*1$: 5 hours on-source time, K-band. $*2$: Area of proposed High Latitude Survey.

Chapter 3

Science Case I – High-z science with ULTIMATE imaging survey

In this Chapter, we describe the high-redshift galaxy science cases which exploit the wide-field imager on the ULTIMATE-Subaru. We assume that the wide-field imager has a $16' \times 12'$ FoV (see details for the instrument in Section 7.2). We note that *broad-band* photometric survey is by far advantageous to space observatories, but we stress that a large number of high-redshift science cases require narrow-band filters and/or medium-band filters, which are not available for space missions.

In Section 3.1, we discuss the survey for detecting the most distant Lyα emitters ($z > 7$). In Section 3.2, we present our science cases for galaxies at the cosmic high noon ($z \sim 2$) with the unprecedentedly deep and wide-field Hα/[OIII] emission line survey with ULTIMATE-Subaru. Finally, we discuss in Section 3.3 our strategy for the medium-band photometric survey to capture Balmer break feature out to $z \sim 5$.

3.1 Search for Galaxies at $z > 7$ with Narrow-band Imaging

Ikuru Iwata[1], **Takatoshi Shibuya**[2]
[1] Subaru Telescope, National Astronomical Observatory of Japan
[2] Institute for Cosmic Ray Research, The University of Tokyo

3.1.1 Introduction

Subaru has been one of the leading facilities pushing the frontier of the distant universe. A unique capability of the prime focus camera (Suprime-Cam) have enabled us to conduct wide-field survey which is essentially important to find very rare objects such as luminous distant galaxies. One of the efficient methods to find distant star-forming galaxies is to detect Lyα emission using narrow-band filter (NBF) imaging. A strongly star-forming object with a redshift $z = \lambda_{\rm NBF}/\lambda_{{\rm Ly}\alpha} - 1$ could appear to be bright in NBF compared to in adjacent broad-band filters. Galaxies detected with this method are called as 'Lyα emitters (LAEs)'. Suprime-Cam observations with NBFs have achieved discoveries of the most distant galaxies (e.g., Kodaira et al., 2003; Taniguchi et al., 2005; Iye et al., 2006; Shibuya et al. , 2012). Wide-field capability has also enabled a construction of statistical sample of distant LAEs to derive luminosity functions (e.g., Ouchi et al., 2008; Kashikawa et al., 2006), discoveries of distant proto-clusters as signature of large-scale structure formation in the early Universe (e.g., Ouchi et al., 2005; Toshikawa et al., 2012).

Currently a large survey with the new prime focus camera for Subaru Telescope in optical wavelength, Hyper Suprime-Cam (HSC), is underway (Subaru Strategic Program with HSC (HSC-SSP)). The observation plan includes sensitive observations with NB921 (for LAEs at $z = 6.57$) and NB101 (for LAEs at $z = 7.30$). HSC-SSP will provide unprecedentedly large samples of LAEs at those epochs. However, the wavelength of the redshifted Lyα for $z = 7.3$ is almost at the long wavelength limit of the CCDs, and finding galaxies at $z > 7.5$ with CCD cameras is impossible. So deep near-IR surveys are mandatory to push the redshift frontier further.

The universe at redshift > 7 is believed to be in the epoch of the cosmic reionization, and star-forming galaxies are supposed to be primary sources of ionizing photons which reionized the neutral Hydrogen. The optical depth measurement of the cosmic microwave background by WMAP suggests that, if we assume an instantaneous reionization, the epoch of the reionization is at $z = 10.6 \pm 1.2$(Komatsu et al., 2011). On the other hand, size measurements of the ionized regions around the quasars suggest the rapid change of either neutral fraction of the intergalactic HI gas or the UV background radiation at $z > 5.7$ (Carilli et al., 2010; Mortlock et al., 2011). These results would imply the cosmic reionization process was not an instantaneous event at a specific epoch but more gradual phenomenon ranging from $z \sim 7$ to 15 (Trac & Cen, 2007).

LAEs at $z \gtrsim 6$ are also one of excellent probes of the cosmic reionization process. Resonant scattering nature of Lyman α photons make them sensitive to the existence of neutral hydrogen, and the fraction of LAEs among UV bright star-forming galaxies is thought to provide constraints on the neutral fraction of hydrogen gas in the inter-galactic mediam (IGM). With a comparison of UV and Lyα luminosity functions, it has been suggested a rapid decline of LAEs at $z > 6.5$ could be caused by the increase of HI fraction (Kashikawa et al., 2006, 2011; Konno et al., 2014).

In order to understand how and when the cosmic reionization has happened and what kind of populations have contributed to that process, we definitely need large sample of the UV sources (star-forming galaxies and AGNs) at different epochs, including faint sources. Also, because the progress of the reionization could be much different for different sightlines, we need to observe the fields as wide as possible to find the average history of the reionization and how much dispersion exists.

Here we examine the feasibility of the search for LAEs at $z > 7$ with ULTIMATE-Subaru.

3.1.2 Survey design

We will use special narrow-band filters (NBFs) which are designed to collect photons with wavelength ranges between the strong OH air glows from the Earth's atmosphere. Here we assume three wavelength ranges as a fiducial set to study the feasibility. The spectral resolutions $R = \lambda/\Delta\lambda$ of these NBFs are ~ 70. For simplicity, we assume the filter transmissions are purely rectangular, and a uniform system throughput (including telescope mirrors) of 30%.

Filter	λ_c	FWHM	$z_{Ly\alpha}$
NB1063	1.0625	0.015	7.74
NB1185	1.1845	0.023	8.75
NB1340	1.340	0.019	10.0
(NB1550)	1.550	0.022	11.75

Table 3.1: Central wavelengths (λ_c in μm), FWHM (in μm), and redshifts of Lyα emission at λ_c for NBFs considered here. Although NB1550 which can be used to probe Lyα at $z \sim 12$ is also listed, sensitivity is worse than other NBFs due to larger background emission and it is not considered.

We assume read-out noise to be $10e^-$ and dark current to be $0.01e^-/s$. The plate scale is set to $0.1''$. Here we consider aperture photometry with diameter $\phi 0.5''$ and $\phi 1.0''$ for observations with GLAO and those under natural seeing, respectively. We neglect the thermal emission from the telescope and

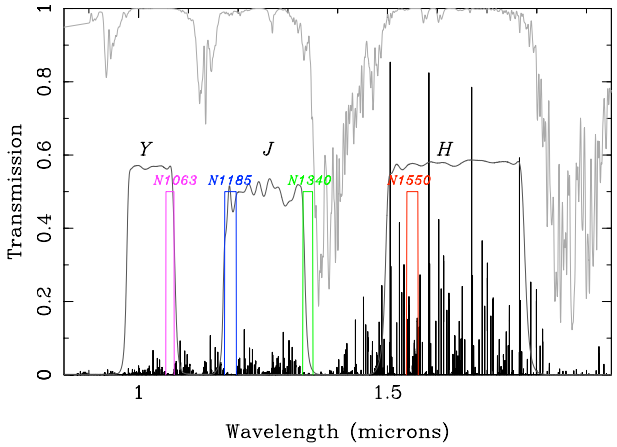

Figure 3.1: Transmission curves of NBFs considered. Transmission curves for Y, J, H-bands and the atomospheric transmission, and OH air glow strength (in arbitrary unit) are also shown.

instruments.[1]

For a comparison, we also calculated expected sensitivities of near-IR space missions such as JWST/NIRCam, WISH, and WFIRST. The telescope mirror sizes, plate scales, and sizes of field-of-view are summarized in Table 3.2.

	Mirror size(m)	Pixel scale (arcsec/pix)	FoV (arcmin^2)
Subaru	8.2	0.1	186
JWST/NIRCam	6.5	0.0317	9.68
WISH	1.5	0.155	840
WFIRST	2.4	0.11	1011

Table 3.2: Mirror size, plate scle, and field-of-view for Subaru, JWST/NIRCam, WISH, and WFIRST.

In Fig. 3.2 and in Table 3.3 we summarize the expected 5σ detection limit with on-source 4 or 8 hours exposures for Subaru under natural seeing, Subaru with GLAO, JWST/NIRCam (N164), WISH(NB109, NB134, NB158). JWST/NIRCam's NBF with the shortest central wavelength is $\lambda = 1.65\mu$m, and thus there is no NBF for NIRCam which can be used to search for LAEs at $z < 12$.[2]

Although broad-band imaging with the ground-based telescopes suffer from strong OH lines and cannot reach the depths comparable to space-based telescopes, photon collecting power of large aperture mirror can be fully exploited with narrow-band imaging.

3.1.3 Expected number of detections

Here we estimate the number of very high-z LAEs based on the expected sensitivities described above and some assumptions on the evolution of the LAE luminosity function (LF).

Kashikawa et al. (2011) examined LAE samples at $z = 6.5$ and 5.7 and argued that while the UV LF of LAEs show little change from $z = 5.7$ to $z = 6.5$ there is a significant decline of Lyα LF, and that could be due to the evolution of neutral HI gas fraction between those epochs. Furthermore, Konno et al. (2014) found significant decrease of Lyα LF from $z = 6.6$ to 7.3 and claimed the accelerate evolution beyond $z = 6.6$. Based on these results, we consider three cases: (1) no evolution of Lyα LF from $z = 6.5$,

[1] Although it may not be so large, we should include thermal emission as one of noise components.

[2] NIRISS has medium band filters such as F140M and F158M, and has a capability of slitless spectroscopy. See http://www.stsci.edu/jwst/instruments/niriss.

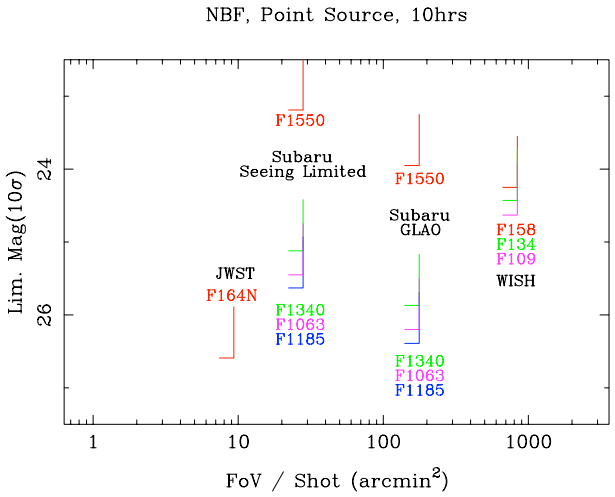

Figure 3.2: Ten-σ limiting magnitudes (in AB) with 10 hours of on-source exposure time for Subaru Telescope (natural seeing and GLAO), JWST/NIRCam, and WISH. See text for details.

		4 hours		8 hours	
Filter	Redshift	NS	GLAO	NS	GLAO
Y	–	25.99	26.74	26.36	27.12
J	–	25.52	26.27	25.89	26.64
H	–	24.79	25.54	25.16	25.91
Ks	–	25.61	26.36	25.98	26.74
NB1063	7.7	25.70	26.45	26.08	26.83
NB1185	8.7	25.89	26.64	26.27	27.02
NB1340	10.0	25.38	26.13	25.75	26.51
(NB1550)	11.8	23.45	24.20	23.83	24.58

Table 3.3: Five-σ limiting magnitudes (in AB) for point sources with 4 hours and 8 hours of on-source exposure time for Subaru Telescope (natural seeing (NS) and GLAO).

	Subaru Telescope				
redshift	Natural seeing	GLAO	redshift	WISH	JWST
7.7	25.86	26.30	8.0	24.63	–
10.0	25.86	26.30	10.0	24.43	–
11.8	23.59	23.94	12.5	24.25	26.69

Table 3.4: Ten-σ limiting magnitudes (in AB) with 10 hours of on-source exposure time for Subaru Telescope (natural seeing and GLAO), JWST/NIRCam, and WISH. See text for details.

(2) extrapolation of Lyα LF evolution from $z = 5.7$ to 6.6 by Konno et al. (2014), and (3) extrapolation of accelerated Lyα evolution from $z = 6.6$ to 7.3 claimed by Konno et al. (2014). They examined both pure-luminosity evolution and number density evolution (Table 6 of Konno et al. (2014)), and here we adopt the number density evolution scenarios.

Case 1: Broad-band images by ULTIMATE-Subaru

In order to select strong line emitter candidates, deep broad-band images are also required. Actually, obtaining sufficiently deep near-infrared broad-band images is the most challenging part for ground-based telescopes in terms of a search for high-z LAEs. The deepest wide-field near-infrared surveys with 4m-class telescopes such as UKIDSS and UltraVISTA reach only 24–25 AB magnitudes (Lawrence et al., 2007; McCraken et al., 2012).

GLAO enables sensitivity improvements for point-like sources as shown in Table 3.3. In this case we consider executing the survey solely with ULTIMATE-Subaru by obtaining both broad-band and narrow-band images. The survey depth is determined by broad-band imaging. Limiting magnitudes used (26.64 in J, 25.91 in H) are for 8 hours on-source time, which would be practically the maximum integration time for single field in the large survey. A color criterion $BB - NB \geq 1.0$ is adopted for LAE candidate selection.

In Table 3.5, we show the number of detections per single field-of-view. Because it is unlikely that there is no evolution in Lyα LF from $z = 6.5$, we should look at either 'slow evolution' or 'rapid evolution' to see the feasibility, and the expected number is not high. Even if we make 100 FoVs survey, the expected numbers for $z = 8.7$ and $z = 10.0$ are ~ 30 and a few, respectively, for the 'slow evolution' case, and no detection is expected for the 'rapid evolution' case.

			Number per FoV		
Filter	redshift	$L_{\rm lim}$	No ev.	Slow ev.	Rapid ev.
NB1063	7.7	4.86×10^{42}	2.9	1.3	0.14
NB1185	8.7	7.05×10^{42}	1.3	0.35	7.7×10^{-3}
NB1340	10.0	1.27×10^{43}	0.10	1.56×10^{-2}	5.6×10^{-5}

Table 3.5: The expected number of detections per single field-of-view with 8 hours on-source exposure time in broad-band (J-band for $z = 7.7$ and 8.7, H-band for $z = 10.0$). 'No ev.' is a case without Lyα LF evolution from $z = 6.5$ (Kashikawa et al., 2011). 'Slow ev.' assumes the LF evolution extrapolated with the one from $z = 5.7$ to 6.6 (Konno et al., 2014). 'Rapid ev.' isfor the LF evolution extrapolated with the one from $z = 6.6$ to 7.3 (Konno et al., 2014). The column $L_{\rm lim}$ shows lower limit Lyα luminosity with the assumed observations in erg/s.

This survey requires on-source 8 hours exposures in J and H-bands and 4 hours in three NBFs. The number of nights required to complete 100 FoVs (~ 5 deg.^{2}) is about 350, without taking the weather loss into account.

Case 2: Broad-band images from other surveys

Since taking sufficiently deep broad-band images with ULTIMATE-Subaru for this survey seems to be difficult, we consider a possibility of using the broad-band data from forthcoming space-based telescopes. Although wide-field $\gtrsim 5$ deg.^{2} survey with JWST/NIRCam may be difficult, WFIRST will provide wide-field data with sufficient depth (~ 28 AB mag.). Here we assume NB surveys with limiting magnitudes to be achieved with 8 hours on-source exposures (see Table 3.3).

In Table 3.6 the expected numbers of LAE detections are presented. Although the numbers expected for LAEs at $z = 10$ are still small, for $z = 7.7$ and 8.7 a survey with an order of ten pointings will provide unique samples of LAEs at these epochs. We will be able to push the observational constraints of neutral hydrogen gas fraction toward $z \sim 10$ by comparing the Lyα and UV LFs. Moreover, these bright LAE candidates are excellent targets for the follow-up spectroscopy by TMT (IRIS and IRMS) not only to confirm their redshifts, but also to clarify the physical nature (size, mass, amount of dust, star-formation rate, metallicity etc.) of these galaxies in the very early stage of formation and evolution. One possibility to boost the expected number of detections or to extend the survey toward fainter luminosity range is

to observe fields with gravitational lensing. When we plan more detailed observing strategy, pointing toward such fields should be considered.

These NBF survey will also probe metal lines such as OIII] 1661,1666 and CIII] 1908 which are the strongest UV lines other than Lyα for distant star-forming galaxies and are good probes of interstellar medisum (ISM) properties such as metallicity and ionization parameters (Stark et al., 2015). For example, NB1340 can be used to find CIII] 1908 emission at $z \sim 6.0$. ULTIMATE NBF survey will provide unique sample of such emitters which can be also further studied with ELTs.

The number of nights required to accomplish 100 FoVs survey with 8 hours on-source time for these three NBFs is ∼300, without taking weather loss into account.

Filter	redshift	$L_{\rm lim}$	No ev.	Slow ev.	Rapid ev.
NB1063	7.7	1.62×10^{42}	36	17	1.8
NB1185	8.7	1.98×10^{42}	31	8.6	0.19
NB1340	10.0	2.91×10^{42}	9.7	1.5	5.3×10^{-3}

Table 3.6: The expected number of detections per single field-of-view with 8 hours on-source exposure time in narrow-band filters. Evolution scenarios are the same as in Table 3.5.

As we already mentioned, JWST/NIRCam does not have an NBF in these wavelengths, and its small FoV makes it difficult to conduct wide-field survey to find rare, bright star-forming galaxies at $z > 7$. Also, wide-field surveyors such as WISH and WFIRST are not capable of achieving good sensitivity in narrow-band imaging due to their smaller telescope apertures. The expected number of detections per FoV at $z \sim 8$ with WISH is > 10 times smaller than the numbers shown here. NBF survey with ULTIMATE-Subaru wide-field imager should provide unique opportunities to probe the cosmic dark age via LAEs.

3.2 ULTIMATE Narrow-band Imaging for the Cosmic High Noon

Yusei Koyama[1], Yosuke Minowa[1], Yuichi Matsuda[2] Kotaro Kohno[3], Tadayuki Kodama[2]
[1] Subaru Telescope, National Astronomical Observatory of Japan
[2] National Astronomical Observatory of Japan
[3] Institute of Astronomy, The University of Tokyo

3.2.1 Introduction

Deep near-infrared observations provide us with the rest-frame optical information of distant galaxies at the peak epoch of galaxy formation (z=1–3). With recent advents of efficient large format of NIR detectors, our understanding on the nature of distant galaxies has been revolutionized over the last ∼10 years. Narrow-band imaging survey at NIR regime is one of the most efficient ways to construct an unbiased, uniform sample of star-forming galaxies and AGNs in the distant universe, and this strategy has been demonstrated to be successful with (seeing-limited) observations using 4–8m class telescopes. The ULTIMATE-Subaru, equipped with wide-field imaging camera ($16' \times 12'$) and assisted by GLAO, will provide us with an unique opportunity to perform a record-breaking, unprecedentedly deep and wide-field NB imaging survey for galaxies at the peak epoch of galaxy formation based on the rest-frame optical emission lines (Hα, [OIII], etc).

It is of course true that NIR "broad-band" photometry is by far advantageous to observations from space observatories, obviously because of their very low background levels. However, for narrow-band imaging, we can take full advantage of large aperture sizes of ground-based telescopes by manufacturing narrow-band filters in between the night sky emissions. In addition, an important advantage of ground-based telescopes is a "flexibility" for filter change: e.g. we can change filters very frequently, or install new filters according to the astronomers' timely requests. Assuming that ULTIMATE-Subaru will have a wide-field NIR camera, it is therefore straightforward for ULTIMATE-Subaru to become a "narrow-band (and medium-band) machine" to fully complement deep broad-band photometry performed by future space missions.

We can now assume high-resolution (∼0.2″), deep and wide-field NIR "broad-band" imaging survey will be available in mid-2020s with WFIRST (J=26.9-mag, H=26.7-mag over ∼2400 deg^2). The ULTIMATE-Subaru "narrow-band" survey can deliver spatially resolved emission-line information for a number of galaxies with the comparable spatial resolution to WFIRST (or HST). This point is worth noting—in particular, narrow-band survey can pick up low-mass, star-forming "building blocks" of galaxies with extremely faint continuum emission, which could potentially be missed even with deep broad-band photometry with HST or WFIRST. In this subsection, we will summarize possible science cases with deep, high spatial resolution, narrow-band imaging for galaxies at the peak epoch of galaxy formation (z=1–3).

3.2.2 Survey design: a record-breaking, ultra-deep Hα imaging survey at $z \sim 2$ as an excellent "target feeder" for TMT

We will perform a blank field survey over ∼4-deg^2. In order to enhance the synergy with Subaru/HSC, we plan to fully overlap the "ULTIMATE-Deep field" with the HSC ultra-deep survey layer. In addition, we will also perform systematic observations of clusters and proto-cluster fields which are rare on sky and might be missed with the simple blank field survey. Of course each cluster has its own redshift, and so this "ULTIMATE-cluster survey" requires a number of custom-made NB filters designed for individual clusters. But again, this is an important advantage of ground-based telescopes. The main target emission line is Hα, but at $z > 3$, [OIII]λ5007 can also be an alternative tool to select emission-line galaxies (Suzuki et al. 2015). We note that the survey field should be determined so as to overlap with deep NIR broad-band survey with space missions in 2020s (e.g. WFIRST), but it is clear that the survey

area should be around equators so that all telescopes located on north and south hemisphere can access to the ULTIMATE field.

(1) ULTIMATE-Deep survey: ∼4-deg^2 scale, record-breaking, ultra-deep NB imaging survey with ULTIMATE-Subaru, with its survey field completely overlapped with HSC Ultra-Deep field. One of the most succesful modern NB emission-line surveys for high-redshift galaxies is HiZELS (HiZ Emission Line Survey: Sobral et al. 2013), which has been undertaken with 4m-class telescope (mainly with UKIRT). HiZELS covers 2-deg^2 field (UDS+COSMOS) with three NB filters to target Hα line at z=0.8, 1.5, and 2.2. Their typical exposure times are ∼5-hours, ∼3.5-hours, ∼5-hours for NB$_J$, NB$_H$, NB$_K$, respectively, which correspond to 3-sigma limiting magnitude of ∼22.0-mag, ∼21.0-mag, ∼20.9-mag (in Vega magnitude). As a good comparison, they also performed 5-hours VLT/HAWK-I observations for a very tiny portion of sky (only 0.015-deg^2), and demonstrated it can go ∼0.5-mag deeper with 8-m class telescope. However, their spatial resolution (seeing) was ∼1.0″ for both UKIRT and VLT data, preventing any spatially resolved studies of their emission lines. ULTIMATE-Subaru will significantly improve the spatial resolution (by a factor of ∼4×), allowing us to go typically ∼2-mag deeper than HiZELS over square degree scale. This unprecedentedly deep emission-line survey will go far below the L_* galaxies at all redshifts, and will allow us to select low-mass star-forming galaxies. Obviously, these newly identified "star-forming building blocks" at the peak epoch of cosmic SF history will become an unique target for TMT. To cover 4-deg^2, we need to spend 64 pointings with the ULTIMATE wide-field camera. Assuming that we will exploit four NB filters (assuming we target z=1.0, 1.5, 2.0, 2.5), and that we require 5-hours integration for each filter and assuming 20% overhead, we request 4 filter × 64 pointing × 5 hours × 1.2 (overhead) = 1536 hours ≈ 150 nights to complete the "ULTIMATE-Deep" survey.

(2) ULTIMATE-Cluster survey: systematic observations of ∼20 (proto-)cluster fields at 0.8<z<3.5 using Hα/[OIII] narrow-band filters: we need to manufacture those NB filters for each target, hence requiring a large number of filter slots. But again, this "flexibility" for frequent filter change is a big advantage of ground-based telescopes. With this strategy, we will be able to fully cover a wide range in environment. In fact, Subaru has exploited this strategy and performed NB Hα survey for a few of distant proto-clusters with seeing-limited observations using MOIRCS (MAHALO-Subaru campaign: e.g. Tanaka et al. 2011; Hayashi et al. 2012; Koyama et al. 2014). With ULTIMATE-Subaru wide-field camera, the FoV will be increased by a factor of ∼5× compared with MOIRCS, allowing us to prove surrounding environments of proto-clusters. In order to make fair comparison between clusters and fields, the survey depths must be comparable to ULTIMATE-Deep survey. Under similar assumptions as for field survey, we request 1 filter × 20 target × 5 hours × 1.2 (overhead) = 120 hours ≈ 12 nights. We note that clusters are not necessarily located in famous deep fields, hence we will also need to take broad-band data with ULTIMATE. In this case, the requested number of nights will be increased to ∼20 nights.

3.2.3 Science goal: tracking down the stellar build-up inside galaxies across cosmic time and environment

The record-breaking deep NB imaging survey achieved with ULTIMATE-Subaru is not only for "selecting" faint emission-line galaxies in the distant universe, but also to "spatially resolve" their emission lines by taking advantage of the significantly improved spatial resolution (K∼0.2″) assisted by GLAO. This is a dramatic improvement from existing seeing-limited NB surveys ever performed. We also stress that the spatial resolution achieved with ULTIMATE-Subaru is comparable to HST/WFC3 or future WFIRST. Below we summarize our important science goals, all of which are highly complementary with these future space missions as well as TMT.

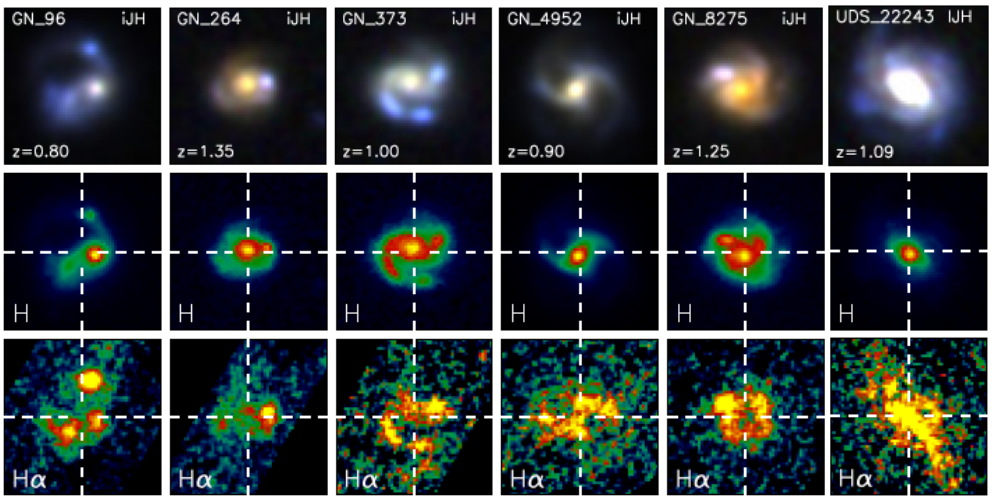

Figure 3.3: Six examples of spatially resolved Hα map for field galaxies at $z \sim 1$ from 3D-HST ($3.4'' \times 3.4''$ for each; Wuyts et al. 2013). This plot demonstrates what we will obtain with the narrow-band Hα imaging for $z > 2$ galaxies with ULTIMATE-Subaru.

Hα morphologies across cosmic time and environments

The Hα line is an ideal tool for studying the star forming activity in galaxies, and therefore the spatially resolved Hα morphologies will allow us to directly identify the site of intense star formation taking place within individual galaxies. Recent studies by 3D-HST project have made a significant improvement in this field. They exploit WFC3/G141 grism on *HST* and extracted spatially resolved Hα spectra over 0.17-deg^2 (see Fig. 3.3; e.g. Brammer et al. 2012; Wuyts et al. 2013). Although the survey area size covered by 3D-HST is limited, a similar approach will also be taken by WFIRST: WFIRST also has grism capability, and we can easily expect that the survey size will be significantly increased. However, an important point here is that both 3D-HST and future WFIRST-grism observations can trace Hα only up to $z \sim 1.5$ because of their wavelength coverage. We stress that pushing this redshift limit up to $z \sim 2.5$ with NB Hα imaging with ULTIMATE-Subaru is crucial, particularly when considering the environmental effects. Many recent studies have pointed out a high star-forming activity in galaxy cluster cores at $z > 1.5$ (e.g. Hayashi et al. 2010; Tadaki et al. 2012; Tran et al. 2010), and there is a piece of evidence that star-forming galaxies in $z > 2$ (proto-)cluster galaxies tend to be more massive and have higher SFRs than field counterparts, suggesting an accelerated galaxy formation in cluster environments at $z \sim 2$ (see Fig. 3.4; Koyama et al. 2013). Going beyond the limit of HST or WFIRST (the wavelength coverage to $\lambda \sim 2.5$ μm is thus critically important to identify the first appearance of environmental effects on galaxy evolution in the early universe, and we stress that this point is an unique advantage of ULTIMATE-Subaru.

We note that recent IFU observations have successfully obtained Hα maps for several subsamples of $z > 2$ galaxies (e.g. with SINFONI/VLT; Förster Schreiber et al. 2009; Swinbank et al. 2012), but the number of AO-assisted IFU data for $z > 2$ galaxies is still very limited ($\ll$100). The number of IFU targets is now progressively increasing with KMOS/VLT, but KMOS observations are always seeing limited, hence internal structures within galaxies can easily be diluted or smeared out. The spatial resolution achieved with ULTIMATE-Subaru is not extreme, but is reasonably good to bridge the seeing-limited observations performed so far and extremely high spatial resolution observations achieved with TMT.

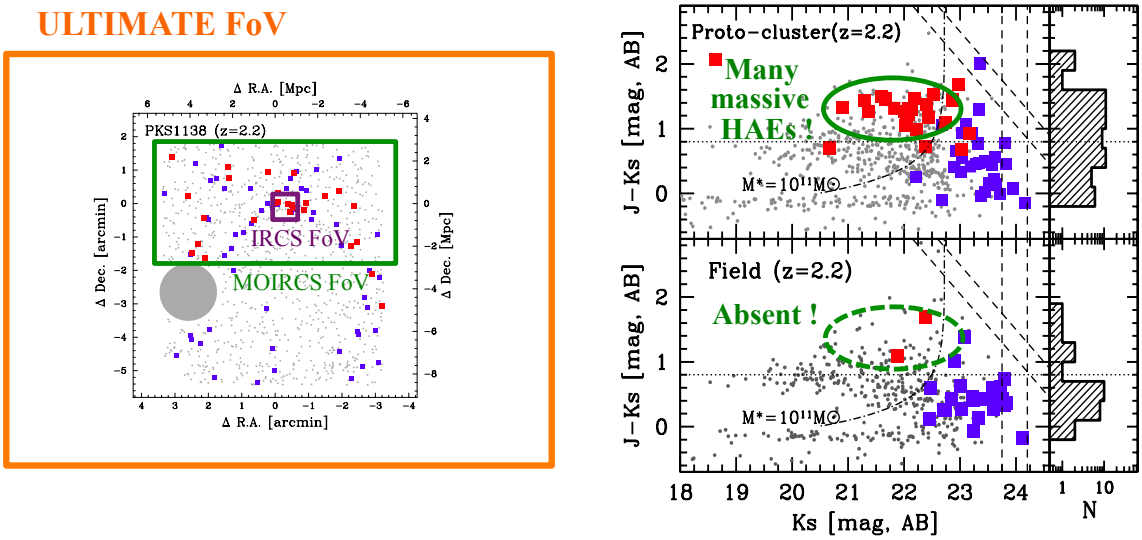

Figure 3.4: (Left): Demonstrating the superb FoV of ULTIMATE-Subaru (in comparison to existing Subaru NIR instruments, MOIRCS and IRCS) on top of a well-studied proto-cluster at $z = 2.2$ (PKS1138–262; Koyama et al. 2013). The red and blue squares show the location of Hα emitters with red and blue $J - K_s$ colours selected with MOIRCS NB imaging survey. (Right): The colour–magnitude diagram for proto-cluster (top) and fields (bottom) at $z \sim 2.2$. The symbols are the same as the left panel. This plot demonstrates that SF galaxies in proto-cluster environments tend to be redder and more massive than field counterparts.

Pinpointing the location of boosted/quenched star formation within individual galaxies via pixel-by-pixel SFR–$M_\star$ diagram

It is important to compare the spatially resolved emission line information with continuum light to understand the distribution of star-forming regions as well as that of stars which are already formed. van Dokkum et al. (2010) performed stacking analyses using NEWFIRM data, and find that massive (elliptical) galaxies on average increase the stellar mass in their outer regions since $z \sim 2$, whilst the mass in their central part is nearly constant (Fig. 3.5a), suggesting the inside-out growth. The situation might be different for Milky Way type galaxies: van Dokkum et al. (2013) showed by using 3D-HST and CANDELS data that the central ∼2-kpc of the Milky Way like galaxies increased by a factor of ∼3 since $z \sim 2.5$ (Fig. 3.5b).

When we discuss the "mass growth" of galaxies, it is important to understand "how" the stellar mass is accumulated (e.g. in-situ star formation or accretion of already formed stars). Another interesting point would be: is this picture applicable for all galaxies across all environments? Considering the fact that merger frequency or merger history is strongly dependent on environment, it sounds over-simplified to assume the stellar build up process is the same in all environments. For example, there is a piece of evidence that early-type galaxies in high-density environments (at high-z) tend to have *larger* size in continuum than field counterparts at fixed stellar mass (Papovich et al. 2012). By comparing the distribution of star-forming regions (with narrow-band) and stellar distribution (with broad-band), we will be able to study the "process" of stellar build up within the galaxies.

ULTIMATE-Subaru will perform deep NB Hα imaging with high spatial resolution across cosmic environments, and is ideally suited for revealing the SF geometry for a statistical sample of galaxies in an unbiased way. Of course, ultra-deep IFU observations with TMT and/or JWST will allow us to do this job, but an important advantage of ULTIMATE is to do this job "without" any pre-selection. Any population should be included in the ∼4-deg^2 ULTIMATE-Deep survey, and their counterparts should

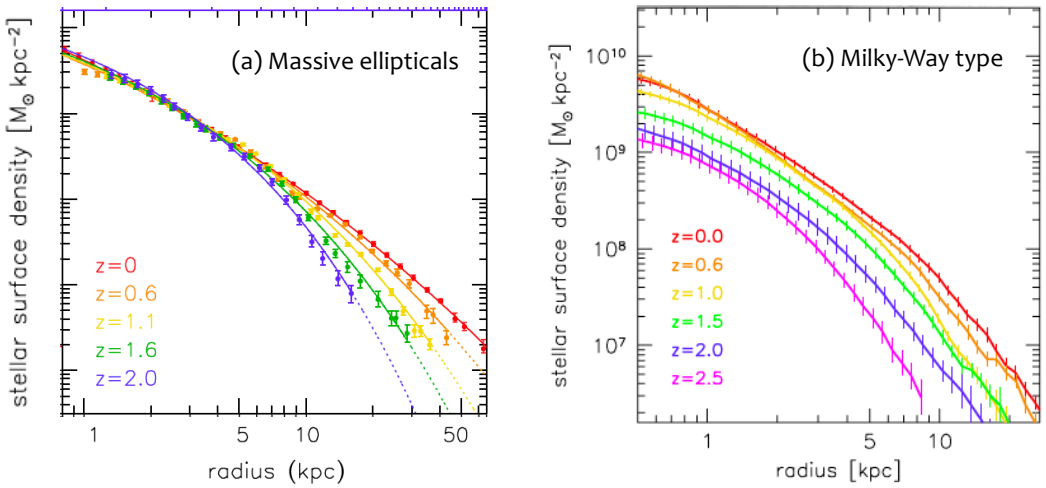

Figure 3.5: Stellar mass surface density profile for massive (elliptical) galaxies and for Milky Way like galaxies from van Dokkum et al. (2010) and van Dokkum et al. (2013), respectively. The formation of central cores of most massive galaxies have already been built up before $z = 2$, while the situation is not the same for more "normal" galaxies.

also be seen in the ULTIMATE-Cluster survey. Interesting sources can directly be provided to TMT for further follow-up work to have a more detailed observations—this is our strategy.

An interesting plot to be made is the spatially resolved, pixel-by-pixel SFR–$M_\star$ diagram to search any deviant pixels (including boosted and/or quenched pixels) for a statistical sample of galaxies across environments. In Fig. 3.7a, we show the example of pixel-by-pixel SFR–$M_\star$ diagram for $z \sim 1$ galaxies constructed by 3D-HST project (Wuyts et al. 2013). It can be seen that the location of SFR–$M_\star$ relation is similar to the "global" star forming main sequence, but an interesting point here is the spatial distribution of boosted/quenched pixels (within the galaxies) and its environmental variation. Recent studies demonstrated that the location of star formation main sequence does not significantly change with environment (Fig. 3.7a; Koyama et al. 2013), but it is totally unclear if this is really the case at pixel-by-pixel basis. Do galaxies with same stellar mass have always the same SF geometry regardless of environment? For example, in the local universe, there is an evidence that star-forming galaxies in Virgo cluster tend to have smaller Hα size (Koopmann et al. 2006), suggesting the gas stripping effect from outskirts of the galaxies. In addition to the direct identification of intense starburst and its sudden quenching which is probably linked to the formation of bulge (this is one of the main topics of ULTIMATE!), it is also of great interest to identify the first appearance of environmental influence of ICM on galaxy SF activity.

3.2.4 Pair filter strategy

Spatially resolved dust extinction levels via Hα/Hβ ratio

The large number of NB filters that we plan to install on ULTIMATE-Subaru wide-field camera should be well organized so that we can study spatially resolved line flux ratios (hence ISM conditions) of individual galaxies, taking advantage of the spatial resolution of ULTIMATE-Subaru. One of the most important flux rations is Hα/Hβ ratio (Balmer decrement) because it can directly be converted to the dust extinction level. Fig. 3.6 shows an example of the pair filter strategy targeting $z = 2.2$ galaxies: we can obtain [OII]λ3727, Hβ, and Hα with NB1185, NB155, and NB209, respectively (Tadaki et al. 2011). We do have this filter set on MOIRCS, but it has been really challenging to detect weak Hβ or [OII]. ULTIMATE は-Subaru can go significantly deeper than the seeing limited MOIRCS observations, and the pair filter strategy should be ideally suited for ULTIMATE. We note that we will obtain an ultra-deep

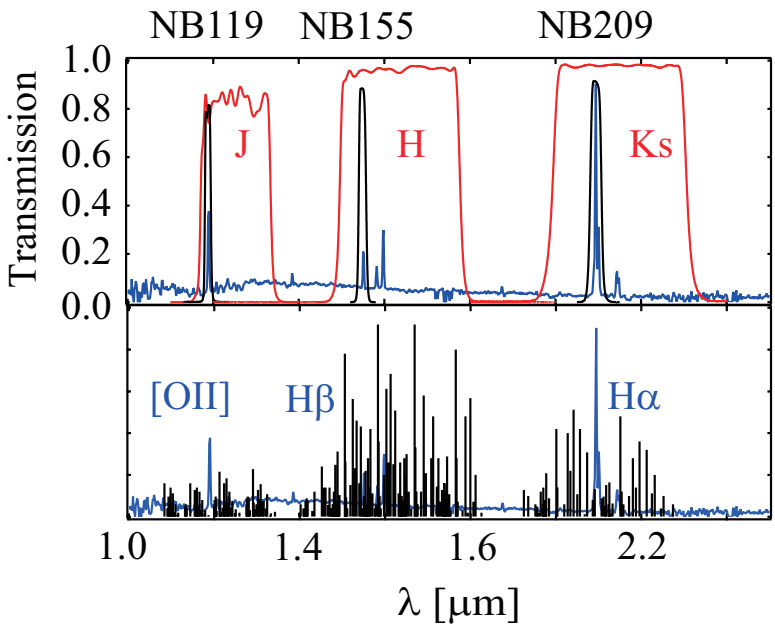

Figure 3.6: An example of triple pair filters to target [OII], Hβ, Hα emission lines for $z = 2.2$ galaxies. These three filters are installed on MOIRCS (Tadaki et al. 2011), but the aim of ULTIMATE-Subaru is to go deeper to firmly detect faint [OII] and Hβ emission, as well as to spatially resolve their emission lines on ∼2-kpc scale.

NB1185 data to search for $z = 7.7$ Lyα emitters (see Section 2.1). We can therefore make use of this deep high-quality data to study [OII] emission at $z = 2.2$. An important advantage of this approach is that we can determine the redshifts of each source without deep spectroscopy, if we detect multiple emission lines.

Our idea is to map the Hα/Hβ ratio for a statistical sample of $z \sim 2$ galaxies. We note that 3D-HST or future WFIRST grism survey can do this study (e.g. Nelson et al. 2015), but they do not have sensitivity for Hα emission at $z > 2$ because of their wavelength coverage. By manufacturing many NB filters in K-band, as well as corresponding pair filters, ULTIMATE-Subaru can thus reveal the geometry of dust extinction within the galaxies and its dependence on environment, taking full advantage of the wide FoV.

Clumps and ISM properties via Hα/[OIII] ratio

With the spatial resolution achieved with ULTIMATE-Subaru, we will also be able to identify giant star-forming "clumps" inside distant galaxies. Most of *HST* studies performed so far need to rely on the rest-frame UV light to identify star-forming clumps, but this approach would be biased to "dust-free" clumps, and would potentially miss "dusty" clumps. Indeed, Tadaki et al. (2014) reported (with seeing-limited Subaru data) that the peak position of Hα is different from that of UV light (see Fig. 3.7b), hence the UV luminous clumps are not necessarily responsible for the major parts of star formation. By searching for Hα luminous (but UV faint) clumps, we will identify the true answer for "where stars form" for a statistical sample of distant galaxies.

In the local universe, there is a tight scaling relation between the size and Hα luminosity for HII regions (e.g. Wisnioski et al. 2012). This relation has recently been investigated out to $z > 2$, and it turns out that the HII regions within high-z galaxies tend to have ∼15× higher luminosity density than local ones, suggesting high-z galaxies are denser and hence more unstable (see Fig. 3.8a; Swinbank et al. 2012). Our specific interest here is the environmental dependence of the properties of SF regions. In the local universe, cluster galaxies have prominent stellar bulges which are believed to be formed in the early universe at $z > 1$. If SF galaxies in high-density environments at high-z tend to be in the phase of

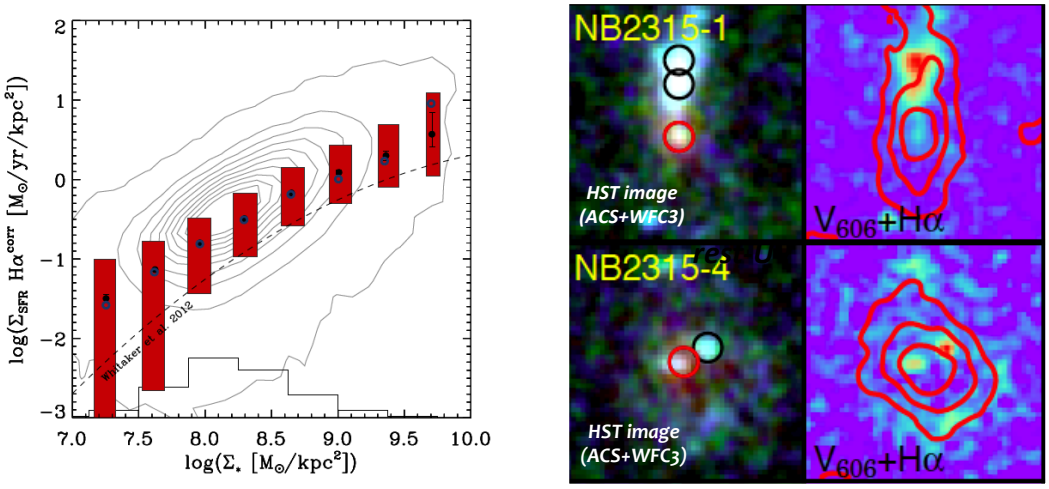

Figure 3.7: (a): Pixel-by-pixel SFR–$M_\star$ diagram for $z \sim 1$ galaxies derived by 3D-HST project (Wuyts et al. 2013). Also shown is the "global" star formation main sequence from Whitaker et al. 2012. Our goal is to draw this diagram out to $z > 2$ galaxies with ULTIMATE NB imaging, and pinpoint the location of boosted/quenched pixels within galaxies across cosmic environments. (b): Two examples of Hα emitters at $z = 2.5$, showing significant offset between the peak positions of Hα and UV. The red contours on the right panels show the Hα (seeing limited) intensity map. This plot demonstrates that UV luminous clumps do not necessarily dominate SFR of galaxies.

"bulge-growth", driven by cluster-specific processes, we will be able to identify more intense starbursts in the galaxy central parts of cluster galaxies (than field galaxies).

Recent studies report that high-z star-forming galaxies often exhibit an unusually strong [OIII] line emission, suggesting a higher excitation level of the ISM (hence their star formation mode is different from local galaxies) (Fig. 3.8b; Shimakawa et al. 2015). By manufacturing the matched Hα+[OIII] "pair" filters and by mapping the [OIII]/Hα ratio over the galaxies, we will identify the site responsible for the strong [OIII] emission (i.e. showing the highest ISM excitation level) for a statistical sample of galaxies. Of course the [OIII] line may also be contributed by the central AGN, but are the [OIII] lines always strongest in the galaxy central cores? It is of great interest to study the distribution of Hα/[OIII] ratio within the galaxies as a function the distance from star formation main sequence (see also Section 4.1 for the spectroscopic survey design with ULTIMATE-Subaru).

Pair filter synergy with HSC: exploring $z > 3$ universe with rest-optical information

We also comment that [OIII]λ5007 lines can potentially be an important tool for extending our studies towards $z > 3$ (Suzuki et al. 2015). The Hα line cannot be used at $z > 2.6$ for ground-based telescopes, but we can use [OIII] line instead, and in this case we can potentially extend our study out to $z \sim 3.5$. This will become another advantage of ultra-deep NB imaging survey achieved with ULTIMATE-Subaru, although it is of course true that we need to learn about the possible bias produced when we use [OIII] lines for selecting star-forming galaxies.

With this respect, a potentially important strategy for ULTIMATE-Subaru is to make NB filters which are matched with HSC NB filters. For example, we plan to manufacture NB2167 filter to target [OIII] emission at $z = 3.33$, which is perfectly matched to NB527 filter on HSC, which can target Lyα emission at exactly the same redshift. High-redshift universe ($z > 3$) has been cultivated by using rest-frame UV information (Lyα emission or Lyman break) so far, but it is worth noting that the systematic [OIII] emitter survey with ULTIMATE-Subaru will allow us (for the first time) to witness the rest-frame optical views of $z > 3$ universe.

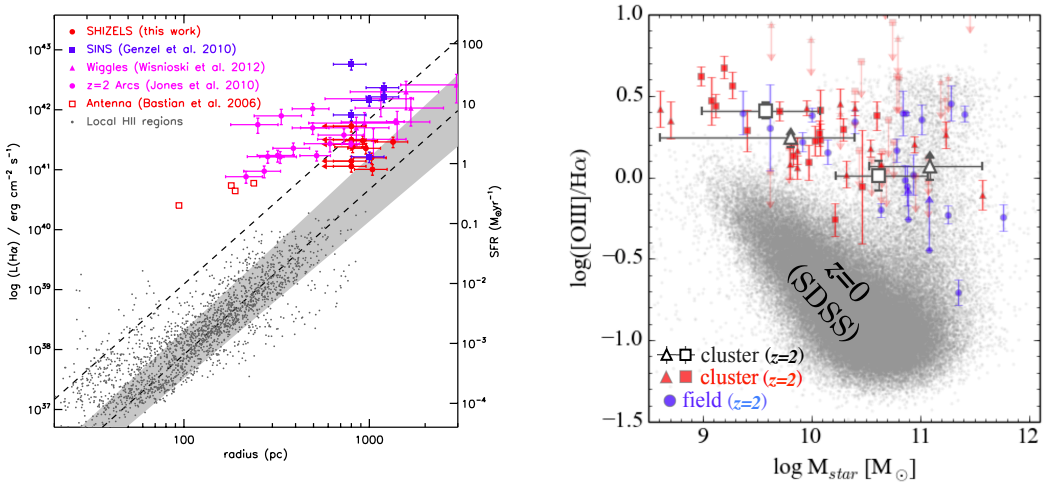

Figure 3.8: (a): The scaling relation between size and Hα luminosity for SF regions (Swinbank et al. 2012). The grey points are local GMC and HII regions, while the filled colored symbols show those for $z > 1$ galaxies. High-z galaxies have $\sim$15$\times$ higher luminosity density than local ones. (b): The mass-excitation (MEx) diagram for $z > 2$ proto-cluster galaxies (Shimakawa et al. 2015; color symbols). The grey contours show the relation for local galaxies, demonstrating a higher excitation level of ISM within high-z galaxies.

3.2.5 Synergy with ALMA and SPICA

The Hα line is one of the best SFR indicators which is well calibrated in the local universe, and therefore our approach with ULTIMATE—i.e. going "deeper" and "sharper" with Hα—is very reasonable, and is straightforward. However, it is also true that even Hα line is heavily attenuated by dust in extremely dusty galaxies. For such dusty galaxies, follow-up observations with ALMA can be a powerful tool to unveil the heavily obscured activity within the galaxies. ALMA can achieve spatial resolution comparable to (or even better than) that achieved with ULTIMATE-Subaru, allowing us to directly map out thermal dust emission from dusty star-forming regions within the galaxies.

We note that the FoVs of ALMA is limited ($<1'$ at maximum), and not ideally suited for "selecting" galaxies. We therefore stress that the role of ULTIMATE is to construct an unique sample of high-z star-forming galaxies based on the rest-optical indicators, and to provide them to ALMA, TMT, etc. Indeed, a good example of synergy work between Subaru NB Hα survey and ALMA has been demonstrated by Tadaki et al. (2015). They made ALMA observation of $z = 2.2$ Hα emitters identified in SXDF field with MOIRCS NB imaging, and find that massive Hα emitters showing red colors are preferentially detected with ALMA. The spatial resolution is still limited in this pioneering work (for both Subaru and ALMA data), but this study has demonstrated that ALMA observation is required for our complete understanding of the nature of internal properties of those massive star-forming galaxies at $z > 2$.

Furthermore, Hα or [OIII] NB survey (and medium-band survey) with ULTIMATE-Subaru will also significantly contribute to the SPICA mission ($\sim$2028). SPICA will perform MIR spectroscopic survey over 10-deg^2, with which we can blindly search dusty galaxies at z =1–3. By overlapping the survey area of ULTAIMTE-Subaru and SPICA, we (Japanese community) can make a complete census of both "normal" galaxies (with ULTIMATE) and "dusty" galaxies (with SPICA). The ULTIMATE-Subaru, equipped with wide-field imager, can thus provide an invaluable legacy data for all future missions we have in 2020s, including wide-field NIR broad-band observation (with WFIRST), ultra-deep spectroscopy or IFU observation (with TMT), and unprecedentedly deep and wide-field blind MIR spectroscopic observation (SPICA), and deep, high-resolution sub-millimeter observation (with ALMA).

3.3 The ULTIMATE–K Medium-band Imaging Survey for Galaxies and Proto-clusters at $3 < z < 5$

Tadayuki Kodama[1], **Yusei Koyama**[1], **Ken-ichi Tadaki**[2], **Kotaro Kohno**[3]
[1] Subaru Telescope, National Astronomical Observatory of Japan
[2] Max-Planck-Institut für Extraterrestrische Physik
[3] Institute of Astronomy, The University of Tokyo

3.3.1 Introduction

The mass assembly history, ie. the evolution of galaxies' stellar mass function (SMF) as a result of new star formation in individual galaxies and mergers between other galaxies, is one of the most fundamental ways of expressing the galaxy formation and evolution with time. Thanks to wide-field infrared imaging surveys conducted on 4–6.5 m class telescopes, such as UKIDSS (UKIRT), ULTRA-VISTA, ZFOURGE (Magellan) surveys, we now have statistically robust measurements of stellar mass functions up to $z = 4$ (Fig. 3.9, Muzzin et al. 2013; Straatman et al. 2014), although we can reach only down to $10^{11}\mathrm{M}_{\odot}$ in the highest redshift bin. Such studies require high precision estimation of photometric redshifts, because it is impractical to obtain expensive spectroscopic redshift measurements for all of those many galaxies to the required depth even with 8–10m class telescopes. Moreover, in order to obtain reasonably good photometric redshifts, we have to capture the Balmer/4000Å-break feature of a galaxy spectrum at 3800–4000Å, the most notable spectral feature in the rest-frame optical wavelength regime. For this reason, the current upper limit in redshift of $z \sim 4$ is set by the situation where we can still straddle the break feature between H and K bands with the ground-based observations (Straatman et al. 2014). We have thus yet very poor knowledge of stellar mass functions beyond $z = 4$ or below $10^{11}\mathrm{M}_{\odot}$ at $z < 4$. The FoV, depth, wavelength coverage and improved photometric redshifts are all key features in order to improve the situation.

Moreover, this type of deep and wide NIR imaging survey will be powerful in finding proto-clusters at $z > 2$, where we have only a few confirmed rich proto-clusters so far. The massive systems of $10^{14}\mathrm{M}_{\odot}$ or larger at $z \sim 2$ are the typical progenitors of present-day richest clusters of $10^{15}\mathrm{M}_{\odot}$ (Chiang et al. 2013). We know from the colours of early-type galaxies in rich clusters today that the majority of stars in those galaxies are formed at $z > 2$. Therefore the proto-clusters at $z > 2$ are the very environments where present-day early-type galaxies are just forming their starsin a short period of time. In fact, Kodama et al. (2007) show that massive galaxies ($>10^{11}\mathrm{M}_{\odot}$) on the red sequence in proto-clusters are first emerging between $z = 3$ and 2. In order to investigate even earlier phase of those progenitors, we should first of all go further in redshifts and discover proto-clusters at $z > 3$, and at the same time, we should go much deeper to explore $\sim 10^{10}\mathrm{M}_{\odot}$ regime.

3.3.2 Survey design

Medium-band imaging survey with GLAO (the ULTIMATE-Subaru project) is the ideal solution for these purposes. First of all, it provides a 200 arcmin^2 field of view at NIR on a 8-m telescope, which is by far the largest among the 8–10m class telescopes. Secondly, the improved seeing sizes of Subaru from $0.4''$ to $0.2''$ on average at the K-band means that we can gain a sensitivity by 0.75 magnitude for point sources by narrowing the photometric apertures. We know that high-z galaxies, in particular quiescent galaxies, tend to be very compact in size ($\sim$1 kpc or $0.15''$), and thus we can go much deeper by 1.5 magnitude than 4-m class telescopes even under excellent natural seeing conditions ($0.4''$). Furthermore, we propose to make 9 medium-band filters that neatly cover the entire near-infrared bands at Y, J, H and K (Fig. 3.10), including three medium-band filters that split the K-band into K1, K2 and K3. With this unique set of medium-band filters, we can not only improve the photometric redshift measurements significantly, but also neatly straddle the Balmer-break feature beyond $z = 3.5$ up to $z \sim 5$ for the first

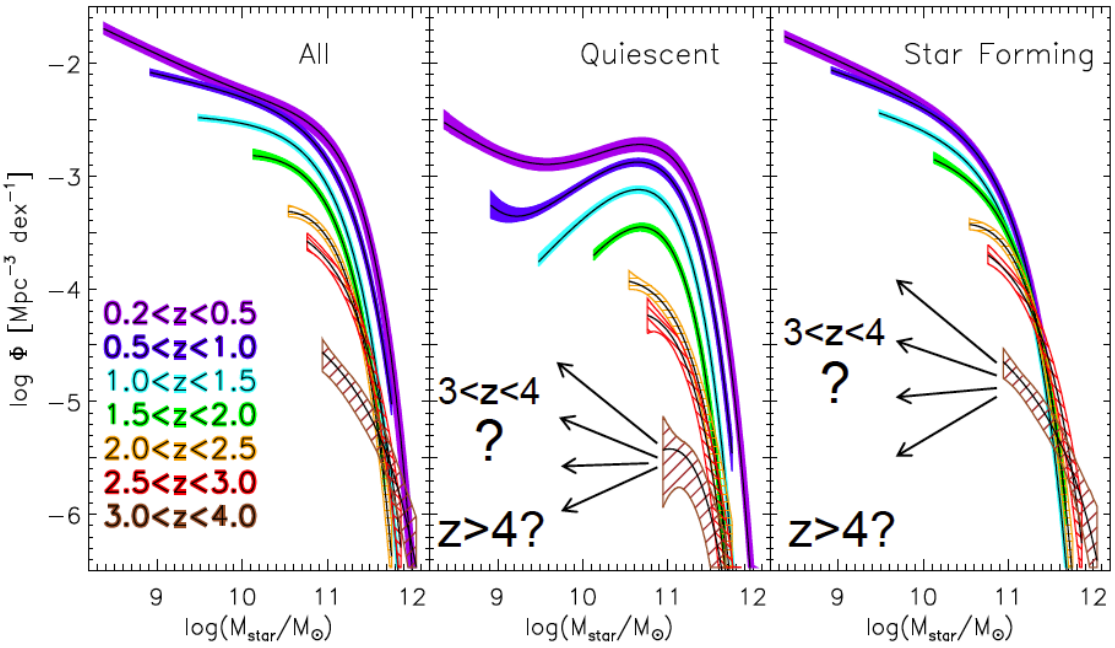

Figure 3.9: The stellar mass functions (SMF) constructed by the ULTRA-VISTA survey (COSMOS; 1.62 deg^2) as a function of redshift up to $z = 4$ (Muzzin et al. 2013). The ULTIMATE–K imaging survey will probe the SMF to much lower masses and to higher redshifts.

time. This is the territory of redshift where only the UV-selections of star forming galaxies have been available, such as Lyman break galaxies and Lyα emitters. The ULTIMATE-Subaru will open a new window to this early epoch of galaxy formation with NIR selected galaxies. We plan to conduct a deep imaging survey for 1 sq. deg. each (18 pointings each) in SXDF-UDS and COSMOS fields where HSC Ultra-Deep optical imaging data (∼28mag) are also available.

If we spend a 10 hr net exposure in each medium-band filter (K1, K2, and K3) per pointing, we can reach down to 26.1 magnitude in AB for point sources (5σ, $0.2''$ seeing, and $0.5''$ aperture). At this depth, in the combined 2 sq. deg. area, we expect to find 2000 and 1200 galaxies in the redshift ranges of $3 < z < 4$ and $4 < z < 5$ down to 5×10^9M$_\odot$ and 10^{10}M$_\odot$, respectively (above 5σ, and for the Kennicut IMF). This estimation was made based on the extrapolation of the ULTRA-VISTA stellar mass function at $3 < z < 4$ ($>10^{11}$M$_\odot$) to fainter mass without any evolution (Fig. 3.9). From such unique truly statistical sample of distant galaxies, the stellar mass functions can be constructed up to $z \sim 5$ for the first time. This size of medium-band survey in the K-band can be completed in 160 clear nights (including 30% overheads) with the ULTIMATE-Subaru wide-field camera (FoV=200 arcmin^2), or ∼400 nights if we complete all the 9 medium-band filters.

As shown in Fig. 3.9, we can go much deeper in stellar mass functions at $z < 4$ compared to ULTRA-VISTA, as well as extending them to $z = 5$ for the first time. This will enable us to explore the earlier phase and lower mass regime of mass assembly history back to the cosmic epoch when the Universe was only 1 Gyr old.

Moreover, over the 2 deg^2 field, we expect to find ∼2 progenitors of Coma-type rich clusters in each redshift interval of Δz=1 up to $z = 5$. In order to find those proto-clusters, we can make best use of the medium-band filter photometry. As shown in Fig. 3.11, medium-band filters are excellent discriminators of redshifts between $2 < z < 5$ especially for quiescent galaxies. Therefore, we can enhance the visibility of the intrinsic red sequence of each proto-cluster in medium-band colours, being much less affected by the projection effect (the contamination is expected to be reduced by a factor of 3). With those newly found proto-clusters, we can then utilize the depth of the photometry to investigate the evolution of

MB filters	λ_c (μm)	FWHM (μm)	z_s(Bal.Lim.) 3645Å	z_s(D4000) 4000Å
Y	1.05	0.10	1.74	1.50
J1	1.17	0.12	2.05	1.78
J2	1.29	0.12	2.37	2.08
H1	1.50	0.12	2.95	2.60
H2	1.62	0.12	3.28	2.90
H3	1.74	0.12	3.61	3.20
K1	2.03	0.14	4.38	3.90
K2	2.17	0.14	4.76	4.25
K3	2.31	0.14	5.14	4.60

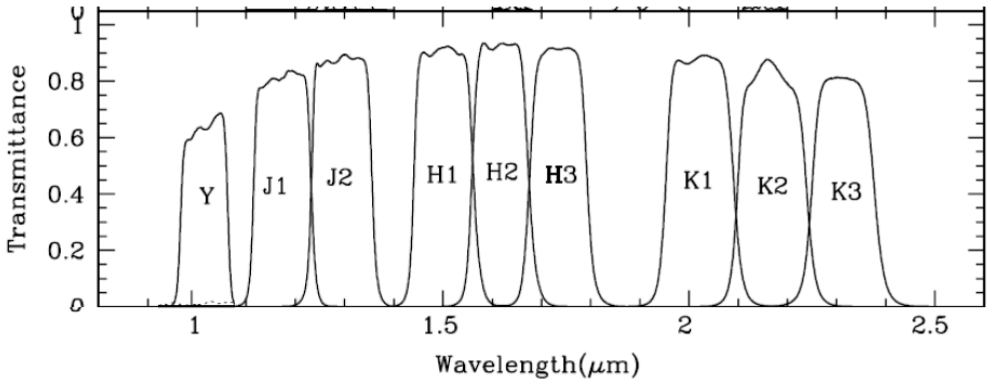

Figure 3.10: The proposed 9 medium-band filters for ULTIMATE-Subaru. These are identical to those made for SWIMS (NIR instrument developed for TAO at IoA, Univ. of Tokyo).

galaxies on the red sequence down to $10^{10}M_\odot$ as a function of redshift for $2 < z < 5$. This analysis will tell us for the first time at this depth when the mass of present-day early-type galaxies are assembled and when the star formation activities are quenched in those systems at $z > 2$, which are currently known only for the brightest galaxies ($10^{11}M_\odot$) up to $z \sim 3$.

3.3.3 Competitiveness

This deep and wide survey in the K-band will be unique in 2020's even in the era of WFIRST and JWST and provide excellent targets for TMT to follow-up. WFIRST is a NIR wide-field space telescope with 2.4-m aperture with 0.28 sq. deg. field of view, which will be the most powerful NIR imager of distant Universe. However, the wavelength coverage is limited to 2μm. Therefore ULTIMATE-Subaru will remain unique in the K-band (2–2.5μm). JWST, a 6.5-m space telescope, will fully cover the K-band and beyond, but the field of view is limited to only a few arcmin^2. Therefore ULTIMATE-Subaru will also remain unique as it provides $\sim$100$\times$ larger field of view.

Combined with the systematic narrow-band imaging at NIR (in particular at K-band) also proposed for ULTIMATE-Subaru (see Section 3.2), we are able to conduct a unique imaging survey in the K-band which can be named as "ULTIMATE–K Imaging Survey"!

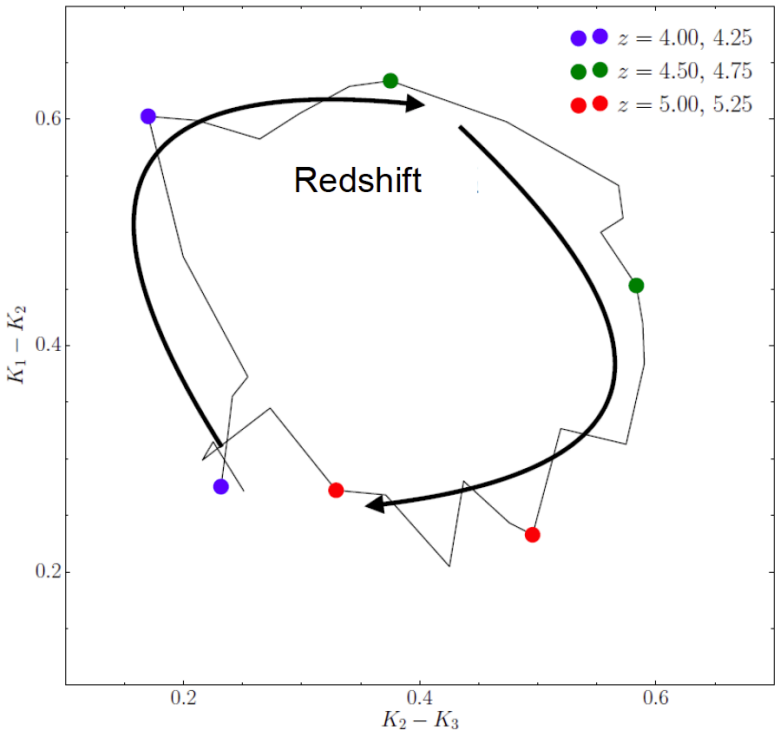

Figure 3.11: A colour–colour diagram in K1, K2, and K3 bands. A colour evolution of quiescent galaxies is shown as a function of redshift from $z = 4.0$ to $z = 5.25$ (J. Toshikawa; private communication). This diagram alone can be used to estimate their redshifts utilizing the sensitive colour change due to the passage of the Balmer/4000Å break feature over these medium-band filters.

3.4 A Possible Plan for ULTIMATE Legacy Survey

Yusei Koyama[1] **Tadayuki Kodama**[2]**, Ikuru Iwata**[1]
[1] Subaru Telescope, National Astronomical Observatory of Japan
[2] National Astronomical Observatory of Japan

In the previous three sections (Section 3.1–3.1), we have presented our high-z science cases using the wide-field imager of ULTIMATE-Subaru. All these sections require NB and/or MB filters, which are not available on space observatories. They require a large observing time, and plan to perform unprecedentedly deep observations covering square-degree scale fields. We believe that the proposed observations will provide a very high legacy value for extra-galactic astronomy as well as space missions in 2020s or later. The survey plan should therefore be organized well through extensive discussions with the Subaru community.

We here describe a preliminary idea for the ULTIMATE legacy survey by assuming the current framework of Subaru Strategic Program (300 nights over 5 years)[3], Assuming that deep broad-band (J an H) photometry is available with WFIRST, we concentrate on the narrow-band and medium-band survey in 2-deg^2 field overlapped with the HSC ultra-deep fields. We note that we need 32 pointings to cover 2-deg^2 field with the ULTIMATE wide-field imager (with $16' \times 12'$ FoV).

- Ultra-deep imaging with NB$_J$($\times$2) filters aiming at detecting very high-z LAEs ($z > 7$). Although it is very challenging to detect $z > 7$ LAEs (see Section 3.1), this is a direct extension of HSC survey for $z < 7$ LAEs, so that the impacts to the community would be large. We will spend 8-hours per pointing (10-hours including overheads), yielding **64 nights** to complete 2-deg^2 survey with the two filters. Another important role of this ultra-deep NB$_J$ data is that they can serve as an unprecedentedly deep Hα observations at $z \sim 1$ or [OII] at $z \sim 2$. By collaborating with the survey for the cosmic noon (see below), the proposed NB observations will bring a high legacy value.

- Deep imaging with NB$_H$($\times$2) and NB$_K$($\times$2), again covering the 2-deg^2 to target Hα, [OIII], and other rest-optical lines of z=1–3 galaxies. Assuming that we will spend 4-hours per pointing (5-hours including overheads), we require 16-nights to complete each filter, yielding **64 nights** in total to complete the survey with four NBs. We note again that we plan to manufacture the "pair filters" so that we can get Hα with NB$_K$, Hβ (or [OIII]) with NB$_H$, and [OII] with NB$_J$ for $z \sim 2$ galaxies (see an example of filter settings in Fig. 3.6). Our goal is to go $\sim$2-mag deeper than HiZELS,

Survey type	Filters	Exp. time per FoV (including overheads)	Limit mag. (5σ, AB)	N. of nights
NB imaging	NB$_J$×2	8.0 (10.0)	27.0	64
	NB$_H$×2	4.0 (5.0)	24.2	32
	NB$_K$×2	4.0 (5.0)	24.1	32
MB imaging	*K1*	10.0 (13.0)	26.1	42
	K2	10.0 (13.0)	26.1	42
	K3	10.0 (13.0)	26.1	42
BB imaging	*K*	3.0 (4.5)	26.1	15
Total time	–	–	–	269

Table 3.7: A preliminary plan for the ULTIMATE legacy survey (covering 2-deg^2 overlapped with HSC ultra-deep fields) using the wide-field imager.

[3]See http://www.naoj.org/Science/SACM/Senryaku/senryaku_E.html.

reaching $SFR_{H\alpha}\sim1$ $M_\odot$/yr at $z = 2$. Assuming that deep K-band data is not available from WFIRST, we need to observe broad-band (K) data by ourselves (4.5 hours per pointing including overheads). This requires additional **15 nights**. We believe that this very deep K-band data will also significantly complement WFIRST data (which covers only λ<2.0μm).

- Ultra-deep medium-band survey (*K1,K2,K3*) to detect Balmer break galaxies out to $z = 5$. To detect $10^{10}M_\odot$ galaxies at $4 < z < 5$, we require 10-hours on-source integration per pointing (13-hours including overheads), yielding **126-nights** to complete 2-deg^2 survey with all three filters. This survey is an extension of NEWFIRM (with KPNO-4m) or ZFOURGE (with Magellan), but we will make full use of our advantage of the improved sensitivity with GLAO correction (and large telescope aperture).

To complete all these NB, MB, BB survey covering 2 deg^2, we require **269 nights** in total. The survey plan is also summarized in Table 3.7. The detailed survey plans (e.g. filter setting) should be determined according to the requirements from the community, hence we need to have continuous discussion.

Chapter 4

Science Case II – High-z science with ULTIMATE spectroscopic survey

The improvement of spatial resolution achieved by GLAO can also enhance the sensitivity of our spectroscopic observations. In this Chapter, we discuss possibilities of future systematic spectroscopic surveys with ULTIMATE-Subaru. In Section 4.1, we describe the possible survey plan assuming that we will have multi-object spectrograph on ULTIMATE-Subaru (see details in Section 7.3). In Section 4.2, on the other hand, we consider a systematic IFU galaxy survey for z∼0.5–1 galaxies as an extension of SAMI project. In this section we assume that we will have a multi-object integral field unit spectrograph (see details in Section 7.4).

4.1 Large Spectroscopic Survey with ULTIMATE-Subaru

Ken-ichi Tadaki[1], **Takatoshi Shibuya**[2], **Masayuki Akiyama**[3], **Masao Hayashi**[4], **Kimihiko Nakajima**[5]
[1] Max-Planck-Institut für Extraterrestrische Physik
[2] Institute for Cosmic Ray Research, The University of Tokyo
[3] Astronomical institute, Tohoku University
[4] National Astronomical Observatory of Japan
[5] Observatoire de Genève, Université de Genève

4.1.1 Introduction and survey design

Spectroscopy of nebular emission lines gives us fundamental information to characterize galaxy properties, as well as a distance to galaxies (redshift). Galaxies exhibit a huge variety of properties and we often face difficult challenges such as a sample bias in the case of studies with a small sample. The Sloan Digital Sky Survey (SDSS; York et al. 2000) is one of the most successful large spectroscopic survey and provides more than 10^6 spectra for local galaxies at $z < 0.2$. This massive database enabled us to statistically study galaxy properties such as stellar masses, star-formation activities, metallicities, black hole masses, and environments in the multi-parameter spaces. Such a large and systematic spectroscopic survey for targeting higher-redshift galaxies is a natural extension. At $z > 2$, all major nebular emission lines (Hα, [OIII], Hβ, and [OII]) are redshifted to near-infrared wavelengths. In the mid-2010s, some large near-infrared surveys have been conducted (MOSDEF; Kriek et al. 2015, KMOS^{3D}; Wisnioski et al. 2015, FMOS-COSMOS; Silverman et al. 2015) but their sample size is still restricted to ∼10^3, which is

not sufficient especially in the sense of involvement with large scale structures. In the early-2020s, more extensive surveys with Subaru/PFS and VLT/MOONS are planned but both do not cover K-band. In addition to them, *Euclid* will also start massive low-resolution near-infrared spectroscopic survey covering 1.1-2.0 μm from space. The spectral resolution will be $R = 250$ and the expected 10σ line detection limit is 1×10^{-16} erg s^{-1} cm^{-2} in the deep field with 20 degree^2. Ultimate-Subaru can achieve 10 times deeper detection limit with relatively short exposure time (∼1hour), and provide high resolution spectra, which is necessary for accurate line ratio diagnostics with rest-frame optical emission lines. Therefore, a large spectroscopic survey with ULTIMATE-Subaru will be still an unique project as we can observe Hα emission lines at up to $z = 2.6$ and [OII] at up to $z = 5.5$ (Figure 4.1).

For an instrument of ULTIMATE-Subaru, we here assume a MOSFIRE-like spectrograph (FoV of $\sim 3' \times 6'$, multiplicity of $\sim$ 30, R$\sim$ 4000). Given that TMT has a similar instrument, a wide-field survey with a short integration time ($\sim$ 1 hour) can be complementary with a much deeper but smaller sample survey. Correction with GLAO improves the sensitivity of ULTIMATE-Subaru by a factor of two. Even with 1 hour integration, the 5σ limiting line flux is 7.4×10^{-18} erg s^{-1} cm^{-2}, which is deep enough to detect a Hα emission line for star-forming galaxies with SFR=1.3 M$_\odot$yr^{-1} at $z \sim 2$. As the most unique advantage of ULTIMATE-Subaru is deep spectroscopy at K-band, core redshift ranges of the survey are $z = 2.0 - 2.6$ and $z = 3.0 - 3.7$, at which major nebular lines are redshifted to K-band. Table 4.1 summarizes target selections in a large spectroscopic survey with ULTIMATE-Subaru. The first targets are selected from star-forming galaxies at $z = 2.0 - 3.7$ whose Lyα and/or [OII] spectra are obtained by PFS. They are initially identified as Lyα emitters (LAEs) or Lyman break galaxies (LBGs) from HSC imaging data. The expected number of these sample is ∼2200 deg^{-2} (Takada et al., 2014). This selection could miss massive galaxies with log M_* >10.5 because their Lyα and [OII] emission lines are strongly attenuated by dust extinction or intrinsically weak due to quiescent properties. We aim to target a stellar mass-selected sample with log M_* >10.5 at $z = 2.0 - 2.6$ whose surface number density is ∼5000 deg^{-2} (Skelton et al., 2014). Including relatively low-density objects such as radio, mid-infrared or X-ray selected galaxies and Lyman break galaxies (or Lyα emitters) at up to $z = 5.2$, we aim to get H and/or K-band spectra for 1.8×10^4 galaxies over 3 deg^2 in 200 nights (overhead of 20%, clear sky rate of 80%, 9 hours per night). The survey area is nicely coordinated with a currently-projected PFS ultra-deep survey (3.5 deg^2) and a mid-infrared spectroscopic deep survey with SPICA (2 deg^2), but we need a larger multiplicity to utilize a PFS deep survey (16 deg^2).

4.1.2 Star formation activity and chemical evolution

Relationships between star formation rate (SFR), gas-phase metallicity, and stellar mass in galaxies give us insight into processes responsible for the galaxy activity. The correlations of the former two properties

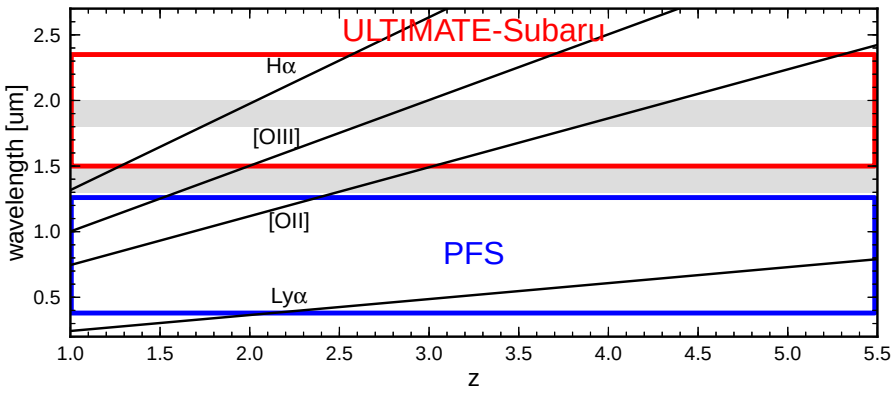

Figure 4.1: Observed frame wavelengths of redshifted nebular emission lines and coverages of ULTIMATE-Subaru (red) and PFS (blue).

with stellar mass are well-known as main sequence of star-forming galaxies for SFR (e.g., Salim et al., 2007; Peng et al., 2010) and mass-metallicity relation for metallicity (e.g., Tremonti et al., 2004). Moreover, some recent observations argue that there is a tight surface in 3D space which consists of all of them (fundamental metallicity relation, Lara-López et al., 2010; Mannucci et al., 2010). The shape and tightness of the correlations are dependent on, for example, time scale of star-formation quenching, star formation efficiency, inflow/outflow of gas, and gas fraction (e.g., Saintonge et al., 2012; Lilly et al., 2013; Zahid et al., 2014). Therefore, understanding the mutual relationships and its environmental dependence properly for galaxies at the cosmic noon is essential to get a complete view of galaxy evolution.

We are about to reach a consensus of the main sequence and the mass-metallicity relation as long as we focus on the local Universe (Tremonti et al., 2004; Peng et al., 2010). This is largely due to the SDSS (Strauss et al., 2002) providing us with overwhelming spectroscopic data with multiple major emission lines in rest-frame optical for the flux-limited sample with high completeness. However, at higher redshifts of z=1.5-3.5, although we agree with the existence of the correlations, we have yet to reach a consensus of the details of the correlations in terms of shape, normalization, and dispersion and the environmental dependence of the correlations (Fig. 4.2). There are non-negligible uncertainties in deriving SFR and metallicity of galaxies at high redshifts because of the limited number of major emission lines used. The size of the existing samples is another cause. The spectroscopic samples of high-z galaxies are still more than 2 orders of magnitude smaller than the local ones (§ 4.1.1). Therefore, the SDSS-like spectroscopic sample of galaxies at z =2.0–2.6, which is achieved by ULTIMATE-Subaru, is sure to revolutionize our understanding of galaxy evolution at cosmic noon, as the SDSS has done in the local Universe.

Target selection	Redshift range	$N_{\rm gal}$
Mass-selected (log M_* >10.5)	$2.0-2.6$	15k
Lyman break (w/ PFS spectra)	$2.0-2.6$	4k
Lyman break (w/ PFS spectra)	$3.0-3.7$	2.5k
Lyman break (w/ PFS spectra)	$4.4-5.2$	0.5k
Lyα emitter (w/ PFS spectra)	2.2, 3.3, 4.9	3.2k

Table 4.1: Number of the target galaxies for the ~ 3 deg^2 survey with ULTIMATE-Subaru. For 1.8×10^4 galaxies out of them, we aim to obtain H and/or K-band spectra.

Hα emission is sensitive to star formation in short time-scale of < 10 Myr. When an initial mass function is assumed, the correction for dust extinction is the largest factor causing the uncertainty in the estimation of SFR. The amount of dust extinction can be estimated by Balmer decrement (the flux ratio of Hα to Hβ). The sensitivity currently considered (§ 4.1.1) enables us to detect relatively faint Hβ (less than $\sim$0.35 of Hα flux) for most galaxies targeted. To derive the Hα/Hβ ratio accurately, we have to take account of the absorption of stellar continuum underneath the Balmer lines and dust extinction curve (e.g., Reddy et al., 2015). It may be difficult to detect the stellar continuum in individual spectra even for bright galaxies. However, the large sample obtained by the ULTIMATE-Subaru survey allows us to divide the sample based on stellar mass, SFR, or environment, and then do stacking analysis to detect the average stellar continuum. Thus, with the most reliable measurement of SFR, we investigate the main sequence of galaxies and the dependence of the main sequence on environment at $z \sim 2$.

The diagnostics with the ratios of major emission lines are used to estimate gas-phase metallicity; R_{23}=([OII]+[OIII])/Hβ, O3N2=([OIII]/Hβ)/([NII]/Hα), and N2=[NII]/Hα (e.g., Kewley & Dopita, 2002; Pettini & Pagel, 2004). Most of the current studies cannot help relying on the stacking analysis to derive the mass-metallicity relation at $z \sim 2$ due to difficulty in the detection of faint emission lines (Fig. 4.2). Thus, it is important to detect the multiple major emission lines for individual galaxies investigated. This is crucial to obtain a consensus of mass-metallicity relation and discuss whether there is a fundamental metallicity relation at $z \sim 2$. We investigate what kind of processes causes the dispersion about the correlations and discuss key processes that play a critical role on galaxy evolution, which cannot be achieved without the large, deep spectroscopic sample by ULTIMATE-Subaru. At present some

studies argue that there is an offset in metallicity at a given stellar mass, while other studies indicate the mass-metallicity relation of cluster galaxies at $z \sim 2$ consistent with field galaxies at similar redshifts (Fig. 4.2 and e.g., Shimakawa et al., 2015; Tran et al., 2015). Revealing the environmental dependence of the correlations is another topic that we should address. Finally, we would like to mention possible synergy with SPICA. The metallicity measurement for dusty galaxies at $z \sim 2$ is considered with emission lines seen in far-infrared as one of key science by SPICA. The survey by ULTIMATE-Subaru, which can detect the emission lines in rest-frame optical, is complementary to the far-infrared study with SPICA.

4.1.3 Properties of interstellar medium

For galaxy formation studies, it is essential to understand physical conditions of inter-stellar-medium (ISM) in galaxies. HII regions are of particular interest, since high-redshift galaxies are actively star-forming. Key properties are: ▷ gas condition (metallicity Z, density n_e, temperature T_e, etc.), ▷ shape of the EUV spectrum, and ▷ ratio of ionizing photons to hydrogen atom (ionization parameter U). They can be examined by the emission lines of hydrogen and other metal lines especially seen in the rest-frame optical regime, as presented in detail below. The deep NIR MOS spectroscopy is thus essential for the study of the ISM properties of high-redshift galaxies at $z = 1.5 - 4$, and possibly at higher-z.

Available major lines `Core redshift 1` ($z = 2.0{-}2.35$): Hα, Hβ, [OIII]$\lambda\lambda$5007, 4959, [NII]$\lambda\lambda$6583, 6548, [SII]$\lambda\lambda$6717, 6731. Also obtainable are [OII]$\lambda\lambda$3726, 3729 doublet (or simply [OII]λ3727) and [NeIII]λ3869 by PFS. `Core redshift 2` ($z = 3.0 - 3.7$): Hβ, [OIII]$\lambda\lambda$5007, 4959, [OII]λ3727 and [NeIII]λ3869.

Electron temperature Although [OIII]λ4363 is not accessible, the other temperature-sensitive oxygen lines of OIII]$\lambda\lambda$1661, 1666 are available that will be identified by PFS at both of the core redshift ranges. Combining with the [OIII]$\lambda\lambda$5007, 4959 lines observed with ULTIMATE-Subaru, we can determine the electron temperatures. The statistical study of the electron temperature of HII regions in high-z galaxies will be one of the most interesting but unexamined subject in the era of ULTIMATE-Subaru. We expect a few percentile of the whole sample (i.e., a few hundreds of galaxies) to have the temperature estimate (cf. Kakazu et al. 2007). The number could be larger, since half of the sample is comprised of low-mass emitters, hence metal-poor galaxies with a high T_e. The T_e measurement enables us to reliably determine the oxygen abundance from the [OIII]$\lambda\lambda$5007, 4959/Hβ and the [OII]λ3727/Hβ ratios. At the moment

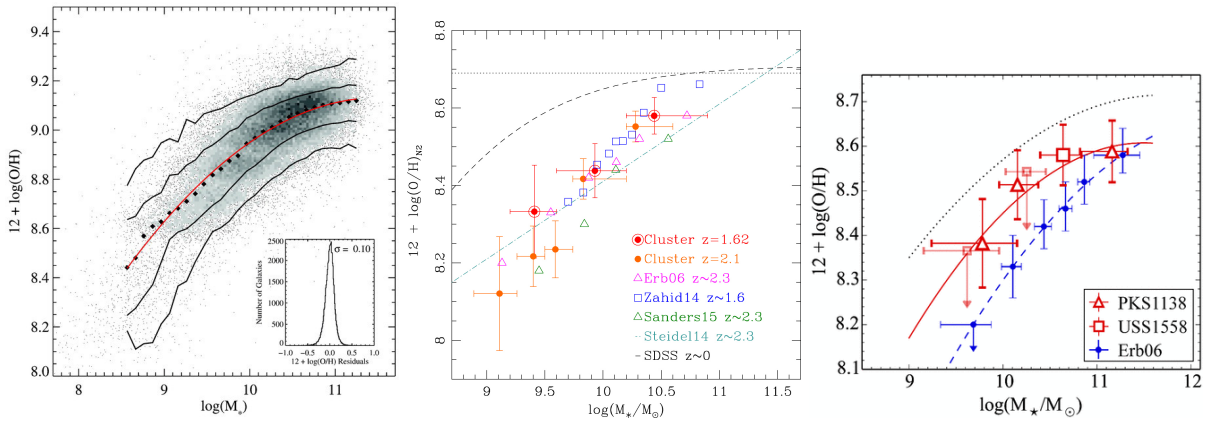

Figure 4.2: (left) Fig. 6 of Tremonti et al. (2004) showing the mass-metallicity relation for ∼53,400 star-forming galaxies in the local Universe. (middle) Fig. 9 of Tran et al. (2015) showing the mass-metallicity relations with the stacked spectra for cluster (red and orange) and field (the other colors) galaxies at $z \sim 1.6$ and 2.3. Tran et al. (2015) argue that there is no offset between cluster and field galaxies. (right) Fig. 6 of Shimakawa et al. (2015) showing the mass-metallicity relations with stacked spectra for proto-cluster (red) and field galaxies (blue) at $z \sim$2–2.5. Shimakawa et al. (2015) argue that the cluster galaxies have higher oxygen abundance than field galaxies at a given stellar mass.

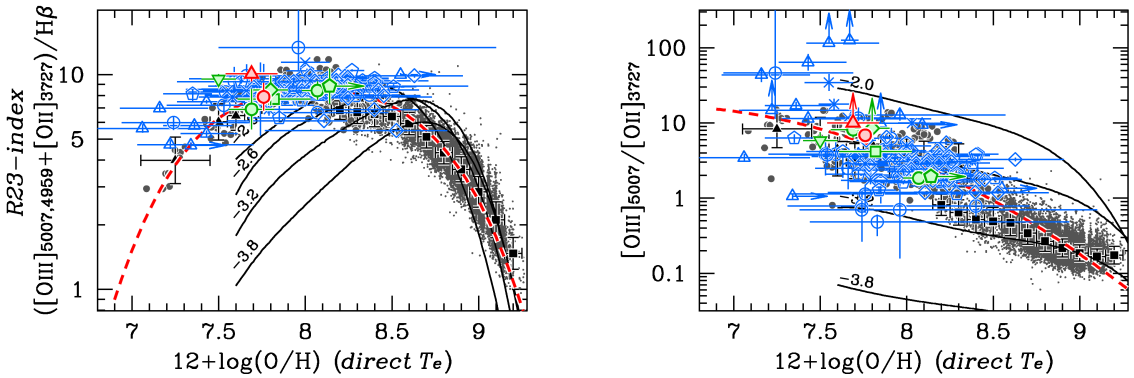

Figure 4.3: R23-index (left) and [OIII]λ5007/[OII]λ3727 ratio (right) as a function of metallicity. The gray dots and the gray triangles and squares show local galaxies. The blue, green, and red symbols present the galaxy samples at $z = 1$, 2 and 3, respectively, whose metallicities are T_e-based. The red dashed curve shows the local empirical relations (Nagao et al., 2006). The black solid curves denote photoionization models (Kewley & Dopita, 2002). The labels on the curves present values of $\log U$.

there are only 6 galaxies at $z \sim 2$ and 2 at $z \sim 3$ whose metallicity is reported based on the temperature (Villar-Martín et al., 2004; Yuan & Kewley, 2009; Erb et al., 2010; Rigby et al., 2011; Christensen et al., 2012; James et al., 2014). ULTIMATE-Subaru will significantly enlarge the size of the sample, provide a conclusive picture of the chemical evolution of ISM in galaxies (§ 4.1.2). Furthermore, the line ratios with the aid of the directly determined metallicities will allow us to examine the detailed physical conditions of the ISM in high-z galaxies. Figure 4.3 shows the ([OIII]$\lambda\lambda$5007, 4939+[OII]λ3727)/Hβ ratio (R23-index) and the [OIII]λ5007/[OII]λ3727 ratio as a function of T_e-based metallicity. There are no significant differences in the relations between the local and the high-z samples, implying that the physical conditions are not dramatically evolving. However, the relations at $z > 2$ are still unclear. By establishing the relations at high-z, we can investigate the other important properties such as the ionization state and the shape of ionizing photon spectrum in detail (see below).

We note that dust extinction effect is needed to be carefully considered for the studies of not only the temperature but the other spectroscopic properties presented below. We can correct for dust extinction for galaxies at the `core redshift 1` *by using the Balmer decrement, the Hα/Hβ ratio. For galaxies at the* `core redshift 2`*, on the other hand, the correction is difficult because the only observable Balmer series from the ground is the β transition. The JWST IR spectroscopy from the space should be encouraged for the direct correction. It might be useful to utilize the color excess of the stellar continuum that is derived from the SED fitting to the broadband photometry (e.g., a prescription given by Reddy et al. 2015).*

Ionization parameter Ionization parameter provides an useful information for our understanding the ionization state of the HII region. Ionization parameter is measured with the use of the ionization fraction of oxygen, (O^{2+}/O^{+}), which is estimated from the [OIII]λ5007/[OII]λ3727 ratio and the electron temperature. Recently, some authors report that a typical ionization parameter increases towards high-z, and suggest the evolution of ionization parameter (e.g., Nakajima & Ouchi 2014). This could just result from the tendency that galaxies with a high ionization parameter and a low metallicity are more dominant in high-z than the local universe. Figure 4.3 indeed suggests that both the high-z and the local galaxies show the comparable ionization parameter at a fixed metallicity. Alternatively, high-z galaxies could have denser HII regions than local galaxies, result to exhibit a higher ionization parameter (Shirazi et al. (2014); see below). Accurate measurements of metallicity, ionization parameter, and density will be key for understanding the physics that govern the HII regions in high-z galaxies.

Electron density Electron density is related to the ionizing photon production rate (Q_0) and the ionization parameter as $U \propto Q_0^{1/3} n_e^{1/3}$ under the assumption of the ionization equilibrium and the homogeneous gas cloud. Combining with the ionization parameter estimates, we can investigate the star-formation conditions at high-z (e.g., Shimakawa et al. 2015; Shirazi et al. 2014). Also, the geometry of the

HII-regions (i.e., volume filling factor) can be examined statistically for the first time. Electron density is measured from the ratio of the doublets of [OII]$\lambda\lambda$3726, 3729 and [SII]$\lambda\lambda$6717, 6731. ULTIMATE-Subaru has a spectral resolution good enough to resolve the doublets.

Abundances of heavy elements The total element abundance can be derived from the abundances of ions seen in the optical spectra using ionization correction factors (e.g., Izotov et al. 2006). Ionization parameter enables us to estimate them. We are thus able to derive the total abundances of heavy elements such as Nitrogen, Neon, Sulfur, etc. that are almost unknown in high-z galaxies. Recently, N/O abundance ratios are inferred to be higher in high-z galaxies (e.g., Masters et al. 2014; Steidel et al. 2014; Shapley et al. 2015). Our Nitrogen abundance estimates will provide a direct picture of the evolution. The abundance of another alpha-element of Sulfur will be useful for the interpretation of the N/O abundance ratio. Since Neon is a noble gas and not affected by dust depletion, the Ne/O abundance ratios can provide the degree of depletion of oxygen onto dust grains. The depletion factors of elements are unknown at high-z, and local values are usually assumed in photoionization modeling (e.g., Kewley & Dopita 2002). There is no clear evolution in the Ne/O abundance ratio from $z = 0$ to 1 (Jones et al., 2015), but high ratios are indicated at $z \sim 2$ (Zeimann et al., 2015). The ionization corrected abundance ratios would provide a clear answer to the possible evolution for $z \lesssim 4$.

Shape of EUV spectrum With the full suite of the nebular lines, we can investigate the shape of the ionizing photon spectrum in high-z galaxies. The SED of the ionizing source is usually assumed in photoionization modeling (blackbodies, or ones generated by stellar population synthesis codes under the assumption of age, stellar metallicity, IMF, etc.), and has not yet been sufficiently examined. Recently, Steidel et al. (2014) discuss the increased effective stellar temperatures at $z \sim 2-3$. However, the argument is not conclusive due to the lack of direct examination of the gas condition (e.g., T_e). By using photoionization models to reproduce the nebular emission line ratios in conjunction with the knowledge of the gas condition (Z, T_e, n_e) and the ionization state (U), we will statistically discuss the ionizing radiation field in high-z HII regions. This could lead to implications for the shape of the IMF (especially for the high mass end) as well as for details of hot and massive stars such as Wolf-Rayet stars at high-z.

4.1.4 Gas kinematics and ISM properties

Lyα line profiles and its velocity shift encode information on various physical properties of high-z galaxies (e.g. Verhamme et al., 2006; Duval et al., 2014). The large-scale galactic outflows make the Lyα line peak redshifting from the systemic redshift ($z_{\rm sys}$) of galaxies. In addition, the Lyα line profiles would be modified by resonant scattering effects depending on the column density of neutral hydrogen ($N_{\rm HI}$) and the gas covering fraction (f_c) of H I gas clouds (see Figure 4.4(a) and the caption). These dependences indicate that detailed analyses of the Lyα line profiles would provide useful hints on gas kinematics and ISM structures for understanding Lyα emitting mechanisms for high-z galaxies.

To dissect the Lyα line profiles, $z_{\rm sys}$ needs to be determined by nebular emission lines (e.g., Hα, [O III], [O II]) from galactic H II regions. Recent deep NIR spectroscopic observations have detected nebular emission lines from $\sim$ 300 LBGs (e.g. Steidel et al., 2010) as well as $\sim$ 100 LAEs at $z = 2-3$, and measured the Lyα velocity shift ($\Delta v_{\rm Ly\alpha}$) from $z_{\rm sys}$ (e.g., Hashimoto et al., 2013; Shibuya et al., 2014; Erb et al., 2014; Trainor et al., 2015). These studies have identified an anti-correlation between Lyα EW and $\Delta v_{\rm Ly\alpha}$ in a compilation of LAE and LBG samples. As described above, the Lyα line profiles depend on $N_{\rm HI}$, f_c, as well as the gas outflow velocity. Combined with the velocity offset of interstellar (IS) absorption lines ($\Delta v_{\rm IS}$) to break the degeneracy, detailed kinematic analyses suggest that $N_{\rm HI}$ could be a key quantity determining Lyα emissivity for $z \sim 2-3$ galaxies. However, such a systematic and statistical study on gas kinematics and ISM structures has not been performed for galaxies beyond $z \sim 3$ due to small galaxy samples with $\Delta v_{\rm Ly\alpha}$ and $\Delta v_{\rm IS}$ measurements (e.g. Schenker et al., 2013, Figure 4.4(b)). A deep and large-area NIR spectroscopic survey is required for constructing a larger sample at $z \gtrsim 3$.

Here we propose a statistical study on gas kinematics and ISM properties for galaxies at $z \sim 2-5$ with ULTIMATE-Subaru. Our target galaxies are $z \sim 2-5$ LBGs and LAEs selected in the Deep and Ultra-Deep fields of the HSC SSP and future NB surveys (ref Table 1). These LBG and LAE samples cover wide ranges of Lyα EW and UV magnitudes, allowing for a systematic study on the relation

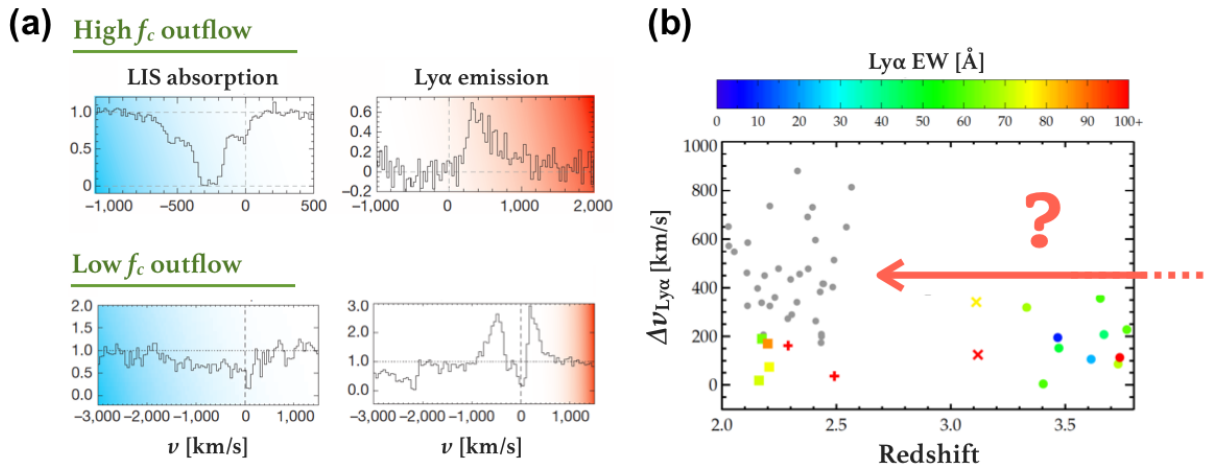

Figure 4.4: (a) IS absorption and Lyα emission lines in velocity space (Erb et al., 2015). The top and bottom panels present gaseous outflows with high and low f_c values, respectively. In the case of the high f_c outflow, a Lyα emission line is redshifted from z_{sys} and blueshifted IS absorption lines (e.g. Si II) are clearly shown on the UV continuum. In the case of the low f_c outflow, $\Delta v_{\mathrm{Ly}\alpha}$ decreases and Lyα flux emerges blueward of z_{sys}. In this case, the LIS absorption lines would be shallow compared to the high f_c outflow due to thin and/or patchy H I gas clouds (i.e. low N_{HI} and/or low f_c). (b) Lyα velocity offsets as a function of redshift (Schenker et al., 2013).

between Lyα emissivity and physical properties. We make use of the rest-frame UV spectroscopic data obtained by the PFS survey for the redshift determinations of Lyα emission and IS absorption lines. The deep ULTIMATE-Subaru and PFS spectroscopy will measure $\Delta v_{\mathrm{Ly}\alpha}$ and/or Δv_{IS} for $\sim 3,000$ LBGs and $\sim 2,000$ LAEs even at $z \gtrsim 3$. The great synergy with HSC, PFS, and ULTIMATE-Subaru will overcome the difficulty of investigating statistically gas kinematics and ISM properties for galaxies at $z \gtrsim 3$.

We will achieve the following major goals:

1. **Column density of H I gas** — We will investigate the evolution of N_{HI} based on the $\Delta v_{\mathrm{Ly}\alpha}$ measurements. Several studies with small galaxy samples have reported that $\Delta v_{\mathrm{Ly}\alpha}$ is probably small at $z \gtrsim 3$ (e.g., Schenker et al., 2013; Stark et al., 2015, Figure 4.4(b)). The possible $\Delta v_{\mathrm{Ly}\alpha}$ evolution may be explained by a low N_{HI} in high-z galaxies. To verify this possibility, we will measure $\Delta v_{\mathrm{Ly}\alpha}$ with the large sample and check whether the evolution of $\Delta v_{\mathrm{Ly}\alpha}$ is shown over the redshift range of $z \sim 2-5$. In addition to the simple $\Delta v_{\mathrm{Ly}\alpha}$ measurements, we also perform Lyα line profile modeling to derive the N_{HI} values (e.g. Verhamme et al., 2006; Hashimoto et al., 2015). We will study the $\Delta v_{\mathrm{Ly}\alpha}$ and N_{HI} dependences on physical quantities such as M_* and SFR for understanding the Lyα emitting mechanisms.

2. **Evolution of galactic outflow velocity** — We will examine the evolution of galactic outflow velocity based on the Δv_{IS} measurements. Gaseous outflows have been ubiquitously identified in star-forming galaxies at $z \sim 2-3$ (e.g. Shapley et al., 2003). However, there is a possibility that $z \gtrsim 3$ galaxies are not able to power strong winds because of a low star-formation activity. The outflow velocity can be more directly estimated from Δv_{IS} than $\Delta v_{\mathrm{Ly}\alpha}$. Among of our targets, the rest-frame UV continuum will be detected by the PFS observations for galaxies with $m_{\mathrm{UV}} < 24.4$ mag (see the PFS white paper). We will measure Δv_{IS} for these bright galaxies on an individual basis. Meanwhile, it is difficult to estimate Δv_{IS} for individual LAEs and LBGs with a high Lyα EW due to their faint UV-continuum emission. We will stack the rest-frame UV spectra to obtain a typical Δv_{IS} for the high Lyα EW sources. The Δv_{IS} analysis will constrain feedback processes and

the early history of metal enrichment caused by the galactic outflows. The direct measurements of outflow velocity are also useful for modeling the Lyα line profiles and constraining $N_{\rm HI}$.

3. **Lyα and LyC escape fractions** — We will infer the Lyα and LyC escape fractions at $z \sim 2-5$. The thin and patchy gas clouds could allow the Lyα and ionizing photons to escape from the central galaxies. In addition, the galactic outflows could enhance the Lyα and LyC escape fractions by making drafty holes through the ISM. To evaluate these escape fractions, we measure Lyα fluxes bluewards of $z_{\rm sys}$ and the depth of LIS absorption lines (e.g., Jones et al., 2013, Figure 4.4(a)). Combined with the results of $N_{\rm HI}$ and $\Delta v_{\rm IS}$, we will examine the relations between these escape fractions and gas kinematics/ISM structures for galaxies near the reionizing epoch.

4.1.5 Growth of super massive black holes

In order to reveal the accretion growth history of super-massive black holes (SMBHs) at centers of galaxies, it is important to examine the cosmic evolution of number density of AGNs. Hard X-ray surveys with various depth revealed number density of non-obscured plus mildly-obscured AGNs as a function of redshift for each luminosity bin (e.g., Ueda et al. (2014); left panel of Figure 4.5). Using the redshift evolution of the luminosity function of AGNs, the average growth history of SMBHs can be quantitatively inferred (e.g., Marconi et al. (2004)): massive $> 10^8 M_\odot$ SMBHs gain their mass around $z \sim 2$, on the contrary, less-massive $< 10^8 M_\odot$ SMBHs increase their mass around $z \sim 1$.

Although X-ray selection is efficient to select mildly-obscured AGNs and not affected by non-AGN objects, still X-ray selection can miss and be biased against heavily-obscured AGNs with obscuration column density of $N_{\rm H} > 10^{24}$ cm^{-2}, i.e., Compton-thick AGNs, for which the high column density makes the optical depth of Compton-scattering for X-ray photons one. Even very hard X-ray 20-40 keV flux of AGNs can be diminished significantly by heavy obscuration and a sample selected in such high-energy band can be biased against Compton-thick AGNs (Malizia et al., 2009). Because summantion of X-ray emission of populations of non-obscured and mildly-obscured AGNs cannot explain the energy density of the Cosmic X-ray Background (CXB) at around its peak energy range ($\sim$ 30 keV), the number ratio of Compton-thick AGNs to Compton-thin AGNs is estimated to be 0.5-1.6 (Ueda et al. (2014); right panel of Figure 4.5).

Rest-frame optical emission-line survey with NIR Multi-Object Spectrograph of ULTIMATE-Subaru can unveil the cosmological evolution of the number density of such heavily-obscured AGNs. In the local universe, a significant fraction of [OIII]-line-selected obscured AGNs are thought to be Compton-thick AGNs. Candidates of obscured AGNs are selected based on strong [OIII]-line from Sloan Digital Sky Survey (SDSS) spectroscopic database (Zakamska et al., 2003). X-ray fluxes of half of them are significantly smaller than that predicted from the strength of the [OIII]-line (Vignali et al., 2010). The large $L_{\rm [OIII]}/L_{2-10{\rm keV}}$ implies that their active nuclei are heavily-obscured even in the hard X-ray band. Such large column density is supported by strong Si 10μm absorption line observed in their MIR spectra (Zakamska et al., 2008).

H and K bands spectroscopic survey with ULTIMATE-Subaru can cover the important AGN/starburst diagnostic lines of Hα-[NII] and Hβ-[OIII] emission lines of galaxies at $z = 2.0-2.6$. The redshift range is important because the number density of AGN with typical luminosity peaks at around $z \sim 1-3$. If we assume the line detection limit of $F_{\rm [OIII]} = 1.5 \times 10^{-17}$ erg s^{-1} cm^{-2} with SN=10, we can detect $L_{\rm [OIII]}$ of 4.1×10^{41} erg s^{-1} and 8.1×10^{41} erg s^{-1} at $z = 2.0$ and 2.6, respectively, which correspond to intrinsic $L_{2-10{\rm keV}}$ of 2.2×10^{43} erg s^{-1} and 4.1×10^{43} erg s^{-1}, i.e. mildly-obscured AGNs with Seyfert-like luminosity.

At high-redshifts, it is possible that the fraction of heavily-obscured AGNs is even larger than that in the local universe. In fact, it is suggested that the obscured fraction of X-ray-selected AGNs at $z > 2$ is 2 times higher than that in the local universe (Ueda et al., 2014). High number density of Compton-thick AGNs at high-redshifts is inferred from 24μm-excess (Fiore et al., 2008; Alexander et al., 2008), MIR plus radio (Martinez-Sansigre et al., 2007), and MIR-SED (Polletta et al., 2006) selections of obscured AGNs. The estimated number densities imply that Compton-thick AGNs are as numerous as non-obscured and

mildly-obscured AGNs (see datapoints in the right panel of Figure 4.5). However, the current knowledge on the number density of Compton-thick AGNs are rather heterogeneous and not conclusive. Because the MIR methods select limited part of heavily-obscured AGNs, furthermore, only a small part of the candidates have spectroscopic redshifts.

The number density of AGNs compared to normal galaxies is small, thus wide field coverage as wide as a few square degree is necessary. If we cover 3 sq.deg of sky, cosmic volume of 2.4×10^7 Mpc^3 will be covered at $z = 2.0 - 2.6$. The large volume is required to cover multiple luminous AGNs. Additionally, it is particularly important to cover galaxies more massive than $M_* > 10^{10.5} M_\odot$ without bias, because X-ray-selected AGNs are mostly associated with galaxies in this mass range even for AGNs as faint as $L_{2-10\ \mathrm{keV}} = 10^{42}$ erg s^{-1} (Akiyama et al., 2015).

The sample of heavily-obscured AGNs discovered in the NIR spectroscopic survey can be complimentary to the AGN samples that will be discovered by future wide-field survey satellites, *ATHENA* and *SPICA*, planned to be launched in late 2020s. *ATHENA* is a next generation wide field X-ray survey satellite, which can cover 40×40 arcmin^2 with 5 times larger effective correcting area than *XMM-Newton*. X-ray spectroscopic imaging survey with *ATHENA* can unveil the strong Fe emission line associated with obscured AGN activity. *SPICA* can conduct deep low-resolution long-slit spectroscopic and imaging survey in MIR/FIR wavelength range within $\sim$ 10 sq.deg to search for AGN activity with hot/warm dust component of AGNs. We need to note the rest-frame optical emission line survey can miss heavily-obscured AGNs without strong rest-frame optical emission line, like fully-covered less-luminous AGNs in the local universe (Ueda et al., 2007). Such objects can be recovered by the MIR AGN selections with *SPICA*.

4.1.6 Morphological transformation

Typical star-forming galaxies (SFGs) are disk-dominated systems ($n \sim 1$) whereas quiescent galaxies (QGs) show a cuspier stellar distribution ($n > 3$). The correlation between star formation activity and galaxy structure appears to be established as early as $z \sim 2.5$ (e.g., Wuyts et al. 2011). If SFGs simply quench their star formation activity, they should have evolved into QGs with an exponential disk but such a population is a minority. To explain the "Hubble sequence" (star formation activity-morphology

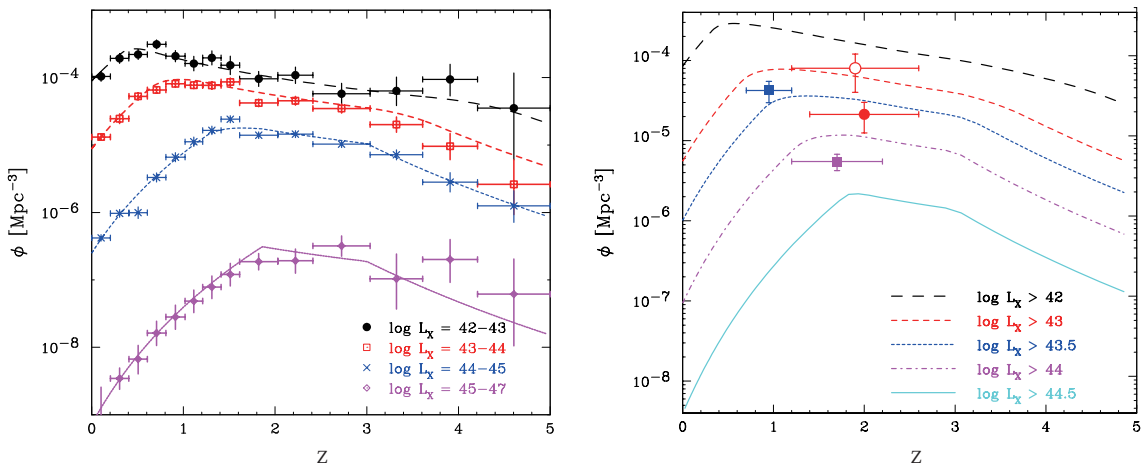

Figure 4.5: The cosmological evolution of number density of Compton-thin (left) and Compton-thick (right) AGN populations (Ueda et al., 2014). For Compton-thin AGNs, large X-ray surveys constrain their number density in the wide luminosity and redshift ranges. On the contrary, the cosmological evolution of Compton-thick AGNs is largely unknown. The solid line in the right panel indicate the expected number density evolution required to explain the strength of the hard X-ray Cosmic X-ray Background.

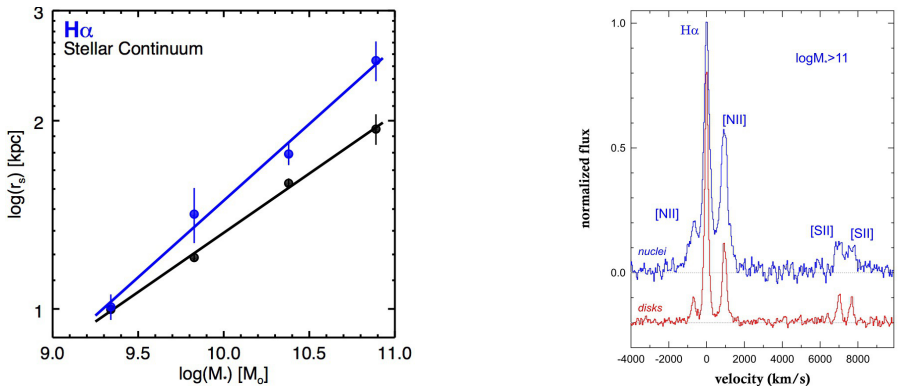

Figure 4.6: (left) For SFGs at $z \sim 1$, Hα emission is more extended than stellar continuum emission at similar wavelengths (Nelson et al., 2015). (right) Spatially resolved Hα spectra for massive SFGs at z$\sim$ 2, which have been obtained with VLT/SINFONI (Förster Schreiber et al., 2014).

relation), it requires mechanisms for transforming galaxy morphologies around the time of quenching star formation. A simple way to observationally address this issue is to know where stars are formed within galaxies. While HST/WFC3 imaging allowed us to draw stellar mass maps for a large sample of high-redshift galaxies (e.g., Wuyts et al. 2012), it is still challenging to trace spatially resolved star forming regions.

High-resolution Hα spectroscopic surveys show that Hα emission is more extended than stellar continuum emission (Figure 4.6). These results suggest that star formation is quenched from the inside out, especially for massive galaxies at $z = 1-2$ (Nelson et al., 2015; Tacchella et al., 2015). However, extended star formation can not change stellar mass surface density profiles from $n \sim 1$ to $n > 3$. On the other hand, submillimeter observations with ALMA reveal an existence of a compact dusty star-forming region for SFGs with log $M_* > 11$ around the main-sequence (e.g, Tadaki et al. 2015). Such an extremely dusty starburst has a great potential for creating a central dense core and transforming the stellar surface density profile. An important agenda in 2020's is to characterize "bulge-forming galaxies" in terms of evolutionary phases and environments.

ULTIMATE-Subaru with GLAO will provide 0.2″-resolution Hα and Hβ 2D spectra for a large sample of SFGs at $z \sim 2$. Spatially resolved Hα/Hβ ratio maps allow us to identify a dusty star-forming region within SFGs (being nearly identical to bulge-forming galaxies). If we put one galaxy on a slit along the major axis per mask, SFR surface density profiles (sizes) and rotation velocities could be measured for ∼600 SFGs. Their evolutionary phase is derived from a stellar-to-dynamical mass ratio and their environment is defined by an enormous spectroscopic sample of 1.8×10^4 galaxies over 3 deg^2 (§ 4.1.1). By looking at bulge-forming galaxies with these parameters, we aim to reveal necessary conditions for transforming galaxy morphologies. Another benefit of 0.2″-resolution spectroscopy is that we can identify outflows on the basis of the Hα line width. A broad component in Hα has been detected in nuclei of massive SFGs at z$\sim$ 2 (Figure 4.6). We aim to characterize the properties (stellar mass and offset from the main-sequence) of galaxies with the outflow signature to clarify the role of outflow in quenching star formation.

4.2 ULTIMATE Multi-object IFU Spectroscopic Survey

Chris Lidman[1], Jessica Bloom[2], Julia Bryant[1,2], Scott Croom[2], Sarah Leslie[3], Lisa Kewley[3], I-Ting Ho[3], Adam Schaefer[3], Fuyan Bian[3], Tiantian Yuan[3]
[1] Australian Astronomical Observatory
[2] University of Sydney
[3] Australian National University

4.2.1 Introduction

Over the last few years, there has been an enormous increase in the volume, quality and complexity of observational data. At the same time, computer simulations of galaxies have become larger (more particles and better resolution) and more sophisticated (better treatment of the processes that cannot yet be tackled through direct simulation). We have learned a lot about galaxy evolution by comparing galaxy simulations with observations and vice-versa.

As computer simulations become larger, more sophisticated and more detailed in their predictions, it is becoming clear that observations also need to become more detailed. Currently, the largest spectroscopic surveys (SDSS, for example) are biased: they only measure the integrated properties of galaxies, and due to the finite size of the fibres used in such surveys, only the central part of the galaxy is measured. Observations are therefore incomplete, which leads to a restricted and perhaps misleading understanding of how galaxies evolve.

In the local universe, these limitations are now being tackled through multi-object IFU surveys, such as MaNGA and SAMI, that resolve the gas and stellar populations across each galaxy. This has led to a flood of new results, some of which are discussed below. In the distant universe, where galaxies are much younger, progress is much slower, because existing instruments either lack the spatial resolution (KMOS/VLT) to match what can be done in the local universe, or can only target one object at a time (SINFONI/VLT, MUSE/VLT, OSIRIS/Keck). The multi-object IFU spectrograph (M-IFS) on ULTIMATE-Subaru is an instrument that overcomes both of these limitations.

Here, we describe the multi-IFU galaxy survey with ULTIMATE-Subaru, which will target galaxies that are between 6 and 9 billion years younger than the galaxies we see today. At these early times, the Universe itself was between 4 and 7 billion years old. The ULTIMATE multi-IFU galaxy survey will provide a detailed view of large numbers of galaxies that is only currently possible for galaxies in the local Universe through surveys like SAMI. The ULTIMATE-Subaru IFU galaxy survey will enable us to understand how these distant cousins evolved to become the galaxies that we see today. We start with a description of the SAMI survey, and then examine what an instrument like the M-IFS on ULTIMATE-Subaru will enable us to do in the field of galaxy evolution.

4.2.2 The SAMI survey

The SAMI Galaxy Survey (Croom et al. 2012; Bryant et al. 2015) is collecting integral field spectroscopy on a sample of 3,400 local galaxies over a range of stellar masses and a wide range of environments, from the field to dense cores of rich galaxy clusters. The survey started in March 2013, and has observed over 1,200 galaxies to date. The median redshift of the SAMI survey is $z = 0.05$.

The SAMI survey uses the SAMI instrument, a multi-object IFU at the prime focus of the AAT. The characteristics of the instrument are listed in Table 4.2. SAMI feeds the AAOmega spectrograph, which consists of two arms (red and blue) split by a dichroic, and variety of VPH gratings that allow coverage of the entire 370-880nm wavelength range at low resolution, or smaller wavelength ranges at higher resolution. The SAMI survey uses a low resolution grating (R=1,700) in the blue arm and higher resolution grating (R=4,500) covering Hα, [NII] and [SII] in the red-arm.

	Spaxel	N. of Spaxels	FoV	N. of IFUs	Patrol field	Minimum separation	Spectral resolution
SAMI	1.6″	61	15″	13	1-deg (diameter)	30″	1,700 (blue) & & 4,500 (red)
ULTIMATE	0.15″	61	1.2″	7–13	14′×8′	25″	3,000–5,000

Survey	Spaxel (1.6″ vs 0.15″)	FoV (15″ vs 1.35″)
SAMI @ $z = 0.05$	1.56 kpc	14.7 kpc
ULTIMATE @ $z = 0.5$	0.92 kpc	8.2 kpc
ULTIMATE @ $z = 1.0$	1.20 kpc	10.8 kpc
ULTIMATE @ $z = 1.5$	1.27 kpc	11.4 kpc

Table 4.2: A comparison between the physical characteristics of the IFUs used by SAMI and the IFUs that are currently planned for M-IFS of ULTIMATE-Subaru. For selected redshifts, angular scales are converted to spatial scales in the second table.

In Table 4.2, we list the angular coverage of the SAMI IFUs and compare it to the angular coverage of the IFUs that are planned for M-IFS of ULTIMATE-Subaru. We note that the physical area covered by the IFUs of M-IFS of ULTIMATE-Subaru at $z \sim 0.5$ is smaller than that of SAMI at $z \sim 0.05$.

In Figure 4.7, we show the spectral coverage of the SAMI survey and compare it to the spectral coverage that would be provided by ULTIMATE-Subaru M-IFS. In this plot, we have used the grisms that are currently available with MOIRCS, and have assumed that the PFS spectrograph can be fed by the fibres of ULTIMATE M-IFS. It should be noted that PFS could cover all the main diagnostic lines up to $z \sim 0.8$. It would be the instrument of choice for a SAMI-like survey at $z \sim 0.5$. Covering all the lines at higher redshifts would require the targets to be observed with both PFS and nuMOIRCS separately.

4.2.3 Survey design

The ULTIMATE M-IFS galaxy survey will observe 3,000 galaxies, spread over three redshifts (z=0.6, 0.9 and 1.4) corresponding to look-back times of 6, 7 and 9 billion years. The number of galaxies has been chosen to match the number of galaxies in the SAMI survey, which has been designed to build statistically significant samples that cover a range of masses and environments. Assuming, that one can observe 13 objects at a time and that exposure times will be of the order of 2 hours, the entire survey will take of the order of 50 nights. If one can double the number of IFUs then the survey would take half this time or one would be able to double the number of objects.

Targets will be selected from the COSMOS and SXDF-UDS fields, each of which covers 1 sq. deg. Both fields are within the HSC Ultra-deep survey region. Likely target densities are discussed later. We now focus on science that will be done with the ULTIMATE M-IFS galaxy survey.

We structure the scientific justification for the ULTIMATE M-IFS galaxy survey as a series of questions. We limit the questions to the ones that can be answered by studying emission lines. With an 8-m class telescope, measuring absorption line strengths and widths will only be possible for the brightest sources at the lowest redshifts. Studying large numbers of such galaxies at high redshifts will need to wait for AO-fed IFU spectrographs on 30-m class telescopes.

In addition to spatial resolution, wavelength coverage and spectral resolution are important considerations. Some studies (for example, measuring the kinematics of the gas, or examining where star-formation has been quenched) can be done with just a single line, and do not need high spectral resolution. Other studies (e.g., identifying shocked regions) need broad wavelength coverage in order to cover multiple lines and high spectral resolution to properly model the board and narrow components.

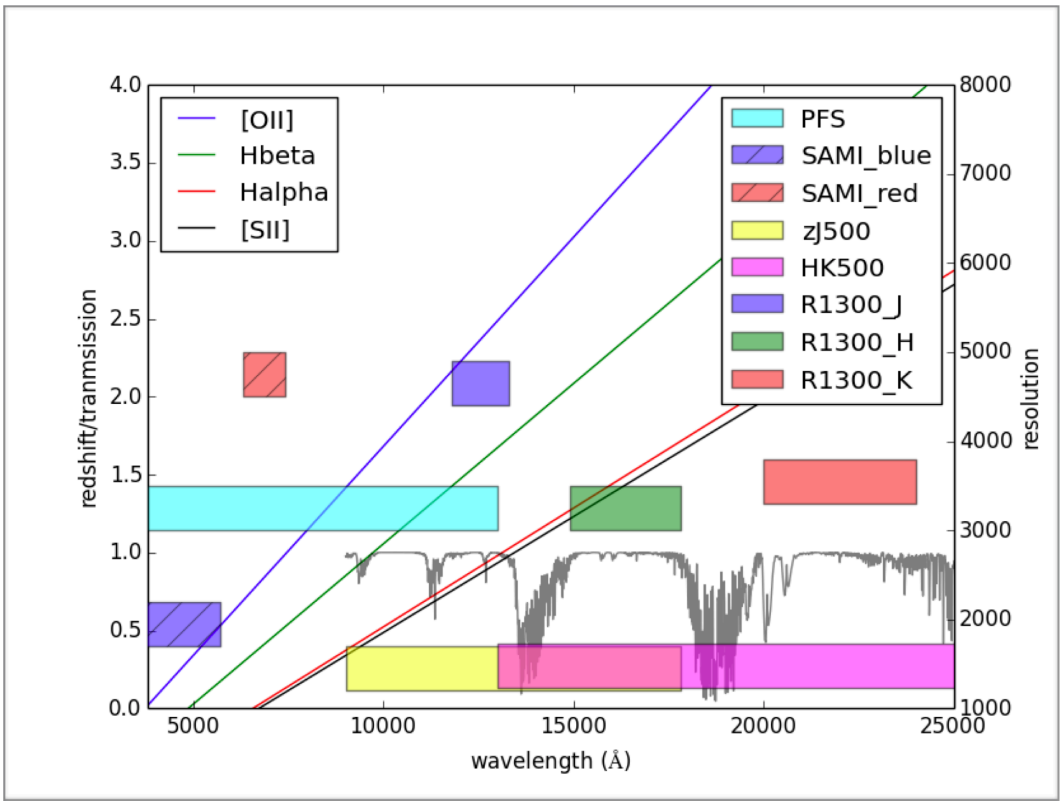

Figure 4.7: The spectral coverage of SAMI (cross hatched region) and M-IFS of ULTIMATE-Subaru as a function of resolution (right hand axis). Also shown is the transmission spectrum of the Earth's atmosphere (grey line) and wavelength of several key emission lines as a function of redshift. The resolution that is shown for PFS is the resolution for PFS fibres, which are 138 μm in diameter. The ULTIMATE M-IFS fibres are almost four times smaller. Assuming that PSF of PFS is two pixels, the resolution using the ULTIMATE M-IFS fibres will be about a factor of two higher than shown here.

4.2.4 How does feedback work and how does it change with cosmic time?

The shape of the galaxy stellar mass function is very different to the shape of the halo mass function. Galaxies at both low and high stellar mass are much less common than what one would infer by scaling the halo mass function to match the density of galaxies at intermediate stellar masses. In order to explain the deficit at both ends of the stellar mass function, semi-analytic models of galaxy evolution invoke a number of mechanisms (generally termed feedback) that expel gas from a galaxy or prevent the gas that is in the galaxy or its halo from forming into stars. In high-mass galaxies, AGN are thought to be the engine driving the feedback. In low-mass galaxies, the feedback is thought it be driven by supernovae and/or star formation.

At $z = 1$, AGN were 100 times more common than they are today, and the amount of star formation (and hence the number of supernovae) was an order of magnitude higher. Galaxies were also less massive. In short, one would expect feedback to be much more common and efficient at $z = 1$ than it is now. Hence feedback must have played an important role (perhaps the central role) in providing the galaxies that we see today.

While semi-analytic models of galaxy evolution have successfully used feedback mechanisms to explain the global statistical properties of the galaxy population, there is a need to verify that these mechanisms actually work in the way that they are implemented in the semi-analytic models.

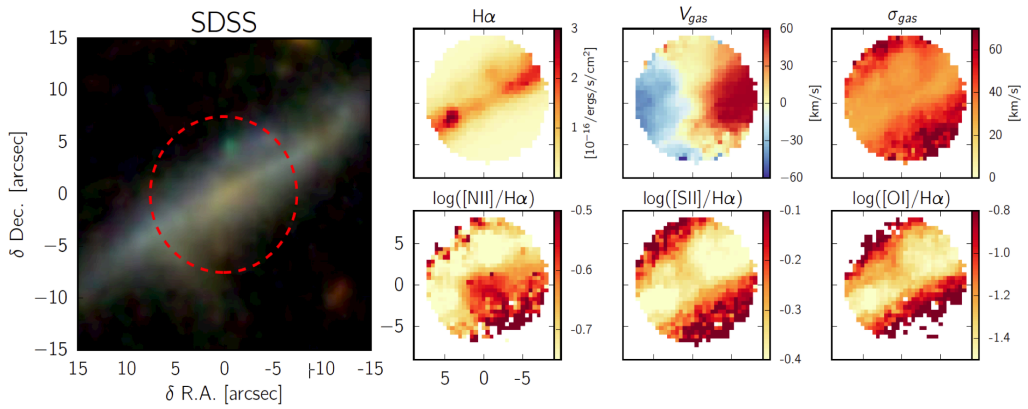

Figure 4.8: SAMI observations of an edge-on disk galaxy. An SDSS image of the galaxy is shown on the left. The dashed red circle corresponds to the SAMI FoV. Results from the SAMI observations are shown on the right. In the top row, the intensity of Hα emission, and the velocity and velocity dispersion of the Hα-emitting gas are plotted. Note the twisted rotation curve and the increasing size of the velocity dispersion as one moves away from the disk. Note also the change in line ratios in the bottom row. Both are indicative of a turbulent outflow of material that is, in this case, being driven by star formation in the disk of the galaxy. Figure taken from Ho et al. (2015).

Understanding the importance of AGN or supernova driven feedback, how they work, and how the relative importance of the two mechanisms evolves with time requires one to separate both, and this requires good spatial resolution (of the order of 1–2 kpc), good spectral resolution (of the order of a few thousand) and broad wavelength coverage (to enable coverage of the major diagnostic lines). An example of a galaxy with a strong feedback is show in Fig. 4.8. These data were taken with SAMI. The M-IFS of ULTIMATE-Subaru is the ideal instrument to extend these studies to higher redshifts.

4.2.5 What causes quenching in dense environments?

In the local universe, dense environments (such as rich groups and clusters) are dominated by early-type galaxies that are no longer forming stars. Before falling into these environments, these galaxies would have been forming stars as vigorously as galaxies in the field. Hence, at some point in time, probably soon after these galaxies entered the cluster for the first time, star formation in these galaxies was quenched.

Numerous quenching mechanisms are possible in the cluster environment. Ram pressure stripping of gas from the galaxy as it passes through the hot intra cluster medium is one mechanism. Another is the disruption of the supply of pristine gas from the galaxy halo (strangulation). Galaxy mergers, which could lead to rapid consumption of the gas reservoir and possibly to AGN activity, which can further inhibit star formation, is another.

All of these mechanisms leave specific signatures. For example, ram pressure stripping might be detectable as a decrease in the star formation rate in the outer parts of a disk galaxy (see Fig. 4.9), or as star formation in material that is swept away from the galaxy. Both signatures have been detected in galaxies at low redshift, for example, the anemic spirals in Virgo and the jellyfish-shaped galaxies in several Abell clusters. At higher redshifts, where clusters are smaller, dynamical timescales are shorter, and the intra-cluster medium is less developed, other factors may be at play. Given that the angular size of these signatures will typically be smaller than the seeing disk, these studies have to be done from space, or from the ground with an AO fed system such as M-IFS on ULTIMATE-Subaru.

At $z \sim 1.7$, for example, Hα reaches the end H-band. At this redshift, galaxy clusters are in a very active phase, and there are now many examples of galaxies in the cores of these clusters with strong Hα, presumably because they are vigorously forming stars. If K-band fibres became available, these studies

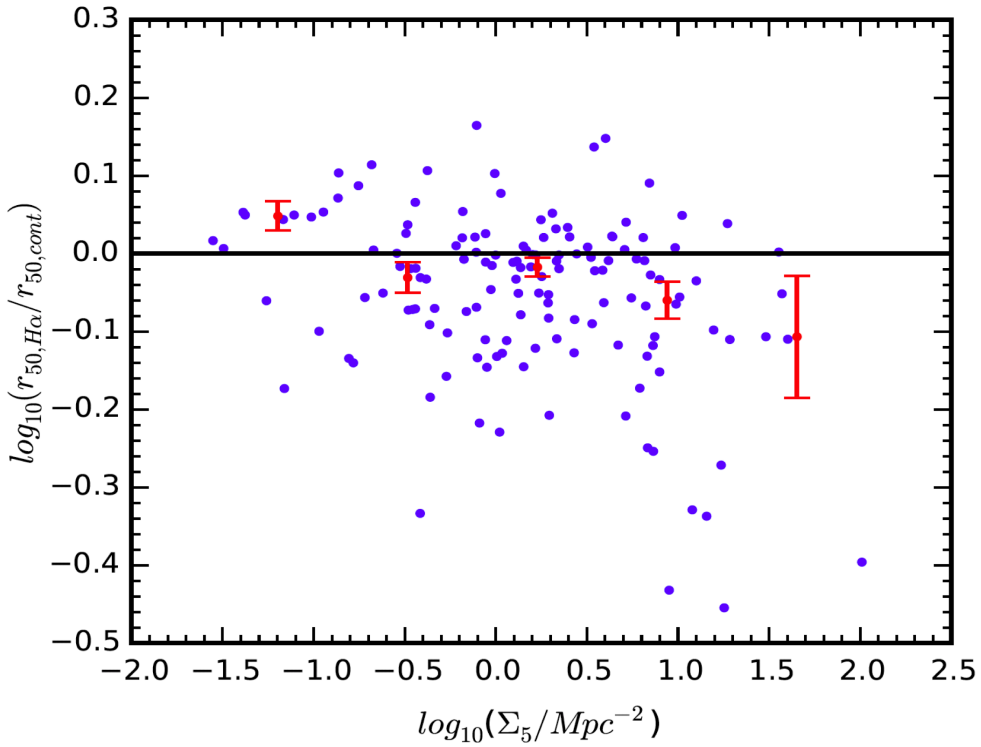

Figure 4.9: The relative size of the Hα emitting region against size of the continuum emitting region plotted against density. Note the progressive decrease in the ratio with increasing galaxy density. The data are from the SAMI survey and the plot has been taken from Schaefer et al. 2015, in prep.

could be extended to higher redshifts.

4.2.6 How does gas accretion change with time?

In current theories of galaxy evolution, it is thought that galaxies are continuously fed by in-falling streams of pristine gas. Without this supply, most galaxies, like our own Milky Way, would have already stopped forming stars. This gas is difficult to observe as it is cold and tenuous. Hence, there are almost no observational constraints on this key theoretical idea.

A handle on the how gas accretion works can be gained from metallicity gradients. According to the inside-out theory of disk formation, we expect higher metallicity gas to be in the centre of disks, as there has been more time for enrichment there. When pristine gas from the IGM accretes on to a galaxy or enriched gas is pushed outwards, this can flatten metallicity gradients.

Though metallicity gradients have been well characterised at low-redshift, it has been difficult to extend these studies to higher redshifts, because low spatial resolution has the effect of flattening gradients, even if they are steep (Yuan et al. 2013). The GLAO correction of ULTIMATE-Subaru is key for providing the needed spatial resolution to study this tracer of gas flows at these redshifts.

As shown in Kewley et al. (2013), the gas-phase metallicity (and the hardness of the ionising photons) can be determined from the location of objects on the Baldwin-Phillips-Terlevich (BPT) diagram (see Fig. 4.11), which uses [OIII]4959,5007, Hβ, Hα and [NII] 6583. At $z = 0.6$, [OIII]4959,5007, Hβ and [OIII] land in the i-band, whereas Hα and [NII]6583 land in the near-IR Y band, which means that both PFS and nu-MOIRCS would be required. At higher redshifts, e.g., $z = 1.4$, all four lines would land in the near-IR J and H bands.

Adequate spatial resolution is crucial to these studies. Even with the spatial resolution provide by

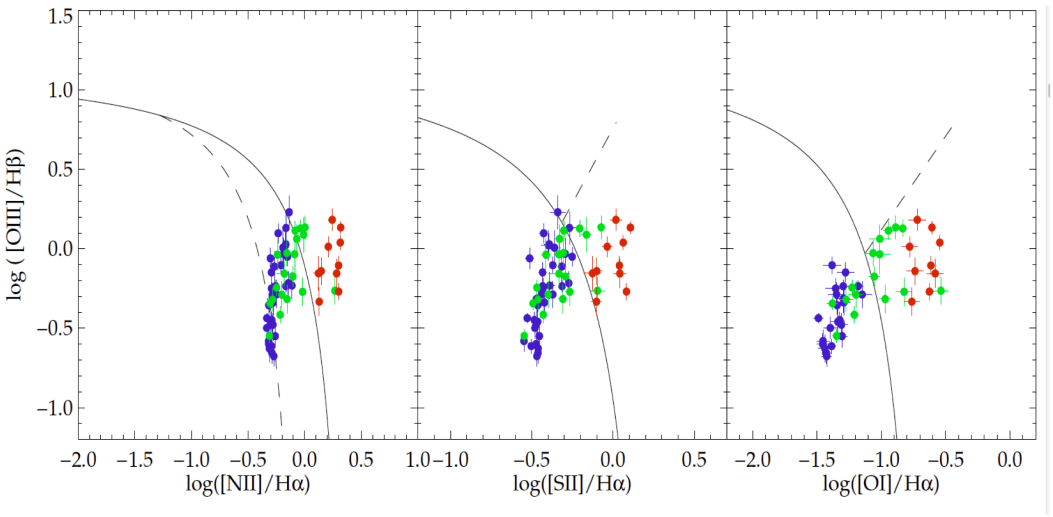

Figure 4.10: The location of the line emitting components of a single SAMI galaxy in the BPT and other similar diagnostic diagrams. The continuous and broken lines split objects according to the source of ionising photons, e.g. star formation, AGN and shocks. The M-IFS of ULTIMATE-Subaru provides the necessary spatial and spectral resolution to isolate these three components. The plot was taken from Leslie et al. (in preparation).

ULTIMATE-Subaru, it may be necessary to study galaxies that are strongly lensed by massive clusters if one is to reach a spatial resolution of 500 pc, which is the resolution needed to resolve the most massive star forming regions in high-redshift galaxies. The multiplex advantage of M-IFS of ULTIMATE-Subaru, means that several lensed galaxies behind a single lensing cluster can be studied simultaneously.

4.2.7 What drives galaxy transformations?

As galaxies become older, they transform from star-forming to passive, disk to spheroid, and blue to red. Much of this transformation occurs between $z = 1$ and today, so the best place to study this transformation is in this redshift interval, a redshift interval that is accessible to M-IFS of ULTIMATE-Subaru.

What are the main drivers of this transformation? As noted earlier, environment has an impact, but the impact of the environment is most keenly felt at low stellar masses. At higher stellar masses, galaxies have already transformed themselves before they become a satellite in a more massive halo.

In addition to environment and stellar mass, other factors may be at play, such as the accretion history, the stability of disks, the mass of the halo, and whether not the galaxy in question is a satellite or a central.

Some of these factors work on the scales of 1–2 kpc. For example, the presence of kinematic instabilities can only be inferred by examining the kinematics of galaxies with a resolution approaching 1 kpc, which at $z = 1$, subtends an angle 0.12 arc-seconds. An example of how the kinematics of the gas is correlated with the location of star formation in nearby galaxies is show in Figure 4.12. This study was done with SAMI. Extending these study to $z = 1$, will require ULTIMATE-Subaru.

4.2.8 Feasibility

We now explore the technical feasibility of using M-IFS of ULTIMATE-Subaru to address the scientific questions raised above. We split this into two parts. We first examine the target density of objects that can be targeted by M-IFS of ULTIMATE-Subaru, and we then compute signal-to-noise ratios.

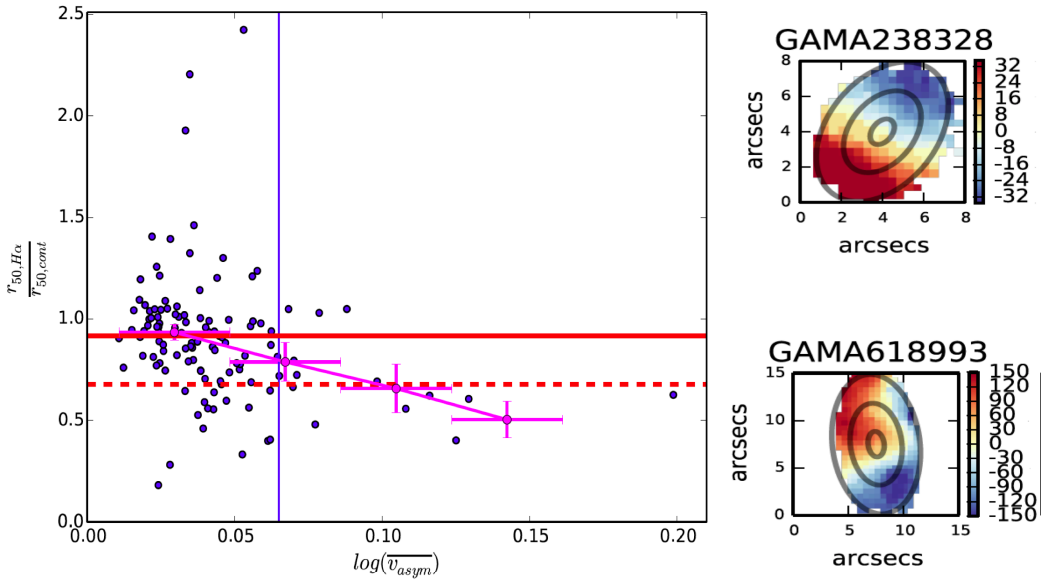

Figure 4.11: On the left, the concentration of star formation relative to the continuum versus the asymmetry in the gas kinematics. On the right, examples of SAMI galaxies, one with symmetric velocity contours and another with asymmetric contours. As can be seen in the plot, star formation becomes more concentrated as the gas in the galaxy becomes more disturbed. The data are from the SAMI survey and the plots have been taken from Bloom et al. (2015).

Survey	Factor decrease in line flux per spaxel
ULTIMATE @ $z = 0.6$	130
ULTIMATE @ $z = 0.9$	260
ULTIMATE @ $z = 1.4$	660

Table 4.3: The surface brightness dimming of galaxies with redshift.

Target density

We have used v4.1 of the UltraVISTA catalogue to estimate the likely number of targets one could observe. We consider only star forming galaxies and three redshift ranges: $0.5 < z < 0.7$, $0.8 < z < 1.0$ and $1.3 < z < 1.5$. The three intervals correspond to Hα landing in the Y, J and H bands, respectively and to look-back times of 5.9, 7.4 and 9.1 Gyr.

In the following figure, we plot a histogram showing the number of galaxies per $16' \times 12'$ region (the FoV of ULTIMATE-Subaru) with star formation rates exceeding the values listed on the horizontal access. The red lines represent the number of M-IFS of ULTIMATE-Subaru, which is 13 in the first phase of M-IFS of ULTIMATE-Subaru (see Section 7 for the meaning of the stages). The intersection of the blue and red lines gives the SFR of the galaxy that is ranked 13th when galaxies are ordered according to star formation rate. We examine the signal-to-noise that one could obtain with M-IFS of ULTIMATE-Subaru for galaxies forming this many stars in the next section.

Using a SFR threshold of 10 solar masses per year there are approximately 30, 80, and 70 galaxies per ULTIMATE-Subaru FoV ($16' \times 12'$) at z=0.6, 0.9 and 1.4 respectively. Over the 2 sq. degrees of the ULTIMATE M-IFS galaxy survey, there would be 800, 2200, and 2000 such galaxies, respectively.

There are limitations to this analysis. The SFR is computed from the broad band photometry and there is no information on how it is distributed throughout the galaxy.

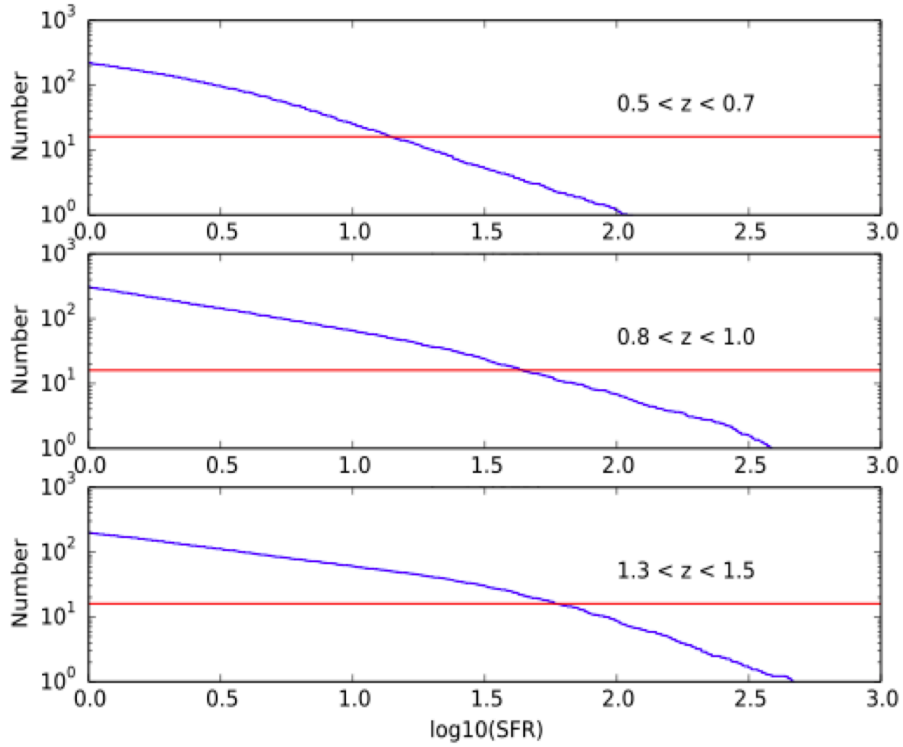

Figure 4.12: The cumulative number of objects that exceed the star formation rates (SFR) listed on the horizontal axis. The star formation rates are measured in solar masses per year. The red lines correspond to the number of IFUs in stage I of M-IFS of ULTIMATE-Subaru.

Signal to noise calculations

The expanding universe affects not only the angular size that an object subtends on the sky but also its surface brightness. Cosmological surface brightness dimming, which goes as $1 + z$ to the 4th power for line fluxes, is especially severe.

In Table 4.3, we show how surface brightness dimming affects the line flux of three hypothetical SAMI-like surveys, each conducted at a different redshift (z=0.6, 0.9, and 1.4). In computing the amount of dimming, we have also taken into account the different telescope diameters (3.9-m for the AAT and 8.2-m for Subaru), and the different areas covered by the spaxels in the respective IFUs.

The amount of flux received by an fibre of M-IFS of ULTIMATE-Subaru is considerably less than the flux received by a SAMI fibre, if one were to simply place the object at higher redshift. At the same time, as features of interest move into the near-IR, the background from the night sky per unit solid angle becomes higher, as does the read-out noise of the detectors. This has important implications about what kinds of projects will be feasible. As redshifts increase, projects based on continuum measurements or line ratios involving faint lines will become infeasible.

Countering the effects of the Earth's atmosphere, cosmology, and detector technology, is the rapid evolution in the size of objects and the star formation density. Objects at higher redshifts are more compact, more clumpy, and are forming more stars, which can lead to a more extreme inter-stellar medium (Kewley et al. 2013). Hence, assessing the feasibility of a particular science case requires detailed simulations and careful consideration of all the factors.

Such a detailed feasibility study is beyond the scope of this study. Instead, we examine the feasibility using a number of assumptions that simplify the calculation. These are:

- The star formation rate is 10 solar masses per year.

Survey	S/N over 1-arcsec^2	S/N per spaxel ($0.15''$)	KMOS ($0.2''\times0.2''$)
ULTIMATE @ $z = 0.6$	108	15.1	10.0 (0.165 nm bin)
ULTIMATE @ $z = 0.9$	80	11.3	7.4 (0.165 nm bin)
ULTIMATE @ $z = 1.4$	69	9.6	2.8 (0.2 nm bin)

Table 4.4: Signal to noise estimates for 1 hour observations of the Hα line in a galaxy with a star-formation rate of 10 $M_\odot$/yr, uniformly distributed over a galaxy disc of radius 8 kpc.

- The star formation is uniformly distributed throughout a disk that is 8 kpc in radius
- The Hα line is represented by a Gaussian and has a width (FWHM) of 0.5 nm
- An exposure of 1 hour

While the signal-to-noise ratios are sufficient for determining the large scale dynamics of the line-emitting gas using the H-alpha line, longer integrations will be necessary for inferring properties of the gas that are derived from weaker lines, such as [NII]6583, [SII]6717,6731, [OIII]4959,5007, Hβ, and [OII]3726,3728.

Chapter 5

Science Case III – Low-z galaxy and Galactic science

ULTIMATE-Subaru is not only for the high-redshift galaxy sciences. The wide-field coverage and the improvements in spatial resolution and sensitivity for both imaging and spectroscopy can also bring significant impacts on a wide variety of astronomy fields. In this Chapter, we present some examples of science cases with ULTIMATE-Subaru on nearby ($z \ll 1$) galaxies or the Milky Way. In the following, we assume to have all the instruments that we are considering on ULTIMATE-Subaru: i.e. wide-field imager, MOS spectrograph, multi-object IFUs, or combination of these.

5.1 Paα Surevy of Nearby Galaxies at $z < 0.3$

Kentaro Motohara[1] **& Yusei Koyama**[2]
[1] Institute of Astronomy, The University of Tokyo
[2] Subaru Telescope, National Astronomical Observatory of Japan

5.1.1 Introduction

Hydrogen Paschen α Emission Line

Although recent studies in the rest-frame mid-infrared to far-infrared observations have revealed starburst activities hidden by large amount of dust, hydrogen recombination lines, which trace the ionizing photon with $>$ 13.6 eV, is still direct and most reliable probes of OB stars and thus on-going star forming activities.

Traditionally-used optical lines are Hα λ6563 and Hβ λ4861, which are the strongest under the case-B condition, and the dust extinction can be also corrected assuming the intrinsic Hα/Hβ line ratio (Balmer decrement). However, under strong dust extinction environment such as in U/LIRGs, both of which are heavily absorbed and it will become impossible to recover the total amount of star formation rate.

Under such environment, Paschen (Pa) α λ18751 emission is expected to be an ideal probe for hidden star formation, which is;

- the strongest hydrogen emission in the near-infrared wavelength, and
- affected by dust extinction far less than Hα .

Figure 5.1 shows the relative strength of various hydrogen lines emitted from HII regions, with varying dust extinction. As the extinction at the wavelength of Paα is $\sim$ 6 times smaller than that at Hα, Paα

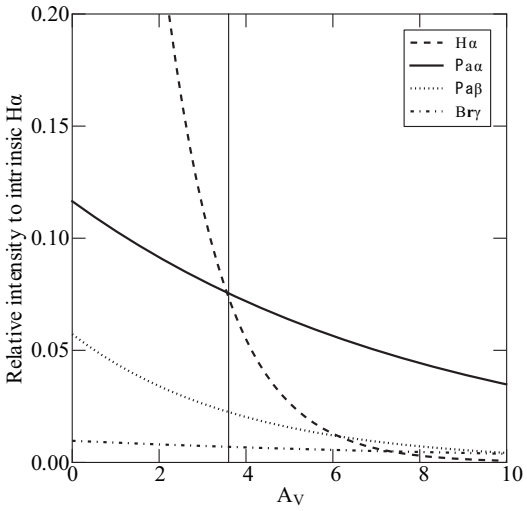

Figure 5.1: Observed relative intensity of various hydrogen recombination lines vs. Calzetti et al. (2000) dust extinction. Taken from Tateuchi (2015b).

becomes the strongest emission line at $A_V > 3.5$. Considering that the typical dust extinction in LIRGs is $A_V > 3$, Paα is the ideal probe for star forming activities in starburst galaxies.

Figure 5.2 shows one example : They are emission-line images of a starburst galaxy UGC 12915 in both Paα and Hα, and it can be seen that at the center of the galaxy, there is a hidden star forming region not detected in Hα.

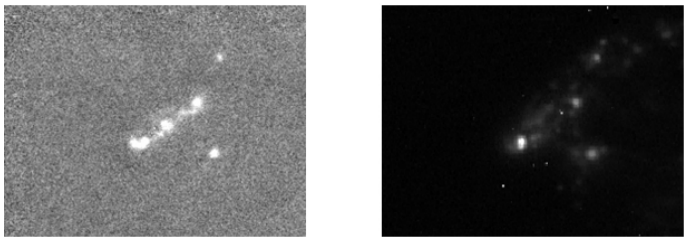

Figure 5.2: Images of UGC 12915 in Paα (left) and Hα (right), taken from Komugi et al. (2012).

However, one large drawback of Paα emission line is its rest wavelength; 1.8751μm is where the terrestrial atmospheric transmittance is very low due to absorption mainly by water vapor (see Figure 5.3), and it is difficult to carry out its observation from ground-base telescopes.

Paα Observations of Nearby Galaxies

One way to avoid above problem is to target at redshifted objects; beyond redshift of 0.01, the atmospheric windows open and Paα becomes observable even at Maunakea. Thus, recently, numbers of Paα observations of nearby galaxies are carried out, and its advantages are having been verified.

Komugi et al. (2012) carried out Paα narrow-band imaging of a merger system Taffy I to probe the relation between the star formation rates and molecular gas masses, so called the Kennicutt-Schimdt (K-S) law, in its star-forming regions. Using Paα-derived star formation rates, they found a surprisingly tight correlation whose dispersion is smaller than that in normal galaxies, suggesting that the dispersion of the K-S law is largely due to the differences in the age of star-forming regions.

Tateuchi et al. (2015a) have carried out Paα imaging survey of 33 nearby LIRGs at $z = 0.01 - 0.03$, and confirmed that extinction corrected Paα star formation rates match well with those estimate from

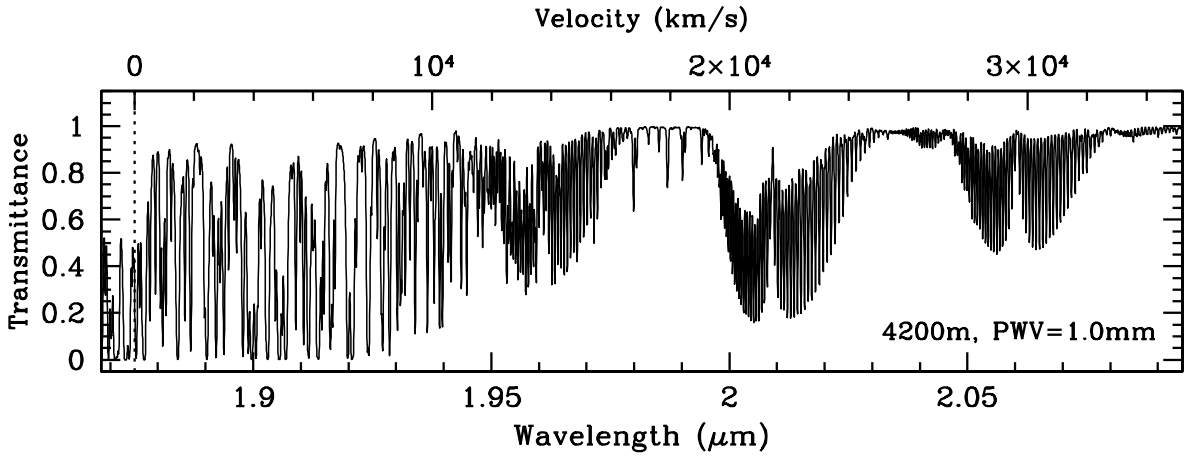

Figure 5.3: Atmospheric transmittance around Paα, with PWV=1mm at Maunakea. The vertical dashed line shows the wavelength of Paα(1.8751μm).

far-infrared luminosities. They have also made a measurement of the star-formation rate surface density ($\Sigma_{\rm SFR}$)of these LIRGs, and confirmed an excess from normal galaxies, which may show "bursty" star formation activities in LIRGs caused by merger or interaction.

Expanding above work, Tateuchi (2015b) have probed the relation between Sersic indices of bulges and size of star-forming regions in LIRGs, which was impossible with other probes. He have found a strong correlation in it; bulges with large Sersic indices (classical bulges) have star-forming region within the bulges, and those with small Sersic indices (pseudobulges) have extended star-forming regions beyond the bulges. Currently it is not clear what mechanism stands between the Sersic indices and star-formation activities, however, this seems to be an important path to understand the formation mechanism of classical and pseudo-bulges.

Obreschkow et al. (2015) have carried out Paα IFU observations of four nearby starburst galaxies with giant HII clumps, which is thought to be "analogs" of $z \sim 2$ star-forming galaxies, to probe their dynamical properties. They have found that the specific angular momentum of these galaxies are smaller than that of normal disk galaxies by factor of 3 which results in smaller Toomre Q value, and thus makes the disks more unstable to cause giant clumps of HII regions.

These results clearly shows that the Paα emission line will be a powerful tool to probe not only star formation activities and their morphologies, but also dynamics and therefore origin of their morphological properties, in dusty starburst galaxies.

We therefore propose Paα imaging survey and spectroscopic follow up beyond redshift of $z \sim 0.05$, where the atmosphere at Maunakea becomes transparent, to probe the morphology and dynamics of star-forming galaxies and to understand their formation.

Panoramic Paα mapping of nearby clusters/groups

The wide-field capability and sub-kpc spatial resolution (at $z < 0.3$) of ULTIMATE-Subaru can serve as an unique tool for studying the formation and evolution of galaxies in clusters or groups. Clusters of galaxies are dominated by quiescent galaxies in the local universe, but it is well established that the fraction of blue (star-forming) galaxies sharply declines from $z \sim 1$ to $z = 0$ (so-called Butcher-Oemler effect; Butcher & Oemler 1984).

Morphologies of cluster galaxies are also strong functions of cosmic time; the relative fraction of spiral galaxies decreases from $z \sim 1$ to $z \sim 0$, whilst the fraction of S0 galaxies increases in the same time interval (e.g. Desai et al. 2007). It is therefore believed that the underlying physics responsible for the transformation of spirals into S0s is the key for understanding the environmental effects. However, the

Table 5.1: Number of U/LIRGs in AKARI/SDSS field (∼9000□°).

$\log L_{\rm IR}$	$z < 0.05$	$0.05 < z < 0.1$	$0.1 < z < 0.2$
11.0–11.5	262	908	97
11.5–12.0	17	139	281
> 12.0	0	3	44

physics behind the rapid build-up of S0 galaxies in dense environments is still a big mystery.

We here propose to manufacture a number of NB filters (in K-band) on the wide-field camera of ULTIMATE-Subaru, to perform a systematic Paα survey for clusters/groups at $z < 0.3$. We will not only be able to identify dust-enshrouded star-forming galaxies, but also to spatially resolve the Paα emission of *all* member galaxies on sub-kpc scale.

Assuming a typical cluster size of ∼2-Mpc, it corresponds to ∼20 arcmin at $z = 0.1$ and ∼10 arcmin at $z = 0.2$. The FoV of ULTIMATE-Subaru wide-field camera ($16' \times 12'$) can thus allow us to cover the entire body of clusters with just one pointing observation, and to perform an unbiased survey for dusty star-forming activity in/around the clusters.

An important suggestion recently made for S0 galaxy formation is that bulges of S0 galaxies are so bright that S0 galaxies cannot be formed by a simple fading of disk star formation of spiral galaxies, but requires a significant bulge growth by e.g. nucleated dusty starbursts (Christlein & Zabludoff 2004; Kodama & Smail 2001).

Recent MIR–FIR observations of $z \lesssim 1$ clusters with Spitzer, AKARI, or Herschel have discovered dusty star-forming galaxies in and around those clusters (Geach et al. 2006; Koyama et al. 2008), and they are believed to be the progenitors of local S0s. However, the spatial resolution of these MIR–FIR observations with IR space telescopes are always very poor, and they cannot tell if their IR emissions are really coming from the nucleated regions. The key approach is therefore to use star-formation indicators free from dust extinction, and at the same time, to fully resolve their emission on sub-kpc scale. The ULTIMATE-Subaru, equipped with the wide-field imager and the high spatial resolution achieved with GLAO, can thus provide the most powerful instrument for the cluster science.

In addition, integral field spectroscopic observations will provide us their dynamical information, such as rotation curve, velocity dispersion, and sign of merger history.

5.1.2 Requirements for the instrument

We propose to carry out Paα survey of starburst galaxies, that is, U/LIRGs, upto redshift of $z = 0.3$, beyond which the atmosphere becomes opaque. Therefore, the wavelength coverage of full K-band is required. Table 5.1 shows the number density of U/LIRGs identified in AKARI All-sky Survey data, where redshifts are extracted from SDSS. It is clear that the number of target candidates is less than one per square degree, meaning that only one object is observable with one pointing.

Assuming size of typical galaxies to be 20 kpc in diameter, it corresponds to $20''$ at $z = 0.05$, $11''$ at $z = 0.1$, and $6''$ at $z = 0.2$. To achieve sub-kpc spatial resolution (i.e. the scale of giant molecular clouds) for redshifted Paα line, we require $<0.3''$ spatial resolution and the full K-band availability.

For observations of individual galaxies, the most powerful instrument would be a wide-field ($>10''$ FoV) integral field spectrograph covering full K-band. The IFU observations deliver the motion of gas and stars inside the galaxies, hence can provide really unique opportunity to understand the physics of starburst galaxies.

For clusters/groups observations, the wide-field capability and the sub-kpc spatial resolution achieved with ULTIMATE-Subaru will provide a powerful tool to perform unbiased survey for dusty star-forming regions for all member galaxies in the targeted fields. This approach can make full use of the wide-field of view of ULTIMATE-Subaru, and our requirements for this science are a wide-field imager ($\gtrsim 15'$) with a number of NB filters available in K-band.

To summarize, the required specification of FoV and spatial resolution for the ULTIMATE-Subaru instrument is;

- An imager with large FoV ($\sim 15'$) with a variety of NB filters in K-band.
- An IFU instrument with large FoV ($\sim 10''$) with spectral resolution of $\lambda/\Delta\lambda > 3000$ to achieve $\sim$ 100km/s velocity resolution to resolve the velocity component.

5.2 Near-IR Imaging of the Local Universe

Jin Koda[1], **Daisuke Iono**[2], **Kentaro Motohara**[3] **& Yusei Koyama**[4]
[1] Department of Physics and Astronomy, Stony Brook University
[2] National Astronomical Observatory of Japan
[3] Institute of Astronomy, The University of Tokyo
[4] Subaru Telescope, National Astronomical Observatory of Japan

5.2.1 Introduction

Near-IR imaging of large nearby objects have tremendous potential. The near-IR is less susceptible to dust extinction than optical imaging, and is advantageous for the census of obscured stellar populations, underlying stellar mass distributions, and star formation activities over the MW and in nearby galaxies. In addition, narrow-band line imaging in near-IR can diagnose the physical conditions of star formation activities and of hydrodynamic shocks, two of the very important events that typically occur in the dense interstellar medium. Unfortunately, such imaging has been limited by the small fields-of-view of previous instruments, and so far focused only on relatively small regions, such as nuclear regions of galaxies, or brightest parts of Galactic star forming regions. A large format near-IR camera on a large telescope is essential as the near-IR line emissions are relatively faint.

ULTIMATE-Subaru will provide the combination of large field-of-view, high sensitivity, and high spatial resolution. It will open up a new window for deep near-IR imaging of large areas and objects in the local Universe. Its targets can span an enormous range – from the whole extents of Galactic star-forming regions and the Galactic center, to nearby normal and starburst galaxies and their ionized outflows, and to the intergalactic medium of galaxy groups and clusters. Previous studies have successfully demonstrated the utility of near-IR lines for diagnostics of star formation activities and hydrodynamic shocks. ULTIMATE-Subaru can extend these studies of small areas and characterize those important activities in the much broader environmental context of the Galaxy, nearby galaxies, and galaxy groups and clusters. Here I summarize a few topics that may be worth investigating for potential ULTIMATE-Subaru science.

5.2.2 Near-IR line narrow-band omaging of the local universe

Near-IR wavelengths include many diagnostic emission lines. Figure 5.4 shows an example spectrum of the nuclear region of NGC 2623 in the K-band wavelength range. It displays star-formation tracer lines (mainly, green lines), shock tracer lines (blue), and very high excitation coronal lines (red). This spectrum covers only a small wavelength range within near-IR, and other interesting lines exist outside this range (e.g., [Fe II] $\lambda 1.2567 \mu m$, [S IX] $\lambda 1.2525$ μm Paβ $\lambda 1.2818 \mu m$).

Most obvious applications of near-IR lines are to locate highly-obscured star forming regions and to measure star formation rates in nearby galaxies. Measurement of star formation rates in galaxies is the first step to understanding the physics of star formation and cosmic star formation history. Star formation occurs in dense molecular clouds, where the extinction, due to their typical column density, is as large as $A_V \sim$ 5-10 mag. Therefore, optical studies can miss the early, obscured stage of star formation when newly-born stars are embedded in the dense molecular and dusty interstellar medium. In this volume, Koyama & Motohara discuss the Paα $\lambda 1.8751 \mu m$ survey of mildly-redshifted ($z > 0.03$) galaxies with ULTIMATE-Subaru. The Paα line at $z \sim 0.0$ is at a very poor atmospheric transmission, but other hydrogen recombination lines, such Paβ and Brγ, are often accessible by ULTIMATE-Subaru even at local redshifts. The combination of these lines can provide an estimate of dust extinction and enables an estimation of the magnitude of star formation and star formation rates at each position over a large galactic disk. The $0.2''$ resolution enables to spatially-resolve individual HII regions in nearby galaxies (Figure 5.5). Figure 5.6 demonstrates the $15' \times 15'$ field-of-view of ULTIMATE-Subaru. It covers the

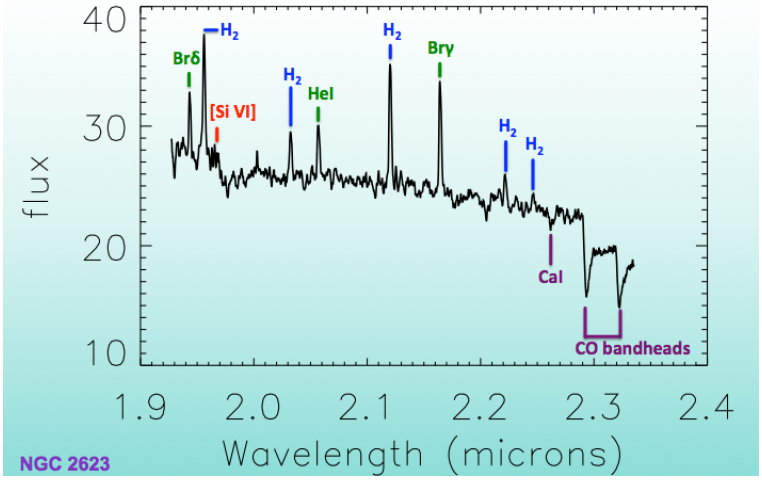

Figure 5.4: An example K-band spectrum of the nuclear region of NGC 2623 observed with the OSIRIS on the Keck telescope. This image is taken from a talk slide by Anne Melding.

whole disk of M83, one of the nearest barred spiral galaxies ($d = 4.5$ Mpc), and therefore sampling all star-forming regions and their relations to the galactic nucleus, spiral arms, and bar.

Shocks are one of the important physical events in understanding the energy input/output balance of the interstellar medium, star formation, galactic outflows and hence baryonic cycles in galaxies. Several vibrational transition lines of molecular hydrogen H_2 exist in near-IR (for example in K-band, 1.958, 2.034, 2.122, 2.224, and 2.248 $\mathring{A}$ for v =1-0 S(3), S(2), S(1), S(0), and 2-1 S(1) lines, respectively). Their excitation mechanisms include UV fluorescence in photodissociation regions around young OB stars or by a nuclear UV continuum source (Mouri, 1994). The H_2 emission can also be excited thermally by slow shocks ($v < 25$ km/s; Shull & Draine, 1987). The intensity ratios among these H_2 lines can distinguish between the nonthermal (star formation, galactic nuclei) and thermal origins (shocks). The ratio of H_2 lines over a star formation tracer, e.g., H_2/Brγ, is also used to differentiate shocks and star formation (e.g., Melding et al., 2015). Near-IR H_2 imaging can be applied to many large nearby objects, including (but not limited to):

- Galactic shocks and associated star formation are predicted by the spiral density wave theory (Roberts, 1969). In fact, large velocity gradients/offsets across spiral arms have been observed in nearby galaxies (e.g., Koda et al., 2009). However, the magnitude of the shocks and their impacts on star formation have not been confirmed observationally. In addition, recent theoretical studies cast doubt on the large-scale coherent galactic shocks by the classic density wave theory, and rather predict less coherent, dynamically-varying spiral arms and therefore shock patterns (Baba, Saitoh & Wada, 2013; D'Onghia, Vogelsberger & Hernquist, 2013). Narrow band H_2 imaging of spiral galaxies may reveal the (in)coherent distribution of galactic shocks and provides an estimate of their impacts on star formation along spiral arms.

- Shocks may play an important role in the intergalactic medium (IGM). For example, mid-IR H_2 lines have been detected in the Stephan's Quintet by the Infrared Spectrograph (IRS) instrument on the Spitzer space telescope (Cluver et al., 2010; Guillard et al., 2012). The cooling time for the warm H_2 is short ($\sim$ 5000 yr) at an observed density, and the on-going shock heating initiated by galaxy collision is suggested as a heating source (Peterson et al., 2012). High-resolution observations of IGM shocks will reveal the shapes and physical conditions of propagating shock fronts, and large-scale near-IR imaging of galaxy groups and clusters will show their distributions across them. There is also a mystery of the survival of H_2 molecules in such a galaxy encounter which typically has a collision velocity beyond the H_2 dissociation limit (> 25 km/s; Shull & Draine, 1987). Multi H_2 line

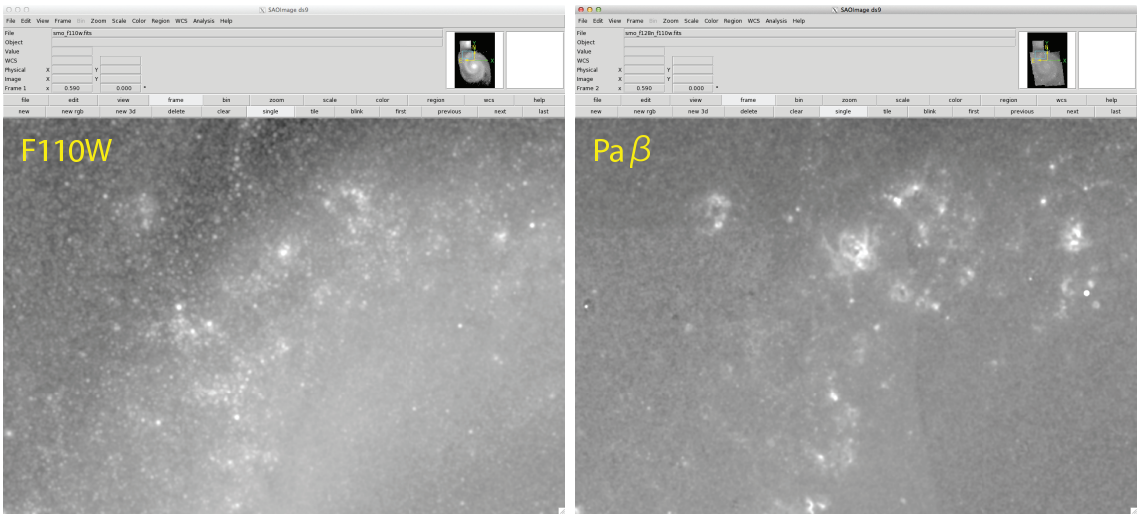

Figure 5.5: *HST* F110W & Paβ (=F128N–F110W) images of the Whirlpool Galaxy M51 ($d = 8.2$Mpc). The images are smoothed to the 0.2″ resolution, and only a small portion of a spiral arm is displayed.

imaging can constrain the physical conditions of underlying gas, and will provide an important clue to understanding the maintenance of the molecular gas, as well as the process of shock propagation and dissipation, in the IGM.

- On a small physical scale within the MW, protostellar outflows interact dramatically with the surrounding gas. Such interaction has been detected in near-IR H_2 line emission in Orion (Usuda et al., 1996). The kinetic energy of the outflows should drive turbulence as they collide with the surrounding gas and may trigger next generation star formation. Large-scale H_2 imaging of Galactic molecular clouds can take a census of outflows over the entire clouds. It will show the complex structures of the interacting surfaces between the outflows and the ISM and reveal an intricate details of the onset of the outflow-environment interaction.

An important synergy can be realized with sensitive and high resolution observations using ALMA. In particular, ALMA is capable of observing, for example, CH3OH, HNCO, and SiO emission, all of which are important tracers of shocks that could exist in spiral arms and bar-ends. The CH3OH molecule can be destroyed by relatively slow shocks (>10—-15 km/s) due to the molecules in the gas-phase of the volatile species (e.g., García-Burillo et al. 2001; Meier & Turner 2005). On the other hand, the dissociation of SiO would require fast shocks (>50–60 km/s) (Garay et al. 2000). The spatial distribution of the different shock tracers will largely complement the shocks traced in the H_2 image obtained with ULTIMATE-Subaru, allowing us to map the complex interplay between the galactic structure and the associated shocks in nearby galaxies.

5.2.3 Near-IR Broad Band Imaging

The combination of large field, high sensitivity, and high spatial resolution of ULTIMATE-Subaru will open interesting opportunities of near-IR broad band imaging. The utility of the broad band capability and its anticipated impacts depend on how fast ULTIMATE-Subaru starts its operation, compared to other space missions. For example, the 0.2″ resolution is enough to resolve asymptotic giant branch (AGB) stars within the bright part of galactic disks (Figure 5.5), and the tip of red giant branch (TRGB) stars in some very nearby galaxies. These populations of stars influence near-IR light and often are the source of uncertainties in stellar population synthesis models and determination of galactic stellar masses (Maraston, 1998). Broad-band imaging of large nearby galaxies with ULTIMATE-Subaru will provide

important calibration data with the problematic AGB population resolved. In star forming regions in the MW, proto-planetary disks around young stars is often searched using the excess emission seen in the Rayleigh-Jeans tail of stellar sphere SED due to thermal dust emission from the disks. With deep L-band imaging, proto-planetary disks can be searched down to very low mass stars and brown dwarfs. A joint analysis with archival UKIDSS survey data enables the measurement of proper motions of stars within nearby dense molecular clouds. Such analysis will show how stars formed in a cluster are dispersed to the Galactic disk.

Figure 5.6: The ULTIMATE-Subaru field-of-view $15' \times 15'$ cut around the nearby galaxy M83. The whole galactic disk is observed in one shot. ULTIMATE-Subaru can, therefore, observe all star-forming regions and large-scale galactic shocks simultaneously over the whole disk.

5.3 Deciphering the Origin of the Galactic Globular Clusters with ULTIMATE-Subaru

Masashi Chiba[1]
[1] Astronomical Institute, Tohoku University

5.3.1 Abstract

As a Galactic Archaeology science using ULTIMATE-Subaru instrument, we propose to carry out systematic near-infrared (NIR) photometry and spectroscopy of candidate globular clusters (GCs) discovered in the highly obscured regions near the Galactic bulge. Our main goals in this survey are to resolve each of member stars in candidate GCs from high resolution imaging and to determine the nature of stellar populations based on their color-magnitude distributions in combination of the spectroscopic data. This instrument also allows us to measure line-of-sight velocity distributions of tidal streams emanating from GCs, whereby the background Galactic gravitational field mostly provided by dark matter is constrained. This NIR survey program will provide important insights into formation and evolution of the GC system in the Galactic bulge.

5.3.2 Introduction: globular clusters in the Milky Way

Our understanding of the GC system in the Milky Way (MW) is still incomplete, although this constitutes one of the ancient Galactic components, witnessing how the MW formed and assembled. A modern picture of galaxy formation through successive merging of many building blocks has been initiated by the work of Searle & Zinn (1978) based on the analysis of halo GCs in the MW. They noted a number of difficulties in reconciling several observed properties of the halo GCs with predictions of the monolithic collapse scenario proposed by Eggen et al. (1962). Among these, the existence of a large (several Gyr) spread in the inferred ages of the halo GCs and the lack of an abundance gradient with distance from the Galactic center were thought to be most crucial: Searle & Zinn suggested that in its earliest epochs the halo component of the Galaxy may have formed prolonged, chaotic accretion of subgalactic fragments. This picture is indeed consistent with modern theory of galaxy formation based on hierarchical clustering of building blocks which consist of non-baryonic and baryonic matter.

However, similar studies of GCs in the Galactic bulge have been seriously hampered by the obscuration arising from thick layers of interstellar dust and thus the nature of these GCs especially related to the formation of the bulge component is unsolved yet. Indeed, Harris (2001) estimated that there were about 20 unknown Galactic GCs hidden behind substantial foreground extinction in the bulge and disk.

Nonetheless, great efforts for discovering new candidate GCs in the direction of the Galactic center have been made recently, such as by 2MASS (Skrutskie et al., 2006), Spitzer/IRAC GLIMPSE (Benjamin et al., 2003), and VISTA Variables in the Via Lactea (VVV) surveys (Minniti et al., 2010). Follow-up studies for some of these candidate bulge GCs have revealed very puzzling features. For instance, high-resolution NIR images of Terzan 5 with VLT/MAD surprisingly reveal the presence of two distinct stellar populations characterized by two horizontal-branch (HB) clumps as shown in Figure 5.7 (Ferraro et al., 2009): the stellar populations showing fainter HB are relatively metal poor ([Fe/H]$= -0.2$) and very old (12 Gyr), whereas those showing brighter HB are metal rich ([Fe/H]$= +0.3$) and young (6 Gyr). This suggests that Terzan 5 has experienced star formation activities at least twice. The similarity in iron abundance between Terzan 5 and the Galactic bulge population is compatible with the hypothesis that the disruption of its progenitor has contributed to the formation of the bulge. Also, another bulge cluster, HP 1, studied by Ortolani et al. (2011) with VLT/MAD has been found to have the metallicity of [Fe/H]$\simeq -1.0$ and very old age of ~ 13.7 Gyr, i.e., ~ 1 Gyr older than the halo average. This suggests that HP 1 may be identified as a representative relic of an early generation of star clusters formed in the proto-Galaxy.

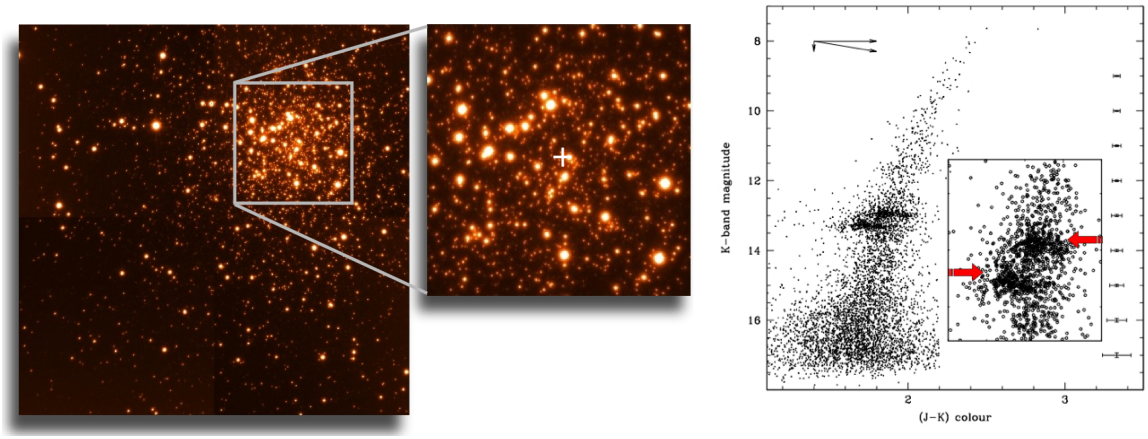

Figure 5.7: (left) VLT/MAD image of Terzan 5 in the K band (Ferraro et al., 2009). The image size is $1'\times1''$ and a small ($16''\times16''$) portion of the image is shown magnified. (right) The two horizontal branch clumps in Terzan 5 revealed from the K vs. $J-K$ diagram (Ferraro et al., 2009).

Thus, some of the bulge GCs with well resolved stars using AO have revealed very unique properties in their stellar population, but whether or not this uniqueness is indeed universal in the field of the bulge is yet unknown. This incomplete understanding of the GCs in this region is largely due to yet incomplete identification of candidate GCs in such highly obscured parts of the sky and also very limited photometric and spectroscopic observations for the known bulge GCs thus far. Further follow-up studies with NIR photometry and spectroscopy have actually been carried out for some of these candidate GCs (Kurtev et al., 2008), but yet a large number of the sample remain unidentified by means of larger telescopes. Thus, the questions such as the multiplicity of stellar population in these GCs, metallicity and age distributions of member stars, and so forth, are largely unanswered yet. It also remains unclear the relation of these GCs to the formation and evolution of the bulge component itself.

Figure 5.8 shows two candidate GCs discovered by VVV survey. Subaru follow-up studies for these star clusters will be useful to obtain detailed photometric data (as shown in Figure 5.7) and understand the nature of stellar populations in more detail. It is also important to carry out high-resolution NIR spectroscopy of member stars to obtain the star formation and chemical evolution history of these candidate GCs in the bulge regions.

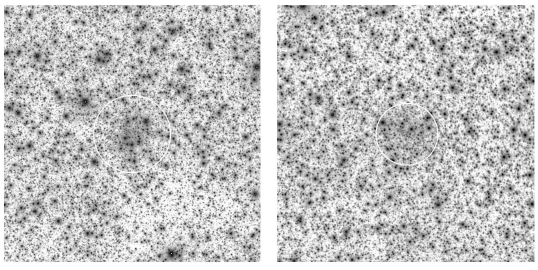

Figure 5.8: $5'\times5'$ K_s-band images from the VVV archive, centered on the two candidate GCs: VVV CL002 (left) and VVV CL003 (right) (Moni Bidin et al., 2011).

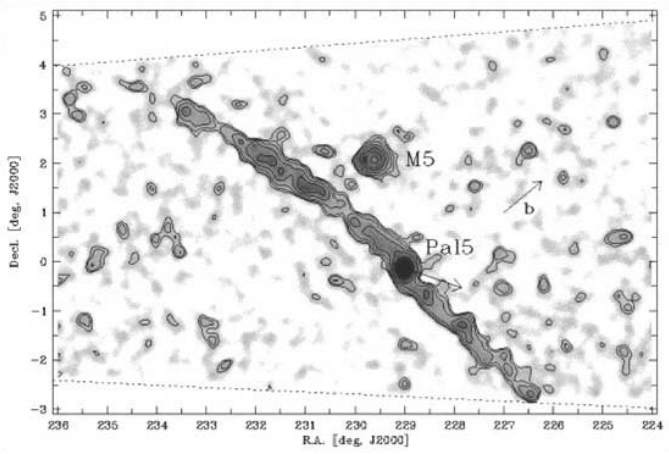

Figure 5.9: Globular Cluster Pal 5 and surrounding stellar-stream structure (Odenkirchen et al., 2003).

5.3.3 ULTIMATE-Subaru survey of candidate GCs in the Galactic bulge

ULTIMATE-Subaru will thus provide us with an excellent opportunity for the detailed photometric and spectroscopic study of these bulge GCs, whereby we may arrive at new pictures for the formation of these star clusters and the relation with the formation of the bulge component. The key issues to be resolved with this program include: (1) what are the overall metallicity distribution and the detailed abundance patterns of member stars in the bulge GCs, especially those showing multiple stellar population like Terzan 5?, (2) are the derived chemical properties of the bulge GCs different from those associated with other Galactic components, i.e., the disk and halo clusters?, and also (3) is there a similarity or difference compared with the abundance patterns of field bulge stars?

The clarification of these issues in GCs and the comparison with the Galactic bulge will offer new insights into the formation of the Galactic bulge, as GCs are possibly the surviving remnants of primordial building blocks that are thought to merge and form the bulge. Our ULTIMATE-Subaru observations of these GCs will place important constraints on when and how the presumed star formation and merging events related to the bulge formation took place. As a consequence, it will be possible to elucidate how an assembly process of fossil building blocks reflects the present fundamental structure of the Galactic spheroids.

In addition to the science of GCs, we expect that wide field-of-view surveys of GCs with ULTIMATE-Subaru may also detect new stream-like structures originated from these clusters, which are caused by tides of the Galactic gravitational field. Indeed, the central parts of the Galaxy are dominated by gravitational fields of both dense bulge stars and dark matter component, whereby star clusters are strongly disturbed by the associated tides, or many of them may have already been disrupted, where only stream-like substructures are remained. These substructures are actually identified for some of GCs, such as Pal 5 (see Figure 5.9) and NGC 5466. It is worth recalling that these stream-like features are a very good tracer of background gravitational field through the analysis of their spatial and kinematical distributions (Eyre & Binney, 2009). Thus, both photometric and spectroscopic observations of many stellar streams originated from bulge GCs enable us to constrain true mass distributions in the relevant areas, namely the Galactic bulge and associated dark matter, which are important components to understand the dynamics of the Galactic bulge.

We also note that dynamical coldness of such GC originated streams, which are thus spatially thin, is quite sensitive to any dynamical perturbations, especially by dark-matter clumps or so-called dark-matter subhalos, many of which are supposed to orbit in a MW like dark halo according to ΛCDM theory. Such dynamical perturbations by subhalos induce characteristic disturbances or gaps in the density distribution of stars along a stream (Carlberg, 2012), depending on the incidence of interaction with orbiting subhalos,

namely their abundance in the MW. Subaru/GLAO observation of these stellar streams originated from bulge GCs will thus be of great importance to set constraints on ΛCDM theory.

Based on this motivation, we propose J-band and K-band imaging observations of candidate GCs in order to resolve stellar population for each of candidate GCs down to $K = 20.0$ and $J = 22.5$ (to consider reddening up to $J - K \sim 2.5$), with FWHM of $0.2''$ and $0.4''$ for K and J, respectively. These limiting magnitudes correspond to about 2.5 mag fainter than likely MSTO stars with $K \approx 17.5$ at the distance of 8 kpc, i.e. at the Galactic center. Further NIR spectroscopic studies provide both chemical abundances and line-of-sight velocities for resolved member stars (as well as for stream stars if they exist), whereby we are able to refine our knowledge for the chemo-dynamical properties of these stars in the direction of the Galactic bulge.

5.4 The Galactic Center: Origion of S-stars and Nuclear Star Cluster

Shogo Nishiyama
Miyagi University of Education

5.4.1 Introduction

At the center of our Galaxy, Sgr A*, the compact radio, infrared (IR), and X-ray source is associated with a supermassive black hole (SMBH) candidate weighing in at $\approx 4 \times 10^6 M_\odot$ (e.g., Eckart & Genzel, 1996; Ghez et al., 2000). In spite of its strong tidal fields, we find a strong concentration of young, B-type MS stars ($\sim 3.5 - 20 M_\odot$) within $\sim 1\farcs0$ (≈ 0.04 pc) from Sgr A* (Fig. 5.10, left panel). The stars are collectively referred to as the "S-stars". The density for a molecular cloud to be stable against tidal disruption is on the order of a few $10^{10} n_{\mathrm{H}_2}$ cm^{-3} at 0.1 pc from Sgr A*. Since this is several orders of magnitude larger than molecular clouds found in the Galactic center (GC) region, normal star formation cannot proceed in this region. We have not understood the reason why so many young S-stars exist near the SMBH.

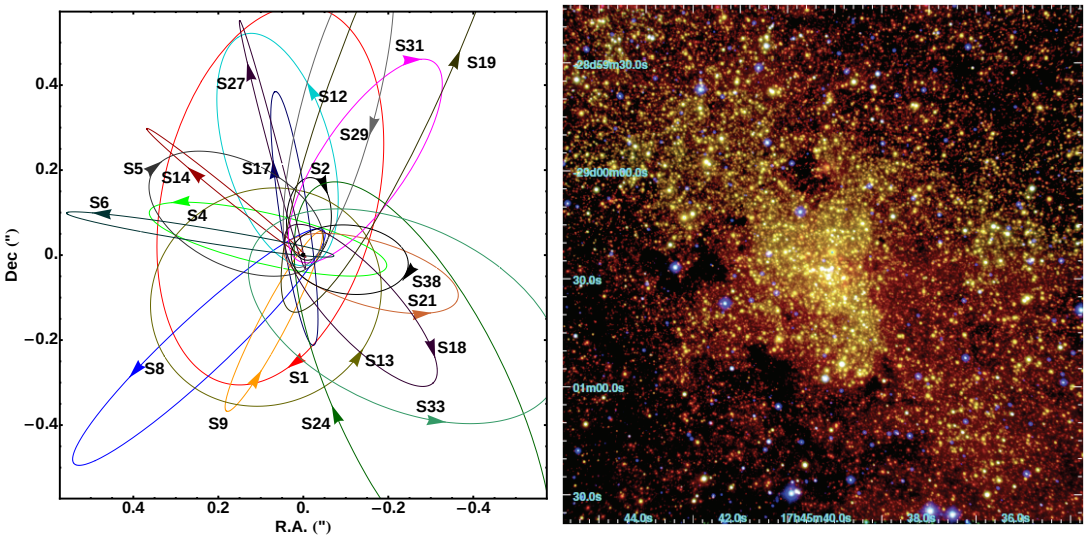

Figure 5.10: *Left*: Stellar orbits of S-stars in the central $1\farcs0 \sim 0.04$ pc of our Galaxy. The coordinate system is chosen to such that Sgr A* is at rest (Fig. 16 in Gillessen et al., 2009). *Right*: Near-infrared three-color (1.19 μm, 1.71 μm, and 2.25 μm) composite image of the central $\sim 150''$ region of our Galaxy (Fig. 2 in Nishiyama & Schödel, 2013). The NSC in our Galaxy has a half-light radius of $\approx 100'' \sim 4$ pc (Schödel et al., 2014).

Most galaxies host luminous nuclear star clusters (NSCs; e.g., Carollo et al., 1998; Côté et al., 2006; Böker, 2010). Many of them have been found to coexist with SMBHs at their center (Seth et al., 2008; Graham & Spitler, 2009; Neumayer & Walcher, 2012). Similar to SMBHs, the mass of the NSCs appears to follow scaling relations with the bulge mass (e.g., Ferrarese et al., 2006), or the mass of the whole galaxy (Erwin & Gadotti, 2012). Unlike SMBHs, NSCs are expected to provide a visible record of gas accretion and star formation at the center of galaxies, and the NSC in our Galaxy (Fig. 5.10, right panel) is the only one which can be resolved into individual stars with current instruments, making it an ideal target for studies of stellar populations and star formation history in NSCs. Studying stellar populations

in our NSC can therefore give us clues as to how stars are formed within the strong tidal field from SMBHs.

Although the Galactic SMBH and NSC are much closer than those in other galaxies, and it is unable to resolve S-star like stars in other galaxies even with 30-m class telescopes, we have significant constraints for observations of them (Schödel, 2015). The interstellar extinction toward the GC is extreme, more than $A_V = 30\,\mathrm{mag}$. It means that we cannot observe stars of the GC in the optical wavelength. In addition, stellar number density is very high, from a few to several tens of stars per square arcsecond within $\sim 100\,\mathrm{pc}$ from Sgr A*. Without adaptive optics (AO), our imaging observations are limited to relatively bright magnitudes, $K \lesssim 15$ due to the crowding. Therefore *near-infrared* (NIR) instruments with *AO* are crucial for observational studies to resolve the issues described above.

5.4.2 Hyper velocity stars and S-stars; are they twins?

The origin of the S-stars, most of them are young B-type stars, and are orbiting around the SMBH within the central $\sim 0.04\,\mathrm{pc}$, is still uncertain. One of the possible explanation for the origin of the S-stars is three-body interactions between a stellar binary system and the SMBH (Hills, 1988). In the interaction, the binary system is disrupted, with one star captured in a tight, elliptical orbit around the SMBH, and the other expelled at high velocity up to several km/s as a hyper-velocity star (HVS)[1]. During this process, the first star loses energy and becomes bound to the SMBH, while energy and angular momentum are transferred from the SMBH to the second star. In this scenario, the S-stars and HVSs are twins get separated by the gravitational breakup. The detection of the HVSs whose birth place is in the GC would therefore be a strong evidence for the presence of the SMBH and the three-body interaction, and provide an important clue to understand the origin of the S-stars.

Since the first discovery, ~ 20 HVSs have been found in the Galactic Halo. The first HVS is a B9 MS star with a Galactic rest-frame velocity of $\sim 700\,\mathrm{km/s}$, and its radial velocity vector suggests the GC in origin (Brown et al., 2005). On the other hand, some HVS stars appears to have an origin not in the GC, but in the Galactic disk. A remarkable example is HD 271791. The Galactic rest-frame velocity of this star ($530 - 920\,\mathrm{km/s}$) exceeds the Galactic escape velocity at its position ($430\,\mathrm{km/s}$). However, the space velocity of HD 271791 constrains the place of birth to the outer Galactic disk, not the GC. The star is also too young ($< 30\,\mathrm{Myr}$) to have originated in the GC. In addition, additional four HVS candidates have been found, and they are unlikely originate from the GC (Li et al., 2012).

Although the three-body interaction between the SMBH and a binary system remains the most promising process in generating HVSs, other scenarios have also been suggested; e.g., a close encounter of a single star with a binary black hole (BH) (SMBH and intermediate-mass BH; Yu & Tremaine, 2003). In this case, a single star gains energy from the binary BH and is flung out of the Galaxy while the orbit of the BH binary shrinks.

In any case, the HVSs in the Galactic Halo are too far away from the GC to go along the opposite direction of the HVSs' velocity vectors, and to perform a full orbit integration with the Galactic potential, to derive the intercept position in the Galactic plane, where is the point of origin of the HVSs if it were ejected from the plane. Finding HVSs near the GC will thus be a key to understand the origin of the HVSs and S-stars.

The GLAO and wide-field NIR camera will be important tools to find HVSs in the GC region. If the origin of the HVSs is in the GC, the HVS density must be largest in the GC region. The region is so crowded that the GLAO plays an important role to resolve HVSs and detect their proper motion. Yu & Tremaine (2003) have studied the ejection rates of the HVSs ($> 1,000\,\mathrm{km/s}$), and found that the rates by the stellar binary-SMBH interaction and the single star-BH binary interaction are $\sim 10^{-5}\,\mathrm{yr}^{-1}$ and $\sim 10^{-4}\,\mathrm{yr}^{-1}$, respectively. If we observe the central $50' \times 50'$ field, ~ 1 and ~ 10 HVSs are expected to be found in the region. More HVSs with lower velocity are also expected. The typical proper motion of the HVSs with $1,000\,\mathrm{km/s}$ is $\sim 15\,\mathrm{mas/yr}$ at the distance of the GC. Such a proper motion is detectable in observations with only several years if GLAO works with a wide-field imager, and a few 100 mas spatial resolution is achieved.

[1] HVSs are generally defined as stars with velocities that exceed the escape velocity of the Galaxy.

5.4.3 Star formation in the Galactic nuclear star cluster

In the Galactic NSC (Fig. 5.10, right panel), stars with a variety of ages have been found, from very old ($\sim 10\,\mathrm{Gyr}$) to young ($\sim$ Myr; Pfuhl et al., 2011). Observations of NSCs including the Galactic one clearly indicate that stars have continuously been born after the formation of the major part of the NSCs.

While the stars are in the same cluster at present, physical conditions when and where they were formed might be different. Outside the central 0.1 pc from Sgr A*, more than 100 stars have been identified as OB main-sequence stars, OB supergiants, and WR stars (e.g., Paumard et al., 2006). A large part of them are distributed at distances from ~ 0.04 to $\sim 0.5\,\mathrm{pc}$ from Sgr A*, and have an age of $2 - 6\,\mathrm{Myr}$. Recent studies have shown that they have a top-heavy initial mass function (IMF; Bartko et al., 2010; Lu et al., 2013).

On the other hand, an old stellar population in the Galactic NSC are likely to have a normal IMF. Using spectroscopic data for more than 400 late-type giants at 1 pc from Sgr A*, i.e., well within the NSC, Pfuhl et al. (2011) have shown that $\sim 80\,\%$ of stars in stellar mass were formed $> 5\,\mathrm{Gyr}$ ago, and mass estimates of the stars favor a normal IMF. There results suggest that old ($> 5\,\mathrm{Gyr}$) and young (several Myr) stellar populations have different IMFs, indicating a different physical condition in their birth place. Did the SMBH have a smaller mass and thus its tidal field is weaker when the old stars were formed? Or were the stars formed in a different place and then gathered into the NSC?

Intermediate-age Population in the Nuclear Star Cluster

An interesting target to understand the variation of the physical condition in the Galactic NSC is an intermediate-age ($\sim 100\,\mathrm{Myr} - 1\,\mathrm{Gyr}$) stellar population. Since the detection of ~ 10 moderately luminous late-type stars (Krabbe et al., 1995), spectroscopic observations have confirmed the presence of such stars inside (Maness et al., 2007) and outside (Blum et al., 2003; Nishiyama et al., 2015) of the central 0.5 pc region. Pfuhl et al. (2011) suggests that while the star formation rate reached a minimum $\sim 1\,\mathrm{Gyr}$ ago, it rose again $\sim 100\,\mathrm{Myr}$ ago. Hence the physical condition in which the intermediate-age stars were formed, the IMF they have, and the reason why the IMF is different from those of the old and/or young stellar populations, are subjects to be studied.

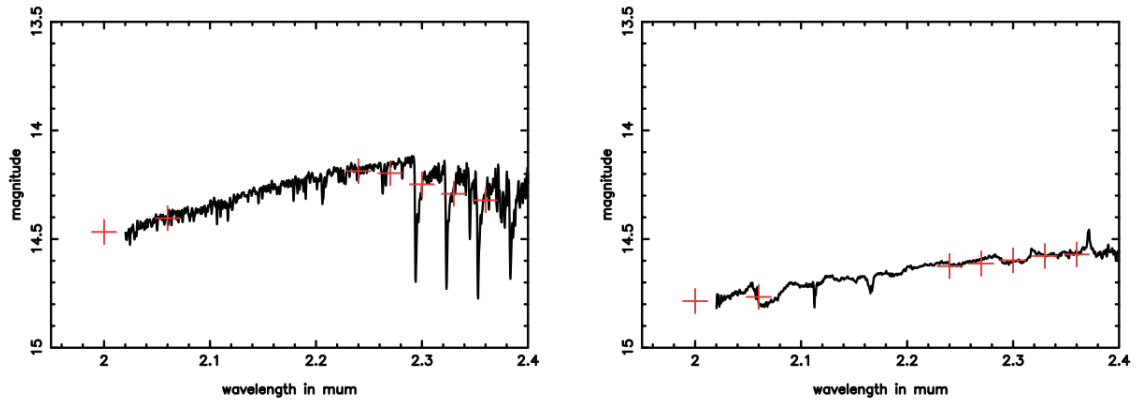

Figure 5.11: Stellar spectra for K4.5 giant (left) and B0 dwarf (right). The red crosses indicate the low-resolution SED at the position of seven narrow-band filters used in Buchholz et al. (2009). Adapted from Buchholz et al. (2009, Fig. 3).

To understand properties of the intermediate-age stellar population, we need to find the population as many as possible to derive their IMF. An efficient way to search for the intermediate-age population is to use narrow-band filters (Genzel et al., 2003; Buchholz et al., 2009; Nishiyama & Schödel, 2013). With narrow-band filters which are sensitive to CO absorption lines at $\gtrsim 2.3\,\mu\mathrm{m}$, a prominent feature for old, late-type stars, we can estimate the CO absorption depth, and then discriminate younger ($< 1\,\mathrm{Gyr}$)

stars from old ones (Fig. 5.11). Recently, we have shown that only two narrow-band filters (2.25 μm and 2.34 μm) are sufficient to distinguish young and intermediate age stars from old, late-type giants (Nishiyama et al., 2015).

Wide-field imager is also required to find as many intermediate-age stars as possible. As shown in Fig. 5.10, the Galactic NSC has a half-light radius of $\sim 100''$, and it is thus quite difficult to complete the survey of the whole NSC region using IFU instruments with a small FoV. Several NIR, wide FoV space missions (Euclid, WFIRST, WISH) are planned, but in most every case, narrow-band filters would not be installed.

Without AO, the discrimination of the intermediate-age population is limited to $K \lesssim 12$ mag due to the confusion limit (Nishiyama & Schödel, 2013). On the other hand, using AO, Pfuhl et al. (2011) have detected intermediate-age stars more than ~ 4 mag fainter than the seeing limited observations. GLAO is expected to help to survey the whole NSC region with detection limit a few mag deeper than the current, seeing limited observations.

Hidden Remnants of Stellar Clusters

Another interesting target is hidden cluster remnants. There are two extraordinary star clusters, Arches and Quintuplet at $\sim 20 - 30$ pc from Sgr A* in projection. They are very young ($2 - 4$ Myr), compact ($\lesssim 1$ pc), and massive (a few $10^4 M_\odot$). The clusters are thus categorized as "young massive cluster" (Portegies Zwart et al., 2010). The clusters might be formed at the distance from several tens to several hundreds pc from Sgr A* (Stolte et al., 2008), where tidal fields from SMBH is weak and thus a normal star formation proceeds.

The existence of the two clusters implies that, in the GC, such massive clusters were frequently formed in the past, and they came to be a part of the NSC. Gerhard (2001) has proposed that massive clusters formed at more than several parsec distance from Sgr A* are followed by an infall toward the central parsec via dynamical friction. The lifetime of the intermediate-age stars mentioned above, more than ~ 100 Myr, is long enough for clusters to migrate from a few tens parsec distance to the central a few parsec region (e.g., Gürkan & Rasio, 2005). A migration of stellar clusters to the center is a natural consequence if clusters are formed in this region, so at least some part of the NSC are expected to be formed as stellar clusters.

However, it is not easy to find such cluster in the GC region. In projection on the sky toward the GC, a density contrast between stellar clusters and inter-cluster fields is reduced because of accumulation of stars along the line of sight. In addition, the clusters expand as they age, and are disrupted mostly by tidal stripping and two-body relaxation. Then the clusters finally dissolve in the tidal fields of our Galaxy. Even for rich clusters like Arches, their projected densities drop below the field stellar density within only a few Myr in the central ~ 30 pc region, making the clusters undetectable after that time (Portegies Zwart et al., 2002).

To identify such hidden cluster remnants, astrometric studies are necessary. In the GC region, the two-body relaxation time for a cluster with a mass of $10^4 M_\odot$ is on the order of a few 10^9 yr (Alexander, 2005). It means that a part of members of the clusters with an age of ~ 100 Myr still have a similar proper motion. If stars with a common proper motion are clustered, they can be identified as a remnant of a cluster. In addition, the cluster velocity carries the imprint of the motion of its native cloud, and studies of the cluster's 3D motion shed light on its origin (Stolte et al., 2008).

It is difficult to predict the proper motions of the hidden cluster remnants, so we consider the Arches cluster to be an example. The Arches cluster has a relative proper motion of ~ 5 mas/yr to the field stars (Stolte et al., 2008; Clarkson et al., 2011, see also Fig. 5.12). If we assume ~ 5 mas/yr as a typical proper motion, an astrometric accuracy of ~ 3 mas is required to detect the proper motion with $> 5\sigma$ within 3 yrs. A typical positional accuracy is expected to be $\sim 1/100$ of stellar FWHMs, so if GLAO works well to obtain a stellar FWHM of $0''.3$, we will be able to detect the hidden cluster remnants. If the remnants are detected, it will be interesting targets of TMT, which has deep photometric capability. TMT will also provide much more accurate proper motion to investigate the origin of the cluster remnants.

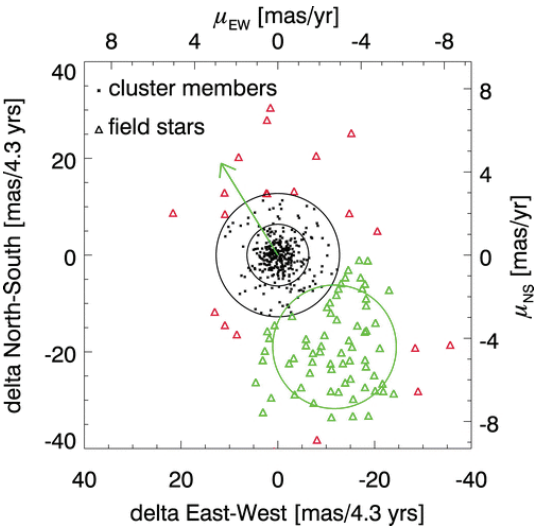

Figure 5.12: Spatial displacement of stars in the Arches cluster over 4.3 yr in the cluster reference frame. Arches candidate members (black dots) cluster around (0,0), while likely field stars (triangles) are mainly distributed to the lower right of the members. Adapted from Stolte et al. (2008), Fig. 3.

5.5 Dark Matter in the Inner 2-Kiloparsecs of the Milky Way

David Nataf[1], **Andy Casey**[1]
[1] Australian National University

The question of the Milky Way's dark matter potential is evolving from one of speculation and order-of-magnitude estimates to being that of a precision science. As is well-known, LSST will study the gravitational potential at large distances, and Gaia at the scale of the solar neighbourhood. Closer to the inner Milky Way, a 4% measurement of the enclosed baryonic+dark mass has recently been achieved by modelling large-scale conventional radial velocity survey data along with spatial density data from photometric surveys. The degeneracy between baryonic mass and dark matter mass will not be an issue due to efforts currently underway to precisely measure the IMF.

We propose to complete the mapping of the dark matter potential from $R_{\rm GC}$=2.0 kpc down to RGC=0.1 kpc, by combining parallaxes and proper motions from the upcoming WFIRST Galactic bulge microlensing campaign with radial velocities from ULTIMATE. Under the assumption of 13 fibres per pointing, we will require ∼400 hours of observing time (50 nights) to obtain spectra of 10,000 stars.

We discuss how this effort requires a large aperture telescope, infrared spectroscopy, and low seeing. A byproduct of this campaign will be an accurate star-formation history of the Milky Way as a function of Galactocentric radius, all the way to the inner bulge.

5.5.1 Introduction

The current state-of-the-art in spectroscopic surveys of the Milky Way galaxy are unquestionably the Gaia-ESO survey (Gilmore et al. 2012), the Apache Point Observatory Galactic Evolution Experiment (APOGEE; Zasowski et al. 2013), and the Galactic Archaeology with HERMES (GALAH; De Silva et al. 2015) survey.

These three surveys will yield a combined assay of millions of stellar spectra, each with informative diagnostics such as the relative abundances for up to ∼30 elements as well as 10% distance estimates and 20% age estimates. The result of these surveys will provide unparalleled characterization of the solar neighbourhood, i.e. the Galactic disk within ∼2 kpc of the Sun.

There will, in contrast, be relatively scant mapping of the inner Milky Way and the outer halo, and zero study of the disk at the other side of the Galaxy, and the inner regions of star clusters and dwarf galaxies. These archaeologically pertinent stellar populations are more challenging to study because they are more distant, more crowded, and in many cases more extincted.

Fortuitously, the general specifications of ULTIMATE for Subaru are exactly what one needs to target these populations for spectroscopic follow-up. The larger mirror aperture increases the signal of more distant (and thus fainter) targets, whereas the smaller seeing decreases the sky noise that currently limits infrared spectroscopy. The smaller seeing and smaller fibres enables targeting of stars in crowded fields, typical of the inner Milky Way and the cores of globular clusters and dwarf galaxies. Finally, the infrared aspect reduces the impact of dust by a factor of ∼5–15 depending on the specifics of the region studied.

The Gaia-ESO and GALAH surveys fail in each of these three criteria, which is why their survey yields will be completely orthogonal and complementary to what we can learn from an ULTIMATE survey of the Galaxy. APOGEE does benefit from infrared imagine, and thus has a more significant Galactic plane component. However, the large fibre size (∼2″) of the APOGEE spectrograph, and the small aperture of its telescope (∼2.5m) limit APOGEE to stars brighter than H∼12.5 (Vega mag), rendering most of the Galactic bar, the inner Galactic bar, and the disk at the other side of the Galaxy out of reach. The large fibres also means it cannot target crowded fields, compounding the previous limitation.

Low resolution spectra (∼2000) in the JHK bands is sufficient for a robust determination of radial velocity, stellar effective temperature, surface gravity, and mean abundance. Given the large aperture and narrow fibre size, low- resolution infrared spectra with ULTIMATE will facilitate high-impact galactic astrophysics that would be otherwise unachievable.

5.5.2 Survey design: spectroscopy of the WFIRST field

Description of WFIRST

The Wide-Field Infrared Space Telescope (WFIRST) is a ∼2.5 billion dollar NASA mission scheduled to launch in 2024 (Spergel et al. 2015). As part of its core mission, WFIRST will spend 357 days observing 10 contiguous fields toward the bulge spanning a total surface area of 2.81 deg^2.

The primary purpose of this bulge component will be the discovery and characterization of ∼3,000 planets for planet-star separations greater than 1 AU, extending all the way to free-floating planets, and thus completing the mapping of the "planet function" begun by Kepler.

The observing seasons are expected to be 72 days each, one per year over six years. During that period, each field will be observed every 15 minutes, with 24/7 cadence during that time span. This yields a total of ∼35,000 photometric measurements.

In the following subsections, we briefly discuss why the spectroscopic follow-up of the WFIRST window needs to be done in the infrared, at low seeing (and large aperture), and then follow with the case for follow-up.

Why WFIRST Spectroscopic Follow-up Needs to be in the Infrared

The typical extinction toward the field is $A_V \approx 6.5$, reaching values as high as $A_V \approx 22$ (Gonzalez et al. 2012; Nishiyama et al. 2008). In contrast, the extinction toward those sightlines are typically ∼5× smaller in J-band, ∼9× smaller in H-band, and ∼16× smaller in K-band (Nishiyama et al. 2008; Nataf et al. 2015). Thus, proper spectroscopic follow-up of these fields require infrared spectroscopy.

Why WFIRST Spectroscopic Follow-up Needs to be From Large Aperture

In Figure 5.13, we show the predicted the distance distribution of stars toward the WFIRST field using the same colour selection as APOGEE does toward the bulge (Zasowski et al. 2013), accounting for the extinction toward this field (Gonzalez et al. 2012), and assuming a simple Galactic model (Ness et al. 2012). We place the Galactic centre at a distance of R_0=8.33 Kpc.

If one selects stars H≤12, there are so few stars that upon setting the histogram scale to be the same for all three panels, it appears as zero stars. The mean distance to the stars is 2.7 kpc, in other words the sample does not even reach the inner Milky Way. If one selects stars satisfying $12 \leq H \leq 14$, the sample expands to a tolerable size, but the mean distance is 7.5 kpc, it remains biased to nearby stars. Finally, for a sample of stars satisfying $14 \leq H \leq 16$, the mean distance probed is 8.6 kpc, with a mode closer to 8.4 kpc. In other words, stars on both sides of the Galactic centre probed, including the interesting stars in the Galactic disk at the other side of the Galaxy, a region now totally unprobed. Thus, to have a sample of stars symmetric about the Galactic centre, and large, we will need to target stars ∼25× fainter than those currently targeted by APOGEE. The ULTIMATE instrument will benefit from a telescope surface area that is ∼12× larger, recovering most of the offset so as to conserve exposure times. Further, the PSF will have a surface area ∼4× smaller at least, and thus signal-to-noise in the infrared should rise by a factor of ∼50 for equal exposure times, or be conserved for exposure time cut by one half.

At 36 stars per configuration, this works out to 72 stars per hour of observing. One can thus acquire 10,000 bulge stars in ∼140 hours of observations, equivalent to 21 nights. This would put the sample on par with ARGOS (Ness et al. 2012) and BRAVA (Kunder et al. 2012) in numbers, but with the benefit of accurate and precise parallaxes, and thus superior diagnostic power.

Why WFIRST Spectroscopic Follow-up Needs to be at Sharp Seeing

We state two reasons for the sharp seeing requirement.

The first, already alluded to in the previous paragraph, is that it decreases sky noise, and thus allows shorter exposure times at fixed signal-to-noise requirements.

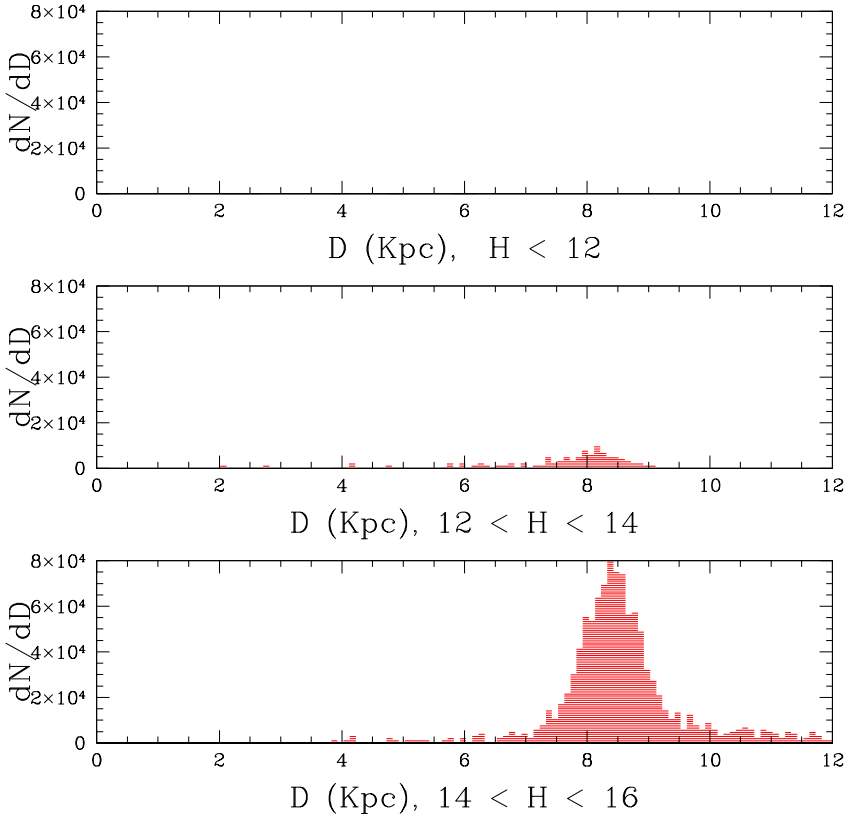

Figure 5.13: Predicted distance modulus toward the WFIRST field as a function of apparent magnitude cut in H-band. More stars are available at fainter magnitudes, and they span a broader distribution in Galactocentric radii.

The second, is that the many of the most interesting fields not targeted by Gaia-ESO, APOGEE, and GALAH are crowded fields. This includes the inner Galactic bulge discussed in this work, but also the Galactic disk, and the inner regions of globular clusters and dwarf galaxies.

5.5.3 The Milky Way's dark matter profile

The stellar populations in the WFIRST Galactic bulge fields will have a wealth of information including parallax, proper motion, colour, and sometimes asteroseismic mass and gravity. For stars brighter than $H = 19$, the expected precision on parallaxes will be greater than 10%, in addition to an expected precision of 0.3% or better in the proper motions (Gould et al. 2015; Spergel et al. 2015). This means five dimensions of kinematics for a huge sample of stars densely spanning the Galactocentric distance range $0.1 \leq \mathrm{RGC} \leq 4.0$ Kpc. The missing kinematic component is radial velocity, which can easily be measured with spectra.

Radial velocities (Kunder et al. 2012) and directions – without proper motions and parallaxes —–have already yielded a ∼4% measurement of the mass content of the Galactic bulge within a rectangular box of ($\pm 2.2\times \pm 1.4 \times \pm 1.2$ kpc) (Portail et al. 2015).

This measurement of the mass content is at relatively large distances since it is constrained by radial velocities measured at separations of 4–10 degrees from the plane, and not the 1–3 degrees from the plane of the WFIRST field. Radial velocity mapping of stars in this window will complete the gravitational potential map (and thus dark matter profile) of the Milky Way, measured by the Gaia mission (Perryman

2005) at the galactocentric scale of the solar neighbourhood and LSST proper motions to large distances traced by halo stars (LSST Science Collaboration et al. 2009).

We note that WFIRST parallaxes will be the only means of precisely mapping the gravitational mapping of the inner Milky Way: the expected accuracy of Gaia parallaxes in this region is ∼30% at best (Brown 2014), typically worse toward regions of high extinction. Thus, the addition of spectroscopic information (from ULTIMATE) will complete the kinematic mapping of these stars and thus also complete the mapping of the Milky Way's dark matter profile.

5.5.4 The Milky Way's star-formation history

For the red giant stars, brighter than $H = 14$, WFIRST will obtain precise asteroseismic values of the masses and radii of the stars (Gould et al. 2015). It has been shown that asteroseismic masses can yield reliable age estimates for red giant stars (**?**) — but only in the Kepler fields and other specialized sightlines, where there is high-cadence, high-precision, long-baseline photometry available. However, the mapping from stellar mass to stellar age is metallicity-dependent.

Spectroscopy of these stars, and thus metallicities, will not only yield the age- metallicity relation and star-formation history of bulge stars, but also the same for Galactic disk stars between the Sun and the bulge, and even on the other side of the Galactic disk. This will complement age-determinations from Gaia-ESO (Gilmore et al. 2012), APOGEE (Zasowski et al. 2013), and GALAH (De Silva et al. 2015) which are surveys of bright stars, dependent on Gaia parallaxes for precise ages, and thus will only yield robust ages in the solar neighbourhood. Solving for the Milky Way's age-metallicity relation not just for the solar neighbourhood, but also for the full range of Galactocentric radii interior to the solar neighbourhood, could resolve the issue of radial migration (Schönrich & Binney 2009).

5.5.5 Fixing the asteroseismic scaling relations

When combined with ULTIMATE spectra, the asteroseismic oscillations detected by WFIRST will be crucial for improving determinations of stellar masses and radii. While giant star masses are derivable from asteroseismic scaling relations for near-solar metallicity stars, there is theoretical and empirical evidence that suggest those scaling relations should have a metallicity dependence (Epstein et al. 2014). The full impact of any metallicity dependence is currently unknown due to the paucity of bonafide metal-poor giant stars with astero-seismic oscillations. Given the wide metallicity distribution of giant stars in the disk and bulge, obtaining ULTIMATE spectra for giant stars observed by WFIRST provides an unparalleled opportunity to understand the dependence of metallicity with asteroseismic oscillations, and unambiguously answer this outstanding problem.

5.6 Chemical Measurements of Stars for Understanding Chemical Evolution of the Milky Way Disk

Noriyuki Matsunaga[1]
[1] Department of Astronomy, The University of Tokyo

5.6.1 Background

The Milky Way is important not only because it hosts our Solar system but also because we can investigate stellar populations and interstellar components in greater detail than any other galaxies. Recent large surveys for stellar populations in various regions of the Milky Way have been revolutionizing the study of its structure and evolution (Ivezic et al., 2012). In addition to many exciting results on the halo, large-scale (10^4 to 10^6 stars) spectroscopic surveys also make it possible to test chemo-dynamical models of the disk with various physical processes like radial migration (e.g. Schönrich & Binney 2009; Haywood et al. 2013). A critical observable feature for investigating the large-scale disk structure is the metallicity gradient, i.e. metallicity distribution as function of Galactocentric distance ($R_{\rm GC}$). However, most of the above large-scale surveys are optical and do not cover distant objects (further than a few kpc) in the disk because of the severe interstellar extinction. As naturally expected, observations in the infrared play crucial roles in studying the wide area of the disk.

The APOGEE project has collected infrared spectra of stars in a wide range of the disk ($0 < R_{\rm GC} < 15$ kpc). Hayden et al. (2014), for example, investigated the metallicity gradient of the disk, i.e. metallicity distribution as function of Galactocentric distance ($R_{\rm GC}$), based on the measurements for $\sim 20,000$ stars. They found a significant gradient with stars with smaller $R_{\rm GC}$ being less metal abundant near the Galactic plane ($|z| < 0.25$ kpc, where z is the distance from the plane), while such a gradient is less evident if any away from the plane ($|z| > 1$ kpc). The metallicity distributions of their samples show enormous scatters. While the large scatter may be real considering the radial migration of stars within the disk, a difficulty in interpreting the APOGEE data is that their sample, mainly red giants, is a mix of stellar populations with a large range of age. Nevertheless, the APOGEE's ability to collect infrared spectra of many stars with 300 fibers are very useful to observe a large number of stars among various stellar populations in the Galactic disk. In addition to the 2.5 m telescope at Apache Point Observatory in the northern hemisphere, their second-epoch project (APOGEE-2) will put the identical spectrograph to 2.5 m telescope at Las Campanas Observatory in Chile to expand the survey to get a global picture of the chemical structure of the Milky Way[2]. An important limit of the APOGEE projects is the limiting magnitude, $H \sim 12$ mag with their typical integration time and ~ 13.5 mag with their deep observations.

5.6.2 Scientific goal

We here consider two types of objects, Cepheids and stellar clusters, as targets of multi-object spectroscopy to investigate the chemical structure of the Milky Way disk. Cepheids are young stars evolved from intermediate-mass stars (10–300 Myr, 4–11 $M_\odot$, Bono et al. 2005) and their distances can be obtained based on the period-luminosity relation (Sandage & Tammann, 2006). Their chemical abundances can be accurately measured, and the abundance gradient traced by this objects is found to be the clearest and tightest in previous studies (Genovali et al., 2014, 2015). Whilst previous, mainly optical, surveys of variable stars are strongly limited by interstellar extinction, recent infrared observations are beginning to reveal Cepheids spread across a wide area of the Milky Way disk (Matsunaga et al., 2011; Feast et al., 2014; Matsunaga, 2014; Dekany et al., 2015).

Stellar clusters are also good tracers of the Milky Way. Their distances and other parameters such as age and foreground extinction can be estimated based on, for example, isochrone fitting. Their

[2] http://www.sdss.org/surveys/apogee-2/

metallicity distribution also indicates the radial gradient (Friel & Janes, 1993; Twarog et al., 1997). Unlike Cepheids, there are clusters with various ages from a few Myr to almost the age of the Milky Way. This makes it possible to study time evolution of the metallicity gradient (e.g. Tsujimoto et al., 2010; Jacobson et al., 2011). Recent infrared surveys have revealed a rich group of massive stellar clusters where several red supergiants are associated (Davies et al., 2012, and references therein). They seem to be preferentially found around the near- and far-side ends of the Galactic bar although the global distribution of such massive clusters in the inner part of the Milky Way remains to be concluded after more complete surveys and detailed studies are done. Surprisingly low metallicities have been reported for some of these massive clusters (Davies et al., 2009; Origlia et al., 2013, 2015), and no firm scenario to explain such low metallicities has been proposed yet.

More and more tracers like the aforementioned Cepheids and stellar clusters are being found from large-scale infrared surveys including VISTA Variables in the Via Lactea (VVV, Minniti et al. 2010) in particular. Their chemical abundances as well as radial velocities would give us new insights into the structure and evolution of (mainly inner parts of) the Milky Way. Strong foreground extinctions of many of these objects will force us to perform, relatively deep, infrared spectroscopy.

5.6.3 Observational requirements

For chemical measurements of the Cepheids and stellar clusters in the obscured parts of the disk, we here consider J-band multi-object spectroscopy with the resolving power of 3000. An advantage of using J-band spectra to measure the chemical abundances of stars is that blending of atomic lines (and molecular lines in case of cool stars) is less severe in this wavelength. Gazak et al. (2014) made a detailed simulation and found that the spectral resolution of 3000–5000 (with S/N larger than 50) is sufficient to measure the metallicity to the accuracy of ~ 0.12 dex. In contrast, a higher resolution is necessary in other wavelengths; for example, H-band spectra get crowded with a large number of molecular lines (CO and OH), and the APOGEE has the spectral resolution slightly higher than 20000.

Decreasing the spectral resolution requires increasing the signal-to-noise ratio to achieve the abundance measurement to similar accuracy if possible at all. Gazak et al. (2014) found that the required S/N is ~ 50 to measure the metallicity to ± 0.15 dex with the resolving power of 5000 while the S/N needs to be over 80 with $R = 3000$. On the other hand, they could not achieve such an accuracy with $R = 2000$. In many applications, chemical abundances accurate within 0.1–0.15 dex are necessary; for example, the spread in α abundances, [α/Fe], is 0.3 dex or smaller (Haywood et al., 2013), and the scatters around the radial metallicity gradient are around 0.15 dex for Cepheids and open clusters (Tsujimoto et al., 2010). Therefore, the resolving power of at least 3000 is required to make useful chemical measurements.

With the distances of 10 kpc and the interstellar extinctions of 2–6 mag in J (corresponding 10–30 mag in V), our targets will be distributed at around 10–18 mag for Cepheids ($M_J = -3$ to -6 mag) and red supergiants in stellar clusters ($M_J = -3$ to -7 mag). 2–4 m class telescopes can be used for brighter objects while fainter (correspondingly older, further, and/or more obscured) objects can be only observed with 8 m class telescopes. Considering the number of targets, multi-object spectroscopy with a large field of view is demanded to draw a global picture of the Milky Way disk.

Each stellar cluster at several kpc is spread within a few arc-minutes, and the field-of-view covering $5' \times 5'$, for example, is sufficient for many purposes. The number of the multi-object slits ~ 100 is also high enough. The density of Cepheids is usually not high enough to include more than one of them within the field-of-view, although there are exceptional cases such as two found in the Galactic center region (Matsunaga et al., 2011). Even if we find only one Cepheid within each field-of-view, multi-object spectroscopy will be useful to search for a possible cluster to which the Cepheid belong and to compare radial velocities, chemical abundances, and foreground extinctions of surrounding stars.

5.7 Near-IR Wide Field Narrow-band Imaging Surveys of Jets in Star Forming Region with ULTIMATE-Subaru

Tae-Soo Pyo[1]
[1] Subaru Telescope, National Astronomical Observatory of Japan

5.7.1 Introduction

Outflows from young stellar objects are found from all early stellar evolution stages from embedded Class 0 to visible young stars Class II (cf. Reipurth & Bally, 2001). Massive star forming regions show powerful outflow activities and many long and sharp irradiated jets (Reipurth et al., 1998; Bally et al., 2000). Outflow is a fossil recorded the mass-loss events from the central sources and shocks against the surrounding material. Since mid-1990s, parsec scale jets (giant HH flows) have been discovered from embedded sources (e.g., Bally & Devine, 1994) and even Class II sources (McGroarty & Ray, 2004). They have a few minute length scale ($>$ 1.8 arc-minute at 1 kpc) and the dynamic ages of several times 10^4 yrs. These large scale jets are evidence that the well collimated jet has long history and are launched at the early stellar evolution phase. Studying the parsec scale jets provides for us with a clue to understand the star formation history. To study the parsec scale jets as a whole, the wide field observation is needed. The most massive star forming regions are far from us, distance $>$ 2 kpc except Orion region. To find out the sharp and long parsec scale jets in the massive star forming region, high-angular resolution is necessary.

5.7.2 NIR narrow-band filter survey

An important characteristic of outflows is the existence of many emission lines induced by shock. In near infrared wavelength region, [Fe II] and H_2 lines are the main emission features from the outflows and jets. [Fe II] emission lines trace the partially ionized atomic jet part, while H_2 emission lines trace the molecular gas flow. These two emissions show different shock type of J-shock ([Fe II]) and C-shock (H_2). Thus they reveal different aspects of outflows and jets (e.g., Reipurth et al., 2000; Hayashi $ Pyo, 2009). Currently the survey in near-infrared region have been done and doing with broad-bands (2MASS, DEN- NIS, UKIDSS, VISTA, etc.). However, to find out the outflows or jets, the narrow-band filter (NBF) imaging is more efficient than the broad-band imaging due to continuum dilution. For a Galactic quadrant ($7° < l < 62°$, $|b| \geq 1.^{\circ}5$), UWISH2 (UKIRT Wide field Infrared Survey for H_2) project with H_2 filter (Froebrich et al., 2011) and UWIFE (UKIRT Wide Field Infrared survey for Fe^+) project with [Fe II] filter (Lee et al., 2014) were performed. Even though this region does not include many major star forming regions, they found a few hundred emission objects in this region.

The morphological and statistical studies of outflows and jets with wide field and high-angular resolution NBF imaging can give us a key on the dynamics of cloud collapse and star formation in the molecular cloud. To make complete census of jets in star forming region, both [Fe II] and H_2 survey are necessary because these two emissions complement each other. The typical scale of each parsec scale jet is within a few arc minute and will be getting smaller along with their distance from us. For the unbiased survey of the parsec scale jets in the various massive star forming regions, the wide field of view, e.g. $>$ 1°, is superb with $\sim 0.''2$ sub-arcsecond spatial resolution by GLAO.

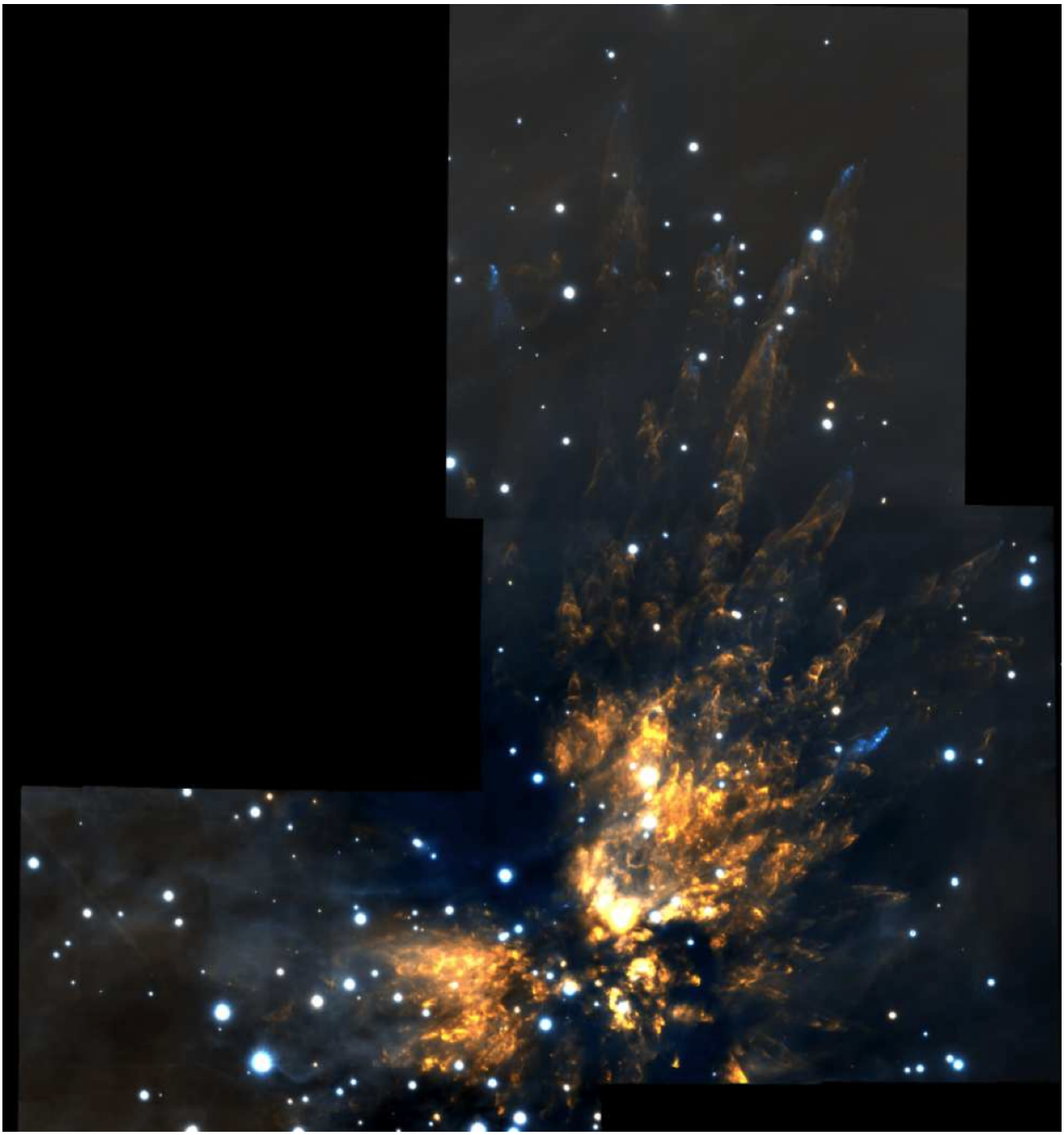

Figure 5.14: Wide field imaging of H_2 (orange) and [Fe II] (cyan) filters taken by GeMS/Gemini with AO (Bally et al., 2015). [Fe II] and H_2 show different spatial distribution. [Fe II] emissions are concentrated on the tip of bow shock fingers while H_2 emissions are widely spread with bow-shock shape.

5.8 Investigation of the Initial Mass Function at Low-mass End: Is It Uniform?

Yumiko Oasa[1]
[1] Saitama University

5.8.1 Introduction

One of the most important issues in star and planetary formation and galactic evolution is to precisely determine the initial mass function (IMF). While the "stellar" IMF is well understood by comprehensive observational studies (e.g., Salpeter 1955), whether it turns over at a certain mass and its form is universal are questions to be explored. This issue is related with stellar physics and the chemical evolution of Galaxy as well as the formation mechanism of substellar objects. It, however, remains still unclear how form and abundant very low-mass objects such as brown dwarfs and extrasolar planets and whether the formation process and statistical properties differs among various regions. At an age of order 1 Myr, substellar YSOs are three to four orders of magnitude more luminous than the field substellar-mass population at the solar age. To investigate their nature and obtain their sensitive inventory, NIR observations are most effective as follows. (1) Similar to young stellar objects (YSOs), substellar objects have an observational advantage of brightness at NIR in their early stage of evolution (Burrows et al. 1997). At an age of order 1 Myr, substellar objects are three to four orders of magnitude more luminous than the field ones at solar age of 5 Gyr. (2) Young clusters are so heavily embedded that optical surveys are not suitable for investigating young substellar-mass objects. These advantages have been used with great success to detect young substellar-mass objets by NIR photometric surverys for nearby star-forming regions (SFRs), which have NIR($H-K$ or $K-L$) excesses ascribed to the emission from the circumstellar matter (e.g. Itoh et al. 1996). Their masses estimated from the NIR luminosities and evolutionary models (e.g. Baraffe et al. 2003) are in the substellar region. Subsequent NIR spectroscopy has confirmed the reality of the **young brown dwarfs (YBDs)** from their cool temperatures (e.g. Itoh et al. 2002; Luhman et al. 2005). Further deeper NIR surveys shed light on a new type of substellar objects. They are likely **planetary-mass objects (PMOs)**, so-called **"free-floating planets"**, characterized by the masses below the deuterium-burning threshold (Burrows et al. 1997). After **the first discovery of the PMO candidates in isolation** (Oasa et al. 1999), similar objects have been detected in a few SFRs (e.g. Lucas & Roche 2000; Zapatero et al. 2000), and YBDs (and probably PMOs) appear to have disks analogous to T Tauri stars (e.g. Luhman et al. 2005). The presence of the isolated PMOs raise new questions about their formation process. There are two main scenarios about the origins of such substellar-mass objects. One proposes that they would form in situ from contracting cloud fragmentation just like low-mass stars or turbulent fragmentation (e.g. Masunaga & Inutsuka 1999; Padoan & Nordlund 2004). The other is that they would be stellar embryos ejected by the dynamical interaction of low-mass fragments from unstable multiple protostellar systems or a circumstellar disk in the early evolutionary stage (e.g. Bate et al. 2003; Stamatellos & Whitworth 2009).

Both models predict several Jupiter mass objects, but there remain significant difficulties such as the low binary property ("BD desert") and significant population of substellar YSOs with NIR excesses indicative of disks. Furthermore, it is not yet clear what they are and whether they significantly contribute to the low-mass end of the IMF. Are YBDs and PMOs ubiquitous?

With the aim of characterizing YBDs, PMOs, and their IMFs, we have been conducting an extensive photometric and spectroscopic program which consists of NIR photometry and spectroscopy with Subaru and UKIRT, within 1 kpc of the Sun. So far, we have carried out sufficiently deep JHK surveys (K limit ∼19-21 mag for about 0.1-0.9 sq. deg each) searching for substellar YSOs in the massive (Cygnus, Orion), intermediate-mass (Perseus, Serpens), and low-mass (Ophiuchi, Lupus) SFRs. **Hundreds of extremely faint YSO candidates (YBDs and PMOs) were identified with NIR excesses indicative of circumstellar disks**. Their masses estimated from a combination of the J-luminosities and the evolutionary models at the typical T Tauri age of 1 Myr (e.g. Takagi et al. 2011) are substellar.

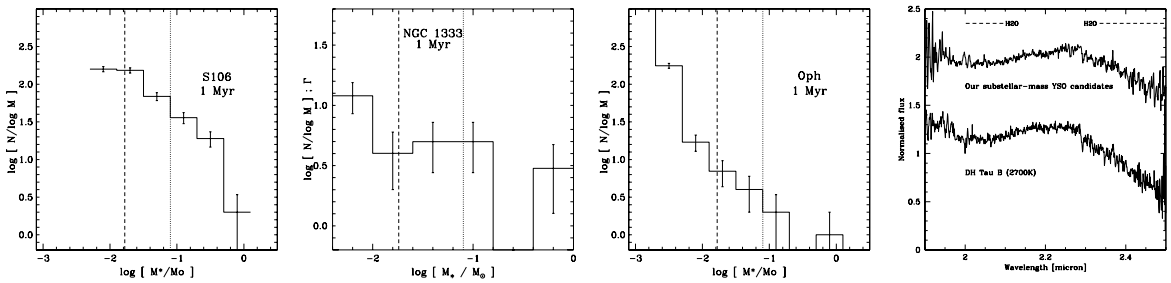

Figure 5.15: The IMFs for the low-mass YSO candidates in S106 [Left], NGC1333 [Second left], Ophiuchi [Second right] respectively, assuming age of 1 Myr (Oasa et al. 2006, Oasa et al. 2008, Oasa et al. in prep.). The vertical dotted and dashed lines denote the stellar/substellar boundary and the completeness limits, respectively. S106 is a massive SFR with O9.5V star, while NGC1333 and Ophiuchi are intermediate-mass and low-mass SFRs, respectively. [Right] K-spectra of a substellar YSO and a YBD (maybe planet) of DH Tau B, taken by Subaru/CISCO or Subaru/MOIRCS. Water absorption features around 2–2.1 and 2.3-2.5 μm indicate that they are indeed cool objects.

Unlike Trapezium (Orion) where the IMF has a turnover near 0.2 $M_\odot$ (e.g. Hillenbrand et al. 1997), the overall shape of IMFs in S106 (Cygnus), NGC1333 (Perseus), L1709 (Ophiuchi), Lupus and Serpens are **still rising down to the substellar-mass regime** (Fig. 5.15; Oasa et al. 2006, Oasa et al. 2008, Oasa et al. in prep.; Sato et al. in prep.). This is also exhibited in ρOph IMF (Marsh et al. 2010). Note that, in S106 and Serpens,**the IMFs do not appear to be universal over spatial scales of 0.9 pc and 0.6 pc**, respectively. In Serpens, deep ($J_{lim} \sim 23$ mag) survey with Subaru/MOIRCS has uncovered several hundreds of young PMO candidates and apparent dearth of YBDs in substellar IMF, even if taken into account of contaminated distant galaxies. A dearth of YBD might be also shown in Lupus IMF although their number is small compared to Serpens. Additionally, in Serpens, Lupus, and Oph, most YBDs are located in the dense cloud while PMOs exist all over the field. Comparison of the IMFs with each other and within the individual clusters (e.g. Jeffries 2012) implies that substellar IMFs may be dependent on the forming environment. If two clusters are found to have a different IMF, star formation could have been different (Kouwenhoven & Goodwin 2010). Is there any low-mass end of the IMF? Are substellar IMFs universal?

Nevertheless, it is not concluded that they are definitely substellar YSOs by JHK photometry alone as follows.
(1) Distant galaxies as well as embedded sources in the cloud were expected to be detected in deep surveys. Each source was classified as either a star or a galaxy via its morphology such as the elongation and FWHM, but some YSO candidates might be galaxies. (2) JHK photometric studies can determine the luminosity and approximate effective temperature($T_{\rm eff}$), but the mass estimate is subject to the uncertainties in the age assumption and theoretical models. Follow-up spectroscopy, one of which has been conducted with Subaru/MOIRCS, and photometry at longer wavelengths are under way for more robust determinations (Takaraha 2014; Oasa et al. in prep.).

5.8.2 Survey design: ULTIMATE wide deep JHK imaging survey and multi-object spectroscopy for young substellar-mass objects

It is now important to understand the characteristics of substellar MFs. The above works, however, have recently been demonstrated in only a part of young clusters. With the intention to address whether or not the substellar MFs are strictly universal and both YBDs and PMOs are ubiquitous in the SFRs, a larger ensemble of young clusters is needed. Here we propose NIR wide and deep photometric survey enough to detect YBDs and PMOs, which will extend these works toward distant SFRs, while the surveys

for very low-mass objects are limited within the nearby (< 1kpc) SFRs so far. Thanks to high spatial resolution and relatively wide field coverage of ULTIMATE-Subaru, which will be increased by a factor of $sim5$ compared to the present MOIRCS, we will be able to detect embedded YBDs and PMOs in the massive clusters. WFIRST will be another powerful NIR wide imager, but it will not be able to provide K-band images. ULTIMATE-Subaru is ideally suited for searching YBDs/PMOs since the JHK color selection is crucial for identifying young objects with NIR excesses, as shown above. For example, JHK photometry with J limiting mag of 25 Vega mag enables us to detect deuterium-burning limit objects with Av of 15 mag at 1Myr in the NGC 7538 cluster which is one of the massive SFRs located at ∼2.7 kpc. Further deep JHK survey (J limiting of 27 mag) will allow us to detect massive YBDs with Av of 20 at W51 which is one of the most luminous star-forming complexes in our Galaxy. The environment here is rich in newly-forming massive stars, compact HII regions, and molecular clouds located at ∼ 7.5 kpc. With ULTIMATE-Subaru deep survey, we will obtain more robust statistics on the substellar IMFs.

In addition, we would like to conduct follow-up multi-object NIR spectroscopy for them. The spectroscopy yields their $T_{\rm eff}$ and hence mass. ULTIMATE-Subaru multi-object spectroscopy will be ideal for our purpose as it allows to take HK spectra for large number of objects simultaneously, similar to MOIRCS and MOSFIRE.

NIR spectra of substellar objects with $T_{\rm eff} \lesssim 3000$ K are expected to be dominated by deep water absorption bands. Water bands are highly temperature sensitive, increasing in strength with decreasing $T_{\rm eff}$ down to the coolest L dwarfs. Thus, **the strength of the water bands allows the measurement of $T_{\rm eff}$ from low S/N spectra.** At the same time, however, water absorption features are sensitive to gravity at low temperature where dust formation is an added complication (e.g. Allard et al. 2001). This is also presented by the spectra of a YBD (maybe a planet), DH Tau B in Fig. 5.15 (Itoh et al. 2005). Since our YSO candidatess have unknown gravity and hence age, which is mostly considered to be lower than dwarfs and higher than giants (Takagi et al. 2011), their $T_{\rm eff}$ could be derived using a relationship of water absorption with $T_{\rm eff}$ intermediate between those of dwarfs and giants. Additional spectral features such as metalic lines are required to more precisely determine $T_{\rm eff}$. According to Itoh et al. (2002), metallic absorption lines such as Ca, Na, K, are good indicators of $T_{\rm eff}$ for cool objects. We will also compare the wide wavelength spectra with the synthesized spectra (Tsuji et al. 2004). Based on our previous studies, the uncertainty is estimated to be ±100 K or 0.01 $M_\odot$ for YBDs. Armed with our estimate of $T_{\rm eff}$ and photospheric luminosity from combining spectroscopy and our previous photometry, we will place these YBDs and PMOs in an H-R diagram to characterize the mass and age in detail. As a first approach, we have conducted NIR multi-slit spectroscopy for more than 100 YSO candidates in S106 using Subaru/MOIRCS. Most of them appear to have water absorption similar to DH Tau B with $T_{\rm eff}$ ∼2700K and $\log(g)$ ∼4.0 (Fig. 5.15). It has succeeded in obtaining spectroscopic mass for dozens of substellar YSOs (Takaraha 2014). ULTIMATE-Subaru will provide us many more HK spectra for YBDs and PMOs in distant clusters. Furthermore, most of faint YBD and PMO candidates in SFRs are clustered in the relatively small field, so it can be carried out only by ULTIMATE-Subaru.

To investigate the environmental differences in IMFs, we would like to perform ALMA observations which have high spatial resolution comparable to ULTIMATE-Subaru. It will allow us to detect very low-mass cloud clump where YBDs and PMOs might be formed. To construct "clump" MF in SFRs with ALMA is complementary to the "stellar" IMF study with ULTIMATE-Subaru.

Our aim is to investigate the census and physical characteristics of the substellar YSOs through ULTIMATE-Subaru JHK wide deep photometric survey and multi-object spectroscopy. This study will enable us to determine the substellar IMFs for young clusters, to examine the claims of non-universality and to search possible environmental dependence of IMFs. Finally, we aim to find what is a key property for controlling IMFs.

Chapter 6

Adaptive Optics

6.1 NgAO Performance Simulation

Olivier Lai[1], Shin Oya[1,2], Christophe Clergeon[1], Yutaka Hayano[1,2]
[1] Subaru Telescope, National Astronomical Observatory of Japan
[2] TMT Japan project office, National Astronomical Observatory of Japan

6.1.1 Atmospheric turbulence profile at Maunakea

Maunakea is an astronomical site well known for its excellent seeing. However in the past decade it has also been identified as an excellent site for Ground Layer Adaptive Optics (GLAO) due to the very thin ground layer and relatively small contribution of the free atmosphere. The performance of GLAO depends crucially on the structure of the atmospheric turbulence profile. The size of the compensated field of view and the uniformity of the delivered PSF over the field depend on the thickness of the boundary layer, while the overall degree of improvement depends sensitively on the ratio of aberrations in the boundary layer to those in the free atmosphere. Tokovinin et al, (2005) found a median free atmosphere seeing of 0.37″ and median ground layer seeing of 0.29″ and 0.44″ using a SciDAR and a MASS/DIMM respectively.

An in-depth study of the turbulence profile was studied extensively for the TMT site study at the site 13N on Maunakea by Schöck et al, (2009), Els et al, (2009).

This turbulence profile was adapted by Andersen et al, (20012) to serve as input to the MOAO RAVEN demonstrator simulations. Image quality measurement from Subaru Observatory were combined with the MASS and DIMM measurements to estimate the boundary layer and dome seeing specific to the Subaru telescope. This was achieved by matching the free atmosphere, as well as the integrated seeing of both sites by adjusting the ground layer contribution at Subaru Telescope. The results are shown in table 6.1 and served as the basis for the simulations carried out by Oya et al, (2012) for ULTIMATE Subaru using the `MAOS` simulation package.

Another turbulence profiling campaign was carried out by Chun et al, (2009) on the Eastern ridge of Maunakea. This study combined the results of SLOpe Detection And Ranging (SLODAR), with the LOw-LAyer Scintillation (LOLAS) instruments installed on the roof of the UH88" telescope. The latter was capable of providing very high resolution profiles indicating that the boundary layer is very thin and most of the turbulence is confined to the first 70m. This turbulence profile was used in another set of independent simulations using `instant_GLAO` and is shown in table 6.2.

The highest altitude of this model is too low to match the MASS profiles but it was set due to constraints in the simulations. Also, this model has a much finer resolution close to the ground, as can be seen from figure 6.1. The relevant height of turbulence that can be corrected by a GLAO system is called the *gray zone* (Tokovinin (2004)) and is equal to $H_{max} \sim \lambda/(\beta\theta_0)$, where λ is the imaging wavelength,

Table 6.1: Model atmospheric turbulence profile used in simulations

Percentile seeing	25%-ile (good)	50%-ile (median)	75%-ile (bad)	speed	Direction
height (km)	fractional contribution			wind	
0.0	0.6823	0.5960	0.4971	5.6m/s	0°
0.5	0.0611	0.0963	0.1382	5.77m/s	50°
1.0	0.0212	0.0325	0.0577	6.25m/s	100°
2.0	0.0172	0.0869	0.0642	7.57m/s	150°
4.0	0.0757	0.0869	0.0833	13.31m/s	200°
8.0	0.0486	0.0684	0.0895	19.06m/s	250°
16.0	0.0939	0.0826	0.0700	12.14m/s	300°
FWHM	0.53″	0.66″	0.85″		
r_0	19.4cm	15.6cm	12.1cm		

Note: FWHM and r_0 are defined at 0.5μm.

Table 6.2: Atmospheric turbulence profile measured on UH88″ roof

height (m)	fractional contribution
0	0.295
15	0.141
30	0.039
90	0.020
270 ...	0.024
1000 ..	0.029
3000 ..	0.191
FWHM	0.65″
r_0	15.2cm

Note: FWHM and r_0 are defined at 0.5μm.

β is the FWHM resolution, and θ_0 is the half angle of the considered field of view. In the case of ULTIMATE-Subaru with $\theta_0 = 7'$, $\lambda = 1.6\mu$m and $\beta = 0.2''$, we find that $H_{max} \sim 800m$. This means that turbulence below 800 meters will be corrected by the DM, and will but will be largely uncorrected above this altitude. Tokovinin (2004) prescribes a vertical resolution of the turbulence profile to be at least on the order of $H_{min} = d/(2\theta_0)$, where d is the deformable mirror's projected actuator spacing. Considering a 16×16 system, we find H_{min} to be on the order of 120 meters, in between the two models. Nevertheless, it can be seen on figure 6.1 that the majority of the turbulence is well below H_{max} for the 13N data. The point at 3000m on the East Ridge data may also be misleading, since it is the highest we can include in the simulations, but is intended to represent the free atmosphere, i.e. we assume that by that altitude, the wavefronts have become sufficiently decorrelated to be representative.

A further step to improve the simulations could be to attempt to merge these models, although doing so would require many assumptions on the effects of local topography; also increasing the number of layers in the model atmosphere becomes computationally intensive. Another step is to carry out measurements from within the Subaru dome, to be able to improve the modeling of dome seeing. This was carried out by Oya (2015) using both a lunar scintillometer (PTP2) and a Surface layer NOn-Doppler Acoustic Radar (SNODAR). These results, shown in figure 6.2 are highly promising but have not been included in the GLAO simulations.

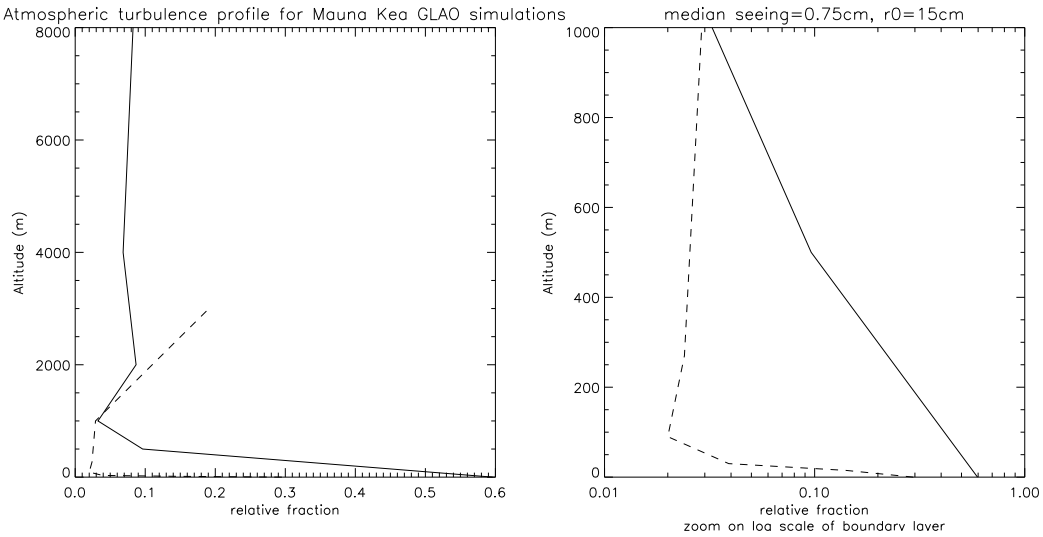

Figure 6.1: Maunakea turbulence profiles used in simulations of GLAO. Thin full lines, 13N measurements adapted to Subaru telescope, thick dashed line: East Ridge SloDAR and LOLAS measurement campaign. the figure on the right shows a log-scale zoom of the boundary layer which appears to be very thin.

6.1.2 GLAO performance

Extensive GLAO performance simulations have been conducted by Oya et al, (2012, 2014), using the `MAOS` simulation package[1]. The performance of MAOS for GLAO was evaluated by comparing the results with those of the "Gemini Ground Layer Feasibility Report", wherein (Appendix F1.) 5 codes independent codes are compared using the Cerro Pachon turbulence profile. The results were found to be in excellent agreement and validated the use of MAOS for the ULTIMATE-Subaru study. It should be noted that the seeing limited FWHM was found to be smaller than that expected for a given r_0 most likely due to the finite size of the phase screens, but this effect was corrected for.

By using the good, median and bad seeing cases for the ground layer and the free atmosphere, these simulations allow to predict the cumulative probability distribution of the GLAO performance as a function of input seeing cumulative probability distribution, shown in figure 6.3, as well as the gain in ensquared energy. It should be noted that not only does the FWHM improve to the $0.2''$ level in the near infrared, but it is also more stable in time. If we define the stability as the standard deviation/average, then we find it is improved from $2 \sim 10\%$ in the seeing limited case to $1 \sim 7\%$ in the GLAO case. The gain in ensquared energy is between 1.5 and 2 depending on the box size, the wavelength and the seeing conditions, figure 6.4.

The system size was optimized taking into account the constraints of the adaptive secondary mirror: a 32×32 deformable mirror was conjugated to -80m. The reconstruction was achieved by averaging the measurements of four sodium laser guide stars of magnitude 10 on a $15'$ diameter. The tip-tilt and focus were obtained from four natural guide star of magnitude 18 also on a $15'$ diameter ring. Sky coverage, zenith angle and seasonal variations were also studied. Based on a comparison of the seasonal variation between the site 13N and the Subaru Telescope image quality, it was possible to estimateGLAO seasonal variations, due to the preponderance of Ground layer turbulence at certain times of year. Finally, we note in passing that the RAVEN MOAO demonstrator confirmed the GLAO simulation results during its commissioning.

Independent simulations were carried out by Lai et al, (2008, 2010) using another simulation package specifically developed for very wide field GLAO.

[1]MAOS is developed by L. Wang, L. Gilles and B. Ellerbroek and is available at https://github.com/lianqiw/maos/

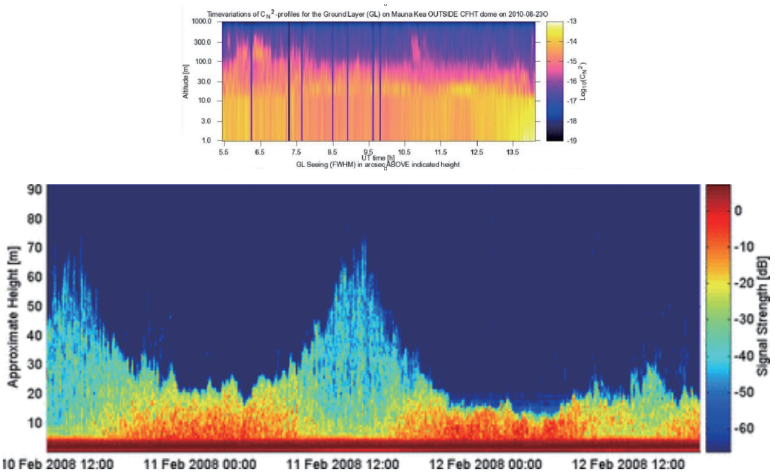

Figure 6.2: High resolution turbulence profiles obtained at or around Subaru Telescope. Top: Lunar SHABAR, PTP2 in Collaboration with University of Victoria. Bottom: Acoustic sounding SNODAR, in collaboration with University of New South Wales.

6.1.3 MOAO performance

In this section, we summarized a performance simulation of MOAO system at Subaru Telescope using 6 LGSs. MOAO can provide higher Strehl ratio than GLAO, so that the maximum extent of field of regards is a major criteria of this study. MOAO compensates the atmospheric turbulence effect only the direction of astronomical target, not the entire area of field of regards. We found that MOAO within the area of $3'$ radius achieve better correction than GLAO using 6 LGSs. The performance of MOAO is reduced at the correction level of GLAO when the 6 LGSs are located wider than $3'$ radius. Also the separation of tip-tilt guide stars is closely related to the residual error of tip-tilt wavefront error.

Configuration of MOAO performance simulation

We use a simulation software code, named MAOS. The atmospheric model is identical to the median seeing condition what we used in the performance simulation for GLAO. The brightness of the laser guide stars and tip-tilt guide stars are bright enough so that there is no performance degradation due to the photon noise. We assumed the height of the sodium layer is 90 km.

Figure 6.6 shows the constellation of guide stars. The upper chart shows the location of natural guide star for tip-tilt sensing, while the lower chart shows the location of laser guide stars. We simplified the location of the natural guide stars is on the corner of triangle, which is not true in reality. At the center and the corner of pentagon are the location of laser guide stars. The performance of MOAO is strongly related the overlapped area of meta pupil at the highest atmospheric layer at around 10 to 12 km. The area of meta pupil is colored in blue circles for natural guide stars and in orange circles for laser guide stars. As you see, the separation of each guide stars are increased from left to right. Here we label each configuration from left to right by numbers from (1) to (5). The blank circle of green doughnut-shape shows the size of the aperture of 8m-diameter telescope. The outer edge of the green doughnut-shape is matched to the range of optical path for 8m telescope with $300''$ radius of field of view. It is important to cover this green area by the meta pupil to ensure the good performance of MOAO for any direction within the FoR. For example, the performance of MOAO is expected to be good for the configuration (1) and (2), however, the performance starts degrade for the configuration (3) or later.

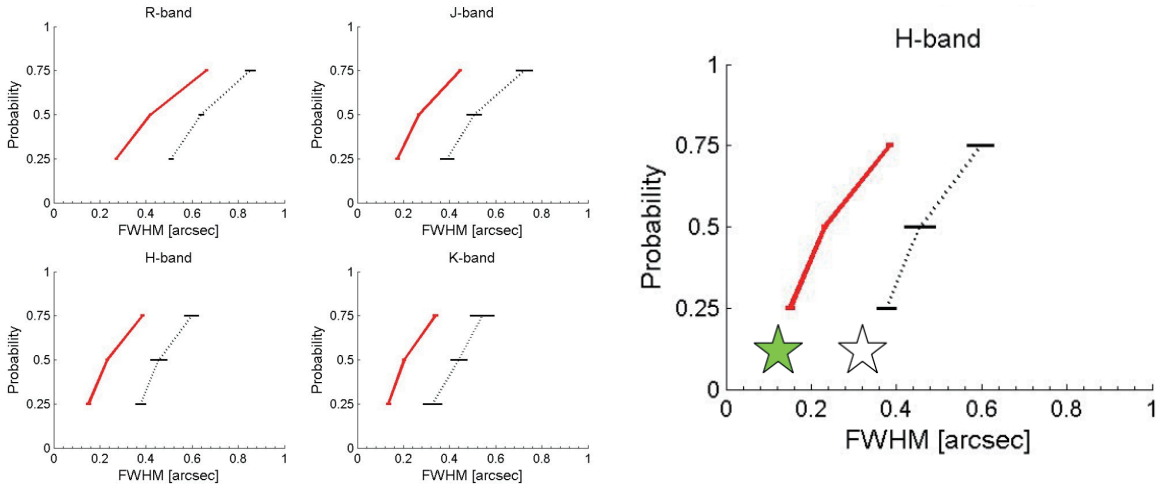

Figure 6.3: Left: Improvement of the seeing probability distribution (dotted line) to GLAO performance probability distribution (red line). The error bars are the standard deviation along the time axis. Right: confirmation of simulation results by Raven used in GLAO mode: the white star shows the result of no correction while the green star is the result of RAVEN.

Result of MOAO performance simulation

We plot the wavefront error in Fig. 6.7. Total wavefront error is shown in filled square. Cross mark shows a tip-tilt wavefront error from natural guide star and open square shows a high-order wavefront error from laser guide star. Plots from upper left to lower right correspond the guide star constellation, which is shown in Figure 6.6 from left to right. The horizontal axis shows a distance from the center of field of view, which starts from the bottom to the top of the guide star constellation shown in Figure 6.6. Three natural guide stars lies at the vertical dash line in triangle, and five laser guide stars at the vertical doted line in pentagon. The horizontal lines at the wavefront error of 350nm and 240nm are equivalent to the Strehl Ratio of 0.4 and 0.2 at K band, respectively. The wavefront error become minimum at the center and positive side of dotted line, where the laser guide star resides. High-order wavefront error increases with larger separation of each guide star. This degradation in performance for wider constellation of laser guide star is caused by the increase of uncovered area by the laser guide star especially at the higher altitude. (See Figure 6.6.) Further, the tip-tilt wavefront error increases in the same manner, because of the large separation of natural guide stars. Tip-tilt wavefront error is smaller than the high-order wavefront error for compact guide star constellation. Both tip-tilt and high-order wavefront errors becomes equivalent at the guide star constellation of (3).

The more practical measures of MOAO performance in observation are Strehl ratio and ensquared energy rather than wavefront error. Strehl ratios are plotted in Figure 6.8. The cross, open square and filled square indicate J band, H band and K band respectively. The values of Strehl ratio are calculated from simulated image of point source, which are consistent with estimated Strehl ratio derived from the wavefront error.

Ensquared energy within the area size of $0.12'' \times 0.12''$ and $0.24'' \times 0.24''$ are plotted in FIgure 6.9 and Figure 6.10. Ensquared energy within $0.12'' \times 0.12''$ is rapidly reduced for the wider constellation of guide stars. When we require the minimum ensquared energy as 50%, the field of regards (FoR) is limited by $60''$ in radius. On the other hand, ensquared energy within $0.24'' \times 0.24''$ is not drastically reduced at wide guide star constellation. The tolerance in reduction of ensnared energy at larger area size is interpreted as follows. The major degradation of wavefront error is caused by the tip-tilt wavefront error due to the wider guide star constellation, not caused by high-order wavefront error. Thus the energy in jittered core of point spread function (PSF) can easily captured by enlarging the area size, while the energy in halo

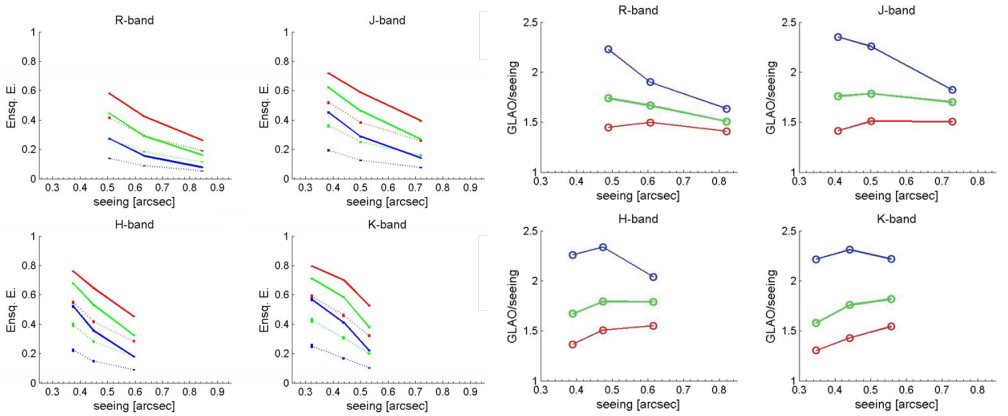

Figure 6.4: Left: comparison of ensquared energy in boxes of 0.24″ (Blue), 0.36″ (Green) and 0.48″ (Red). Solid lines show GLAO performance and dotted line are seeing limited. Right: the ratio of ensquared energy in Seeing conditions over GLAO correction. showing a gain of 0.15 to 2 is possible.

of PSF contributed by high-order wavefront error does not so much change.

Here is a brief summary of MOAO performance simulation. The performance changes by the separation of guide stars. For compact guide star constellation, high-order wavefront error is dominant, which is about 200nm within the field of regards almost uniformly. When the separation of guide stars becomes as large as 100″, tip-tilt wavefront error is equivalent to high-order wavefront error. The more increasing the separation of guide star, the larger high-order wavefront error within the guide star constellation. And gradually the performance of MOAO approaches to that of GLAO, while the separation of guide star increases. The performance of MOAO and GLAO has no difference when the radius of constellation is greater than 3′. Thus, MOAO has no advantage over GLAO anymore. Under this configuration, the ensquared energy within 0.24″ × 0.24″ is estimated as 30∼50%.

Summary

The maximum radius of constellation of six guide stars, one is at the center and others at the corner of pentagon, is 3′. There is no advantage over GLAO wider than 33′ in radius of field of regards. Additionally, we need enough number and density of natural guide stars within the field of regards, otherwise the tip-tilt wavefront error degrade the performance. However, the ensquared energy within the larger area size, such as 0.24″ square, does not so much affect by the increase of tip-tilt wavefront error, which broadens the core size by jitter but not so much energy is scattered to the halo of PSF.

6.1.4 Trade off system study for Subaru NgAO

The first and second generation adaptive optics at Subaru Telescope are the combination of bimorph deformable and curvature wavefront sensor. The first generation AO at Subaru Telescope, AO36, uses only the single natural guide star. The second generation AO, AO188, added one sodium laser guide star to expand the sky coverage. These are single conjugate AOs. For the next generation AO at Subaru Telescope has to pursue tomography AO, using multiple guide stars and wavefront sensors. Tomography AO is categorized in four basic AO systems, LTAO (Laser tomography AO), MCAO (Multi-Conjugate AO), MOAO (Multi-Object AO) and GLAO(Ground Layer AO). (See Figure 6.11.)

LTAO shown in upper left of Figure 6.11 is aimed to cover the uncovered atmospheric turbulence layer due to the cone effect of laser guide star. For this purpose, several laser guide stars are created in some constellation pattern. One or more natural guide stars is necessary to compensates the tip-tilt and

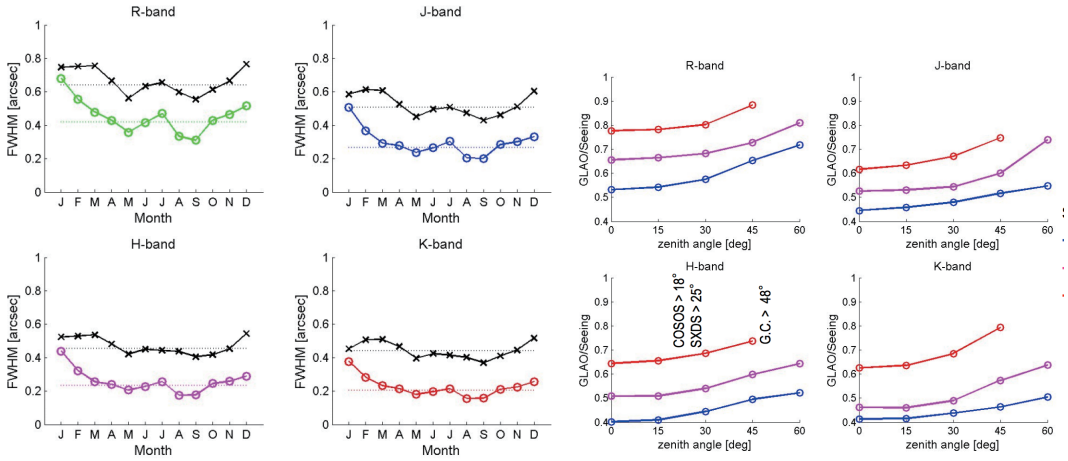

Figure 6.5: Left: Seasonal variations of GLAO performance at R, J, H and K wavelengths. Right: Zenith dependence of GLAO correction given in arcseconds versus zenith angle; blue is for good seeing, magenta for median seeing and red for poor seeing.

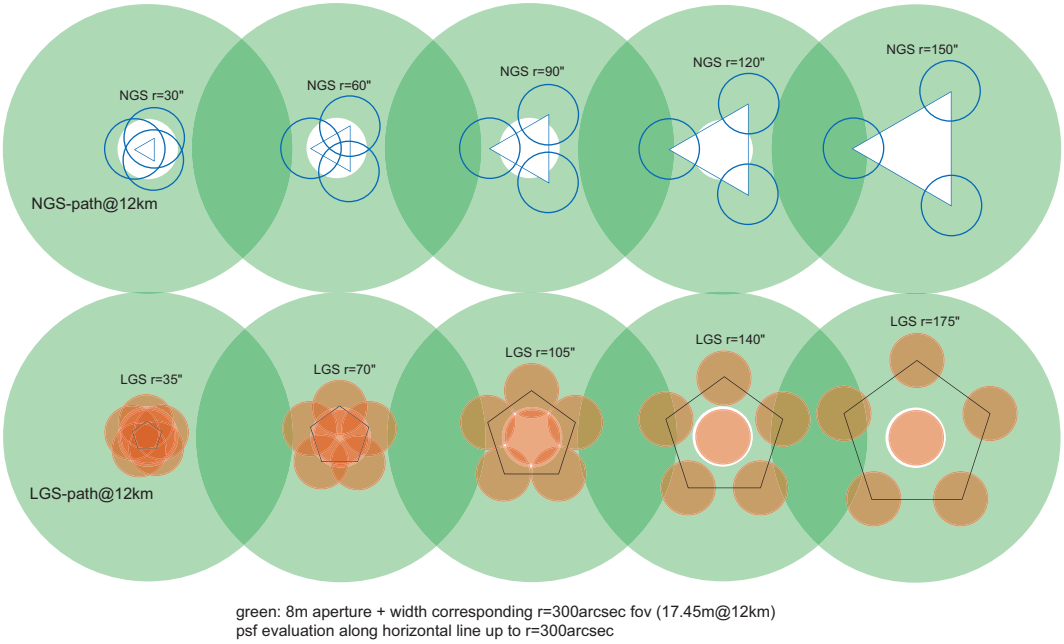

Figure 6.6: Constellation of natural guide stars (above) and laser guide stars (below).

focus. Adaptive optics in visible targeted to higher Strehl ratio requires LTAO technique. The purpose of MCAO, shown in upper right, is to obtain uniform PSF at certain Strehl ratio within entire field of view. Atmospheric turbulence from the ground to upper atmosphere is estimated by multiple laser guide stars and wavefront sensors. Two or more deformable mirrors, which are conjugated to several altitude in the atmosphere, compensate each wavefront errors. Figure 6.11 represents two-layered MCAO. One layer is conjugated in ground and another layer is in the middle altitude of atmosphere. The increase of number of guide stars, wavefront sensors and deformable mirrors improve the performance of AO and covered field of view. There is one on-sky MCAO system at Gemini South, named GeMS, which covers 87″ square

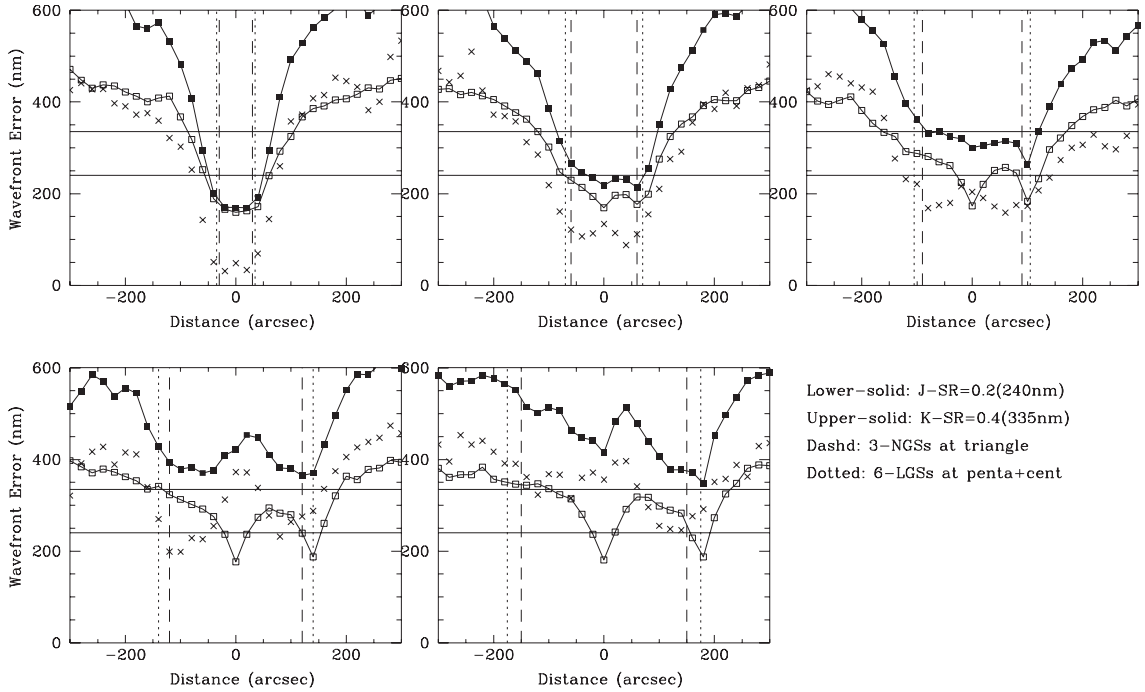

Figure 6.7: Wavefront error of MOAO performance simulation. Filled square, open square and cross mark indicates the total wavefront error, high-order wavefront error and tip-tilt wavefront error, respectively. Plots from upper left to lower right correspond the guide star constellation, which is shown in Figure 6.6 from left to right.

field of view at moderate Strehl ratio around 0.2 to 0.4. Five laser guide stars are configured in diamond shape with center by 2′. MCAO with larger field of view, such as more than 5′, is theoretically feasible, however, it is not realistic to build more than 10 laser guide stars and wavefront sensors. Lower left of Figure 6.11 shows GLAO. System configuration of laser guide stars and wavefront sensors are similar to MCAO, however, only the turbulence near the ground, which is considered that the half of the turbulence power is included, is estimated and compensated. The biggest advantage of GLAO is the capability of expanding the field of view in the order of 1 degree, since the turbulence at the ground layer is common to all direction on the sky. Unique characteristics of MOAO at the lower right in the Figure 6.11 is an open loop AO system. Estimation of atmospheric turbulence from the ground to upper atmosphere is common with MCAO, LTAO, however, atmospheric compensation is performed only for targeted objects one by one. Therefore, no deformable mirror is placed in the optical path of wavefront sensors, so that the wavefront sensor of MOAO measures uncorrected wavefront, not corrected wavefront by deformable mirror.

Characteristics of tomography AOs are summarized in Figure 6.12 and Table 6.3.

Subaru Telescope is famous and has strength of having prime focus wide field camera and spectrograph in visible and near infrared. Thus, wide field AO and near infrared instrument has enormous synergy with these prime focus instrument. The first target of next generation AO at Subaru Telescope is GLAO for this reason. The strawman basic specifications of GLAO are shown in Table 6.4

The field of view of science instrument has to be at least 15′ in diameter. Outside of the field of view for instrument, four laser guide stars are configured. Patrol field for natural guide star is in the science field of view. Shack-Hartmann wavefront sensors are used for laser guide star. The wavefront sensor type for tip-tilt and focus sensing by natural guide star is still open. Basically we use 2×2 Shack-Hartman sensor, but there would be an option to use pyramid wavefront sensor. Considering the sky coverage of natural guide star, near infrared wavefront sensor is an alternative solution worth investigating further.

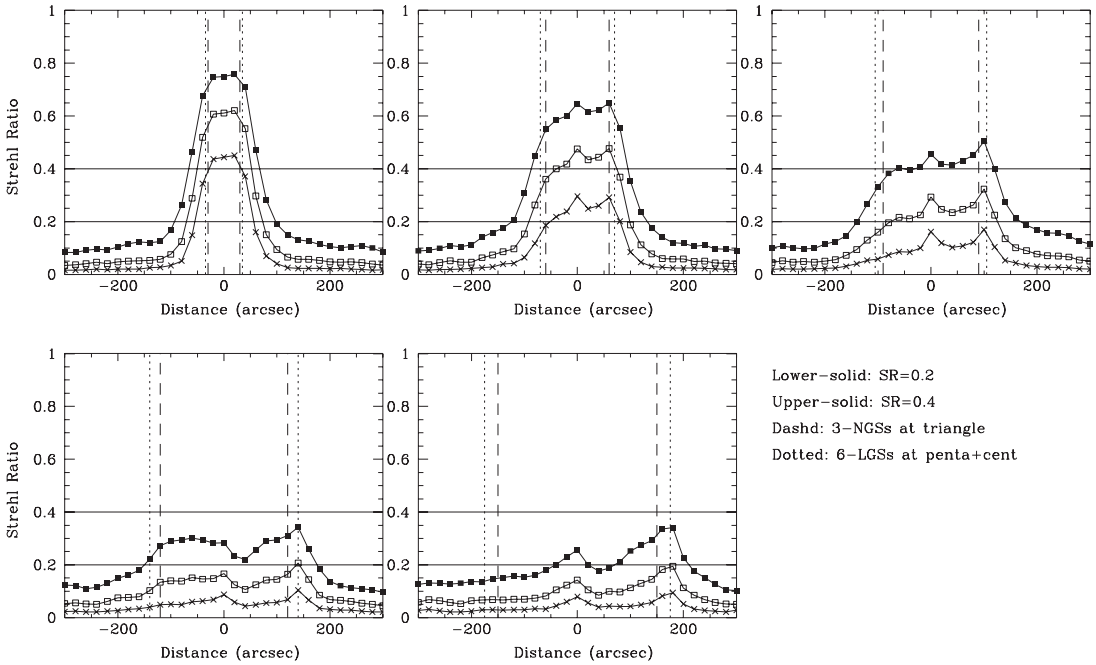

Figure 6.8: Plot of Strehl ratio. The cross, open square and filled square indicate J band, H band and K band respectively.

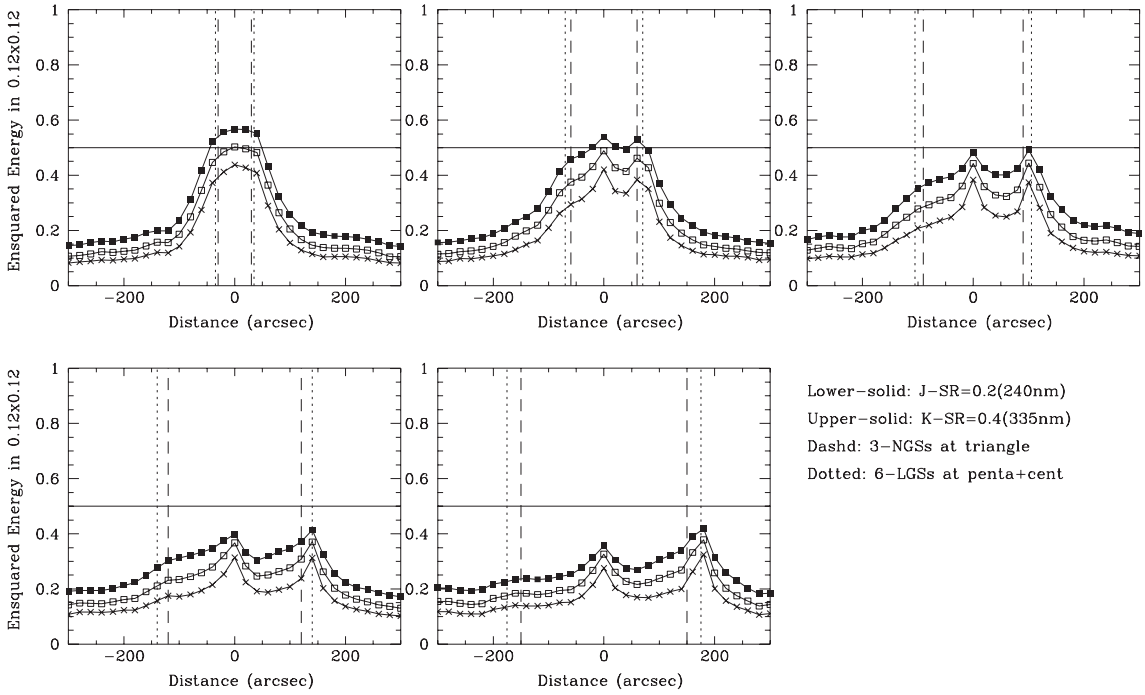

Figure 6.9: Ensquared energy within $0.12'' \times 0.12''$. Symbols are identical in the Figure 6.8.

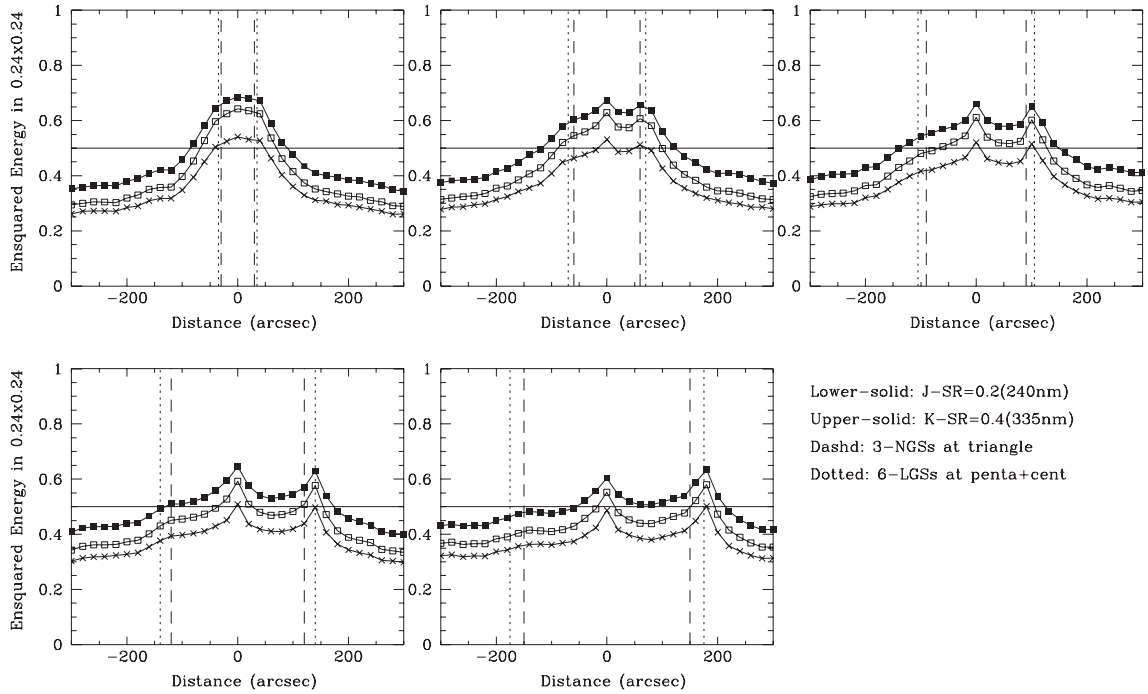

Figure 6.10: Ensquared energy within $0.24'' \times 0.24''$. Symbols are identical in the Figure 6.8.

Our GLAO simulation shows that the number of subapertures is enough as 100, but it is worth investigate feasibility to increase the number of subapertures. In order to take full advantage of GLAO, adaptive secondary mirror is mandatory. Refer to the adaptive secondary mirror for VLT, the number of actuators are around 1000. Although GLAO is our main target for next generation AO at Subaru Telescope, LTAO or Extreme AO can be operated without any large modification.

6.1.5 Complementary AO mode

The adaptive secondary mirror is a most critical component for Subaru GLAO system. The advantages of higher throughput and less thermal emissivity due to the less number of optical surfaces are greatly important, even though the conjugation plane of adaptive secondary mirror is below the ground. Mis-conjugation from the ground layer causes a limited corrected field of view. It becomes critical for smaller aperture telescope, however, 8 to 10m class telescopes are not so much effect on mis-conjugation.

On the other hand, adaptive secondary mirror can be used the other AO mode, such as LTAO, single conjugate AO (SCAO), ExAO, MCAO and MOAO. Moreover, not only the Cassegrain focus, but the

Type of AO	LTAO	MCAO	GLAO	MOAO
Laser guide stars	3∼5	3∼5	3∼5	3∼5
Natural guide stars	3	3	3	3∼6
Deformable mirrors	1 or 3	2∼3	1	5∼20
Strehl ratio	>0.4	>0.4	>0.05	>0.4
FWHM	Diffraction limited	Diffraction limited	$0.2''$–$0.3''$	Diffraction limited
Field of view	$< 30''$	$\sim 2'$	$10'$	$5'$

Table 6.3: Comparison of tomography AO

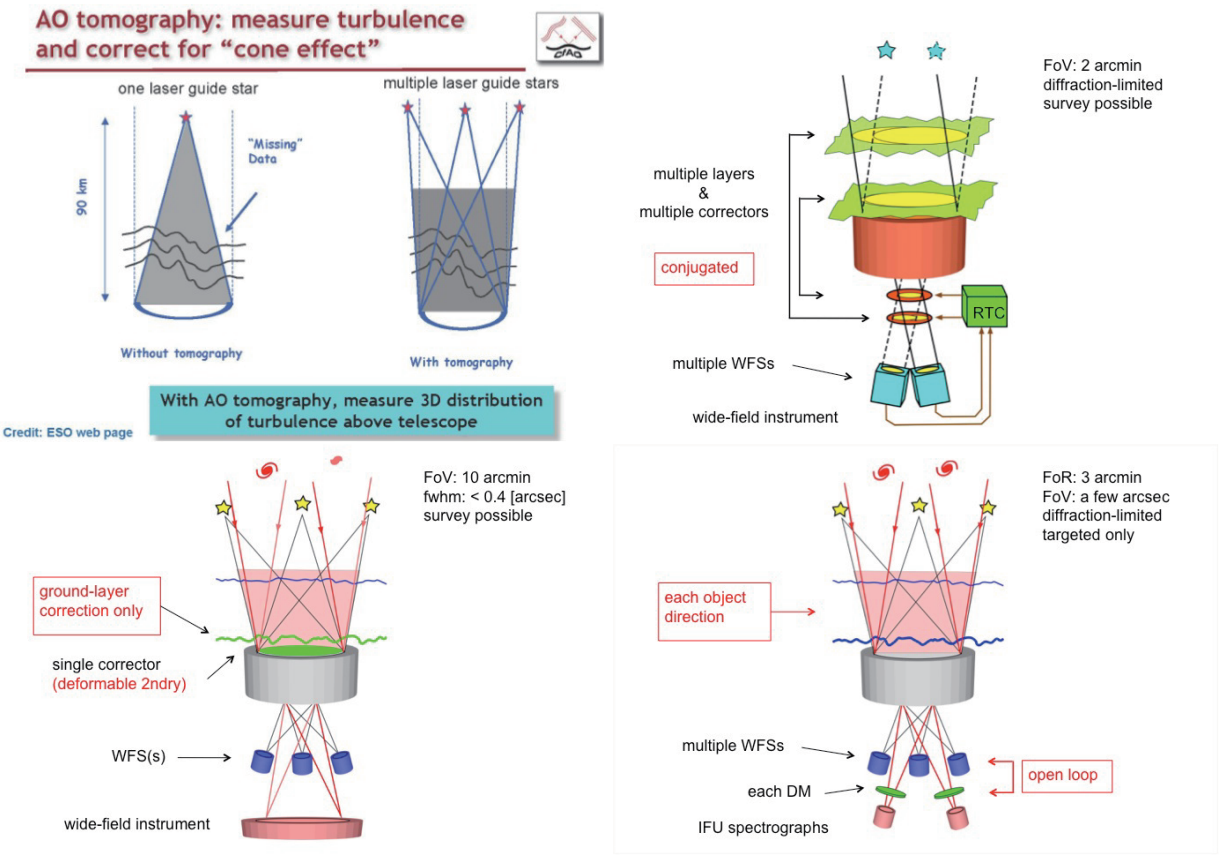

Figure 6.11: LTAO (upper left)、MCAO (upper right), GLAO (lower left), MOAO (lower right). (slide from Center for AO, Workshop on next generation AO, Oya's presentation.)

Nasmyth foci on both sides are fed by the AO corrected wavefront by adaptive secondary mirror. Once we install the wavefront sensor by modifying auto guider unit, AO corrected image can be provided at all foci of Subaru Telescope.

LTAO or SCAO is targeted for diffraction limited AO correction on axis or very narrow field of view, however, it is a very attractive telescope capability to build a new narrow field of view instrument in near infrared as well as optical wavelength. There is a merit to add about 1000 element adaptive secondary mirror to the existing extreme AO system, SCExAO, at Nasmyth platform and following instruments.

The configuration of MCAO with adaptive secondary mirror has several solution, compared to the conventional MCAO system. As usual of MCAO, all wavefront sensors can be placed after the second deformable mirror, which is conjugated at the higher altitude, but there is a possibility to pick off the guide star before the second deformable mirror. The ground layer turbulence can be controlled in closed loop, however, the upper layer turbulence is corrected in open loop. This has also have a merit that it is not necessary to put large dichroic mirror at the science path to feed the light into the wavefront sensor. Then, optical design becomes more simple and higher throughput is achievable. Further system analysis of modified MCAO is required, though, drawbacks of conventional MCAO are overcome. Similar to MCAO, there are MOAO with adaptive secondary mirror has flexibility to modify the configuration from original MOAO system. All wavefront sensors measure the partially corrected wavefront by adaptive secondary mirror. There are some options of correction mode of adaptive secondary mirror. One is a usual GLAO correction by adaptive secondary mirror. Uncorrected upper atmospheric turbulence is corrected by AO module for each targeted object. Other is a tweeter-like function by adaptive secondary

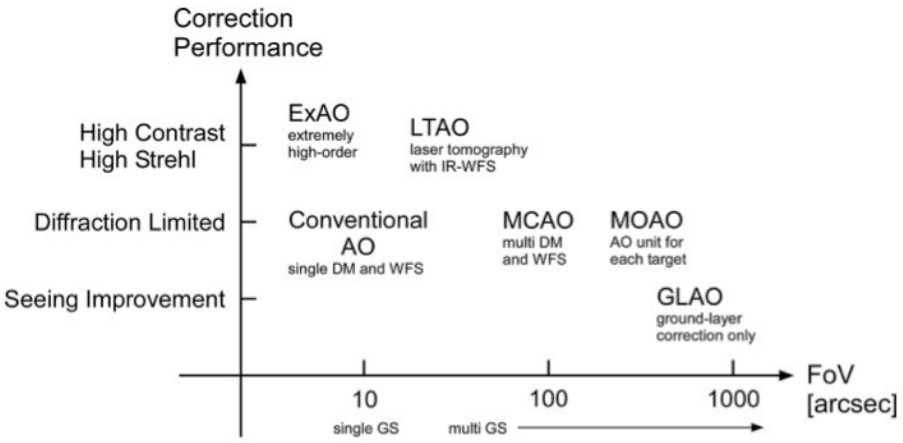

Figure 6.12: Various types of AO system. Horizontal axis shows the field of view (FoV) and vertical axis shows correction performance (Streahl Ratio). Conventional AO is placed lower left. Advanced AO system, such as LTAO, MCAO, MOAO and GLAO are moved toward right or upper of the chart. (Workshop on next generation AO taken by Oya's presentation)

Item	Specification
Guide stars	4 LGS, NGS(2∼4)
Location of guide stars	The edge of FoV $> 15'$ (LGS), Within the FoV (NGS)
Wavefront sensors	Each guide stars (Guide star oriented)
Wavefront sensor type	Shack-Hartmann
Tip-tilt wavefront sensor type	2×2 Shack-Hartmann wavefront sensor or pyramid. (visible or NIR)
Sub apertures	> 100
Frame rate of wavefront sensor	> 500Hz
Deformable mirror	Adaptive secondary mirror
Actuators	∼1000
AO control type	GLAO (LTAO, ExAO modes)

Table 6.4: Basic specification of next generation AO at Subaru Telescope.

mirror. The number of actuator of adaptive secondary mirror is about 1000, it can be used as a tweeter. Then low-order correction is made by each AO module. Thus, the number of actuator of deformable mirror of AO module can be minimized to reduce the complexity, size, weight and beam size.

Consequently, the adaptive secondary mirror expands the possibility for all AO modes on the telescope, stimulates new ideas of AO system and provide new concepts of instruments. Therefore, the adaptive secondary mirror is one of the most important infrastructure of 8m-class telescope in the era of ELT.

6.2 System Modeling of NgAO at Subaru

Yutaka Hayano[1,2], Olivier Lai[1], Shin Oya[2], Christophe Clergeon[1]
[1] Subaru Telescope, National Astronomical Observatory of Japan
[2] TMT Japan project office, National Astronomical Observatory of Japan

6.2.1 Field of view analysis

Current FoV of Cassegrain focus is about 8 arcmin. This is mainly defined by the limited clear optical path of atmospheric dispersion corrector (ADC). At the bottom part of the telescope, we have what we call Cassegrain flange, in which the ADC, slit viewer, calibration light source, auto-guider and Shack-Hartmann camera for primary mirror analysis are stacked in layered unit. (See Fig. 6.13.) The wavefront sensors for LGSs and tip-tilt and focus NGSs have to be located inside the Cassegrain flange, so most of the existing units and components must be removed or modified. Practically, the ADC has to be removed. Thus Cassegrain instruments in optical wavelength have to be survive without ADC. Slit viewer is also be removed, because we will not use single slit instruments any more. Calibration light source may have to be modified for new near-infrared instruments. Current auto-guider and Shack-Hartmnann sensor are decommissioned. Both function will be taken over by new wavefront sensors. We expect that these modification to enlarge the field of view of Cassegrain focus results in having about 16 arcmin FoV in diameter.

One of the wavefront sensor has to inherit a function of auto-guider and a Shack-Hartmann sensor for primary mirror analysis. Based on the function of auto-guider, tip-tilt and focus wavefront sensor for natural guide stars are well fit. On the other hand, a Shack-Hartmann wavefront sensor for laser guide star will be used for primary mirror analysis. Therefore, the patrol field of regard (FoR) of these wavefront sensor should cover the optical axis of Cassegrain focus, the outside of FoV of other Cassegrain instrument, and FoR of LGSs or tip-tilt and focus NGSs.

Additionally, the baffle at tertiary mirror unit, the exchange mechanism of two tertiary mirrors for two Nasmyth foci also restrict the FoV. Our vignetting analysis shows that we can obtain clear FoV about 12 $\times$ 14 arcmin^2, if we use existing tertiary mirror unit and baffle. (See Fig. 6.14.) If we need wider FoV, we have to re-design the structure of tertiary mirror unit, however, it is costly and difficult.

6.2.2 Adaptive secondary mirror

An adaptive secondary mirror for Ultimate Subaru

One of the main upgrade of Subaru telescope and key component of the GLAO system is its adaptive secondary mirror (ASM). The use of an ASM will permit to increase dramatically the Subaru AO performances improving the throughput of the telescope, the sensitivity above 2 microns wavelength, and the size of the corrected field of view.

Largest adaptive secondary mirrors are composed of a thin reflective glass shell activated by force actuators. This promising technology have been already tested in two astronomical observatories since 2010 (MMT and LBT) and permitted to achieve the best AO performances on sky:

- A 642 mm diameter convex secondary mirror with 336 actuators for MMT telescope (Mt Hopkins in Arizona),
- Two 911 mm diameter with 672 actuators concave secondary mirrors at LBT (Mt Graham Arizona).

The VLT (Chile) is one of the next ASM to be tested on sky with a 1120 mm diameter mirror and 1170 actuators for adaptive optics correction.

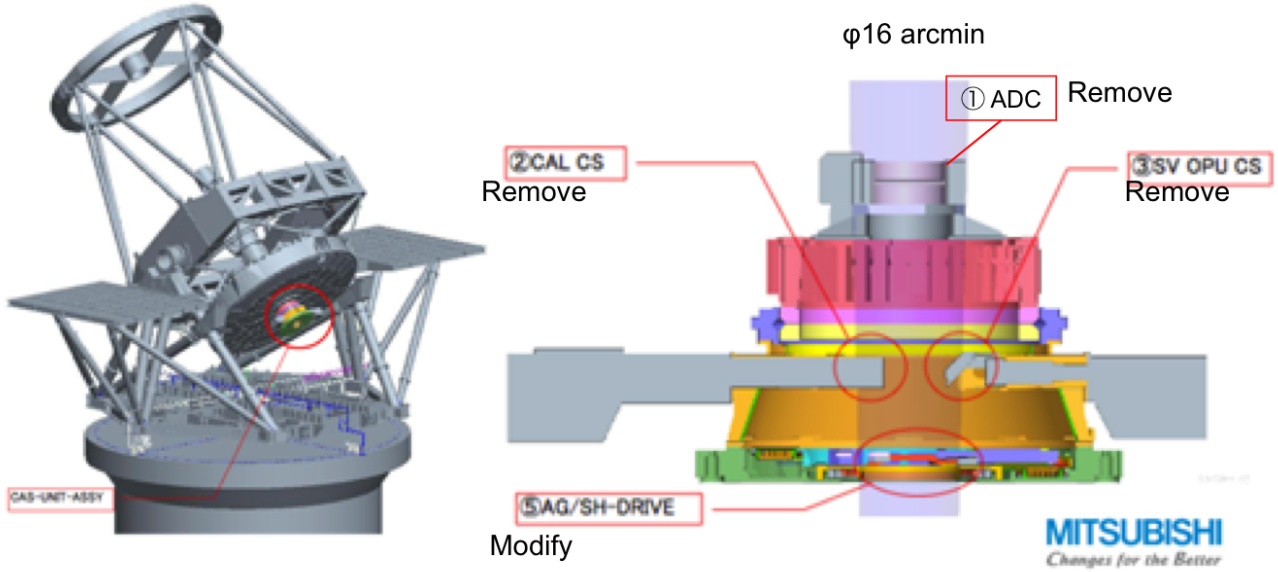

Figure 6.13: Modification plan of Cassegrain area.

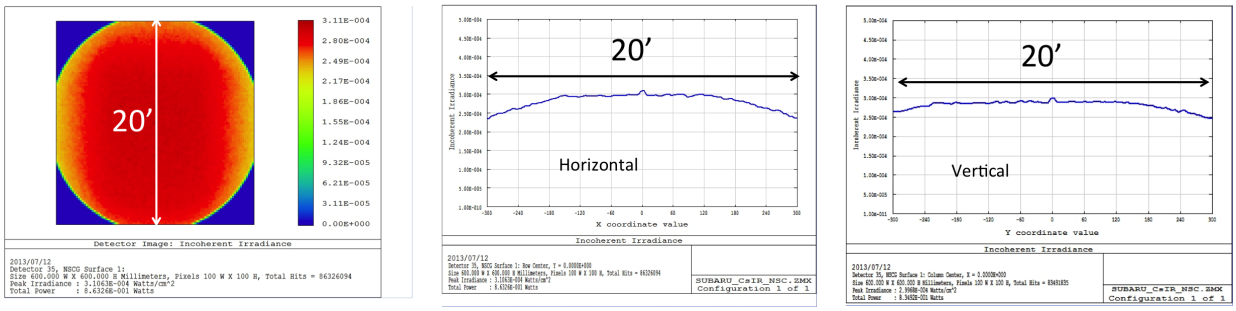

Figure 6.14: Unvignetted FoV at Cassegrain focus.

To compete with the next generation AO systems, Ultimate Subaru will be the first telescope on Maunakea equipped with a 1265 mm adaptive secondary mirror activated by a 1000 actuators.

The modeling of ASM for Subaru Telescope is comparable with the VLT deformable mirror, with similar diameter and optical parameters. However, the ASM technology described in this document is quietly the same from one ASM equipped telescope to the other.

The following paragraphs describe the information gathered during Subaru scientists visit of LBT in June 2015. This visit occurred during the ASM maintenance insured by the designer and builder of the ASM, Microgate.

This meeting with LBT AO team and Microgate engineers permitted us to exchange about the different aspects of using an ASM, like the different problems encountered during the last 6 years ASM operation at LBT, the optimization tested and integrated on the new generation of ASMs and also the basic advices concerning the general handling and maintenance of this powerful but complex equipment.

Overview of the LBT Adaptive secondary mirror

The Large Binocular Telescope (LBT) is equipped since 2010 with two adaptive secondary mirrors based on 672 voice-coil force actuators. Each mirrors are 911 mm concave mirrors.

The ASMs are the results of collaborations between different companies and institutes:

- Microgate (Italy), the main partner of LBT in charge of the design, production and maintenance of the LBT ASMs,
- A.D.S International (Italy) in charge of the mechanical design and the opto-mechanical integration,
- Mirror Lab (Steward Observatory Arizona) who produced the reference plate and the thin ASM shells,
- The Observatorio di Arcetri (Italy), which led the conceptual design and performed the diagnostic/calibration and acceptance tests of the ASMs.

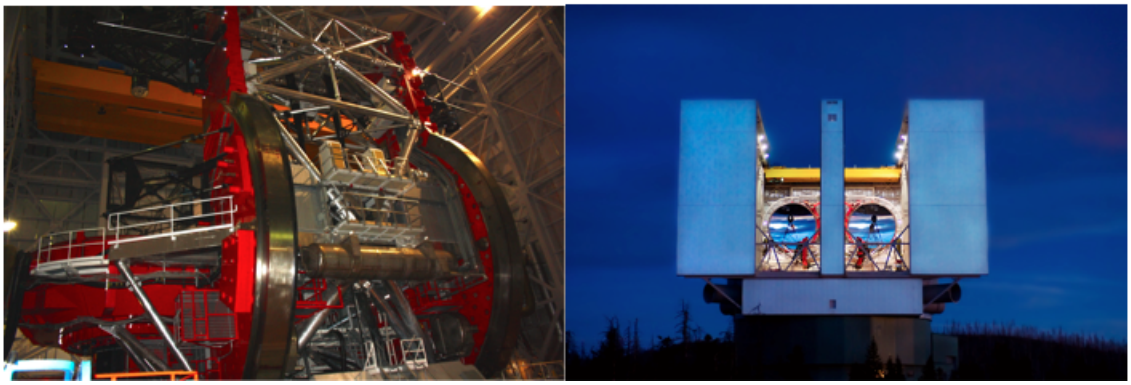

Figure 6.15: LBT - Mont Graham, Arizona

The ASM is composed of 5 mains subsystems:

- SS1: The control electronics containing the digital signal processors (DSPs) that perform the wavefront reconstruction, determine the force command for each actuators and control the actuators.

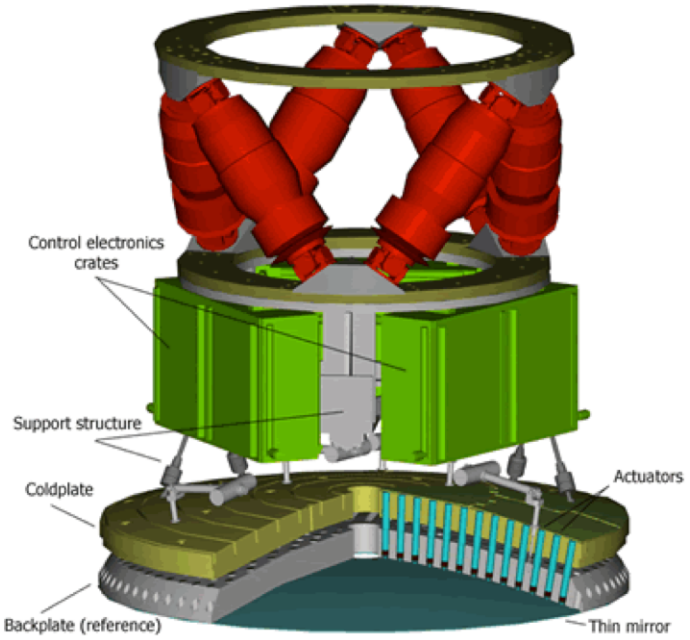

Figure 6.16: ASM explode view (Microgate)

- SS2: The coldplate, an aluminum plate supporting and dissipating the 672 voice-coiled actuators heat. The cooling distribution is provided by copper pipes, inside the internal grooves of the cold plate.

- SS3: The actuators: 672 voice-coiled. Each coil (12mm diameter) are placed on aluminum cold finger tips (composing the structure of the actuator itself and conduct the heat for its dissipation; see SS2) in front of a magnet glued on the thin mirror shell (see SS5). The force applied by each coil on each magnet deforms locally the thin mirror shell. Each actuator is connected to an electronic small board providing the contacts to pick the capacitive sensor (SS4) signal and related pre-amplification and demodulation electronics. All analog signals are converted to digital on the DSP boards (SS1) at 72 KHz. Reducing this size further brings also complications at the level of the voice coil, but also would reduce the actuator stroke (force).

  Beside the controlled force, each actuator provides a passive bias force pulling the magnet to hold the shell against the reference plate even when the system is switched off: a permanent magnet is installed in each actuator body and acts on the corresponding magnet attached to the shell to support 85% of the local weight when at zenith. At 60-degree elevation angle the actuators no longer support any of the shell's weight, and below that they must on average push rather than pull. Because the actuator power dissipation goes as the square of the force, the permanent magnet greatly reduces the total power requirement.

- SS4: The backplate or reference body (Zerodur glass plate of 50mm). Composed of bored holes and attached to the cold plate. The goal of the plate is to be a position reference for the downstream thin mirror shell. The actuators (coil cold-fingers) supported by the cold plate pass through the bored holes to reach the deformable mirror.

  A ring of conductive material (silver, chrome, aluminum, gold) is deposited around each magnet glued on the shell (SS5) and is mirrored on the reference body. These two opposite coatings constitute a capacitance used as space sensor.

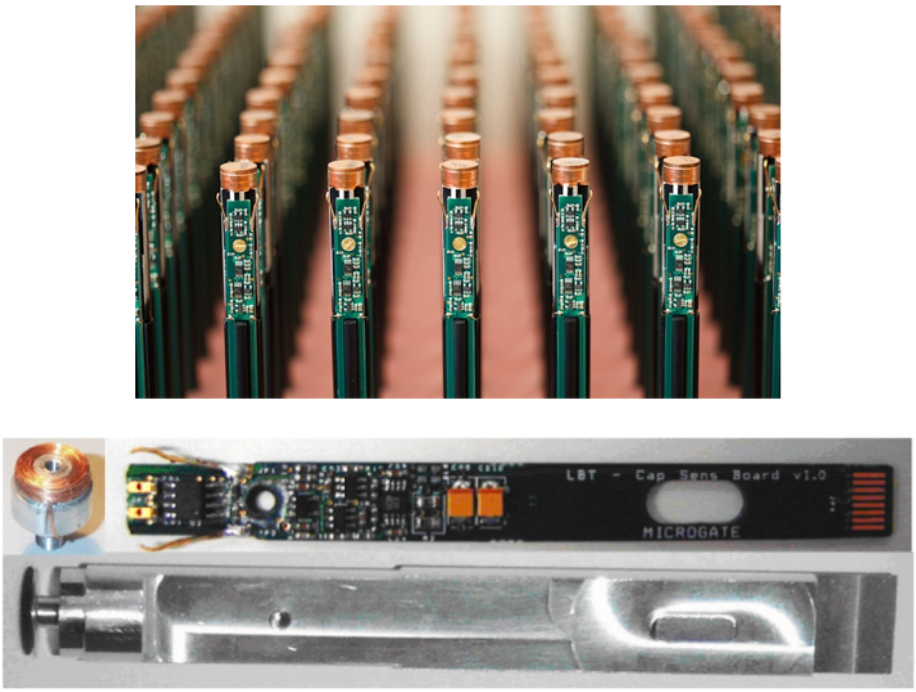

Figure 6.17: Voice coil actuators and the cold finger tips (Microgate)

Co-located capacitive sensors are checking in real time the mirror position deformed by the actuators.

- SS5: The deformable zerodur concave shell - mirror, the main and most critical part of the system. For LBT the diameter of the glass shell is 911 mm with a thickness of 1.6mm. 672 magnets are glues at its surface for activation. Back surface of the shell is spherical and match the reference plate. The Shell also has a central hole where connected membrane is attached to provide lateral and rotational constraints (position adjustments).

  The thin shell remains a high-technology, costly, high risk venture. Up to mid 2009 only the Steward Observatory Mirror Lab has been producing successfully thin shells from Zerodur blanks. In January 2012, SAGEM successfully finished the first thin for the DSM.

Ultimate Subaru ASM

The modeling of ASM for Subaru Telescope utilize the design of ASM for VLT, whose diameter and optical parameters are similar with each other.
First we set a diameter as 1265 mm, which is identical to the existing secondary mirror for infrared at Subaru Telescope. The diameter, 1265 mm, is slightly larger than that of VLT, however, the space between each actuator is widen as approximately 35 mm compared with VLT design.

The geometrical pattern of actuator is concentric ring, and pattern has rotational trifold symmetry. We have reflecting cone at the center of existing secondary mirror, which avoid the thermal background from the structure of telescope especially for mid-infrared instrument.

The size of the center cone is 350 mm in diameter. Thus we have a large area in the central portion, which makes it easier to design the supporting mechanism of thin mirror for ASM. In total, the number of actuators is 924, which is less than that of VLT.

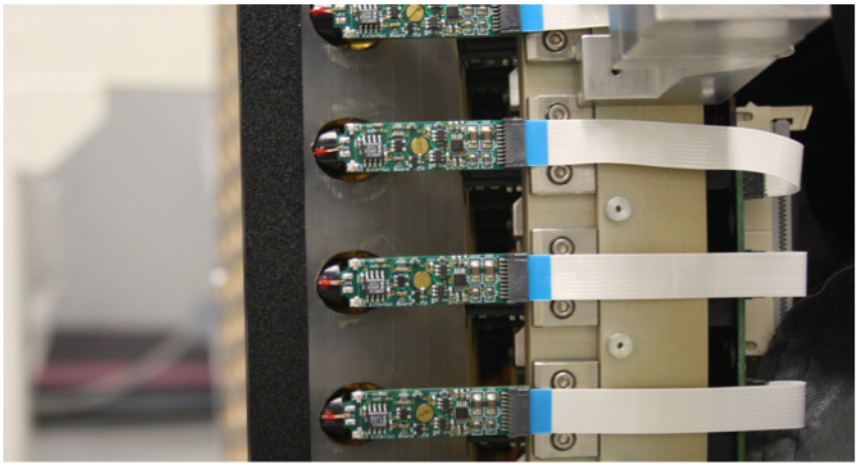

Figure 6.18: Reference plate and voice-coil actuators (side view)

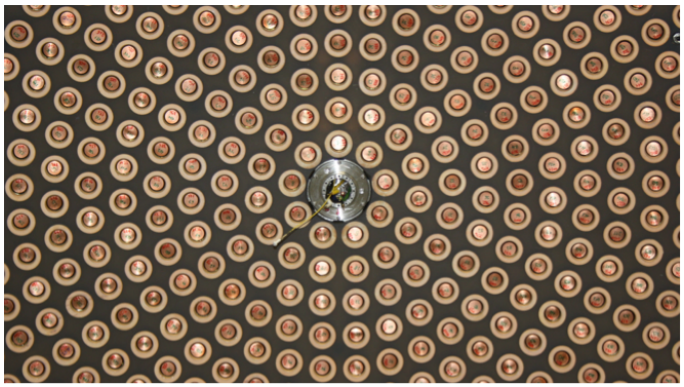

Figure 6.19: Reference plate and voice-coil actuators visible when the reflective shell is removed (top view)

We expect that there are no major impact or difficulty to design main components of ASM, such as thin shell, reference plate, cold plate, control electronics for actuators, cooling system, communication system. The total size and weight of preliminary ASM model can be matched into the existing IR secondary unit. Estimated total mass, weight, center of gravity, are also within the required specification of top unit of Subaru Telescope.

LBT ASM experience

Disable actuators

Problem discovered

Since 2011 the LBT secondary mirrors didn't required any maintenance. Nevertheless, since it's first light in 2010, many actuators started to encountered issues. In January 2015 almost 100 actuators over 672 were neutralized to protect the mirror shell.

Even with this actuators loss, the performances on sky for LBT AO system is still unbeatable: 90% SR achieved with 10% actuators disabled. Nevertheless, LBT AO team and Microgate pursued investigations

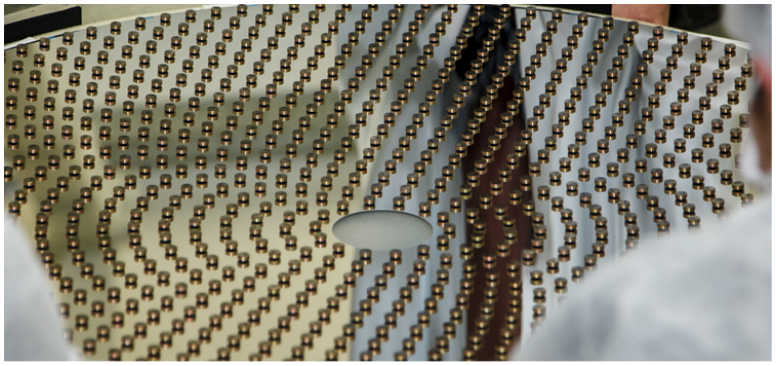

Figure 6.20: Back side of the reflective shell with magnets manually glued to it (Microgate)

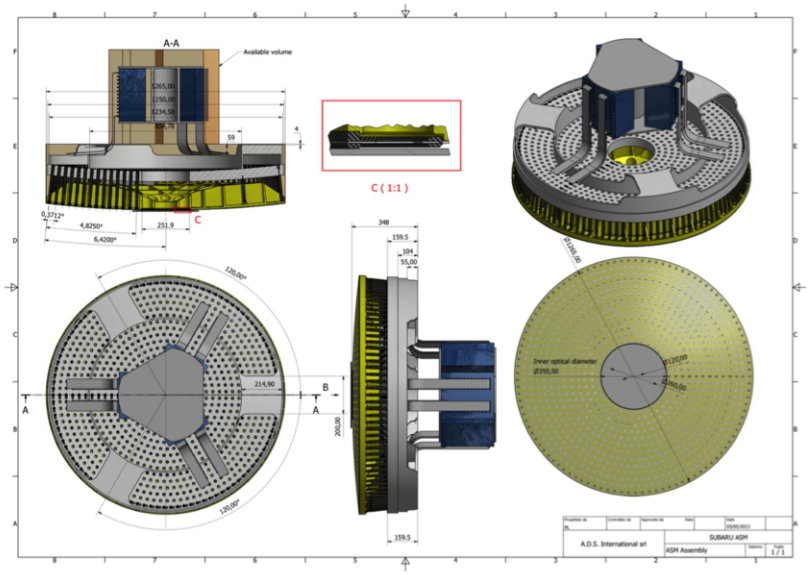

Figure 6.21: Subaru ASM preliminary model, credit NAOJ Microgate

to correct this problem on the next ASM generation.

To neutralize the actuator when a strange behavior is detected, the operator from LBT update a log file with the list (i.e. ID) of the actuator to be ignored. When activating the ASM, the log file is constantly consulted. The disabling of the defective actuators does not locally stick the shell because they are noncontact voice-coil actuators; they are simply free floating when deactivated.

Analysis of the actuator problems

Some actuators at the beginning were defective due to an excess of noise or a drift of the capacitive sensor signal (actuator jumps). When LBT started the maintenance work in 2015, they found out that 16 actuators were literally knocked off (disconnected) from the shell.

The most probable explanation comes from two aspects:

- The passive bias force from the permanent magnet installed in each actuator body. When pointing the telescope to lower elevation, the internal magnets don't support efficiently the weight of the

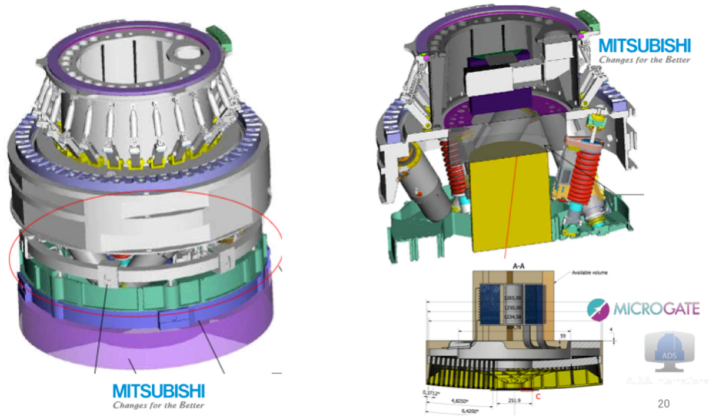

Figure 6.22: Subaru ASM and available space in the existing IR secondary mirror

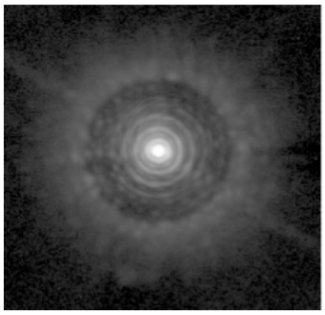

Figure 6.23: LBT PWFS First light image with the two ASMs. Esposito and al. (2010). 10 detectable diffraction rings SR 80% in H band.

shell. The membrane at the center of the shell prevents from the shell to rotate, fall or translate but a small motion of the shell remains unavoidable.

- The manually placed and glued magnets on the shell are not perfectly centered with the actuators holes in the reference plate.

The motion of the shell and the miss alignments between the reference plate holes and the shell magnets create a pressure of the shell magnets on the capacitive sensor edge (reference plate). This could conduct to the magnet disconnection off the shell.

When disconnected, the magnet from the shell is trapped by the coil explaining the erratic signal from the capacitive sensors.

Solution for new ASM

The main solution is to minimize the decentering error between the glued magnet on the shell and the coil actuator. An effort will be apply for the new ASM specifying precisely the position of the magnet glued manually on the shell and the position of the actuator in the cold plate.

The mis-centering doesn't affect the performance of the ASM but can lead to a magnet knock-off as encountered at LBT. This solution should reduce and avoid the number disconnected actuators.

Figure 6.24: reference plate alignment with the reflective shell (Microgate)

Gap contamination

Problem discovered

During LBT ASM experience, water and dust particles have been contaminated the gap between the reference plate and the mirror shell when turning off the mirror control.

These contaminants are from the LBT telescope atmosphere environment, which is at lower (3300m) altitude than Maunakea and surrounded by vegetation.

In general the gap is not directly opened to air thanks to an elastic band overlapping and covering it.

When turning off the unit, the gap moves by about 400 microns (50 microns when ASM is ON), creating a possible suction of air accompanied by water particle and dust.

In 4 years and with two ASMs in operation, only one contamination case has been detected.

When dust particles accumulate on the deformable mirror actuators, a large positional error is detectable. This usually occurs at the edge of the ASM.

Solution

From LBT and Microgate, it is not clear what caused this dust contamination. With only one event in 4 years, especially happening in LBT, they are pretty confident with the actual ASM design and don't expect any modification of it.

Nevertheless, they are advising to keep the ASM ON to prevent the air suction effect keeping the shell in contact with the reference body.

In case of dust contamination the mirror shell needs to be removed for cleaning the dust.

When water contamination occurred, LBT teams let the water evaporate (one week) to prevent from electrochemical effects when turning on the unit. The other option proposed would be to purge the shell with dry air (never tested).

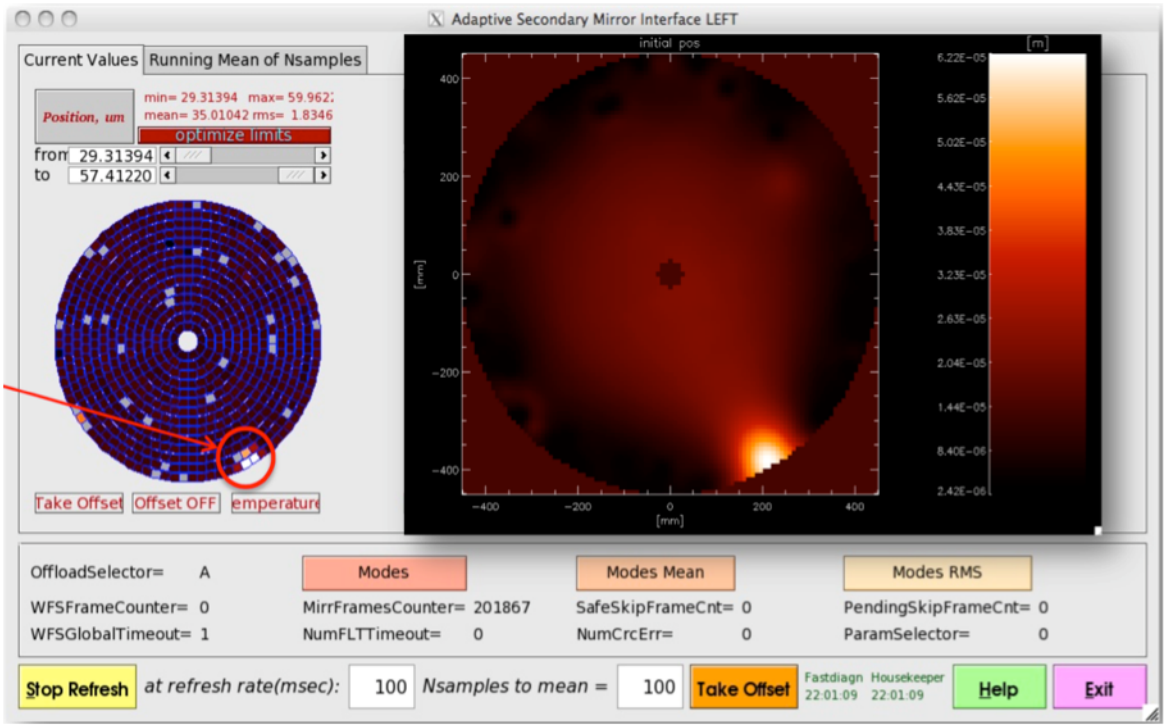

Figure 6.25: large positional error due to dust contamination at the edge of the deformable mirror (credit LBT)

The pie shape issue

Problem

The measurement of the gap between the shell and the reference body is done with the capacity sensors. An input signal, a scare wave, is injected directly on the back coating (aluminum) of the shell through the central distribution board.

This board carries the signal for the actuator control to the six individual sectors on the backside of the thin shell.

Due to a poor connection on the Central Distribution Board, the control of 1/6th of the DM got lost different times creating the visual pie shape on the ASM control GUI.

A temporary solution for LBT was to glue small pads of gold directly with conductive glue on the central distribution board ring to optimize the transmission of the signal.

For Microgate, the problem is now well defined. Engineers are looking for new solutions (new material coating) to implement and test on next generation of ASM.

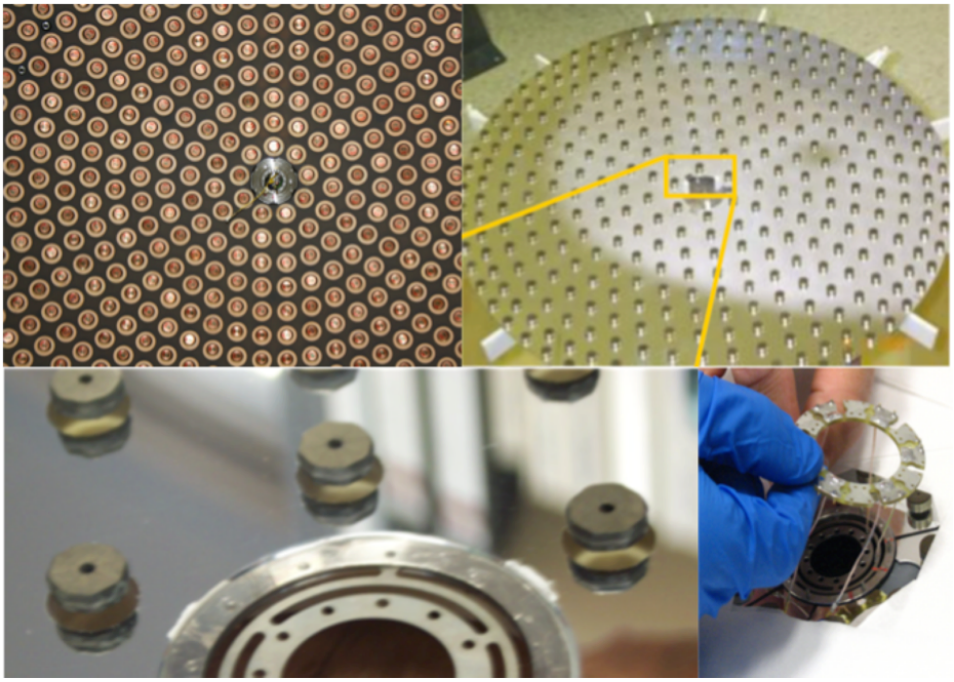

Figure 6.26: Top left: reference plate with the central distribution board input cables. Top right and bottom: central distribution bard on the reflective shell backside (with glued magnets) credit NAOJ and LBT.

Overcooling system accident
In 2014 one of the first LBT ASM encountered an overcooling accident. Due to a valve issue, the cooling went astray and cooled the main unit to -20 degrees Celsius in less than an hour. Due to condensation on the shell, ice accumulated on the shell and around the reference plate.

When warming up the water from melting ice contaminated the gap. After drying salt accumulated under the shelf. Force had to be applied to break up the salt, the shell wasn't usable anymore and this required a major overhaul of electronics, actuators & contacts.

Couples of months were necessary to restart the ASM with a new shell.

In case of ice accumulation on the shelf, LBT and Microgate advice to slowly bring the temperature of the system above the frost point but below zero and wait for the ice to sublime, preventing water to go inside the gap.

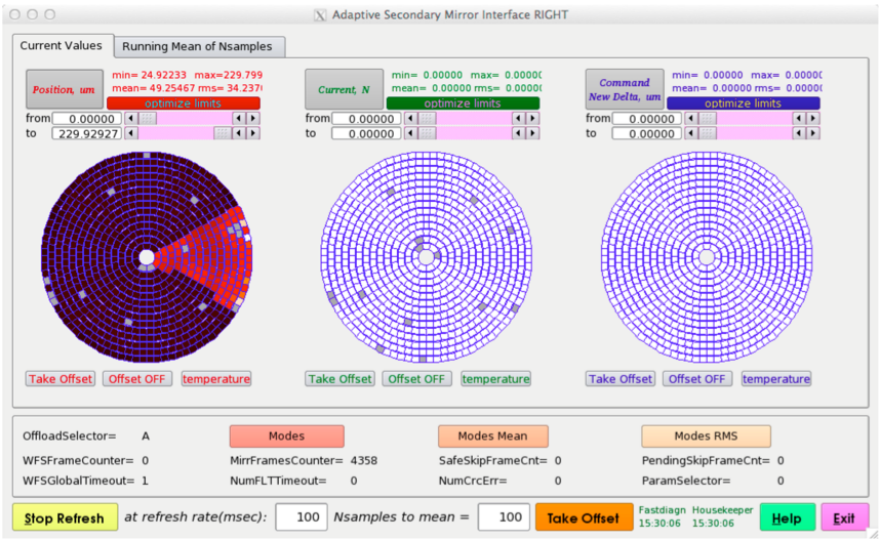

Figure 6.27: Pie shape phenomenon observed on the ASM control GUI at LBT (credit LBT).

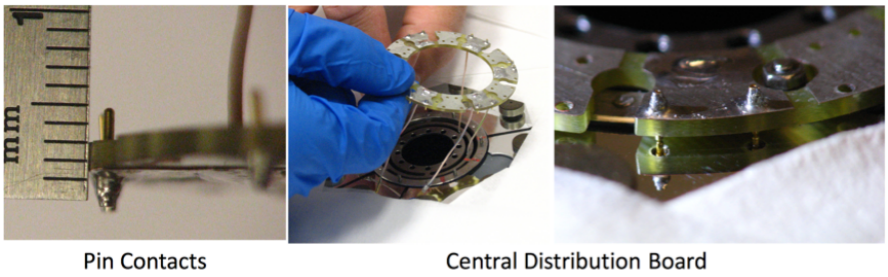

Figure 6.28: Central Distribution Board (credit LBT).

ASM service

During our visit, LBT and Microgate were performing the first maintenance of their ASMs since the first light in 2010. The maintenance starts with the disconnection of the ASM from the telescope and the transportation of the unit to the clean room.

Following, times budgeted for each steps of this delicate operation:

- Disconnect the electronic when crane attached to the ASM and move the ASM to clean room (3 hours)
- Detach the ASM unit from its hub with brackets (6 hours)
- Installation of the ASM unit on tilting bench. The maintenance team have then access to the electronics, the cooling system.

If access to the shell and actuators is required (for service or incidents as listed previously), the unit needs to be unsealed especially around the membrane supporting the shell at its center. This delicate work takes one full day and required 3 technicians.

The thin shell can then be disconnected from the membrane and delicately place on a foam bed.

Figure 6.29: LBT clean room inside the observatory

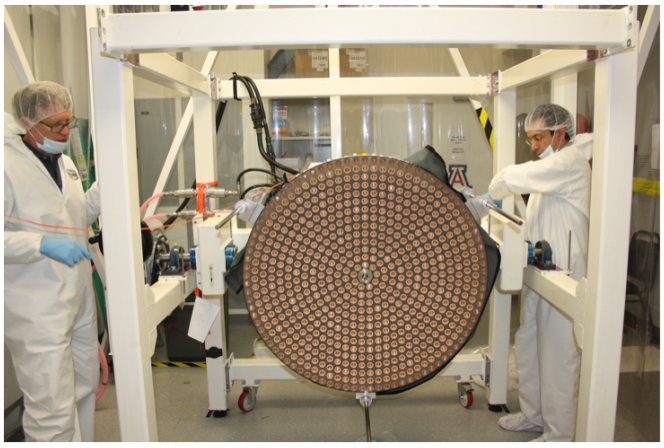

Figure 6.30: ASM without the reflective shell installed on the titling bench

Depending on the quality of the mirror coating the mirror shell can be recoated periodically to optimize the performance of the ASM (contaminated by the Mount Graham pine trees dust and iron dust).

In case of recoating, the mirror is sent to Tucson (AZ) transported on a foam bed. This is a really critical handling since the shell is highly fragile.

LBT advised to have a recoating chamber at summit to minimize transportation issues. Front and back shell recoating can be done without removing the magnet.

The cleaning process takes a month. The cleaning is done after having installed protective covers around the magnets on the shelf.

This process is very complex since it needs the use of tools to move the cleaning liquid around all protected magnets. This cleaning technic is, from LBR perspective, not perfect.

When the shelf is removed, parts from the unit, including the back-plate and cold-plate can be easily

accessible, permitted for example to control each voice-coiled behavior or replace them if necessary.

Conclusion

Due to the ASM previous experiences, most of the technical difficulties to fabricate and operate the ASM have been already solved.

Thanks to the perfect collaboration with our colleagues at MMT, LBT and Microgate and the perfect transparency during these information exchange, Subaru's ASM will benefit from this experience maximizing it's performances goals for it's first light.

6.2.3 Laser guide star system

More than decades of pursuing the optimum laser system for generating laser guide star for adaptive optics, we are almost reach one of the final solution, based on the fiber laser technology. Initially, gas or liquid laser system, such as using copper vapor or dye, used, and moved to an all solid-state laser technology. However, the stability or huge size of system are the drawback of these laser system. The project to built AO facility at VLTs has developed a 20W fiber laser system at 589nm recently. The stability, ease of operation, repeatability, optimization of return photon from sodium layer and so on were intensively taken into account. The product of this laser systems, manufactured by TOPTICA, are use widely in the world, not only at the VLT (4 laser system including spare), Keck II, Starfire Optical Range. The laser upgrade for the second generation AO system at Subaru Telescope, AO188, is progressing to replace from all solid-stage sum frequency laser system at 4.5W to TOPTICA fiber laser system.

We need four LGSs to estimate the turbulence at ground layer. At least two TOPTICA laser system are installed on the telescope and each laser beam is split in two beam, then four beams in total are launched on sky. Preliminary experiment at Keck II using TOPTICA fiber laser reported that the generated LGS is brighter than 9th magnitude equivalent. Even if we split the laser beam in two, we create LGS brighter than 10th magnitude equivalent.

6.2.4 Wavefront sensor

Thank to the prominent progress in high-sensitive, low readout noise CCD or CMOS devices, we have various selection of detectors and camera system for wavefront sensor. The typical sodium laser guide stars, generated by up-to-date laser system are estimated to be brighter than 12th magnitude equivalent. Thus, the sensitivity of wavefront sensor is not so critical. The manufacturer of camera system, such as E2V, First Light, provides us well-engineered products. Also high sensitive and low noise CMOS camera and two dimensional APD devices have been developed recently. These are also alternative candidates for wavefront sensors. Major concerns of wavefront sensors are weight, heat exhaust system, size for ULTIMATE-Subaru, because the available space inside the Cassegrain flange is very tight. We need at least four wavefront sensors for laser guide stars and three tip-tilt and focus wavefront sensors for natural guide stars. The pick-off location of laser guide stars have quite limited searching range, except for one Shack-Hartmann wavefront sensor, which has to pick off the natural star at the optical axis of Cassegrain focus for primary mirror analysis. On the other hand, the pick-off location of natural guide star has to be very flexible. Also one pickoff arm of natural guide star can reach to the optical axis for auto-guiding mode to conduct telescope pointing analysis. For this reason, quite complicated optomechanical system has to be safely packed in the Cassegrain flange.

Also we have to consider the optimum field of view of Shack-Hartmann sensor. Even though spot size of laser guide star for each subapreture becomes half during the closed loop of GLAO, uplink tip-tilt error and spot elongation are erase this merit. But the laser field of view on the wavefront sensor increase the diameter of optical elements in the pickoff and relay optics for the wavefront sensor.

Moreover, in term of natural guide star initial acquisition, the field of view or patrol field size for tip-tilt wavefront sensor has to be carefully designed. Due to the limited space at the Cassegrain flange, hybrid acquisition system, such as a combination of wide field camera and small pickoff mirror of narrow field of view, is challenging to pack in. However, pickoff mirror with larger field of view requires larger optics behind it.

Consequently, further trade-off study, in terms of limited space, field of view, guide star acquisition method, optomechanical feasibility and so on, is required to design the wavefront sensor optics.

6.3 Interface with Subaru Telescope System and Modification Plan

Yutaka Hayano[1,2], Olivier Lai[1], Shin Oya[2], Christophe Clergeon[1]
[1] Subaru Telescope, National Astronomical Observatory of Japan
[2] TMT Japan project office, National Astronomical Observatory of Japan

6.3.1 ASM and secondary mirror unit.

Interface between the secondary mirror and the top unit of Subaru Telescope are well defined and fixed. Current secondary mirror for IR observation (IRM2) are shown on the left of Fig. 6.22. As you see, clamping mechanism to the top unit of Subaru Telescope on top, six actuators in the middle section embedded and contacting surface of secondary mirror are well engineered. Therefore, we plan to upgrade the IRM2 to adaptive secondary mirror.

On the right side of Fig. 6.22, the plan to incorporate the adaptive secondary mirror unit into the structure of IRM2 are shown. We checked mechanical conflict between the existing IRM2 and modeled adaptive secondary mirror modified from VLT design. We found that the electronics unit at the top and a plate in the middle of IRM2 unit have conflict. We confirmed that we can make room for the electronics unit to cut the plate partially. Also we perform FEM analysis after we remove a part of the plate, and found that there is very small impact to the flexure to IRM2 and there is nothing required to enforce the IRM2 mechanical structure after we take out a part of the plate.

Table. 6.5 shows the mass distribution of existing IRM2. The total mass of existing secondary mirror is 651 kg. The allowed maximum weight of secondary mirror unit, which is limited by the secondary exchange robots, is 3000 kg. Therefore, the maximum mass, allocated to the adaptive secondary mirror unit, is 1584 kg.

Infrared M2 components	Mass (kg)	remarks
Secondary mirror	168	
Mirror cell	118	
Tip-tilt mechanism	258	including voice coil actuators
Mount table	107	
Sub total	651	
Six actuators	391	
Active springs	82	
Frame	621	
Clamping mechanism	244	
Others	78	safety lock, bolts etc.
Sub total	1416	
Total	2067	

Table 6.5: Mass of existing infrared secondary mirror

The secondary mirror is controlled by six actuators. Analysis of loads to each actuators shows that maximum mass of adaptive secondary mirror is about 1200kg. The loads to each actuators are always compressed within this mass at any location of center of gravity of adaptive secondary mirror. The maximum mass of 1200kg has enough margin for adaptive secondary mirror, modeled by Microgate.

Interface to the control system of telescope and instrument with adaptive secondary mirror has to be well studied and make a well defined interface control document between telescope and GLAO system. Mechanically, current IRM2 mechanical interface can be used so that there is no big impact to the

existing system. However, installing and removing the adaptive secondary mirror unit has to be carefully organized. Adaptive secondary mirror system has to be powered on all the time so that we have to switch power line from telescope facility to the battery inside the adaptive secondary mirror unit. After installed to the telescope, we have to switch back to the telescope facility power system. Electricity, cooling line and communication interface is also important.

Control system and software interface has a big complexity. Position control of adaptive secondary mirror is done by six actuators, according the telescope pointing and temperature environment. This can be separate from AO control system and ASM control system. However, offloading the tip-tilt and focus offset to the telescope has not been studied yet. This is a task for next design phase.

6.3.2 Laser system and LLT

The first candidate of laser system is TOPTICA fiber laser system. Thank to the other telescope laser upgrade plan, plenty of experiences and lesson learned are already exist. The TOPTICA fiber laser system consists of electronics rack and laser head. Electronics rack has a size of about 1m $\times$ 1m $\times$ 2m and its weight is about 700kg. VLT decided to mount both electronics rack and laser head on the telescope, however, we rather prefer to mount only the laser head, similar to Keck II laser system. Electronics rack is located around the Nasmyth platform, possibly where the current laser clean room is built. Subaru Telescope has squared-shaped huge structure at the elevation axis, what we call center section. We have a lot of room to place the laser head around this center section. The weight of laser head is about 100kg, and possibly relay optics unit with laser launching telescope has similar weight or slightly more. Preliminary analysis to mount 100kg on the corner of center section shows that only few micron deformation is calculated by FEM analysis. This is negligible even if the total weight of laser launching system increased by double or triple.

6.3.3 Maximize the FoV

As we described in the subsection of "Field of view analysis", we have to modify the Cassegrain flange and M3 unit to obtain the field of view larger than $15^{\times}$ square. Calibration light source may have to be modified for new near-infrared instruments. The bottom layer, what we cal AG/SH (AutoGuider/Shack-Hartmman) layer is completely changed to wavefront sensing layer. Current AG/SH layer has a thickness of 20cm, however, we can use a space above of AG/SH layer, where other components, such as slit viewer or calibration source, are placed.

Additionally, cell cover of primary mirror and M3 unit has to be modified. However, this is a minor modification to enlarge the field of view.

6.3.4 Other modifications

As we mentioned above, the modification of Cassegrain Flange, including maximization of field of view as well as wavefront sensor system is a big impact to the telescope. As we mentioned in the subsection of adaptive secondary mirror, control system of adaptive secondary mirror unit and interface to the telescope control system, GLAO control system is very complicated. However, there are very less studies on these issue at this moment. These are the important study and investigation for the next project phase of ULTIMATE-Subaru.

Chapter 7

Instruments for ULTIMATE-Subaru

Takashi Hattori[1], **Yosuke Minowa**[1], **and Ikuru Iwata**[1]
[1] Subaru Telescope, National Astronomical Observatory of Japan

7.1 Introduction

We have been discussing about future instruments of the Subaru telescope in 2020s when new generation telescopes such as TMT or JWST will start operation. In the next decade, the Subaru telescope will offer unique wide-field imaging and spectroscopic capabilities at the prime focus using Hyper Suprime Cam (HSC) and Prime Focus Spectrograph (PFS). However, these instruments only provide the data in optical or short infrared wavelength ($< 1.3\mu$m). To further strengthen the Subaru's wide-field capabilities, we have studied the feasibility and conceptual design of wide-field near-infrared instruments with an aid of ground layer adaptive optics (GLAO) system. Our studies of the GLAO performance and optical design of the telescope suggest that we can expect to obtain uniform seeing improvement over the field of view (FoV) of $\phi \leq 16'$ at the Cassegrain focus. This is the widest field of view compared to the FoVs of the near-infrared instruments at the 8-10m class telescopes. However, the FoV of our current near-infrared wide-field instrument, MOIRCS, is about $4' \times 7'$, which is much smaller than the Subaru GLAO FoV. To fully utilize the wide-field capability with GLAO, we definitely need to develop new near-infrared instruments with wider field and higher multiplex capabilities than existing instruments. We have conducted the conceptual studies of the wide-field imager, the multi-object slit spectrograph, and the multi-object integral field unit (IFU) spectrograph in collaboration with NRC-HIA/Canada and AAO/Australia.

Our main goal is to perform unprecedented legacy survey with the GLAO assisted near-infrared instruments and to provide Subaru's original targets to follow-up with TMT in 2020s by combining with the imaging and spectroscopic survey data from HSC and PFS. Table 7.1 summarizes the baseline specifications of the ULTIMATE instruments compared with the other wide-field near-infrared instruments at 8-10m class telescopes in 2020s. The most unique capability of the ULTIMATE instruments is the widest FoV among the other near-infrared instruments. In this section, we describe conceptual studies of the wide field near-infrared imager, multi-object slit spectrograph, and multi-object IFU spectrograph, which fully utilize the capabilities of the GLAO corrected spatial resolution and the widest FoV.

Table 7.1: Baseline specifications of the ULTIMATE-Subaru instruments compared with wide-field near-infrared instruments at 8-10m class telescopes in 2020s.

Instrument/Telescope	FoV	Multiplicity	$\lambda(\mu$m)	R	AO
Imager					
ULTIMATE/Subaru	$\phi \leq 16'$[a]	–	0.9–2.5	–	GLAO ($\sim 0''.2$)
HAWK-I/VLT	$7'.5 \times 7'.5$	–	0.9–2.5	–	GLAO ($\sim 0''.2$)
Flamingos2/Gemini-S	$6'.1 \times 6'.1$[b]	–	0.9–2.5	–	MCAO ($< 0''.1$)
Multi-Object Slit Spectrograph					
ULTIMATE/Subaru	$\phi \leq 16'$[a]	∼100 (TBD)	0.9–2.5	∼3000(TBD)	GLAO ($\sim 0''.2$)
MOSFIRE/Keck	$6'.1 \times 6'.1$	~ 46	0.9–2.5	∼3500	NOAO ($\sim 0''.5$)
Flamingos2/Gemini-S	$2'.0 \times 6'.1$	∼80	0.9–2.5	∼3000	MCAO ($< 0''.1$)
Multi-Object IFU Spectrograph					
ULTIMATE/Subaru	$\phi \leq 16'$[a]	> 24 (TBD)	0.9–2.5	∼3000(TBD)	GLAO ($\sim 0''.2$)
KMOS/VLT	$\phi \sim 7'.2$	24	0.9–2.5	∼4000	NOAO ($\sim 0''.5$)

[a] There is ~ 10 % vignetting at the edge of the field. No vignetting within the FoV of $\phi \sim 12'$.
[b] MCAO corrected FoV is about 2 arcmin.

7.2 Wide-field Imager

Takashi Hattori[1], **John Pazder**[2], **Tomoyasu Yamamuro**[3], **and Yoko Tanaka**[1]
[1] Subaru Telescope, National Astronomical Observatory of Japan,
[2] Herzberg Institute of Astrophysics, National Research Council of Canada, [3] OptCraft

7.2.1 Four barrel imager design (J. Pazder, HIA)

Here we summarize a conceptual study by John Pazder (NRC-NSI-AST/HIA) based on his technical note "Subaru concentric corrector and four barrel GLAO imager Optical Design Concept" (5/29/2013). Because the available field-of-view at Subaru Cassegrain focus was still under study at the time when this technical note was written, $\sim \phi 20'$ is assumed in this study.

The concentric corrector consists of two elements of Infrasil-302 with spherical surfaces and 690mm in diameter. It provides a universal 22′.8 diameter field of view (at f/12.4) with residual optical design aberrations less than 66mas. This corrector is designed to feed multi-barrel optical systems without pupil miss-match.

The imager design concept is a four-barrel imaging system feed by this corrector with each barrel having a 4k×4k H4RG detector covering a $6'.8 \times 6'.8$ field of view (0″.1/pixel sampling). The total imager field of view is 185 square arc minutes.

Figure 7.1 shows the optical layout of this system. The cameras are within a volume of 2.1 m in length and 0.8 m in diameter. A window has been put at the entrance to the cameras, with the intention of the cameras being enclosed in the Dewar with the corrector and wave front sensors outside the Dewar. The cameras have been designed with a sharp pupil image.

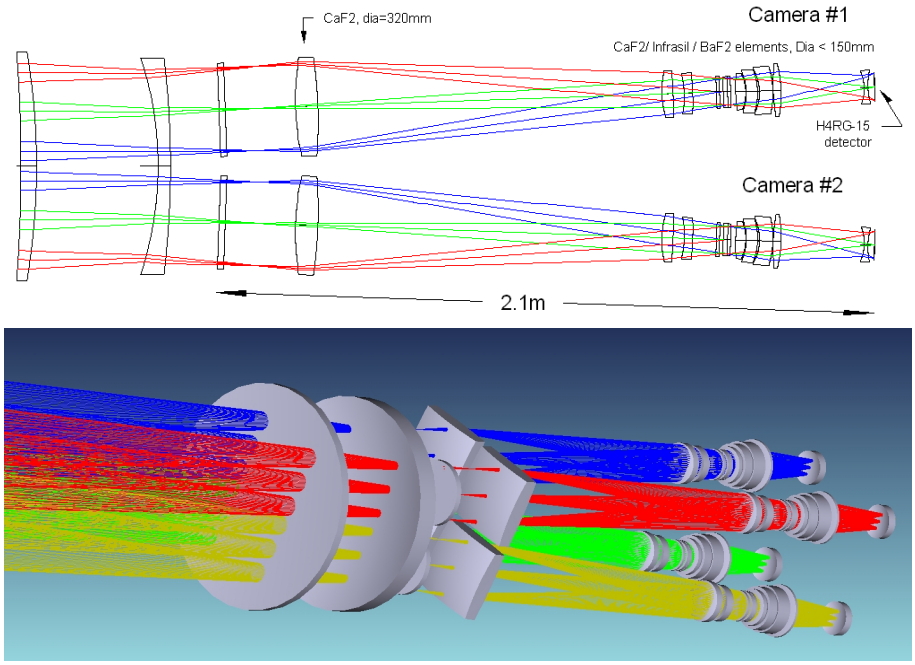

Figure 7.1: Optical layout of the corrector and imager system (J. Pazder, section 7.2.1)

The image quality is shown in Figure 7.2. Spot quality is less than pixels at all points except at the outside corner where the image quality is marginally more at 16 μm RMS spot diameter.

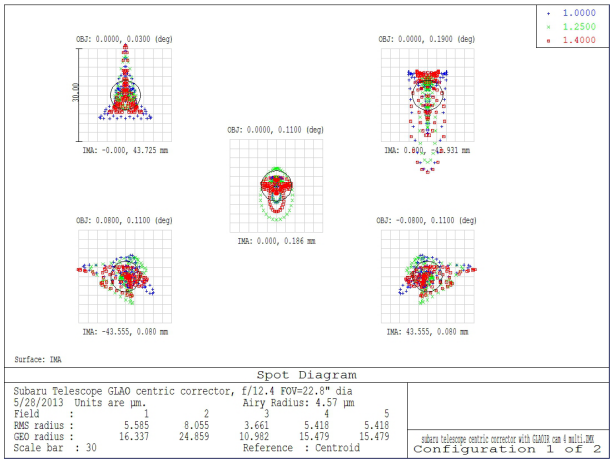

Figure 7.2: Spot diagram for one of the imagers. The box is 2 pixel width. (J. Pazder, section 7.2.1)

7.2.2 Imaging performance of wide-field near-IR multi-object dpectrograph (T. Yamamuro, OptCraft)

In this section, we summarize the imaging performance of the Wide-Field Near-IR Multi-object Spectrograph designed by Tomoyasu Yamamuro (OptCraft). Please see section 7.3.1 for the details of the designs.

Figure 7.3 show the spot diagram for the imaging mode of design I-A-2. The diameter of the FoV is $\phi 12'.6$ and the RMS diameter of the spots is better than the specification, $0''.15$, except for 0.8-0.9 μm around the edge of the FoV as indicated in the figure.

Figure 7.4 shows the spot diagram for the imaging mode of designs II-B divided to four wavelength regions. It is for one of the four FoV segments and the size is $11'.5 \times 11'.5$. The spot size is $20 - 30$ μm ($0".11 - 0".16$) at most positions but worsens to $30 - 50$ μm ($0".16 - 0".27$) at the edge of the FoV.

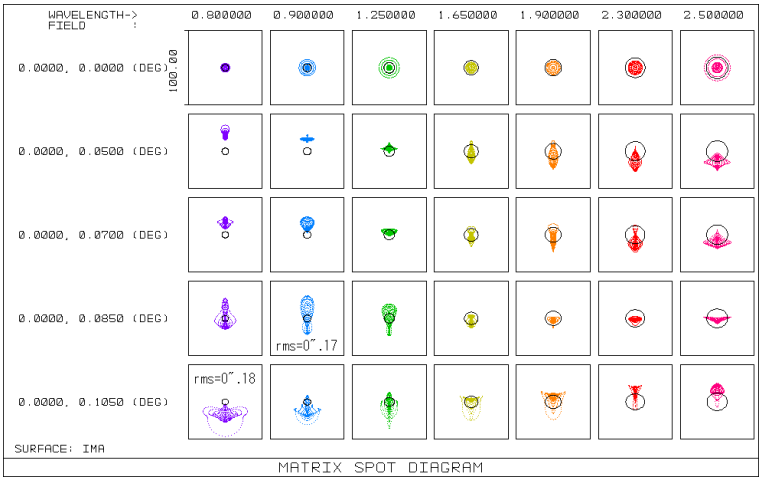

Figure 7.3: Spot diagram for the imaging mode of the design I-A-2. The RMS diameter is smaller than the specification, $0''.15$, except for 0.8-0.9 μm around the edge of the FoV as indicated in the diagram at the lower-left corner. (T. Yamamuro, section 7.2.2)

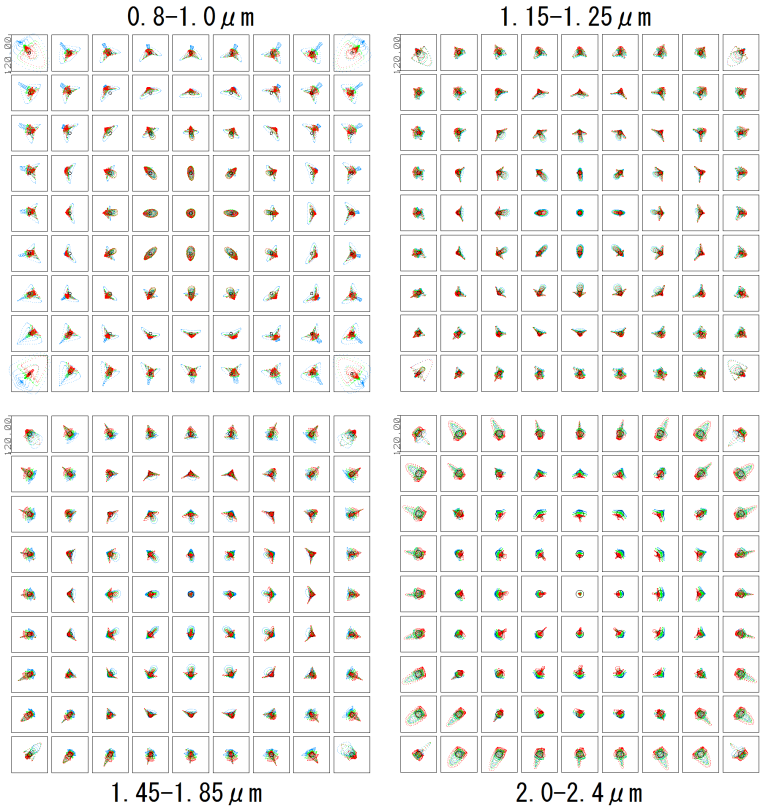

Figure 7.4: Spot diagram for the imaging mode of the design II-B divided to four wavelength regions. It is for one of the four FoV segments and has the size of $11'.5 \times 11'.5$. (T. Yamamuro, section 7.2.2)

7.2.3 Wide-field imager with reflective optics (Y. Tanaka, Subaru)

This section summarizes the optical design study by Yoko Tanaka (Subaru) for a wide-field imager with large reflecting mirrors.

The optical layout and spot-diagrams are shown in Figure 7.5 and Figure 7.6. It is composed of a folding mirror ($\phi 745mm$), a spherical mirror ($\phi 565mm$), and 7 lenses. The scale at the detector is 194 μm/arcsec. RMS diameter of the spot diagrams ranges 0".05 to 0".13 at $0'$ to $8'$ from the field center.

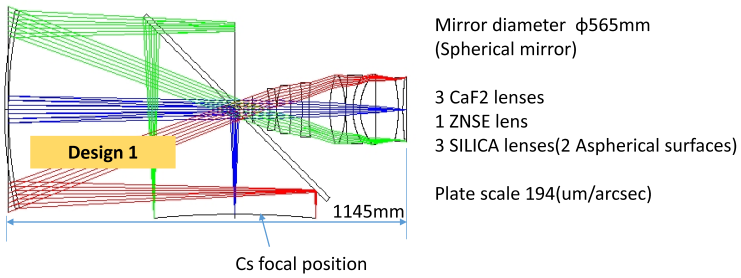

Figure 7.5: Optical layout of the wide-field imager system (Y. Tanaka, section 7.2.3)

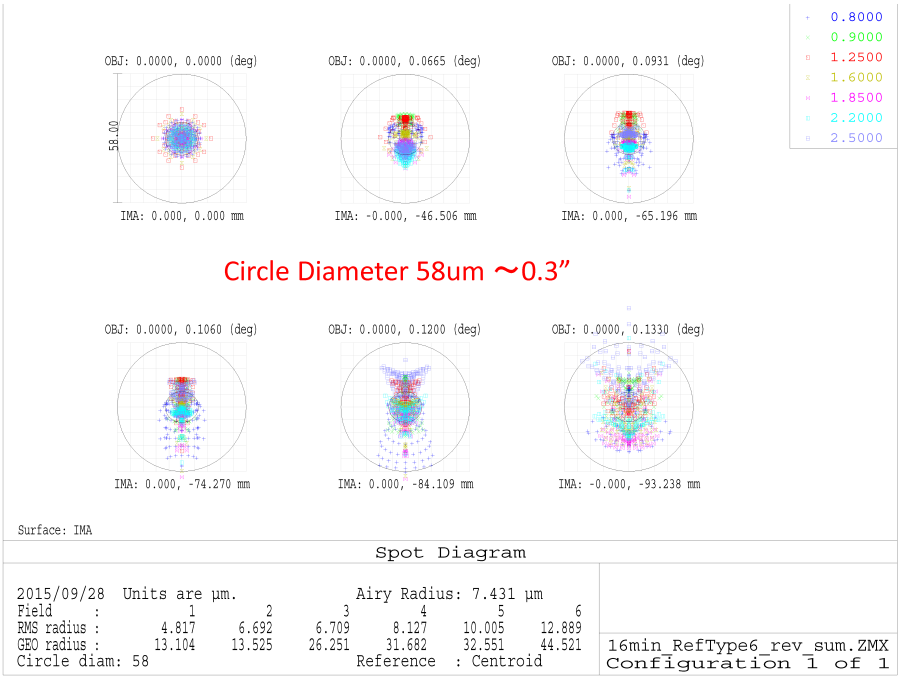

Figure 7.6: Spot-diagram for the wide-field imager system (Y. Tanaka, section 7.2.3)

7.3 Multi-object Spectrograph

Takashi Hattori[1], **Tomoyasu Yamamuro**[2], **Yuji Ikeda**[3], **Yoko Tanaka**[1], **and Yosuke Minowa**[1]
[1] Subaru Telescope, National Astronomical Observatory of Japan, [2] OptCraft, [3] Photocoding

7.3.1 Wide-Field near-IR multi-object spectrograph (T. Yamamuro, OptCraft)

In this section, we summarize the optical design study by Tomoyasu Yamamuro (OptCraft) for the Wide-Field Near-IR Multi-object Spectrograph based on his documents CP0046-11-RP001 (3/30/2012) and CP0046-12-RP001 rev.1 (3/15/2013). The studies were done with the following conditions.

- Wavelength range is 0.8 to 2.5 μm
- The target image quality is FWHM $< 0''.15$
- The maximum size of CaF_2 glass is 400 mm
- In some of the designs, it is allowed to change the parameters of the secondary mirror and/or the shape of the primary mirror up to 12 μm which is within the stroke of the actuators.

There are five optical designs as summarized in Table 7.2.

Table 7.2: Summary of optical designs by Yamamuro, OptCraft

Design name	I-A-1	I-A-2	I-B-2	II-A	II-B
Secondary mirror parameters	current	current	new	current	new
Change to the primary mirror shapre	no	no	yes	yes	yes
Field of view	$\phi 13'.2$	$\phi 12'.6$	$\phi 16'.2$	$8'.5 \times 8'.5$ $\times 4$	$11'.5 \times 11'.5$ $\times 4$
Field flattener for MOS	no	yes	yes	yes	yes
Number of lenses and window	17	19	19	21 ($\times 4$)	21 ($\times 4$)
fore-optics/window	1	3	3	5	5
collimator	9	9	9	9	9
camera	7	7	7	7	7

Figure 7.7 shows the optical layout of the design I-A-2. Image quality for this design is calculated by using a grism made of fused silica with 160 lines/mm and blaze angle 35°. The image positions and resulting spot diagrams are shown in Figure 7.8. In most cases, the image quality satisfies the goal, $< 0''.15$. But it becomes worse at the edge of the field-of-view ($5'.1-6'.3$) and the wavelength ($0.8-0.9\mu m$ and $2.5\mu m$) with FWHM$=0''.18 - 0''.2$.

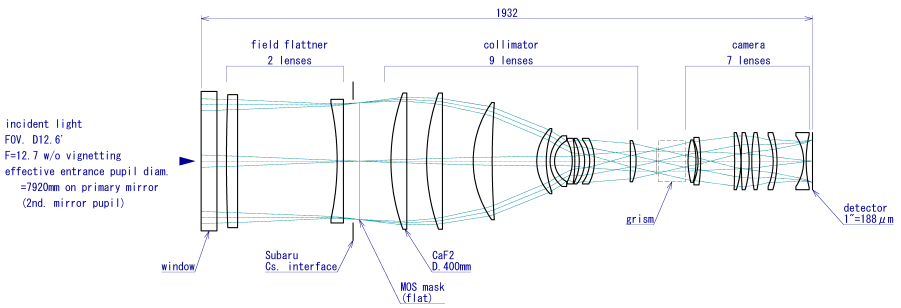

Figure 7.7: Optical layout for the design I-A-2

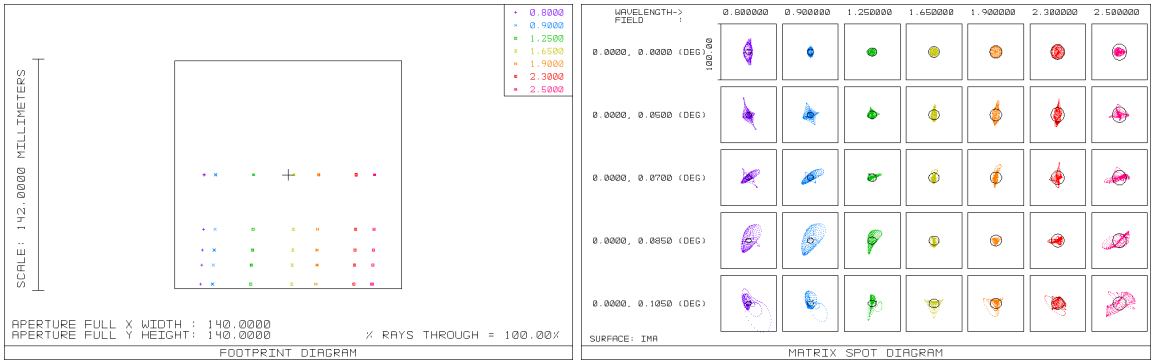

Figure 7.8: Spectroscopic image positions (left) and spot diagrams (right) for the design I-A-2. For the calculation, a grism made of fused silica with 160 lines/mm grooves and blaze angle 35 ° is assumed. (T. Yamamuro, section 7.3.1)

To explore the possibility of wider FoV, studies of optical design with FoV split into four segments were also made (design II-A and II-B). Figure 7.9 shows the FoV configuration of design II-B. The gap between the FoVs can be used to pick AO guide stars. The four FoVs are symmetric and have an identical structure. The optical layout including the telescope for one of the FoVs is shown in Figure 7.10. The resulting pixel scale is 0".08/pixel for $15\mu m$/pixel. To examine the optical performance of spectroscopy mode, we assumed the grisms listed in Table 7.3. The spectral resolution is calculated for the design II-A and 0″.4 slit width. The resulting spot diagrams are shown in Figure 7.11. The RMS diameter of the spots is $\sim 0''.15$ at the field center and $\sim 0''.3$ at the edge of FoV.

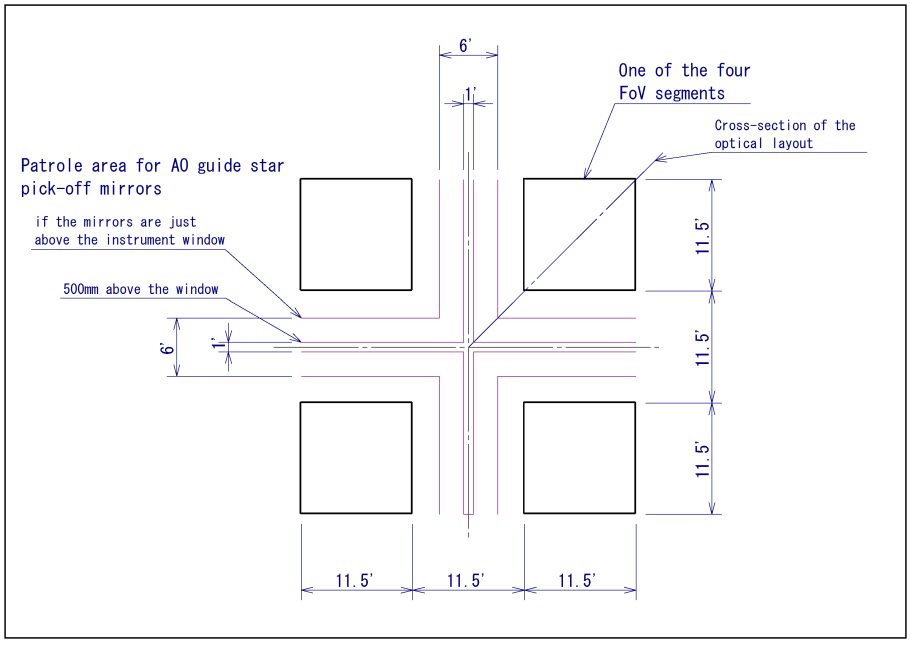

Figure 7.9: FoV configuration of the design II-B (T. Yamamuro, section 7.3.1)

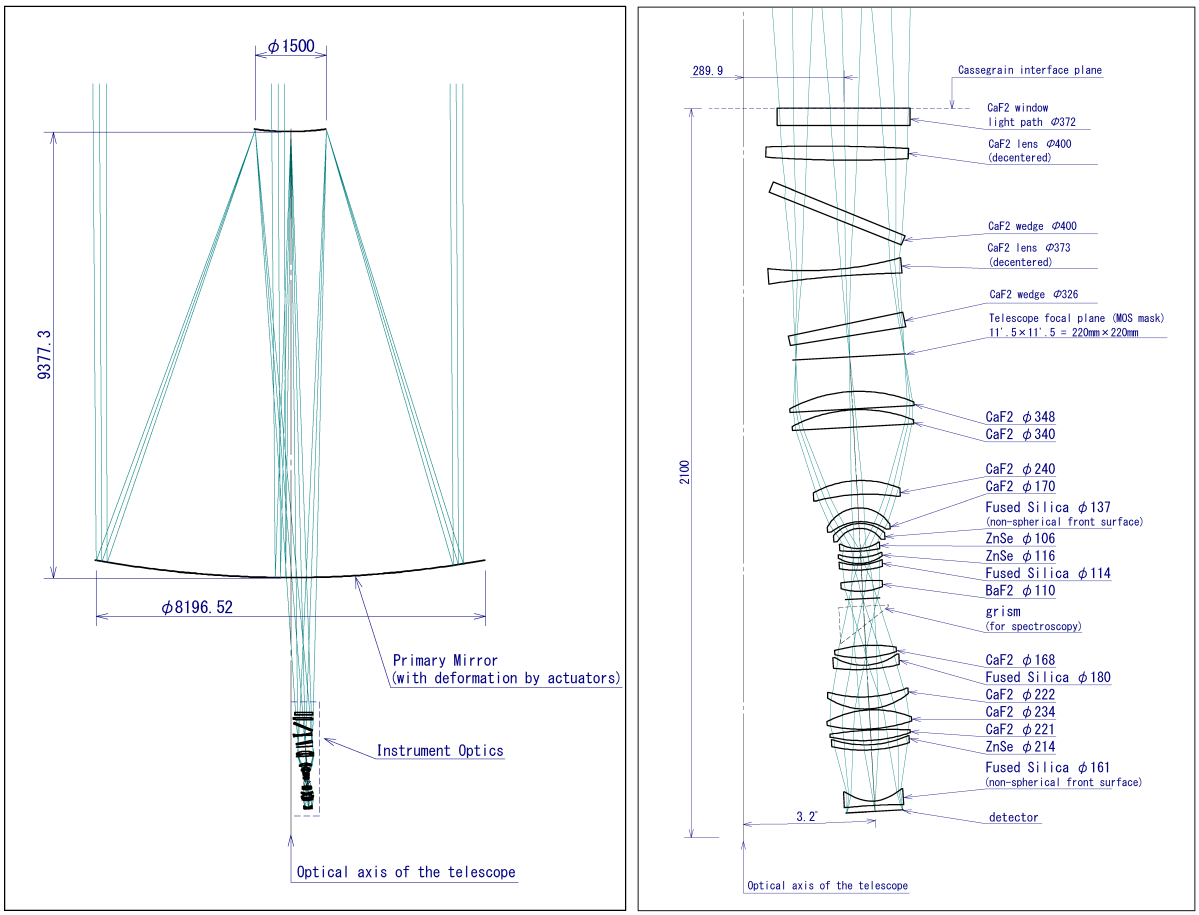

Figure 7.10: Optical layout for one of the four FoVs in design II-B (T. Yamamuro, section 7.3.1)

Wavelength Range (μm)	**Glass Material**	**Groove** (gr/mm)	**Blaze Angle** (degree)	**Spectral Resolution** ($\lambda/\delta\lambda$)
$0.95 - 1.15$	ZnSe	670	27.9	∼3300
$1.1 - 1.4$	ZnSe	580	29.0	∼3400
$1.5 - 1.8$	Silicon	480	18.5	∼3400
$2.0 - 2.4$	Silicon	370	19.3	∼3500

Table 7.3: Grism parameters used to calculate the optical performance of the spectroscopy mode in design II-B. The spectral resolution is for slit-width of $0''.4$.

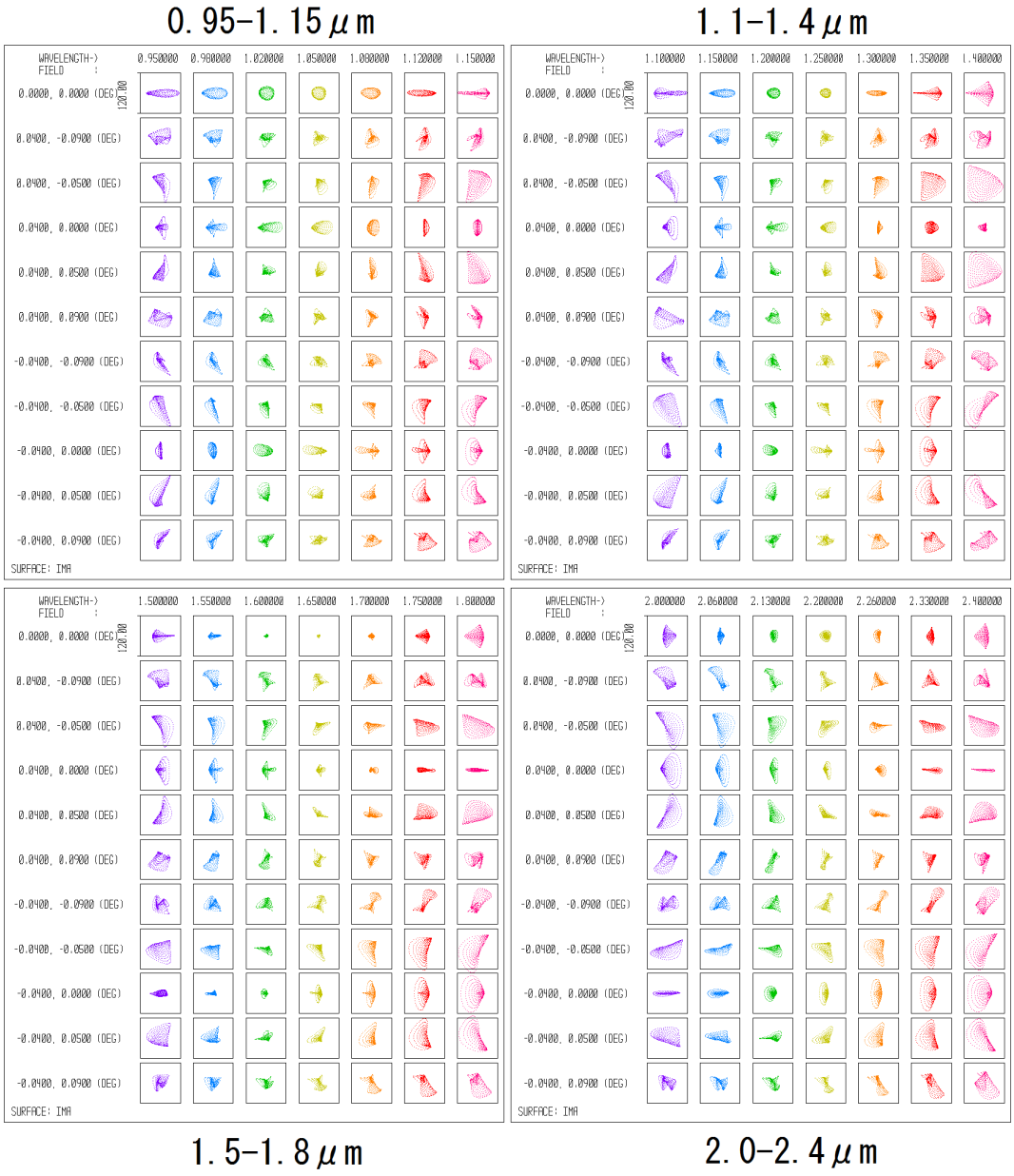

Figure 7.11: Spot diagrams for the spectroscopy mode of design II-B. See Table 7.3 for the assumed parameters of the grisms for each wavelength.
range.

Cryogenic and Mechanical feasibility

For the design II-B, as the most extreme case, we asked Sumitomo Heavy Industries ltd. (SHI) to examine the cryogenic and mechanical feasibility under the conditions listed in Table 7.4.

temperature of the optics	120K
temperature of the detectors	77K
temperature of the MOS mask unit	120K
diameter of windows	$4 \times \phi$380mm
total weight of the optics and holders	1,520 kg
total weight of the instrument	< 3t

Table 7.4: Conditions of the cryogenic and mechanical feasibility study for design II-B

Based on the case for an instrument with the optics and support structures weight of 360 kg, SHI estimated the heat loads and total weight of the instrument as shown in Table 7.5.

radiation heat from the Dewar wall	85 W
radiation heat from the windows	250 W
conduction	40 W
weight of main Dewar	2,560 kg
weight of support structure	500 kg

Table 7.5: Estimated heat load and total weight by SHI for design II-B.

The total heat load of 375 W will require 6 cryocoolers, RDK400B, in addition to 4 cryocoolers for the MOS mask units. The total number of 10 cryocoolers far exceeds the capacity at the Cassegrain focus. Also, the total weight of the instrument, $2,560 + 500 + 1,520 = 4,580$ kg is beyond the tentative weight limit of 3 t for the Cassegrain focus.

Grism Efficiency

For the grisms used to calculate the optical performance of the spectroscopy mode in design II-B (Table 7.3), we asked Photocoding to examine their diffraction efficiency. The conditions are summarized below.

- Diffraction efficiency is calculated by Rigorous Coupled Wave Analysis
- The apex angle equals to the Blaze angle.
- Unpolarized light is assumed
- No reflection at the incident surface is assumed (perfect anti-reflection coating)
- No anti-reflection coating on the emitting surface (grating surface)

The results are shown in Figure 7.12. The expected diffraction efficiency is about 55% to 60%. Because of the large refractive index of the used materials, the Fresnel reflection loss at the grating surface is rather large; 18.1% in Y- and J-band, 30.5% in H- and K-band. On the other hand, the large refractive index allows small apex angles which result in the small variation of the diffraction efficiency on the slit position. If higher efficiency is required for the dispersion element, we will need to explore the possibility of AR-coating on the grating surface or other type of grism such as VPH grism.

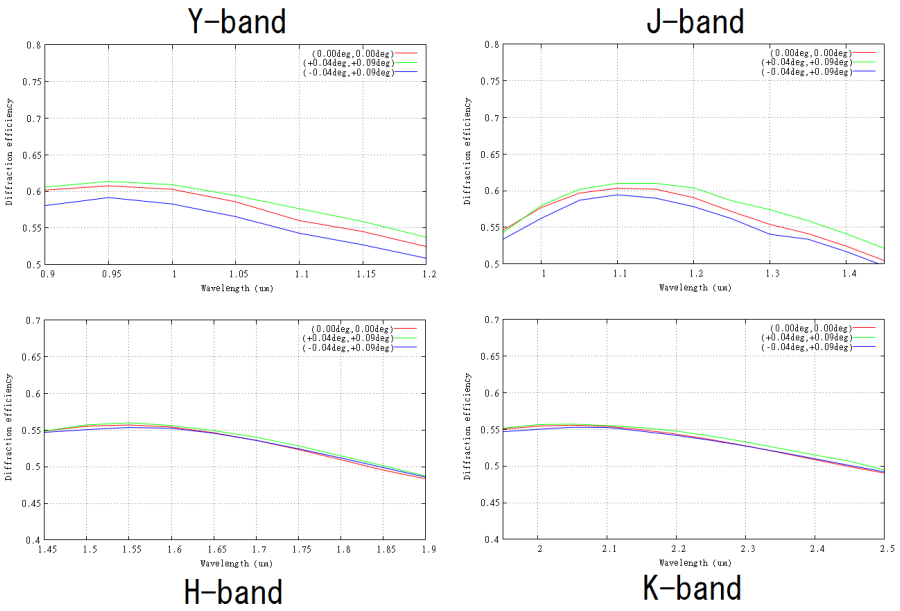

Figure 7.12: The diffraction efficiency of the four grisms listed in Table 7.3. The Fresnel reflection loss at the grating surface is 18.1% in Y- and J-band and 30.5% in H- and K-band.

7.3.2 Wide-field multi-object spectrograph (Y. Tanaka, Subaru)

This section summarizes the optical design study by Yoko Tanaka (Subaru) for a wide-field spectrograph.

The optical layout and spot-diagram are shown in Figure 7.13. It is composed of 15 lenses including 5 aspherical surfaces. The scale at the detector is 171 μm/arcsec. In the spot diagram, the RMS diameter ranges $0''.04 - 0''.07$ ($1.6\mu m$) to $0''.17 - 0''.28$ ($2.5\mu m$).

7.3.3 IRMS

The InfraRed Multi-Slit Spectrometer (IRMS) is a is a near-IR ($\sim 0.97 - 2.45\mu$m) spectrograph with 46 slits designed as one of the first light instrument for TMT. IRMS is almost a clone of MOSFIRE, which was successfully deployed on Keck in 2012. One of the unique feature of IRMS (and MOSFIRE) is that its multiplex advantage of up to 46 slits, which is achieved using a cryogenic Configurable Slit Unit (CSU). The CSU is re-configurable under remote control in less than 5 minutes without any thermal cycling of the instrument. Slits are formed by moving opposable bars from both sides of the focal plane. When the bars are removed to their full extent and the grating is changed to a mirror, IRMS becomes a wide-field imager.

During the Keck-Strategy meeting in 2014, there was a discussion between the Subaru and Caltech Astronomy about the idea to use IRMS at Subaru as a GLAO instrument for several years before starting the commissioning of IRMS at TMT, which is expected to be 2024 or later. Since TMT is planning to use IRIS as a first light instrument, the development and commissioning of IRMS is most likely to be delayed by several years after the first light of TMT. Compared with the other instrument plan, this idea could potentially have merit in terms of the cost and risk for developing the instrument as IRMS will be developed for TMT based on the well verified technology as used in Keck/MOSFIRE. The demerit of this idea is that there is big uncertainty on the possibility of starting the IRMS development earlier than TMT planned to adapt to the schedule of the Subaru's GLAO development. Putting this uncertainty on the schedule aside, we first studied the technical possibility for accommodating IRMS at Subaru as a GLAO instrument.

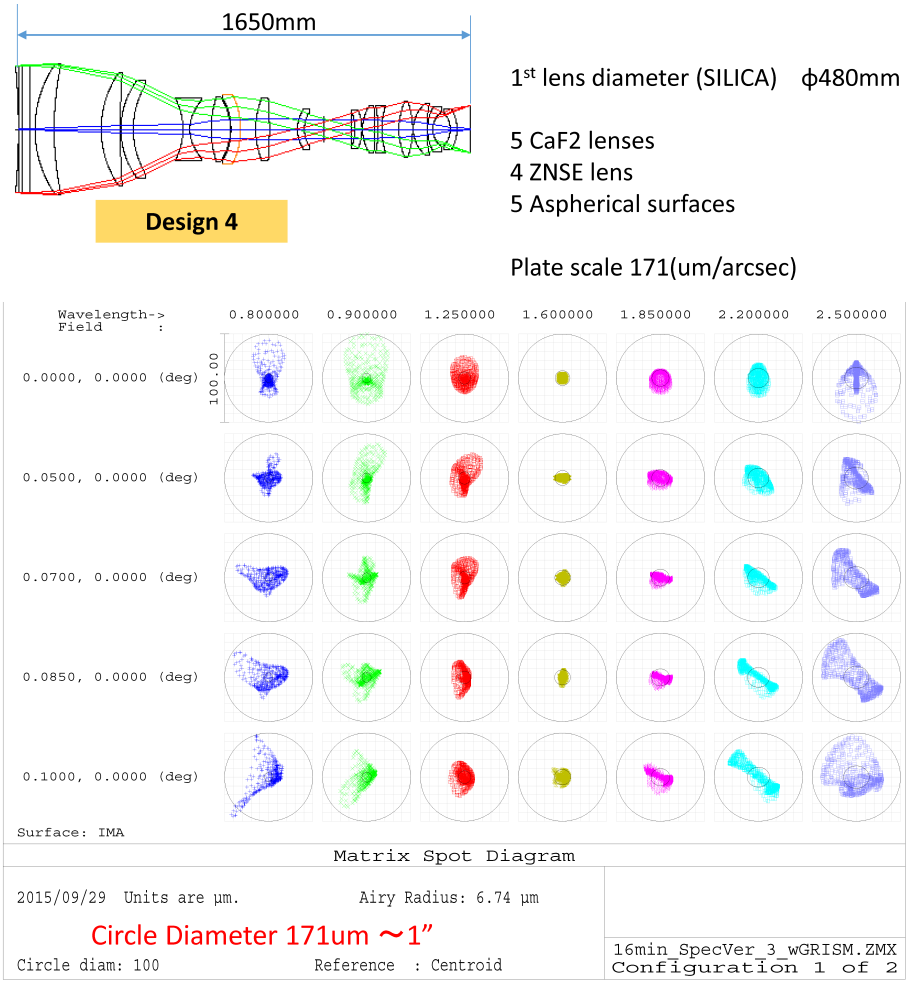

Figure 7.13: Optical layout and spot-diagram of the wide-field spectrograph (Y. Tanaka, section 7.3.2)

Optical interface

Since IRMS is not designed to attach to the Cassegrain focus, we investigated the possibility of installing IRMS onto the Subaru Nasmyth platform. The maximum field of view (FoV) at the Nasmyth focus is ϕ ~3.5 arcmin with the K-type image rotator and ϕ ~4.0 arcmin without the image rotator. If we remove the image rotator unit from the Nasmyth, we can extend the maximum FoV up to $\phi \sim 6.0$ arcmin. Since IRMS is supposed to use its own instrument rotator to de-rotate the field rotation, we considered the case with the FoV of $\phi \sim 6.0$ arcmin for this study.

Figure 7.14 shows the overall optical layout of MOSFIRE (McLean et al., 2010), which is almost identical to that of IRMS. The IRMS optical system mainly consists of the dewar windows, the CSU module, the collimator lens system, the pupil mechanism (Lyot stop), the filters/grating, and the camera lens system. The IRMS is designed to keep the original design of MOSFIRE as much as possible. The changes to the MOSFIRE's optics are driven by the difference in the telescope optical parameters (IRMS Conceptual Design Report v1.7). Since the radius of field curvature provided after TMT/NFIRAOS is steeper and has sign opposite to Keck, the design of the CSU for IRMS is different from that for MOSFIRE. The optical powers of the field lens and collimator lens system were optimized for IRMS to force the pupil to the Lyot stop. The size of the Lyot stop was adjusted to match the beam size delivered

from TMT/NFIRAOS. Other than these modifications, the camera lens system was slightly optimized for IRMS. The optimization of the optical elements was performed without changing their position, meaning that there is no impact on the optomechanical mounting. To adapt IRMS to the Subaru telescope, same modifications of the optical design from MOSFIRE to IRMS, but in opposite way, is required. We need to develop a new CSU optimized for the Subaru's field curvature and new lens for the collimator system, which contains a large CaF2 field lens and separated group of 5 lens. The modification of the camera lens system should not be necessary since the difference between MOSFIRE and IRMS is very small.

Table 7.6 summarizes the optical parameters of IRMS at the Subaru Nasmyth focus, compared with those of Keck/MOSFIRE and TMT/NFIRAOS+IRMS. The pixel scale of IRMS at the Subaru is expected to be 0.25 arcsec/pixel, which is not optimized for the expected seeing size ($< 0''.2$ at K) obtained by GLAO. The FoV of IRMS at the Subaru is limited by the maximum FoV at the Nasmyth focus, which is $\phi \sim 6'.0$. This limitation in the FoV reduces the number of the available slits from 46 to 36.

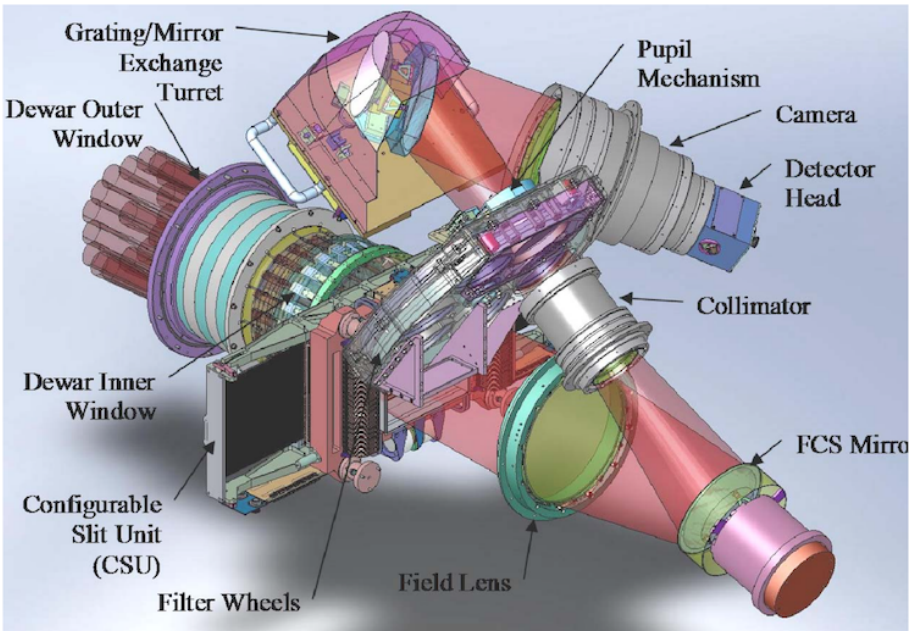

Figure 7.14: The optical layout of MOSFIRE (McLean et al., 2010), which is almost identical to IRMS.

Mechanical interface

IRMS is designed to use at the Nasmyth focus of the TMT in upright on top of NFIRAOS. The outer envelope of IRMS is about $\phi \sim 2.0$m $\times$ 4.0m ($\phi \sim 3.5$m including the support structure). Since the nominal focal point at the Nasmyth (Ns) focus is located at about 1.0m from the inner edge of the Ns platform and 1.5m above the floor of the Ns platform, the back focal length has to be increased to install IRMS at the Ns platform in upright. Figure 7.15 shows the schematic view of the IRMS installed at the Ns platform of the Subaru telescope. In this figure, we increased the back focal length by about 1400mm and use a beam-splitter to reflect near-infrared light upward to IRMS and transmit visible light to a wavefront sensor (WFS). The back focal length can be increased by moving the secondary mirror position toward the primary mirror. We found that the back focal length is increased by 1420mm by moving the secondary mirror by 25mm. However, changing the back focal length will induce additional spherical aberration. We performed the simulation to compensate the aberration by deforming the shape of the primary mirror and secondary mirror. We found that changing the conic constants for the primary mirror and secondary mirror from -1.0197 to -1.0064 and from -1.9173 to -1.74163, respectively can nicely compensate the aberration induced by the change of the back focal length. The modified conic constant

Table 7.6: Summary of the optical parameters for the IRMS at Subaru Nasmyth focus, compared with those for Keck/MOSFIRE and TMT/NFIRAOS+IRMS.

	Keck/MOSFIRE	TMT/NFIRAOS+IRMS	Subaru/IRMS at NsIR (w/o IMR)
Effective focal length (m)	149.572	450.0	108.512
Aperture diameter (m)	10.3	30.0	7.9
Focal ratio	14.5	15.0	13.7
Exit pupil distance (m)	20	188	17.6
Field curvature radius[a](m)	2.1	-1.3	1.0 (2.5)[b]
Pixel scale (arcsec/pix)	0.18	0.06	0.25
Field of view (arcmin^2)	6.1×6.1	2.0×2.0	$\phi \sim 6'.0$[c]
Wavelength coverage	0.975−2.400μm (Y, J, H, K)		
Detector	2048×2048 Teledyne H2-RG (2.5μm cutoff, 18μm/pix)		
Spectral Resolution	3600 (K) 0″.7 slit (2.8pix)	5300 (K) 0″.16 slit (1.9pix)	6300 (K) 0″.5 slit (1.6pix)
Multiplex	46 slits 7″.1 long for each	46 slits 2″.4 long for each	36[d] 10″.0 long for each

[a] The radius of the field curvature is positive when the field is curved toward the sky
[b] The value in the brackets shows the curvature radius when the back focal length is increased by 1420mm.
[c] The detector has a FoV of 8.5×8.5 arcmin^2, but the actual FoV is limited by the maximum FoV at the Nasmyth focus.
[d] Some of the slits are located outside of the $\phi \sim 6'.0$ FoV.

of the primary mirror is similar to the shape of the primary mirror for the Nasmyth Optical platform (without image rotator). By changing the conic constant of the secondary mirror, the mirror shape is deformed by up to 20μm at the edge of the mirror, which is within the range of the expected stroke of the deformable secondary mirror ($\sim \pm 60\mu$m). Total weight of IRMS including the instrument rotator and supporting structure is about 6000 Kg. The maximum weight that can be supported at the Ns floor is about 7000 Kg. To install IRMS at the Ns floor, we need to remove the existing AG/SH layer and K-type image rotator, which weigh more than 1000 Kg in total, as well as all of the other instruments on the same floor.

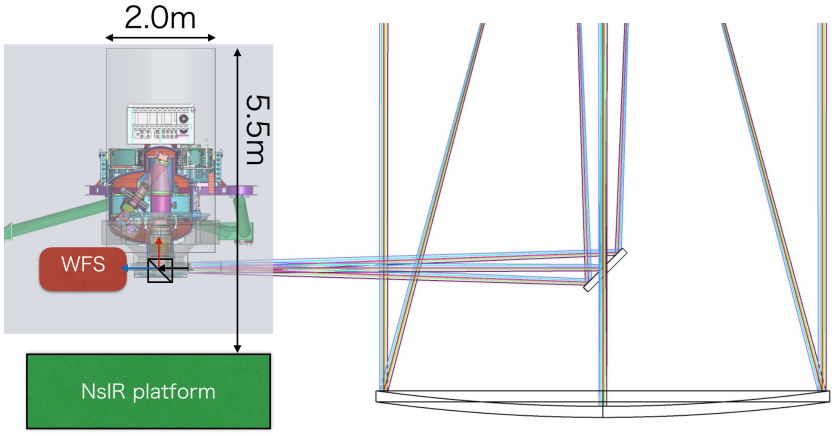

Figure 7.15: Schematic view of IRMS installed at the Nasmyth IR floor of the Subaru telescope.

7.4 Multi-object Integral Field Unit Spectrograph (Starbug+IFU)

Simon Ellis[1], AAO instrumentation group[1], and Yosuke Minowa[2]
[1] Australian Astronomical Observatory (AAO),
[2] Subaru Telescope, National Astronomical Observatory of Japan

We first considered a VLT/KMOS type multi IFU instrument, which uses a number of robotic pick-off arms for selecting a small field from the focal plane of the telescope. However, we found that the number of deployable pick-off arms on the Subaru's Cassegrain focal plane should be less than the number of KMOS pick-off arms because of the limitation in the space around the focal plane, although the FoV of the ULTIMATE is about 4 times larger than that of KMOS. Moreover, since KMOS weighs more than the weight limit for the Subaru's Cassegrain instrument (∼2,500 Kg), we should consider the instrument smaller than the KMOS.

To overcome the weight limit for the Cassegrain focus and increase the number of IFUs, we came up with the idea to separate the instrument into the IFU system and the spectrograph. In this idea, the IFU system is attached to the telescope Cassegrain focus and feed the light into the spectrograph located at the floor using optical fibers. Australian Astronomical Observatory (AAO) brought the idea to use fiber bundle IFUs, which are deployable anywhere on the focal plane using robotic positioners, called "Starbug", developed at the AAO for the TAIPAN instrument being built for the UK Schmidt telescope. The positioner system shares much of the technology with the TAIPAN system which is currently working in the laboratory and will be demonstrated its on-sky feasibility in early 2016. Basically, the Starbug IFU system can be connected to any spectrograph through the fibers. We first considered the case of using our existing near-infrared spectrograph MOIRCS. In this case, the number of deployable IFUs is limited by the size of the spectrograph and is smaller than KMOS as described below. However, the number of the IFUs can be increased by developing a new dedicated spectrograph in future. In this section, we describe the multi-IFU spectrograph using newly developed Starbug positioners and our existing based on the conceptual study conducted by the AAO (Ellis et al., 2015).

7.4.1 Instrument description

The instrument is cosidered to consist of four main sub-systems as shown in Figure 7.16. The wide field corrector corrects the astigmatism of the Ritchey-Chretien telescope, and provides a telecentric input into the IFU optics. Deployable IFUs are positioned on a field plate at the corrected Cassegrain focal plane of the telescope. The IFUs are positioned using robotic Starbug positioners. These can move independently of one another and over a large patrol distance, enabling efficient and versatile configuration of the IFUs. Each Starbug contains a single IFU, consisting of a hexagonally packed array of 61 hexagonal lenslets. Each lenslet subtends 0.15 arcsec on the sky (from flat-to-flat), giving a total field of view per IFU of 1.18 sq. arcsec[1]. The IFUs image the pupil onto cores of a fibre array, and thereby feed the bench mounted spectrograph via a fibre cable, which terminates in a slit unit, which is housed, and cooled within the MOIRCS fore-dewar.

Wide field corrector unit

The wide field corrector unit consists of the wide field corrector (WFC) itself and a field plate on which the Starbugs are located (Figure 7.17). The WFC has two functions. First, it corrects the astigmatism of the Ritchey-Chrtien focus over a 15 arcmin diameter field-of-view. Secondly, it provides a telecentric input for the IFU optics. Note that the Ritchey-Chrtien telescope is designed to deliver a wavefront with no spherical aberration or coma, and these properties are preserved by the WFC. The curvature of the field remains uncorrected, but is accommodated by use of a curved field plate. The WFC delivers

[1]The Milky Way dark matter mapping science described in Sec.5.5 requires different configuration of Starbugs with smaller number of elements per IFU and possibly larger number of IFUs. Using such different sets of IFUs could be considered

Table 7.7: Instrument parameters of Starbug based IFU spectrograph

IFUs	
Number of IFUs	8-13[a]
Number of elements per IFU	61 Hexagonally packed
Spatial sampling per element	0.15 arcsec
Total field of view per IFU	1.18 square arcsec
Total patrol area	$\phi \sim 15$ arcmin[b]
Minimum separation between IFUs	25 arcsec
Spectrograph (MOIRCS)	
Wavelength coverage	0.9-1.8 μm
Spectral resolving power	500-3000
Dispersion	1.6 $\mathring{A}$ per pix (J), 2.1 $\mathring{A}$ per pix (H)
Sampling	2-5 pixels in FWHM
Combined properties	
Total efficiency	9% (J), 12% (H)

[a] This number can be increased by using a new larger spectrograph.
[b] FoV of the wide field corrector.

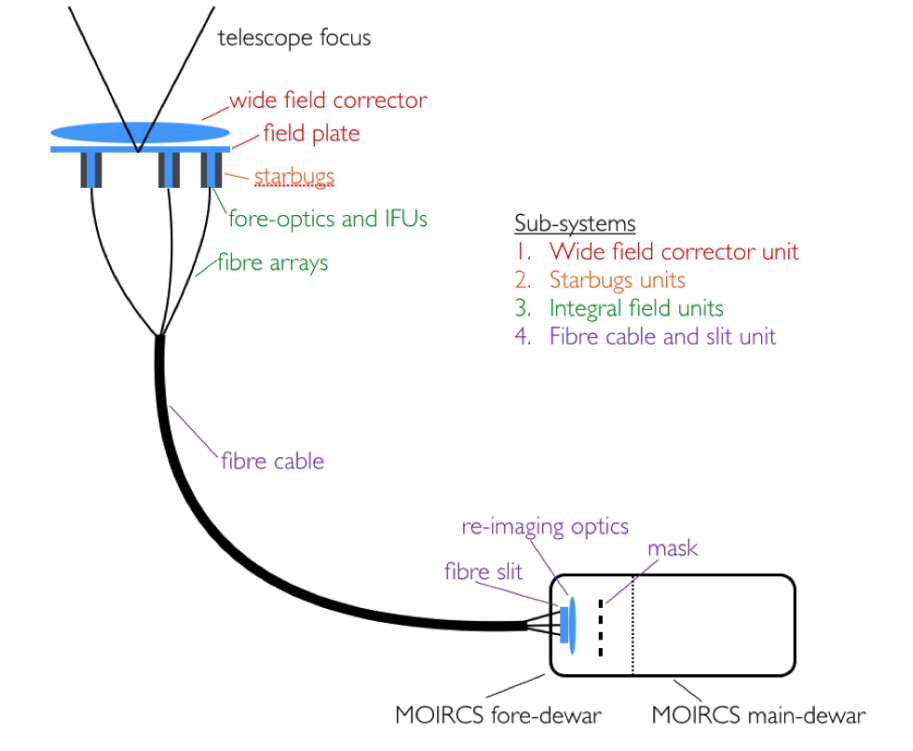

Figure 7.16: Block diagram of the starbug-based multi fiber IFU system, showing the sub-systems.

excellent image quality across the entire field of view across all MOIRCS spectroscopic bands, J, H and K (Figure 7.17). The field plate provides a surface for the Starbugs to move around the focal plane. The field plate is curved to accommodate the Petval curvature of the telescope focus, ensuring that there is no defocus across the patrol field.

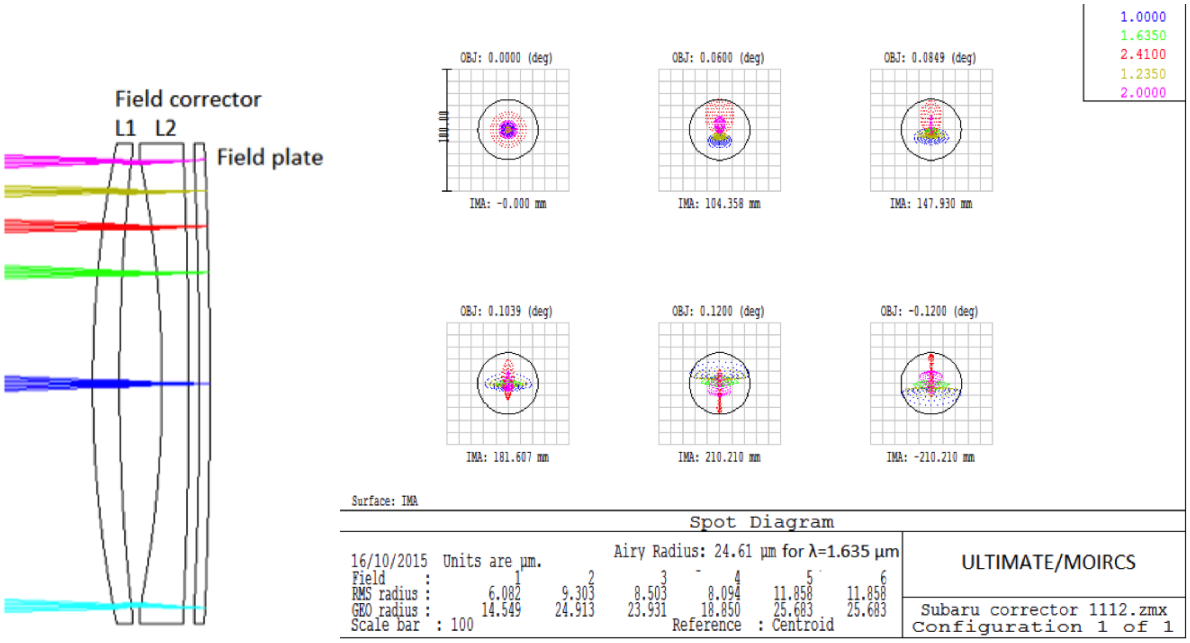

Figure 7.17: (Left) Ray tracing diagram of the wide field corrector optics, including the field plate. (Right) Spot diagrams for the Subaru telescope plus wide-field corrector.

Starbug unit

The Starbugs will be located on the underside of the field-plate. The Starbugs adhere to the glass by creating a negative pressure within the Starbug body, which is routed from an external vacuum system. The principle of operation of a Starbug is illustrated in Figure 7.18. Each Starbug consists of two coaxial piezo-electric tubes. The fore-optics and IFU are housed within the central tube. The Starbug is made to walk by electronically controlling the piezo-tubes such that they extend, contract and bend as shown by the sequence in the middle panel of Figure 7.18. Precise closed loop control of directional

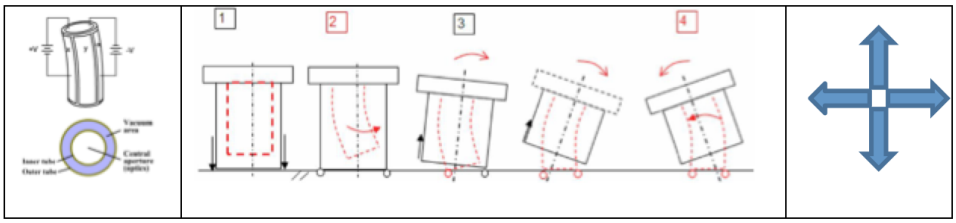

Figure 7.18: The principle of operation for a Starbug.

and rotational motion is enabled by an on-axis metrology camera, which observes three backlit metrology

fibres (fiducials) on each Starbug, as shown in Figure 7.19. The IFU axis is defined with respect to these metrology fibres. Additionally there are a number ($\sim$ 16) of circumferential fiducials on the glass-field plate. Thus, fine positioning is then achieved while the telescope is on target by referencing the Starbug fiducials to the field-plate fiducials. Acquisition is then achieved by aligning guide bundles to guide stars.The positional accuracy of Starbugs is better than 5 microns, corresponding to 10 milli-arcseconds on sky, and typical reconfiguration times are achievable within the time taken to slew the telescope.

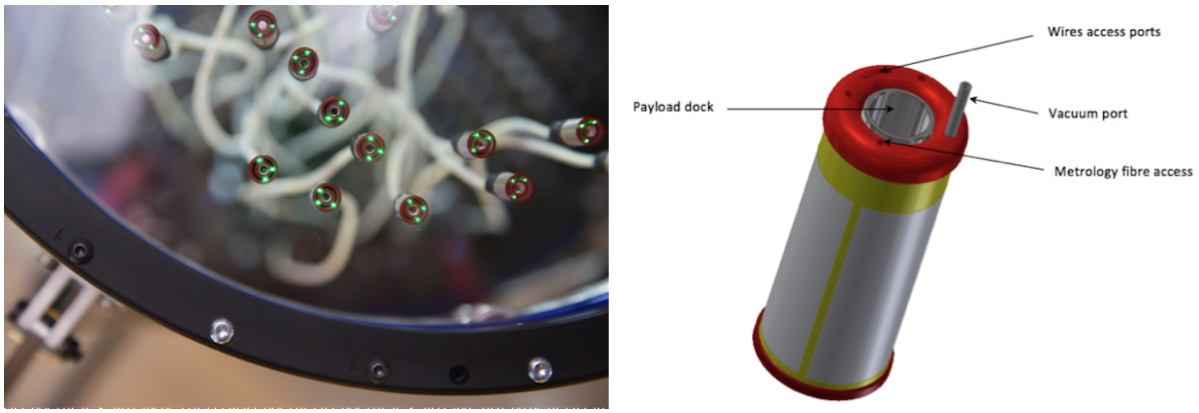

Figure 7.19: (Left) Starbugs on a field-plate, showing the green back-lit metrology fibres, and the red slippers. (Right) Schematic view of the Starbug, showing the payload dock tube, metrology fibres, vacuum port and wires access ports on the backside. The Starbug system used in the ULTIMATE instrument shares much of the technology with the TAIPAN system which is currently working in the laboratory and will be demonstrated its on-sky feasibility in early 2016.

The Starbug fiber positioner is a new technology developed by AAO. The Starbug will be used for the TAIPAN instrument at the UK Schmidt telescope. TAIPAN is being built by AAO to carry out a comprehensive spectroscopic survey and to prove the concept of the Starbug positioner, which is proposed to use on the Giant Magellan Telescope. TAIPAN will start its commissioning in early 2016 and demonstrate the feasibility of the Starbug technology, reducing the risk for the future ULTIMATE instrument. The ULTIMATE Starbugs differ from the TAIPAN Starbugs in that they have a larger diameter, carry a heavier payload, and will operate at a lower atmospheric pressure. Therefore the vacuum necessary to adhere the Starbugs to the field-plate and allow normal operation will be tested by prototyping the Starbugs for the ULTIMATE instrument.

Integral field unit

The IFU unit consists of three main components, the fore-optics, the lenslet array, and the fiber array. These components are aligned and glued into position in a stainless tube and then the tube is inserted into the Starbug.

The fore-optics magnify the beam from the telescope to provide an appropriate plate scale for the lenslet array (magnification is about 3.5 to have a lenslet width of 250 μm for a sampling of $0''.15$ per lenslet). In principle, one could place the lenslet array directly at the focal plane of the WFC without using the fore optics. However, there are advantages to a larger physical lenslet size. Most fundamentally, a large lenslet size compared to the fibre core diameter minimize shifts in the pupil image and geometric focal ratio degradation (FRD). Secondly, small lenslets are not readily available from manufacturers and are likely to be expensive and to pose a significant risk in meeting the required specifications. AAO has significant experience working with larger lenslets, having used a 40×25 250 μm lenslet array. Additionally the use of fore-optics has advantages other than its effect on lenslet size. First, the spatial sampling of

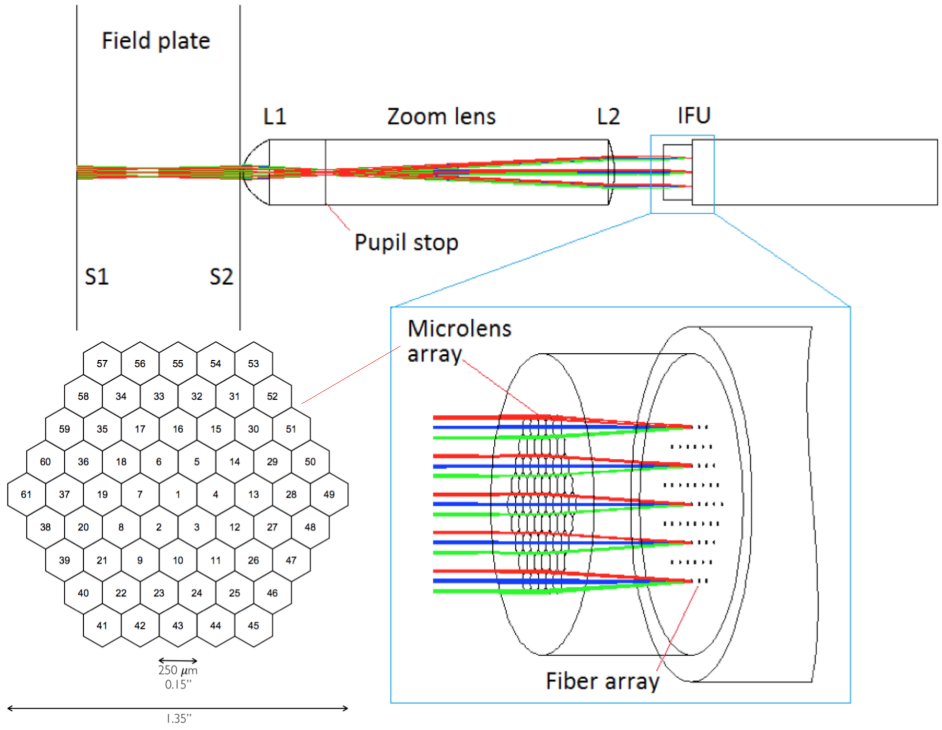

Figure 7.20: Ray diagram for the ULTIMATE fore optics and lenslet array.

the IFUs could be changed by changing the fore-optics, without changing the lenslet array. Secondly, the use of fore-optics allows one to incorporate a pupil stop to minimize thermal emission and stray-light. A ray diagram for the fore-optics is shown in Figure 7.20. The fore optics consist of two plano-convex lenses that are bonded together. The planar face of the second lens will be coated in a low emissivity material in order to create a pupil stop at the interface between the two lenses. Additionally the outer surface of the second lens will also be coated in low emissivity material in order to shield thermal and stray light from within the Starbug.

The lenslet array samples the image in order to provide spatially resolved spectroscopy. There are several advantages to using a lenslet array for the sampling, over using a bare fibre array (e.g. PPAK, MANGA). A lenslet array provides a contiguous field of view with high fill-factor, as it is unaffected by the cladding of the fibres, which otherwise create dead space in the array. A lenslet array allows the formation of a pupil on the face of the fibre. Both the size of the pupil, and the focal ratio can then be chosen so as to optimise the coupling efficiency into the fibre. We will use a 250 μm pitch hexagonally packed lenslet array with 61 elements will be used. Each lens subtends an angle of $0''.15$ on the sky, measured from flat-to-flat (Figure 7.20). The microlens array will be bonded to a fibre array. The fibre array will consist of multi-bore ferrule at the same pitch (250 μm) as the microlens array, and precisely aligned to it.

The assembly of the IFU with the fore-optics will be prototyped to verify its technical feasibility. The throughput across the full wavelength range will be measured for the Starbug optics assembly taking into account internal transmission, AR coating performance and the filling factor of microlens array. The magnification lens is design to perform close to diffraction limit. This will be confirmed experimentally. Additionally the method for housing the optics in the docking tube will also be prototyped.

Fibre cable and slit unit

The fiber core diameter (~ 35 μm) is determined to include whole pupil image formed by the microlens array (~ 29 μm) with some room for misalignment (± 3 μm). To accommodate 13 IFUs with 61 fibers for each along the slit of MOIRCS, the cladding should be less than 120 μm. A separation of 80 μm (TBD) between fibres along the slit is sufficient to ensure the fibre-to-fibre cross-talk due to the instrumental PSF is less than 1%, and thus there is no requirement for cladding less than 80 μm (TBD).

For good transmission at $\lambda < 1.8$ μm, it is necessary to use a low OH fibre. Figure 7.21 shows the transmission of Polymicro FI fibre as an example. An alternative to the low OH silica fibres is to use ZBLAN fluoride fibres to extend the transmission of the fibres into the K band. Historically, K band fibres have seen only limited use in astronomical applications because of poor transmission and fragility of the fibres. However, recent developments now make these fibres a viable option. Figure 7.21 shows the measured transmission of a ZrF_4 made by Le Verre Flouré. The ZBLAN fibre has not been well tested for its handling (e.g., inserting fibres into ferrules at the fibre array, or into V-grooves at the fibre slit) and the FRD properties. The cost of ZBLAN fibres is likely to be much more expensive than silica fibres. The K band fibres appear to be very promising, but laboratory tests are necessary to gain experience and understanding of their properties.

The slit unit will be attached to the spectrograph side edge of the fibre cables. The purpose of the slit unit is to align the fibres with the MOIRCS entrance slit, and to convert the output back to an f/12.4 telecentric beam. The slit relay optics magnifies the fibre core from fibre slit to the aperture mask, then the spectrograph optics de-magnifies the mask image so that each fibre is matched to 2 pixels on the MOIRCS detector, which has 18 μm square pixels. The slit unit will consist of a number of identical slitlets, each containing 30−40 fibres, each of which feeds its own set of reimaging optics (see Figure 7.22). The entire slit unit will be housed in the MOIRCS fore-dewar, which the fibres enter via a vacuum feed-through. This will minimise thermal emission from the slit blocks and relay optics. The slitlet reimaging lenses (zoom lenses and field lens) are mounted into a block of V-grooves. All the fibre slitlets and all lenses will be bonded to the slit block using cryogenic compatible glue. The output of the fibres is reimaged onto a mask which follows the curvature of the focal surface of the Subaru telescope (~ 2425 mm convex toward the spectrograph).

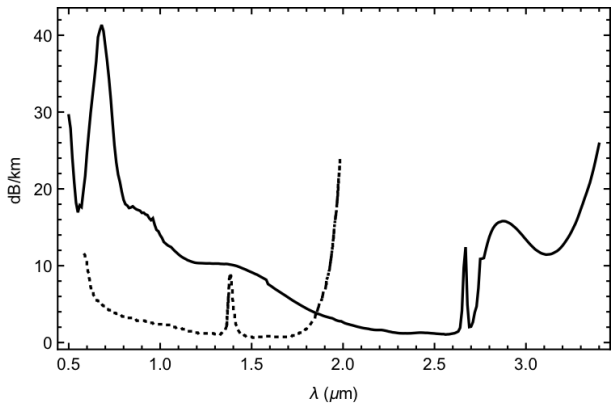

Figure 7.21: Measured transmission of Le Verre Flouré ZrF_4 fibre (solid) compared to Polymicro FI (dotted).

7.4.2 Compatibility with the wide-field imager

The Starbug IFU system can be made to be compatible with a wide-field GLAO corrected Cassegrain imager, such as the one described in Section 7.2, to reduce the cost of the imager and to avoid frequent Cassegrain instrument exchange by using the same wide-field corrector (WFC). This assumes that the image quality achieved by the WFC is sufficient to feed the Starbug IFUs (i.e. the WFC cannot rely on

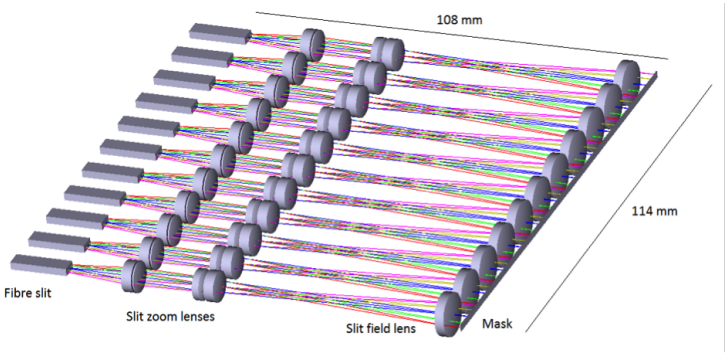

Figure 7.22: Schematic view of the slit unit.

the imager to correct any aberrations., if it is also to be used for the Starbug IFU system). To enable the same WFC to be employed for both imaging and integral field spectroscopy, none of the ancillary components of the Starbug IFU system must vignette the beam when the Starbug IFU is not in use. The metrology camera needs to be located above the WFC, but it can be located in the shadow of the secondary mirror and will not affect the imager. The Starbug electronics and connector plate can be positioned out of the beam permanently. The bug-catcher, which suppots the Starbug positioners, must be retractable, such that when the Starbug IFU system is in use it moves under the field plate to position the Starbugs, and when the Starbug IFU system is not in use, it houses the Starbugs, and moves out of the beam. Therefore, the compatibility of ULTIMATE with the wide field imager requires sufficient space between the field plate and the imager to position the Starbugs and bug-catcher, and sufficient space at the Cassegrain focus to locate the electronics and connector plate out of the beam.

7.4.3 Development plan

The development of the Starbug IFU system will take place in 5 stages, as follows.

Stage 1. Prototyping plan
This stage summarizes the science case, the optical design for the IFU and fore-optics, the stray light analysis for the fore-optics, the background and performance model, the plan for prototyping the instrument, and detailed cost analysis for the project. This stage has been completed at the end of 2015 and documented by AAO (Ellis et al., 2015).

Stage 2. Prototyping and instrument conceptual design
This stage will consist of prototyping and testing the critical components of the instrument: the Starbugs, IFU, and fibre cable (including K-band fibre). These tests will result in the final concept design, including the optical design, scattered light analysis, mechanical design and a prototyping test report, as well as detailed costings and schedule for the next phase. The prototyping and tests will be carried out in the laboratory at AAO. In addition, further on-sky tests of the prototype IFUs will take place at the Anglo-Australian Telescope (AAT) or Subaru telescope.

Stage 3. Instrument build and commissioning
This stage will complete the final design, fabrication, assembly and commissioning of the Starbug IFU system at the Subaru telescope.

Stage 4. Spectrograph upgrade
This stage will involve the upgrade of the spectrograph to increase the throughput, support an increased number of IFUs and support OH suppression fibres.

Stage 5. OH suppression
This stage will involve the introduction of OH suppression fibres to the fibre feed.

7.5 Performance Modeling

Yosuke Minowa[1], Simon Ellis[2], and AAO instrumentation group[2]
[1] Subaru Telescope, National Astronomical Observatory of Japan,
[2] Australian Astronomical Observatory (AAO)

We conducted the simulation of the observations with wide-field NIR imager, multi-object slit (MOS) spectrograph, and multi-object fiber integral field unit (IFU) spectrograph. Table 7.8 summarizes the specifications of the simulated instruments. To predict the sensitivity of the instruments, we have modeled the throughput and the background emission for the instruments. The system throughputs of the simulated instruments are assumed to be similar to VLT/HAWK-I (Kissler-Patig et al., 2008) and Keck/MOSFIRE (McLean et al., 2010) for the imager and MOS spectrograph, respectively. The throughput of the multi-object fiber IFU system is estimated from the expected throughput of each component of the instrument, including the all sub-systems (WFC, IFU, fiber, and slit unit) and MOICS. The background emission is consist of the sky emission line, the thermal emission fro the telescope and the instrument, and detector emission (dark current and readout noise). We have used the Maunakea sky emission data provided at the Gemini Telescope's web site[2] for the imaging and MOS spectroscopy simulation and the model developed by AAO (Ellis et al., 2015) for the fiber IFU simulation. The thermal emission of the telescope and the instrument has been modeled by assuming that each component of the telescope and instrument emit black body radiation characterized by a temperature T with an emissivity ϵ of one minus throughput. We assumed that the temperature of the non-cooled components is about 276 K. The detectors of the instruments assumed in this simulation are H2RG or H4RG. The expected dark current for such detectors is < 0.01 e$^-$/pix. The effective readout noise with Fowler or up-the-ramp sampling is expected to be $\sim$4 e$^-$/pix.

Table 7.8: Specifications of the simulated instruments.

	Imager	MOS	Multi-Object IFU
Wavelength Coverage	0.8-2.5μm		
Plate Scale	0.10 arcsec/pix		0.15 arcsec/spaxel
FOV	$\phi \leq 16'$		IFU: 1$''$.18×1$''$.18, Patrol area: $\phi \sim 15'$
Filters	YJHK + NB filters	0.9−2.4 μm	0.9−1.8 μm
Spectral Resolution	−	$\sim$3000 (0$''$.4 slit)	500−3000
Multiplicity	−	$\sim$100 slits (TBD)	8−13 IFUs (TBD)
Detector	4×H4RG(Teledyne)		2×H2RG(Teledyne)
Efficciency[a]	$\sim$ 48%(J,H), $\sim$40%(K)	$\sim$33%(J),$\sim$35%(H,K)	$\sim$7%(J),$\sim$10%(H)

[a] Total Efficiency includes atmosphere, telescope, and instrument (optics + detector).

7.5.1 GLAO PSF

We used the PSF obtained from the GLAO simulation performed by Oya et al. (2014). We assumed that the GLAO system uses 4 laser guide stars ($R \sim$ 10mag) and 4 low-order natural guide stars ($R \sim$ 18mag) located at the outer edge of the FOV. A number of the PSF in optical and NIR bands are calculated by taking into account the location of the PSF in the FOV, the observing condition (natural seeing), seasonal variation of the turbulence profile, and dependence on the zenith angle. To simulate the observations of galaxies in famous deep fields, COSMOS, Subaru Deep Field (SDF), and Subaru/XMM-Newton Deep survey Field (SXDF), we used a different PSF depending on the field as summarized in Table 7.9. Since we found that the PSF profile does not change very much within the FOV, we used the PSF at the center of FOV under the moderate seeing condition (FWHM$\sim$0".44 in K band) in each deep field.

[2]http://www.gemini.edu/sciops/telescopes-and-sites/observing-condition-constraints/ir-background-spectra

Table 7.9: Summary of the GLAO PSF used in the simulation.

Field	COSMOS	SDF	SXDF
RA,DEC	10:00:28.60,+02:12:21.0	13:24:21.3,+27:29:23.0	02:18:00.00,-05:00:00.0
Zenith Angle	15 deg	15 deg	30 deg
Month	Feb.	Apr.	Oct.
FWHM(seeing)	0".67(J),0".59(H),0".48(K)	0".58(J),0".50(H),0".46(K)	0".61(J),0".58(H),0".48(K)
FWHM(GLAO)	0".27(J),0".22(H),0".21(K)	0".20(J),0".19(H),0".18(K)	0".26(J),0".23(H),0".21(K)

7.5.2 Imaging

We performed the simulation of broad-band (K-band, $\sim 2.2\mu$m) and narrow-band (Brγ, $\sim 2.16\mu$m) imaging observations of $z \sim 2$ galaxies and evaluated the sensitivity and spatial resolution achieved with the ULTIMATE-Subaru. In case of the narrow-band (NB) imaging, we assumed that Hα emission line from $z \sim 2$ galaxies is shifted to the wavelength coverage of the NB filter.

We used HST/WFC3 H-band (F160W) images of $z \sim 2$ galaxies to model the rest-frame optical profile and brightness of $z \sim 2$ galaxies. Sample of $z \sim 2$ galaxies are taken from CANDELS (Koekemoer et al., 2011) GOODS-South survey whose survey area is compatible to the ULTIMATE-Subaru. We selected $K_{AB} < 23.9$ star-forming BzK galaxies at $z = 2.1 - 2.6$ in the GOODS-South from MUSYC (Cardamone et al., 2010) catalog, whose redshift are spectroscopically confirmed. Although we used the highest spatial resolution NIR images of $z \sim 2$ galaxies obtained from the HST/WFC3 archive data, simple convolution of the WFC3 image may not reproduce well the GLAO image since the WFC3 spatial resolution (FWHM$\sim 0''.18$) is a bit worse than the best GLAO resolution (FWHM$\sim 0''.15$). Thereby, we extracted galaxy morphological parameters, effective radius (R_e), Sersic index (N), axis ratio, and position angle, from the HST images of sample galaxies, constructed the model galaxy images from the extracted morphological parameters, and then convolved the model galaxy imaged with the simulated GLAO PSF. Finally, we added the noise corresponds to 5 hours integration time to evaluate the sensitivity limitation in a single night observation.

Figure 7.23 shows that the 5 σ limiting magnitude achieved with 5 hours integration time at COSMOS, SDF, and SXDF as a function of the effective radius of the star-forming galaxies at $z \sim 2$. In the same plot, we also show the limiting magnitude achieved with seeing (no AO) and diffraction-limited (SCAO) conditions. We found that the sensitivity gain with the ULTIMATE-Subaru compared with the seeing instrument is 0.3−0.6 mag in both K-band and Brγ filters for galaxies with $R_e < 3.0$ kpc. The Brγ imaging simulation shows that we can reach Hα emitters with the star-formation rate (SFR) < 10 M$_\odot$/yr for $R_e < 3.0$ kpc galaxies with 5 hours integration time of the ULTIMATE-Subaru imager.

Figure 7.24 shows that the simulated S/N map of the NB (Brγ) imaging of Hα emitters with 5 hours integration time made from the HST/WFC3 images of star-forming galaxies at $z \sim 2.3$ in SXDF (Tadaki et al., 2014). The clumpy structures in the galaxies are clearly resolved in the ULTIMATE-Subaru image, while they are not resolved in the seeing image.

To examine the possibility for studying the morphology of $z \sim 2$ galaxies with the ULTIMATE-Subaru imager, we tried to derive the morphological parameters, Sersic index (N) and effective radius (R_e), from the model galaxies with N=1 (disk) and 4 (elliptical) that are convolved by the GLAO PSF and embedded in the simulated K-band image with 5 hours integration time. The radius (R_e) of the model galaxies were changed depending on the stellar mass estimated from K-band magnitude. We used the mass-size relations of star-forming BzK galaxies (Yuma et al., 2012) and passively evolving galaxies (Cassata et al., 2010) for $N = 1$ and 4 model profiles, respectively. Figure 7.25 shows that the derived morphological parameters (Sersic index and effective radius) from the model galaxies embedded in the K-band image as a function of K-band magnitude (or stellar mass). The input model parameters are also shown in the same plots. The ULTIMATE-Subaru image can nicely reproduce N and R_e other than N for the less-massive galaxies with $\log(M_*/M_\odot) \sim 9$, while the seeing image cannot reproduce N for most of the case and R_e for the less-massive galaxies with $\log(M_*/M_\odot) \sim 9$.

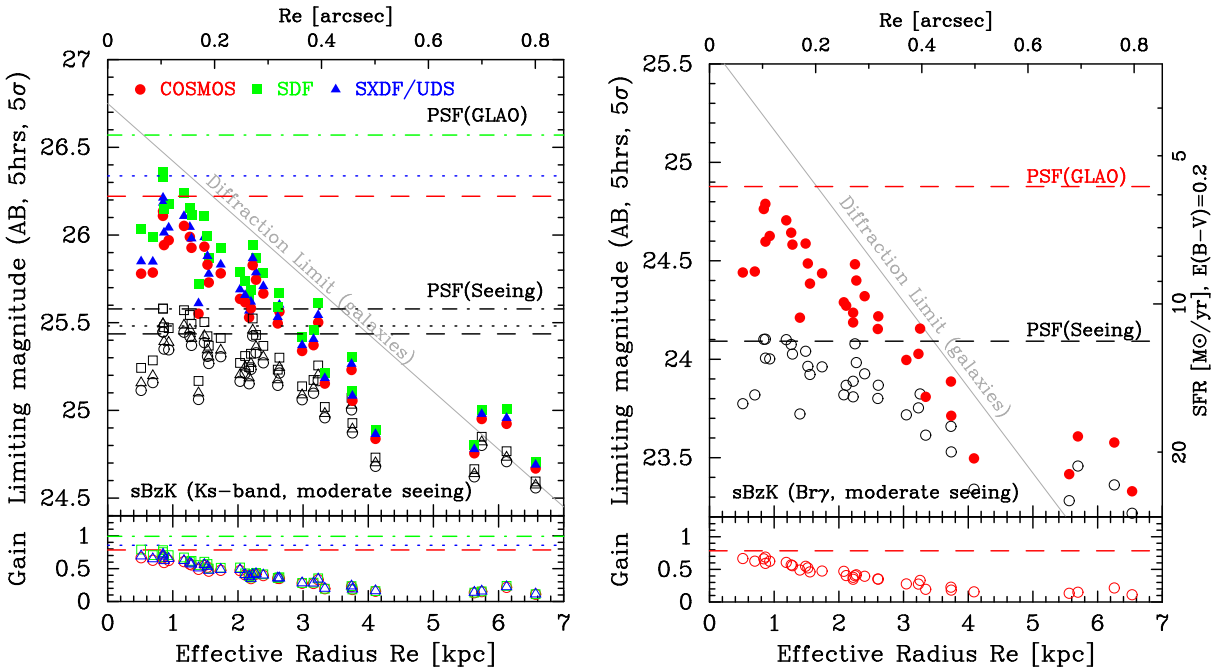

Figure 7.23: The expected 5 σ limiting magnitude (AB) for star-forming galaxies at $z \sim 2$ in broad-band (K, left) and narrow-band (Brγ, right) achieved with the ULTIMATE-Subaru (GLAO) as a function of the size (R_e) of the galaxies. Filled circles, squares, and triangles show the limiting magnitude obtained with GLAO correction at COSMOS, SDF, and SXDF. Open symbols show the limiting magnitude without GLAO correction in each field. Thin solid line shows the expected limiting magnitude with SCAO (diffraction limit). Horizontal dashed, dotted, and dot-dashed lines show the expected limiting magnitude for point sources in COSMOS, SDF, and SXDF, respectively, with and without GLAO correction. Since we found that the field dependence of the limiting magnitude for the galaxies is small, we only show the limiting magnitude in the COSMOS field for the NB imaging in the right panel. In the lower panel, we show the sensitivity gain due to the GLAO correction over the seeing condition.

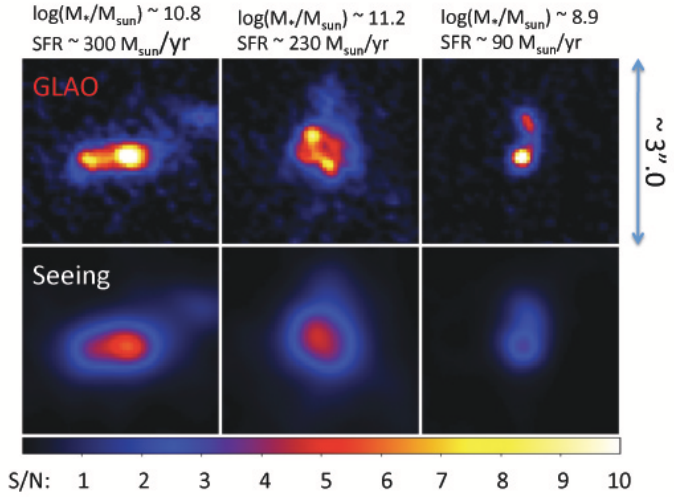

Figure 7.24: Simulated S/N maps of Hα emitters at $z \sim 2.3$ obtained by the ULTIMATE-Subaru NB (Brγ) imaging with 5 hours integration time. Top and bottom panels show the maps with and without GLAO correction, respectively.

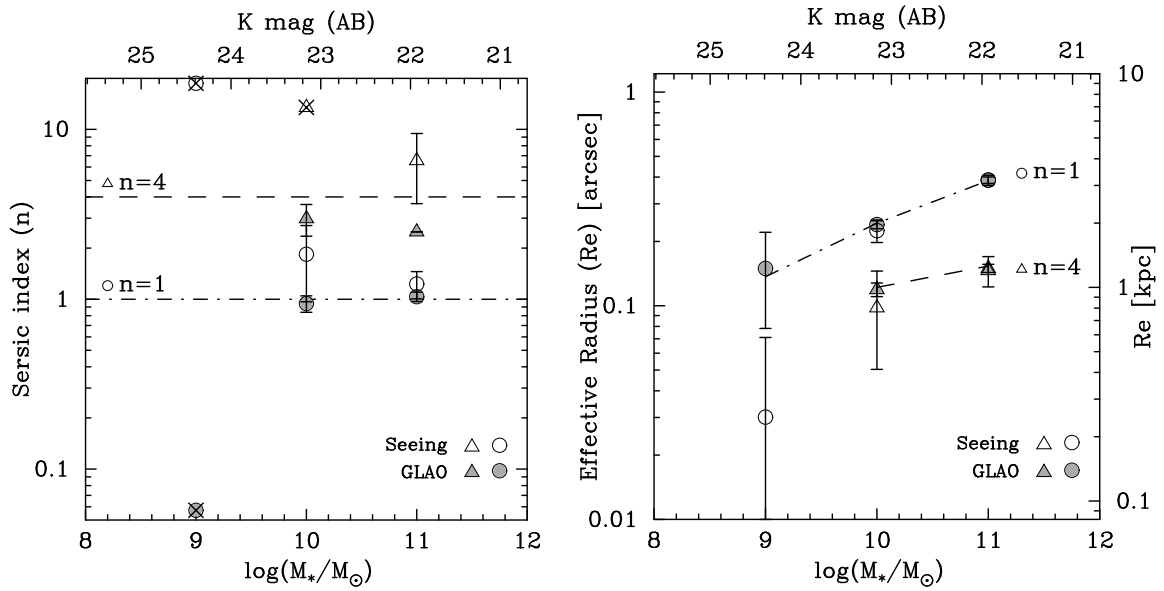

Figure 7.25: Sersic indexes (N, left) and effective radii (R_e, right) derived from the images of model galaxies embedded in the ULTIMATE-Subaru K-band image with 5 hours integration time. The image of the model galaxies are created from the Sersic profiles with $N = 1$ (circles) and 4 (triangles). The size (R_e) of the model galaxies are changed depending on the K-band magnitude (or stellar mass M_*). The images of the model galaxies are convolved by the PSF with and without GLAO correction. Open and filled symbols show the derived parameters from the seeing (without GLAO correction) and GLAO corrected images, respectively. Dashed and dot-dashed lines show the input morphological parameters as a function of the K-band magnitude (or stellar mass). Symbols with crosses show that the parameter derived from the simulated images is not correct.

7.5.3 Slit spectroscopy

We performed the simulation of the observations with Keck/MOSFIRE type slit spectrograph with the aid of the GLAO correction. In case of the spectroscopy, we assumed that $z \sim 2$ galaxies have Sersic profile with $Re \sim 0''.25$, which roughly corresponds to $\sim$2 kpc at $z \sim 1 - 3$, and $N = 1.0$, which is similar size as the clumpy structures in massive star-forming galaxies at $z \sim 2$. The profile of the model galaxy was convolved with the GLAO PSF in the COSMOS field (the worst case among the simulated PSFs). Finally, we added the noise corresponds to 5 hours integration time and evaluated the sensitivity for detecting emission line with $\sim$ 100 km/s velocity width and continuum from galaxies. The spectral resolution with the simulated instrument is assumed to be $\sim$ 3000 with $0''.4$ slit and is assumed to be 3 pixels along the dispersion axis on the detector.

Figure 7.26 shows the emission line flux detected at 5 σ in 5 hours integration time in J, H, and K bands that are expected for GLAO and no AO (seeing). We found that the limiting line flux with the ULTIMATE-Subaru spectrograph can be about 2.4 and 1.9 times deeper than seeing limited spectrograph, such as Keck/MOSFIRE, for point sources and extended sources, respectively. The slit spectroscopy provides better sensitivity than the NB imaging (see Figure 7.23). This enables us to perform redshift confirmation of the Hα emitters discovered by the NB imaging survey.

Figure 7.27 shows 5 σ limiting AB magnitude for detecting continuum from galaxies in 5 hours integration time. The expected limiting magnitudes of the ULTIMATE-Subaru are $\sim$1.0 mag deeper for point sources and $\sim$0.7 mag deeper for extended sources than those expected with the seeing limited spectrograph. The expected 5 σ limiting magnitude for extended sources in K band is about 22.6 mag in the best case. This limiting magnitude is not deep enough to observe less-massive galaxies with $M_* < 10^{10} M_\odot$ which have not been well investigated so far.

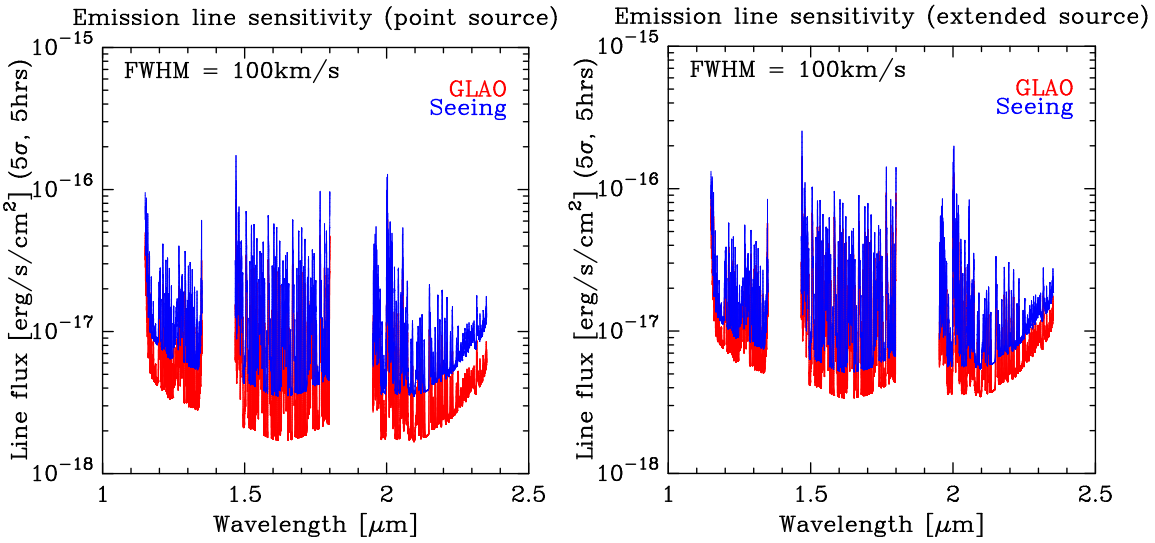

Figure 7.26: Expected emission line flux detected at 5 σ in 5 hours integration time as a function of wavelength in NIR (1.0-2.5μm). Left and right panels show the limiting line flux for point sources and extended sources with the Sersic profile of R_e=0".25 ($\sim$ 2 kpc at $z = 1 - 3$) and $N = 1$, respectively. Red lines show the expected sensitivity of the ULTIMATE-Subaru (GLAO), while bleu lines show the expected sensitivity with no AO correction (seeing, equivalent to Keck/MOSFIRE). We assume that the emission line has a velocity dispersion of 100 km/s in FWHM.

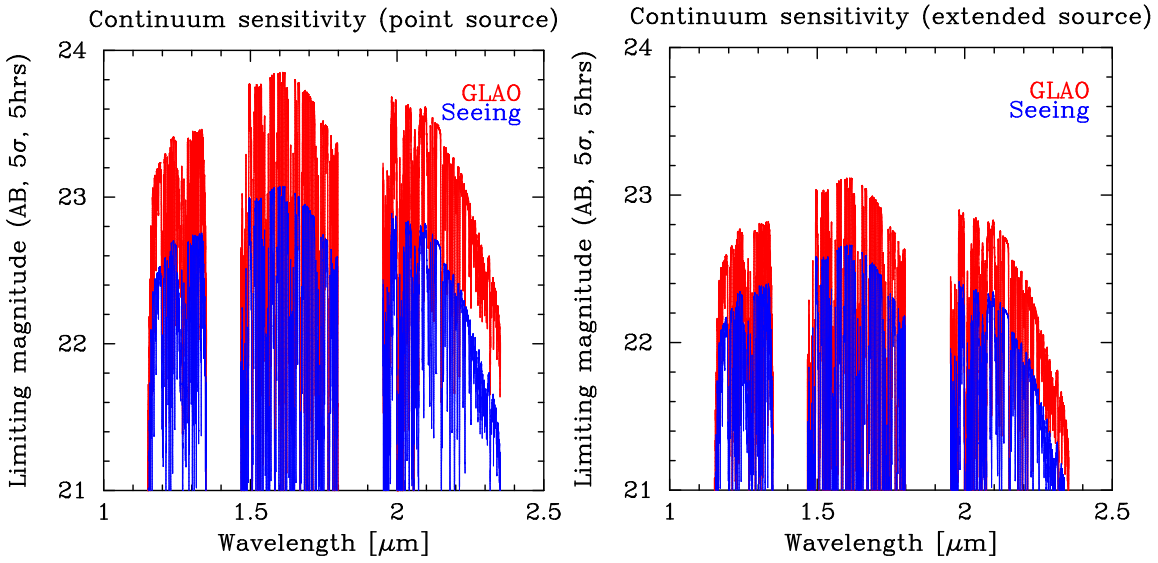

Figure 7.27: Expected continuum flux in AB magnitude detected at 5 σ in 5 hours integration time. Left and right panels show the sensitivity for point sources and extended sources (same as Figure 7.26), respectively. Red and blue lines show the expected sensitivity for the ULTIMATE-Subaru (GLAO), and no AO (seeing, equivalent to Keck/MOSFIRE), respectively.

7.5.4 Fiber IFU spectroscopy

One of the primary science cases of ULTIMATE requires the detection of emission lines in the discs of galaxies at redshifts $0.4 < z < 1.7$. Assuming the Kennicutt et al. (1998) relations between star-formation rate and Hα luminosity, we have calculated the surface brightness of the Hα line as a function of redshift for star-formations rates of 3, 10 and 30 $M_\odot$/yr, assuming that the emission is uniformly distributed over a disc 8 kpc in radius. Figure 7.28 shows the resulting surface brightnesses.

We will assume typical surface brightness of targets of 1.0×10^{-17}, 1.0×10^{-16}, and 5.0×10^{-16} erg/s/cm^2/arcsec^2 (we now use a fixed surface brightness, and not a fixed star-formation rate). Further assuming a typical line width of Gaussian FWHM = 5.0 $\mathring{A}$, we have calculated the signal-to-noise ratio as a function of time and wavelength. Figure 7.28 shows the signal-to-noise ratio per spaxel integrated over the emission line width for 1 hour on source.

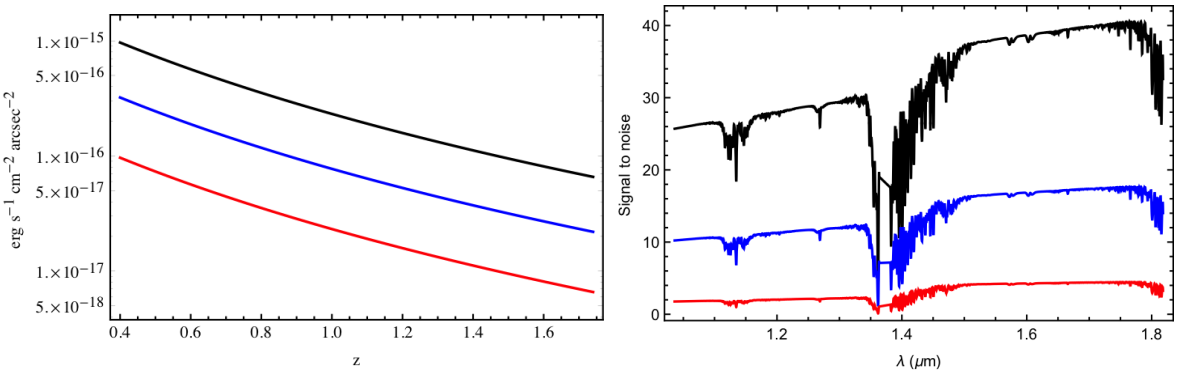

Figure 7.28: (Left) The surface brightness of the Hα line assuming a star-formation rate of 3 (red), 10 (blue) and 30 (black) $M_\odot$/yr, and that the emission is uniformly distributed over a disc 8 kpc in radius. (Right) The signal to noise per spaxel in one hour of exposure time on source, integrated over the width of the emission line, for line surface brightnesses of 1.0×10^{-17} (red), 1.0×10^{-16} (blue), and 5.0×10^{-16} (black) erg/s/cm^2/arcsec^2.

Chapter 8

Development Plans

Ikuru Iwata[1], **Yosuke Minowa**[1]
[1] Subaru Telescope, National Astronomical Observatory of Japan

8.1 Team Organization

ULTIMATE-Subaru is the project to develop the next-generation facility instrument(s) for Subaru Telescope. Also, the implementation of Ground-Layer Adaptive Optics (GLAO) is a major upgrade of the telescope capabilities, which will be able to provide significant benefits to various instruments. Therefore, we believe that the ULTIMATE-Subaru development should be led by initiatives by Subaru Telescope with strong supports from communities using the Subaru Telescope and collaborating institutes. In Fig. 8.1 we show the organization structure currently we have in mind. The PI of the project should be the director of Subaru Telescope. The project manager (PM) will be responsible for the progress of the entire project, including hardware and software development and organizations of science projects using the instruments. The PI and PM will work together to ensure funding for the project (described in the following section).

The development consists of multiple parts; developments of the GLAO system and facility instruments using the GLAO capabilities can be fairly independent. However, the specifications and interface information should be shared very closely among these developments so that the scientific requirements can be achieved. PM should be responsible to ensure sharing the necessary information among parties.

There will be two instrument scientists (IS). One is responsible for the GLAO development, while the other is responsible for the development of new infrared instruments. The GLAO-IS will be an assistant professor of NAOJ which we plan to open the position shortly, and the person will assist PM to plan the GLAO development, play a central role in designing the GLAO system, defining the interface between the telescope system and the GLAO system, and overseeing the development process. There will be the engineering team in Subaru Telescope under the GLAO-IS's supervision, and the GLAO-IS will also take responsibility in communications between the Subaru GLAO development team and possible external developers.

Although we are considering multiple new instruments, there will be one instrument scientist for the instrument developments. The IS will play a central role in organizing the development plans for the instruments, be responsible for defining the interface between the telescope / GLAO system and instruments, and oversee the development process. As we expect major contributions from the external institutes for the development of these instruments, the IS is expected to spend significant efforts to communicate with the external developers.

The project scientist (PS) is a person responsible for organizing development of science team for the project. ULTIMATE-Subaru will be offered to Subaru users community as facility instruments. Also, we expect that there will be large survey(s) to maximize the science outputs from the project. Those will be Subaru Strategic Program(s)[1]. With these prospects in mind, PS will organize communications among science communities (in Japan and collaborating countries) to define the science requirements for both the GLAO system and the instruments in the early stage of the project. Then PS will continue organization of science teams to design the survey programs. PS should be involved the decision making processes of the hardware / software developments to ensure the science goals the communities wish to achieve with the project can be realized.

One important aspect among the software development for such survey-oriented project is the data pipeline and archive. Currently, for HSC large survey (HSC-SSP) Subaru Telescope are working with Kavli IPMU and Princeton University for the development of the pipeline and data archive, and are about to initiate development process of the data archive for PFS. Subaru Telescope wishes to continue to be a central source to provide data products of the surveys with ULTIMATE-Subaru. The development plan for the data pipeline and data archive should be addressed in the early phase of the conceptual design.

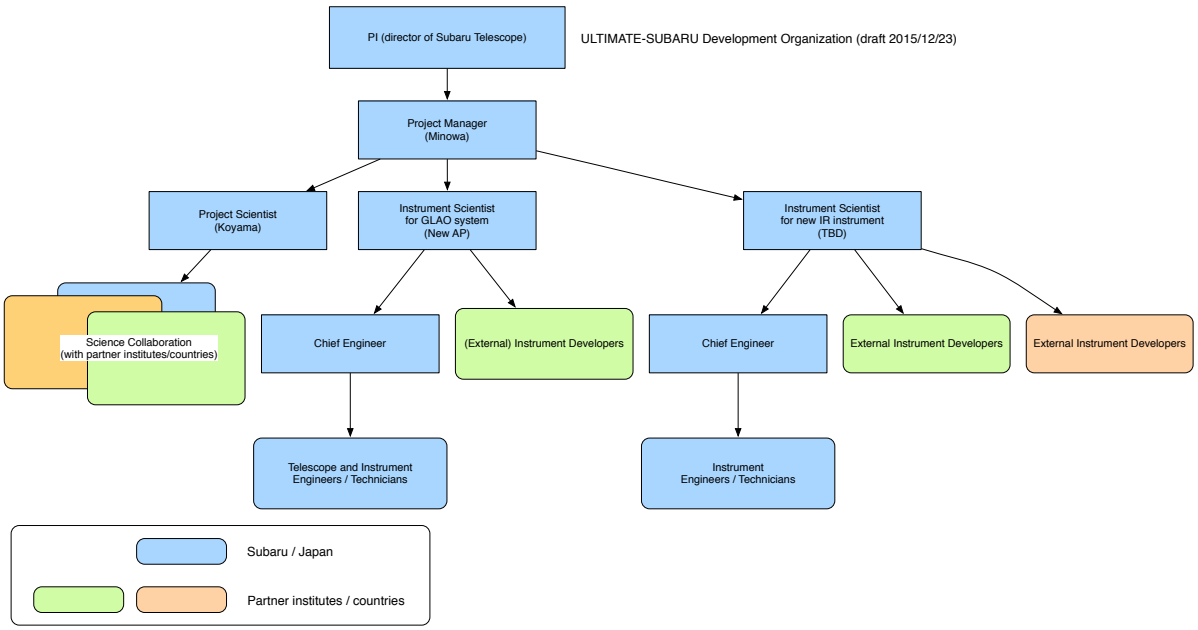

Figure 8.1: Organization structure of the ULTIMATE-Subaru project.

In order to show the minimum number of staff members for the development of the ULTIMATE-Subaru project we consider necessary, in Fig. 8.2 the number and FTEs of Subaru/NAOJ staff members in annual basis are presented. This table basically does not include human resources from other institutes (e.g., universities in Japan or non-Japanese institutes; only one engineer for the GLAO development is included), but we are expecting the main bodies of the instrument development will be other institutes. Two post-doc positions for the GLAO development are expected to be funded by JSPS (Kakenhi).

The commissioning of PFS is expected to happen during the period of 2017–2019 (engineering first light will be in 2018). As we show in the later section, for ULTIMATE-Subaru, these years are the period of preliminary design and the beginning of the detailed design. These years will be the busiest season as commissioning of PFS and development of ULTIMATE-Subaru overlap significantly. Ideally, such major overlap of development activities should be avoided, but it is necessary to commence the engineering observations of the GLAO system in 2023, as timeline described in Section 8.3 shows. If we fail securing

[1] http://www.naoj.org/Science/SACM/Senryaku/

ULTIMATE-SUBARU Human Resources (NAOJ Only)

	Source	2016	2017	2018	2019	2020	2021	2022	2023
PM	NAOJ	0.50	0.70	0.70	0.70	0.70	0.70	0.70	0.70
GLAO									
GLAO-IS	NAOJ	0.25	0.40	0.50	0.70	0.70	0.70	0.70	0.70
Chief Engineer	NAOJ		0.50	0.75	0.75	0.75	0.75	0.75	0.75
PD	JSPS		0.50	0.50	0.50	0.50	0.50	0.50	
PD	JSPS			0.50	0.50	0.50	0.50	0.50	0.50
Engineer	NAOJ				1.00	1.00	1.00	1.00	1.00
Engineer	Ext?			0.50	0.50	0.50	0.50	0.50	0.25
Tech	NAOJ			0.10	0.10	0.25	0.25	0.25	0.25
Tech	NAOJ			0.10	0.10	0.25	0.25	0.25	0.25
Instruments									
Instrument Sci	NAOJ		0.50	0.50	0.70	0.70	0.70	0.70	0.70
Engineer	NAOJ			0.25	0.25	0.50	0.50	0.50	0.50
Engineer	NAOJ				0.25	0.25	0.25	0.25	0.25
Engineer (Optical)	NAOJ	0.25	0.25	0.25	0.25	0.25			
Engineer (Software)	NAOJ			0.10	0.10	0.30	0.30	0.30	0.30
Tech	NAOJ			0.10	0.10	0.10	0.20	0.20	0.20
Tech	NAOJ				0.10	0.10	0.20	0.20	0.20
Pipeline / Archive									
Scientist	NAOJ			0.20	0.20	0.20	0.50	0.50	0.50
PD	NAOJ				0.50	0.50	0.50	0.50	0.50
Engineer (Software)	NAOJ				0.20	0.30	0.50	1.00	1.00
Engineer (Software)	NAOJ						0.20	0.50	0.50

Scientists #	NAOJ/JSPS	2	4	6	7	7	7	7	6
Engineers FTE	NAOJ	0.25	0.75	1.35	2.80	3.35	3.50	4.30	4.30
Tech FTE	NAOJ			0.30	0.40	0.70	0.90	0.90	0.90

Figure 8.2: The number and FTE of Subaru/NAOJ staff members required for ULTIMATE-Subaru development. The positions with red background indicate new recruitments. Here we assume one engineer in a different institute could participate significantly to the GLAO development.

manpower required for the development of ULTIMATE-Subaru, the development schedule will have some delays.

In Fig. 8.3 the annual changes of FTEs are plotted. Without two post-doc positions to be funded by JSPS, the total FTE peaks in 2019 (18 FTEs), and then gradually decreases to 16.3 FTEs in 2023. Although we plan to reduce the number of existing facility instruments around 2018–2019 to ease the heavy workload, this plan already takes into account such reduction of existing instruments. Additional manpower (∼2 scientists or engineers) would be necessary to realize active development for ULTIMATE-Subaru during PFS commissioning phase.

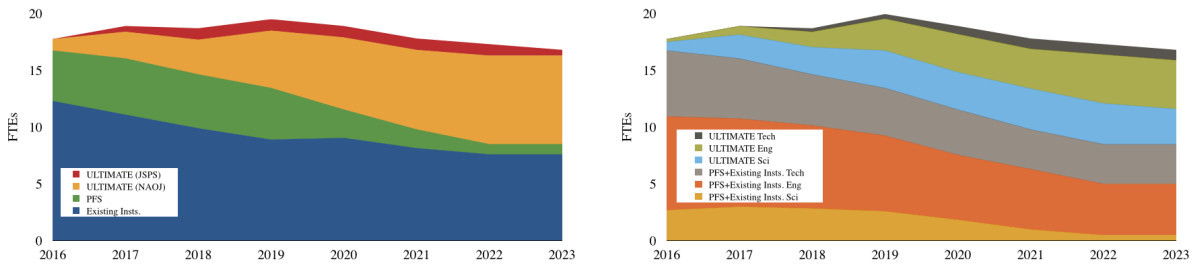

Figure 8.3: Annual FTE changes. (*left:*) total FTEs (scientists, engineers, and technicians) split by their projects (maintenance/upgrade of existing instruments (including HSC), PFS, and ULTIMATE-Subaru). (*right:*) FTEs for technicians, engineers, and scientists for existing instruments and PFS and those for ULTIMATE-Subaru.

8.2 Budget and Funds

8.2.1 Cost for GLAO development

Table 8.1 shows the rough estimate of costs required to build the GLAO system for Subaru Telescope. The costs for Adaptive Secondary Mirror (ASM) and laser system are based on preliminary discussions with vendors and are not based on actual quotes nor vendor proposals. The cost estimate for wavefront sensor system comes from past experiences and unofficial communications with vendors.

This estimate does not include costs for additional human resources.

One large uncertainty in the cost estimate lies in that for the telescope modifications. Those include (1) modifications around top-ring of the telescope required for accepting ASM, (2) modifications around the Cassegrain focus to enlarge the field-of-view, and (3) telescope software modifications. These modifications will be made through contract with Mitsubishi Electric Co (MELCO). In FY2012 MELCO made a conceptual study on the enlargement of the Cassegrain focus field-of-view, and their very preliminary cost estimate is 600 M JPY (∼7.2 M USD with the current exchange rage) in three years. The modifications required for the installation of ASM are not yet discussed with MELCO. The discussion among the ASM builder, telescope builder (MELCO), and Subaru Telescope is needed to identify the interface and defining responsibilities. The control of ASM as a part of GLAO system will be done independently from the telescope control software, and the software development for the GLAO system will be done by the development team as a part of the GLAO system.

Item	Cost (M USD)	Notes
Adaptive Secondary Mirror	5.0	
Laser system	3.0	
Wavefront sensor system	3.5	
Computers	0.2	
Subtotal	11.7	
Telescope modifications	10.0	
Contingency (∼20%)	4.0	
GLAO system total	25.7	

Table 8.1: Budget plan for GLAO development

8.2.2 Cost for wide-field imager development

Currently no cost estimate has been made. While in the technical note by John Pazder (HIA/NRC) about 18 M$ is mentioned as the total cost for the wide-field imager, we need to determine the conceptual design of the instrument to have a cost estimate. We plan to start preliminary opt-mechanical design study in FY2016, and that will give us some basic idea of cost required. Note that the wide-field corrector for Multi-IFU system could be shared with the wide-field imager.

8.2.3 Cost for multi-IFU spectrograph development

AAO is proposing the conceptual study and proto-typing to address the major technical risks and obtain better estimate of total costs required for the multi-object IFS. The cost estimated for this conceptual study, proto-typing and testing is 570,000 AUD (concept development and proto-typing)+ 200,000 AUD (tests at AAT and Subaru).

AAO defers to perform detailed cost estimate for the entire project until proto-typing and testing are completed. The rough estimate of $5 to $7 million USD has been mentioned.

8.2.4 Funding sources

The total cost required for ULTIMATE-Subaru (both GLAO and instrument development) will be approximately 40–50 million USD. Subaru Telescope operation budget does not include funds for the development. Any recent instrument development projects have been asked to obtain external funds. However, ULTIMATE-Subaru working group believes that for the GLAO system development, Subaru telescope's operation budget should be a primary source of funds, for two reasons.

1. The GLAO system is an upgrade of the Subaru telescope. It brings seeing improvement to all existing and future instruments. Such upgrade of fundamental improvement of the telescope capabilities should be performed in a responsibility of Subaru Telescope / NAOJ.

2. What the GLAO system provides is the seeing improvement in a wide field-of-view, and that should have a great benefit to various science goals. However, obtaining external funds such as JSPS Kakenhi requires immediate science goals which will be achieved by the program. Since the cost required for the GLAO system and instruments exceed the size of the major JSPS Kakenhi programs (about 10 million USD), if we submit the proposal for the GLAO development, that will not contain the new instrument development, and enhancement of scientific capability is significantly limited without new wide-field instruments.

Although we expect major funds from Subaru/NAOJ operation budget, for FY2016 two Kakenhi proposals have been submitted. One is a new frontier proposal (PI: Hideki Takami). The proposal is a collaboration with biology group, and laser tomography development for Subaru Telescope is included as a part of next-generation AO development. Expected budget to be allocated for Subaru AO development is 3.6 M USD in five years. Another proposal is 'S'-class research project to understand the formation history of galaxies (PI: Nobuo Arimoto). This proposal includes installation of fibre laser system (as an upgrade of AO188 laser system) and development of laser tomography. The expected size of the budget is 1.6 M USD in five years.

For the instrument development part, we expect a primary contributions from the external institutes, but we will work closely with other institutes to obtain external funds (in Japan and overseas).

8.3 Timeline

Here we describe the expected timeline for the development of three components of ULTIMATE-Subaru, i.e., GLAO, wide-field imager (WFI), and multi-object IFU spectrograph (M-IFS). We wish to commence the engineering observations of the GLAO system in early 2020s so that Subaru Telescope become ready for the epoch when ELTs start science operations.

For the GLAO and WFI about 1–1.5 years for both of conceptual and preliminary design studies, and about two years for detailed design are assumed. After the critical design review (CDR), 2–2.5 years will be required for fabrication, and two years for assembly, integration and testing. One caveat for the GLAO development is that the fabrication of ASM will require more than two years, and in order to reach the engineering first light in 2023, we need to start fabrication of ASM *before* we pass the CDR for the entire GLAO system. We consider that is possible if we can clearly set the specifications of ASM and define the interface between ASM and other GLAO system components (and telescope system). We would need to have a separate sub-system CDR for ASM. We consider the major funding source for the GLAO system (including ASM) is Subaru Telescope's operation budget from NAOJ / Japanese government (as a telescope upgrade project). Because Subaru / NAOJ will continue to have large investment for PFS until FY2018, the production of ASM will not be started after 2019.

The technical issues required to be addressed during the Conceptual design phase for GLAO and telescope modifications are described in Section 6.

For wide-field imager (and multi-object spectrograph), as we describe in Section 7.1 and 7.2, the design study is still in early stage. We have some optical designs which will be able to provide performance required from the science cases, but feasibility to be built as instrument, mechanically and opt-mechanically

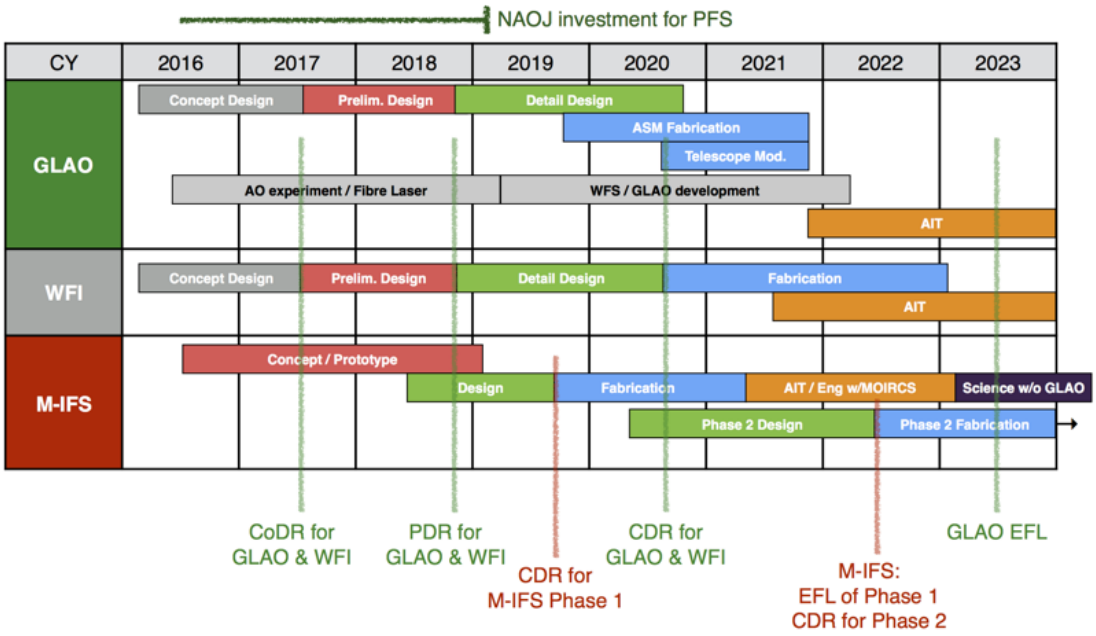

Figure 8.4: Timeline of the ULTIMATE-Subaru project.

has not been examined. Such feasibility study should be the items we need to carry out as the next step for these instrument concepts.

For M-IFS two-step development is conisdered; first we will develop the fibre positioners using Starbug technology, the wide-field corrector, and necessary optical and fibre components to use MOIRCS as a spectrograph. This is called Phase 1. Then if we successfully design the Phase 1 instrument and if the funds are available, we will proceed to consider a new spectrograph optimized for fibre IFUs and possibly incorporate some new technologies (Phase 2). In Fig. 8.4 we show three phases; conceptual study / prototyping (Stage 2 of Phase 1), design, fabrication, AIT and commissioning for Phase 1 instrument (Stage 3 of Phase 1), and Phase 2. Because M-IFS can carry out unique science observations even without GLAO, we think this instrument can start science operations ahead of the GLAO commissioning to science observations.

The technical issues need to be addressed by the prototyping for M-IFS are follows (based on inputs from the AAO team):

- **Bug-catcher.** A concept will be developed to place starbugs on an upwards looking curved field plate. This may involve tumbling the field plate, designing a special bug-catcher than can retract away from the bugs on a curved plate, or possibly another solution not based on the TAIPAN bug-catcher.
- **Starbugs.** Starbugs of the size and mass necessary for ULTIMATE will be built and tested.
- **IFU.** An entire IFU, including fore-optics, microlens array, fibre array and mating with the starbugs will be built and tested. One of the main issues to be tested here is the assembly of the fibre array. Image quality and thermal emission will be measured.
- **Fibres.** Fibre transmission will be tested for various fibre types. This will include thorough tests of the K band fibres, including FRD, end face preparation, thermal emission and handling.
- **Slit unit.** The packing of the fibres along the slit will be analysed thoroughly, in order to maximise the number of fibres whilst maintaining the ability to extract the spectra without contamination from adjacent fibres.

References

Chapter 3: High-z science cases with imaging

Brammer, G. B., van Dokkum, P. G., Franx, M., et al. 2012, ApJS, 200, 13

Carilli, C. L., Wang, R., Fan, X., et al. 2010, ApJ, 714, 834

Chiang, Y.-K., Overzier, R., & Gebhardt, K. 2013, ApJ, 779, 127

Förster Schreiber, N. M., Genzel, R., Bouché, N., et al. 2009, ApJ, 706, 1364

Hayashi, M., Kodama, T., Koyama, Y., et al. 2010, MNRAS, 402, 1980

Hayashi, M., Kodama, T., Tadaki, K.-i., Koyama, Y., & Tanaka, I. 2012, ApJ, 757, 15

Iye, M., Ota, K., Kashikawa, N., et al. 2006, Nature, 443, 186

Kashikawa, N., Shimasaku, K., Malkan, M. A., et al. 2006, ApJ, 648, 7

Kashikawa, N., Shimasaku, K., Matsuda, Y., et al. 2011, ApJ, 734, 119

Kobayashi, M. A. R., Totani, T., & Nagashima, M. 2010, ApJ, 708, 1119

Kobayashi, M. A. R., Totani, T., & Nagashima, M. 2007, ApJ, 670, 919

Kodaira, K., Taniguchi, Y.,Kashikawa, N., et al. 2003, PASJ, 55, L17

Kodama, T., Tanaka, I., Kajisawa, M., et al. 2007, MNRAS, 377, 1717

Komatsu, E., Smith, K. M., Dunkley, J., et al. 2011, ApJS, 192, 18

Konno, A., Ouchi, M., Ono, Y., et al. 2014, ApJ, 797, 16

Koopmann, R. A., Haynes, M. P., & Catinella, B. 2006, AJ, 131, 716

Koyama, Y., Kodama, T., Tadaki, K.-i., et al. 2014, ApJ, 789, 18

Koyama, Y., Smail, I., Kurk, J., et al. 2013, MNRAS, 434, 423

Koyama, Y., Kodama, T., Tadaki, K.-i., et al. 2013, MNRAS, 428, 1551

Lawrence, A., Warren, S. J., Almaini, O., et al. 2007, MNRAS 379, 1599

McCraken, H. J., Milvang-Jensen, B., Dunlop, J., et al. 2012, A& A 544, A156

Mortlock, D. J., Warren, S. J., Venemans, B. P., et al. 2011, Nature, 474, 616

Muzzin, A., Marchesini, D., Stefanon, M., et al. 2013, ApJ, 777, 18

Nelson, E. J., van Dokkum, P. G., Momcheva, I. G., et al. 2015, arXiv:1511.04443

Ouchi, M., Shimasaku, K,, Akiyama, M., et al. 2005, ApJ 620, L1

Ouchi, M., Shimasaku, K., Akiyama, M., et al. 2008, ApJS, 176, 301

Papovich, C., Bassett, R., Lotz, J. M., et al. 2012, ApJ, 750, 93

Shibuya, T., Kashikawa, N., Ota, K., et al. 2012, ApJ, 752, 114

Sobral, D., Smail, I., Best, P. N., et al. 2013, MNRAS, 428, 1128

Stark, D. P., Richard, J., Charlot, S, et al. 2015, MNRAS, 450, 1846

Straatman, C. M. S., Labbé, I., Spitler, L. R., et al. 2014, ApJL, 783, L14

Suzuki, T. L., Kodama, T., Tadaki, K.-i., et al. 2015, ApJ, 806, 208

Swinbank, A. M., Smail, I., Sobral, D., et al. 2012, ApJ, 760, 130

Swinbank, A. M., Sobral, D., Smail, I., et al. 2012, MNRAS, 426, 935

Tadaki, K.-i., Kodama, T., Ota, K., et al. 2012, MNRAS, 423, 2617

Tadaki, K.-i., Kodama, T., Tanaka, I., et al. 2014, ApJ, 780, 77

Tadaki, K.-I., Kodama, T., Koyama, Y., et al. 2011, PASJ, 63, 437

Tanaka, I., Breuck, C. D., Kurk, J. D., et al. 2011, PASJ, 63, 415

Taniguchi, Y., Ajiki, M., Nagao, T., et al. 2005, PASJ, 57, 165

Toshikawa, J., Kashikawa, N., Ota, K., et al. 2012, ApJ, 750, 137

Trac, H., & Cen, R. 2007, ApJ, 671, 1

Tran, K.-V. H., Papovich, C., Saintonge, A., et al. 2010, ApJL, 719, L126

van Dokkum, P. G., Whitaker, K. E., Brammer, G., et al. 2010, ApJ, 709, 1018

van Dokkum, P. G., Leja, J., Nelson, E. J., et al. 2013, ApJL, 771, L35

Whitaker, K. E., van Dokkum, P. G., Brammer, G., & Franx, M. 2012, ApJL, 754, L29

Wisnioski, E., Glazebrook, K., Blake, C., et al. 2012, MNRAS, 422, 3339

Wuyts, S., Förster Schreiber, N. M., Nelson, E. J., et al. 2013, ApJ, 779, 135

Chapter 4: High-z science cases with spectroscopy

Akiyama, M., Ueda, Y., Watson, M.G., et al. 2015, PASJ, in press

Alexander, D.M., Chary, R.R., Pope, A., et al.. 2008, ApJ, 687, 835

Bryant, J. J., Owers, M. S., Robotham, A. S. G., et al. 2015, MNRAS, 447, 2857

Christensen, L. Laursen, P., Richard, J., et al. 2012, MNRAS, 427, 1973

Croom, S. M., Lawrence, J. S., Bland-Hawthorn, J., et al. 2012, MNRAS, 421, 872

Dijkstra, M., and Wyithe, J. S. B., 2010, MNRAS, 408, 352

Duval, F., Schaerer, D. Östlin et al., 2014, A&A, 562A, 52

Erb, D. K., Pettini, M., Shapley, A. E., et al. 2010, ApJ, 719, 1168

Erb, D., Steidel, C. C., Trainor, R. F. et al. 2014, ApJ, 795, 33

Erb, D., 2015, Nature, 523, 169

Fiore, F., Grazian, A., Santini, P., et al. 2008, ApJ, 672, 94

Förster Schreiber, N. M., Genzel, R., Newman, S. F., et al. 2014, ApJ, 787, 38

Hashimoto, T., Ouchi, M., Shimasaku et al. 2013, ApJ, 765, 70

Hashimoto, T., Verhamme, A., Ouchi, M. et al., 2015, arXiv150403693

Ho, I.-T., Kudritzki, R.-P., Kewley, L. J., et al. 2015, MNRAS, 448, 2030

Izotov, Y. I., Stasińska, G., Meynet, G., et al. 2006, A&A, 448, 955

James, B. L., Pettini, M., Christensen, L., et al. 2014, MNRAS, 440, 1794

Jones, T. A., Ellis, R. S., Schenker et al. 2013, ApJ, 779, 52

Jones, T., Martin, C., & Cooper, M. C. 2015, ApJ accepted, ArXiv e-prints, arXiv:1504.02417

Kakazu, Y, Cowie, L. L., & Hu, E. M. 2007, ApJ, 668, 853

Kewley, L. J., Dopita, M. A., Leitherer, C., et al. 2013, ApJ, 774, 100

Kewley, L. J., Dopita, M. A. 2002, ApJS, 142, 35

Kriek, M., Shapley, A. E., Reddy, N. A., et al. 2015, ApJS, 218, 15

Lara-López, M. A., Cepa, J., Bongiovanni, A., et al. 2010, A&A, 521, L53

Lilly, S. J., Carollo, C. M., Pipino, A., et al. 2013, ApJ, 772, 119

Malizia, A., Stephen, J.B., Bassani, L., et al. 2009, MNRAS, 399, 944

Mannucci, F., Cresci, G., Maiolino, R., et al. 2010, MNRAS, 408, 2115

Marconi, A., Risaliti, G., Gilli, R., et al. 2004, MNRAS, 351, 169

Martinez-Sansigre, A., Rawlings, S., Bonfield, D.G., et al. 2007, MNRAS, 379, 6

Masters, D., McCarthy, P., Siana, B., et al. 2014, ApJ, 785, 153

Nagao, T., Maiolino, R., & Marconi, A. 2006, A&A, 459, 85

Nakajima, K., & Ouchi, M. 2014, MNRAS, 442, 900

Nelson, E. J., van Dokkum, P. G., Förster Schreiber, N. M., et al. 2015, arXiv:1507.03999

Peng, Y.-j., Lilly, S. J., Kovač, K., et al. 2010, ApJ, 721, 193

Pettini, M., Pagel, B. E. J. 2004, MNRAS, 348, L59

Polletta, M.dC., Wilkes, B. J., Siana, B., et al. 2006, ApJ, 642, 673

Reddy, N. A., Kriek, M., Shapley, A. E., et al. 2015, ApJ, 806, 259

Rigby, J. R., Wuyts, E., Gladders, M. D., et al. 2011, ApJ, 732, 59

Saintonge, A., Tacconi, L. J., Fabello, S., et al. 2012, ApJ, 758, 73

Salim, S., Rich, R. M., Charlot, S., et al. 2007, ApJS, 173, 267

Schenker, M. A., Ellis, R. S., Konidaris et al. 2013, ApJ, 777, 67

Shapley, A. E., Steidel, C. C., Pettini, M. et al. 2003, ApJ, 588, 65S,

Shapley, A. E., Reddy, N. A., Kriek, M., et al. 2015, ApJ, 801, 88

Shibuya, T., Ouchi, M., Nakajima et al. 2014, ApJ, 788, 74

Shimakawa, R., Kodama, T., Tadaki, K.-i., at al. 2015, MNRAS, 448, 666

Shirazi, M., Brinchmann J., & Rahmati A. 2014, ApJ, 787, 120

Silverman, J. D., Kashino, D., Sanders, D., et al. 2015, ApJS, 220, 12

Skelton, R. E., Whitaker, K. E., Momcheva, I. G., et al. 2014, ApJS, 214, 24

Stark, D. P., Johan, R., Stéphane, C. et al. 2015, MNRAS, 450, 1846

Steidel, C. C., Erb, D. K., Shapley et al. 2010, ApJ, 717, 289

Steidel, C. C., Rudie, G. C., Strom, A. L., et al. 2014, ApJ, 795, 165

Strauss, M. A., Weinberg, D. H., Lupton, R. H., et al. 2002, AJ, 124, 1810

Tacchella, S., Carollo, C. M., Renzini, A., et al. 2015, Sci, 348, 314

Tadaki, K., Kohno, K.,; Kodama, T., et al. 2015, ApJL, 811, 3L

Takada, M., Ellis, R. S., Chiba, M., et al. 2014, PASJ, 66, 1

Trainor, R. F., Steidel, C. C., Strom et al. , 2015, ApJ, 809, 89

Tran, K.-V. H., Nanayakkara, T., Yuan, T., et al. 2015, ApJ, 811, 28

Tremonti, C. A., Heckman, T. M., Kauffmann, G., et al. 2004, ApJ, 613, 898

Ueda, Y., Eguchi, S., Terashima, Y., et al. 2007, ApJ, 664, 79

Ueda, Y., Akiyama, M., Hasinger, G., et al. 2014, ApJ, 786, 104

Verhamme, A., Schaerer, D., Maselli, A., 2006, A&A, 460, 397

Vignali, C., Alexander, D.M., Gilli, R., et al. 2010, MNRAS, 404, 48

Villar-Martín, M., Cerviño, M., & Delgado, R. M. G. 2004, MNRAS, 355, 1132

Wisnioski, E., Förster Schreiber, N. M., Wuyts, S., et al. 2015, ApJ, 799, 209

Wuyts, S., Förster Schreiber, N. M., van der Wel, A., et al. 2011, ApJ, 742, 96

Wuyts, S., Förster Schreiber, N. M., Genzel, R., et al. 2012, ApJ, 753, 114

York, D. G., Adelman, J., Anderson, Jr., J. E., et al. 2000, AJ, 120, 1579

Yuan, T. T., & Kewley, L. J. 2009, ApJ, 699, L161

Yuan, T.-T., Kewley, L. J., & Rich, J. 2013, ApJ, 767, 106

Zahid, H. J., Dima, G. I., Kudritzki, R.-P., et al. 2014, ApJ, 791, 130

Zakamska, N.L., Strauss, M.A., Krolik, J.H., et al. 2003, ApJ, 126, 2125

Zakamska, N.L., Gomez, L., Strauss, M.A., et al. 2008, AJ, 136, 1607

Zeimann, G. R., Ciardullo, R., Gebhardt, H., et al. 2015, ApJ, 798, 29

Chapter 5: Low-z and Galactic science cases

Alexander, T. 2005, Physical Reports, 419, 65

Allard, F. et al., 2001, ApJ, 556, 357

Baba, J., Saitoh, T. R., and Wada, K. 2013, ApJ, 763, 1.

Bartko, H., et al. 2010, ApJ, 708, 834

Bally, J., & Devine, D. 1994, ApJ, 428, L65

Bally, J., O ' Dell, C. R., & McCaughrean, M. J. 2000, AJ, 119, 2919

Bally, J., Ginsburg, A., Silvia, D., & Youngblood, A. 2015, A & A, 579, A130

Baraffe, I., Chabrier, G., Barman, T. S., Allard, F., & Hauschildt, P. H. 2003, A&A, 402, 701

Bate et al. 2003, MNRAS, 339, 577

Benjamin, R. A. et al. 2003, PASP, 115, 953

Blum, R. D., Ramírez, S. V., Sellgren, K., & Olsen, K. 2003, ApJ, 597, 323

Böker, T. 2010, in IAU Symposium, Vol. 266, IAU Symposium, ed. R. de Grijs & J. R. D. Lépine, 58–63

Bono et al. 2005, ApJ, 621, 966

Brown, A. G. A. 2014, EAS Publications Series, 67, 307

Brown, W. R., Geller, M. J., Kenyon, S. J., & Kurtz, M. J. 2005, ApJL, 622, L33

Buchholz, R. M., Schödel, R., & Eckart, A. 2009, A&A, 499, 483

Burrows, A. et al. 1997, ApJ, 491, 856

Butcher, H., & Oemler, A., Jr. 1984, ApJ, 285, 426

D. Calzetti et al., 2000, ApJ 533, 682

Carlberg, R. 2012, ApJ, 748, 20

Carollo, C. M., Stiavelli, M., & Mack, J. 1998, AJ, 116, 68

Christlein, D., & Zabludoff, A. I. 2004, ApJ, 616, 192

aClarkson, W., Ghez, A., Morris, M., Lu, J., Stolte, A., McCrady, N., Do, T., & Yelda, S. 2011, ArXiv e-prints

Côté, P., et al. 2006, ApJS, 165, 57

Cluver, M. E., Appleton, P. N., Boulanger, F., et al. 2010, ApJ, 710, 248.

Davies et al. 2009, ApJ, 696, 2014

Davies et al. 2012, MNRAS, 419, 1860

de Jong, R. S. 1996, 313, 377.

Dekany et al. 2015, ApJL, 799, L11

Desai, V., Dalcanton, J. J., Aragón-Salamanca, A., et al. 2007, ApJ, 660, 1151

De Silva, G. M., Freeman, K. C., Bland-Hawthorn, J., et al. 2015, MNRAS, 449, 2604

D'Onghia, E., Vogelsberger, M., & Hernquist, L. 2013, ApJ, 766, 34.

Eckart, A., & Genzel, R. 1996, Nature, 383, 415

Eggen, O. J. et al. 1962, ApJ, 136, 748

Epstein, C. R., Elsworth, Y. P., Johnson, J. A., et al. 2014, ApJL, 785, L28

Erwin, P., & Gadotti, D. A. 2012, Advances in Astronomy, 2012

Eyre, A. & Binney, J. 2009, MNRAS, 400, 54

Feast et al. 2014, Nature, 509, 342

Ferrarese, L., et al. 2006, ApJL, 644, L21

Ferraro, F. R. et al. 2009, Nat, 462, 483

Friel & Janes, 1993, A&A, 267, 75

Froebrich, D., et al. 2011, MNRAS, 413, 480

Garay, G., Mardones, D., & Rodríguez, L. F. 2000, ApJ, 545, 861

García-Burillo, S., Martín-Pintado, J., Fuente, A., & Neri, R. 2001, ApJL, 563, L27

Gazak et al. 2014, ApJ, 788, 58

Geach, J. E., Smail, I., Ellis, R. S., et al. 2006, ApJ, 649, 661

Genovali et al. 2014, A&A, 566, A37

Genovali et al. 2015, A&A, 580, A17

Genzel, R., et al. 2003, ApJ, 594, 812

Gerhard, O. 2001, ApJL, 546, L39

Ghez, A. M., Morris, M., Becklin, E. E., Tanner, A., & Kremenek, T. 2000, Nature, 407, 349

Gillessen, S., Eisenhauer, F., Trippe, S., Alexander, T., Genzel, R., Martins, F., & Ott, T. 2009, ApJ, 692, 1075

Gilmore, G., Randich, S., Asplund, M., et al. 2012, The Messenger, 147, 25

Gonzalez, O. A., Rejkuba, M., Zoccali, M., et al. 2012, A&A, 543, A13

Gould, A., Huber, D., Penny, M., & Stello, D. 2015, Journal of Korean Astronomical Society, 48, 93

Graham, A. W., & Spitler, L. R. 2009, MNRAS, 397, 2148

Guillard, P., Boulanger, F., Pineau des FOrtets, G., et al. 2012, ApJ, 749, 158

Gürkan, M. A., & Rasio, F. A. 2005, ApJ, 628, 236

Harris, W. E. 2001, in Star Clusters, Saas-Fee Advanced Course 28, eds. L. Labbardt & B. Binggeli

Hayashi, M., & Pyo, T.-S. 2009, ApJ, 694, 582

Hayden et al. 2014, AJ, 147, 116

Haywood et al. 2013, A&A, 560, A109

Hillenbrand, L. A. 1997, AJ, 113, 1733

Hills, J. G. 1988, Nature, 331, 687

Itoh, Y., Tamura, M., & Gatley, I. 1996, ApJL, 465, L129

Itoh, Y. et al. 2002, PASJ, 54, 561

Itoh, Y. et al., 2005, ApJ, 620, 984

Ivezic et al. 2012, ARA&A, 50, 251

Jacobson et al. 2011, AJ, 142, 59

Jeffries, R.D., 2012 EAS Pub Series, 57, 45

Koda, J., Scoville, N., Sawada, T., et al. 2009, ApJL, 700, 132.

Kodama, T., & Smail, I. 2001, MNRAS, 326, 637

S. Komugi et al., 2012, ApJ, 757, 128

Kouwenhoven & Goodwin 2010, IAUS, 262, 368

Koyama, Y., Kodama, T., Shimasaku, K., et al. 2008, MNRAS, 391, 1758

Krabbe, A., et al. 1995, ApJL, 447, L95

Kunder, A., Koch, A., Rich, R. M., et al. 2012, AJ, 143, 57

Lee, J.-J., Koo, B.-C., Lee, Y.-H., et al. 2014, MNRAS, 443, 2650

Li, Y., Luo, A., Zhao, G., Lu, Y., Ren, J., & Zuo, F. 2012, ApJL, 744, L24

Lu, J. R., Do, T., Ghez, A. M., Morris, M. R., Yelda, S., & Matthews, K. 2013, ApJ, 764, 155

Lucas, P., & Roche, P. 2000, MNRAS, 314, 858

Luhman, K. L. et al. 2005, ApJ, 635, 93

Kurtev, R. et al. 2008, A&A, 489, 583

MacArthur, L. A., Courteau, S., Bell, E., & Holtzman, J. A. 2004, ApJS, 152, 175.

Maness, H., et al. 2007, ApJ, 669, 1024

Maraston, C. 1998, MNRAS, 300, 872.

Marsh, K.A et al. 2010, AJ, 719, 550

Masunaga, H. & Inutsuka, S. 1999, PASJ, 510, 822

Matsunaga et al. 2011, Nature, 477, 188

Matsunaga, 2014, EAS Publications Series, 67–68, pp. 279–282

McGroarty, F., & Ray, T. P. 2004, A&A, 420, 975

Meier, D. S., & Turner, J. L. 2005, ApJ, 618, 259

Melding, A. M., U., V., Rich, J. A., Kewley, L. J., Armus, L., Dopita, M. A., Max, C. E., Sanders, D. Sutherland, R. 2015, MNRAS, 448, 2301.

Minniti, D. et al. 2010, New A., 15, 433

Moni Bidin, C. et al. 2011, A&A, 535, A33

Mouri, H. 1994, ApJ, 427, 777.

Nataf, D. M., Gonzalez, O. A., Casagrande, L., et al. 2015, arXiv:1510.01321

Ness, M., Freeman, K., Athanassoula, E., et al. 2012, ApJ, 756, 22

Neumayer, N., & Walcher, C. J. 2012, Advances in Astronomy, 2012, 15

Nishiyama, S., & Schödel, R. 2013, A&A, 549, A57

Nishiyama, S., Schoedel, R., Yoshikawa, T., Nagata, T., Minowa, Y., & Tamura, M. 2015, ArXiv e-prints

Nishiyama, S., Nagata, T., Tamura, M., et al. 2008, ApJ, 680, 1174

Oasa, Y. et al. 1999, ApJ, 526, 336

Oasa, Y. et al. 2006, AJ, 131, 1068

Oasa, Y. et al. 2008, AJ, 136, 1372

D. Obreschkow et al., ApJ submitted / arXiv:1508.04768 (2015)

Odenkirchen, M. et al. 2003, AJ, 126, 2385

Origlia et al. 2013, A&A, 560, A46

Origlia et al. 2015, arXiv1510.06870

Ortolani, S. et al. 2011, ApJ, 737, 31

Padoan, P. & Nordlund, A. 2004, ApJ, 617, 559

Paumard, T., et al. 2006, ApJ, 643, 1011

Perryman, M. A. C. 2005, Astrometry in the Age of the Next Generation of Large Telescopes, 338, 3

Peterson, B. W., Appleton, P. N., Helou, G., et al. 2012, ApJ, 751, 11.

Pfuhl, O., et al. 2011, ApJ, 741, 108

Portail, M., Wegg, C., Gerhard, O., & Martinez-Valpuesta, I. 2015, MNRAS, 448, 713

Portegies Zwart, S. F., Makino, J., McMillan, S. L. W., & Hut, P. 2002, ApJ, 565, 265

Portegies Zwart, S. F., McMillan, S. L. W., & Gieles, M. 2010, ARA&A, 48, 431

Reipurth, B., & Bally, J. 2001, ARA&A, 39, 403

Reipurth, B., Bally, J., Fesen, R. A., & Devine, D. 1998, Nature, 396, 343

Reipurth, B., Yu, K. C., Heathcote, S., Bally, J., & Rodriguez, L. F. 2000, AJ, 120, 1449

Roberts, W. W. 1969, ApJ, 158, 123.

Salpeter, E. E. 1955, ApJ, 121, 161

Sandage & Tammann, 2006, ARA&A, 44, 93

Schödel, R. 2015, ArXiv e-prints

Schödel, R., Feldmeier, A., Kunneriath, D., Stolovy, S., Neumayer, N., Amaro-Seoane, P., & Nishiyama, S. 2014, A&A, 566, A47

Schönrich, R., & Binney, J. 2009, MNRAS, 396, 203

Searle, L. & Zinn, R. 1978, ApJ, 225, 357

Seth, A., Agüeros, M., Lee, D., & Basu-Zych, A. 2008, ApJ, 678, 116

Shull, J. M., & Draine, B. T. 1987, in Interstellar Processes, ed. D. J. Hollenbach & H. Thronson, Jr. (Dordrecht: Reidel), 283.

Silva Aguirre, V., Davies, G. R., Basu, S., et al. 2015, MNRAS, 452, 2127

Skrutskie, M. F. et al. 2006, AJ, 131, 1163

Spergel, D., Gehrels, N., Baltay, C., et al. 2015, arXiv:1503.03757

Stamatellos, D., & Whitworth, A. P. 2009, MNRAS, 392,413

Stolte, A., Ghez, A. M., Morris, M., Lu, J. R., Brandner, W., & Matthews, K. 2008, ApJ, 675, 1278

Takagi, Y., Itoh, Y., Oasa, Y., Sugitani, K. 2011, PASJ, 63, 677

Takaraha, Y. 2014, Master thesis

K. Tateuchi et al., 2015, ApJS 217, 1

K. Tateuchi, PhD Thesis, University of Tokyo (2015)

Tsuji, T. et al., 2004, ApJ, 607, 511

Tsujimoto et al. 2010, PASJ, 62, 447

Twarog et al. 1997, AJ, 114, 2556

Usuda, T., Sugai, H., Kawabata, H., Inoue, M. Y., Kataza, H., & Tanaka, M. 1996, ApJ, 464, 818.

Yu, Q., & Tremaine, S. 2003, ApJ, 599, 1129

Zapatero Osorio, M. R. et al. 2000, Science, 290, 103

Zasowski, G., Johnson, J. A., Frinchaboy, P. M., et al. 2013, AJ, 146, 81

Chapter 6: Adaptive Optics

Andersen, R. A., Jackson, K.J., Blain, C., et al. 2012, PASP, 124:469–484

Chun, M., Wilson, R., Avila, R., et al./ 2009, MNRAS 394:1121-1130

Els, S.G., Trouvaillon, T., Schöck, M., et al. 2009, PASP, 121:527-543

Lai, O., Chun, M., Cuillandre,J. C., et al. 2008, SPIE, 7015, 4H

Lai, O., Lai, O., Chun, M., Pazder, J.,et al. 2010, SPIE 7736, 1D

Oya, S., Akiyama, M., Hayano, Y., et al. 2012, SPIE 8847, 3V.

Oya, S., Hayano, Y., Lai., O., etal. 2014, SPIE 9148, 6G

Oya, S., 2015, Journal of Physics: Conference Series 595: Adapting to the Atmosphere 012024

Schöck, M., Els, S., Reedle, R., et al. 2009, PASP, 121:384-395

Tokovinin, A.,2004, PASP, 116:941–951

Tokovini, A., Vernin, J., Ziad, A., Chun, M., et al. 2005, PASP, 117:395-400

Chapter 7: Instruments for ULTIMATE-Subaru

Cardamone, C. N. et al. 2010, ApJS, 189, 270

Cassata, P. et al. 2010, ApJL, 714, L79

Ellis, S., Zhelem, R., Brown, D., et al. 2015, ULTIMATE Instrument Concept and Prototyping Plan

Kennicutt, R. C., Jr. 1998, ARA&A, 36, 189

Kissler-Patig, M., Pirard, J. F., Casali, M., et al. 2008, A&A, 491, 941

Koekemoer, A. M. et al. 2011, ApJS, 197, 36

McLean, I. S., Steidel, C. C., Epps, H., et al. 2010, Proc. SPIE, 7735

Oya, S. et al. 2014, Proc. SPIE, 8447

Wright, S. A. et al. 2010, Proc. SPIE, 7735

Yuma, S. et al. 2012, ApJ, 761, 19